

Application of Layered High Entropy Oxides as Cathode Materials for Li/Na-ion Batteries

1. Lithium/Sodium-ion Batteries; Cathode Material; Electrochemical Properties; Cyclic Voltammetry

2. High Entropy Compounds; Layered Transition Metal Oxide; Phase Transformation



TECHNISCHE
UNIVERSITÄT
DARMSTADT

Vom Fachbereich Material- und Geowissenschaften
der Technischen Universität Darmstadt

zur Erlangung des akademischen Titels Doktor-Ingenieur (Dr.-Ing.)

genehmigte Dissertation von
M.Sc. Junbo Wang geboren in People's Republic of China

1. Gutachten: Prof. Dr. -Ing. Horst Hahn
2. Gutachten: Prof. Dr. Ulrike Kramm

Darmstadt 2022

Junbo Wang: Application of Layered High Entropy Oxides as Cathode Materials for Li/Na-ion
Batteries

Darmstadt, Technische Universität Darmstadt,

published in TUprints 2022

Date of the viva voce 25.07.22

Published under CC BY-SA 4.0 International

<https://creativecommons.org/licenses/>

Erklärung zur Dissertation

Hiermit versichere ich, dass ich meine Dissertation selbstständig und nur mit den angegebenen Quellen und Hilfsmitteln angefertigt habe. Diese Arbeit hat in gleicher oder ähnlicher Form noch keiner Prüfungsbehörde vorgelegen.

Junbo Wang

Darmstadt, 05.09.2022

Abstract

With the increasing fossil energy consumptions and environmental concerns, new sustainable energy sources and new energy storage fields are playing increasingly important roles in modern society. A series of energy storage devices such as lithium-ion batteries (LIBs) and sodium-ion batteries (SIBs) have received global attentions from researchers and urgent demands for social developments. In LIBs/SIBs, the cathode material as the main component is critical factor affecting the property of full cells presently. As one of the earliest systems, layered oxide cathode materials have good commercial prospects until to now, therefore, a lot of strategies, such as new materials developing, elemental doping and surface coating, etc., have been explored to improve the electrochemical performance of them. To develop novel electrode materials and inspired by the design concept of high entropy alloys (HEAs), high entropy oxides (HEOs) as a new class of material were developed in recent years and studied as an anode material for LIBs starting in 2018. It shows unexpected reversibility compared to other non-high entropy compositions due to the unique entropy stability property. Subsequently, increasing number of researches have been reported on the use of high entropy materials in energy storage devices. The virtually infinite variety of multi-elemental compositions for a single-phase structure allows the tailoring of their physical properties and enables unprecedented materials design. A series of HEOs were prepared by nebulized spray pyrolysis (NSP) and solid-state reaction in this work. In order to explore the use of HEOs in LIBs/SIBs, the terms of materials design, synthesis method, crystal structure evolutions accompanied with charge compensation and electrochemical performance of HEOs are studied.

The transfer of the high entropy concept to electrode materials may provide new strategies and technologies for material design and the preparation of novel compounds with unprecedented properties. Based on these results, it can be expected that the high entropy strategy can open new insights into electronic and structural chemistry for advanced electrode materials.

Zusammenfassung / Abstract

Angesichts des steigenden Verbrauchs fossiler Brennstoffe und der damit verbundenen Umweltprobleme spielen neue nachhaltige Energiequellen und neue Energiespeicher eine immer wichtigere Rolle in der modernen Gesellschaft. Eine Reihe von Energiespeichern wie Lithium-Ionen-Batterien (LIBs) und Natrium-Ionen-Batterien (SIBs) haben die Aufmerksamkeit von Forschern weltweit auf sich gezogen und werden für gesellschaftliche Entwicklungen dringend benötigt. Bei LIBs/SIBs ist das Kathodenmaterial als Hauptbestandteil ein entscheidender Faktor, der die Eigenschaften der Zellen beeinflusst. Als eines der ersten Systeme haben geschichtete Oxidkathodenmaterialien bisher gute kommerzielle Aussichten, so dass viele Strategien wie die Entwicklung neuer Materialien, Elementdotierung und Oberflächenbeschichtung usw. erforscht wurden, um ihre elektrochemische Leistung immer weiter zu verbessern. Um neuartige Elektrodenmaterialien zu entwickeln, wurden in den letzten Jahren, inspiriert durch das Designkonzept von Hochentropie-Legierungen (HEAs), Hochentropie-Oxide (HEOs) als neue Materialklasse entwickelt und ab 2018 als Anodenmaterialien für LIBs untersucht. Aufgrund ihrer einzigartigen Entropiestabilität und den interelementaren Wechselwirkungen weisen sie eine unerwartete Reversibilität im Vergleich zu anderen, nicht hochentropischen Zusammensetzungen auf. In der Folge wurde eine zunehmende Zahl von Forschungsarbeiten über die Verwendung von Materialien mit hoher Entropie in Energiespeichern veröffentlicht. Die praktisch unendliche Vielfalt an multielementaren Zusammensetzungen für eine einphasige Struktur ermöglicht eine maßgeschneiderte Anpassung ihrer physikalischen Eigenschaften und ein noch nie dagewesenes Materialdesign. In dieser Arbeit wurde eine Reihe von HEOs durch Sprühyrolyse (NSP) und Festkörperreaktion hergestellt. Um die Verwendung von HEOs in LIBs/SIBs zu erforschen, werden die Bedingungen für das Materialdesign, die Synthesemethode, die Entwicklung der Kristallstruktur im Zusammenhang mit dem Ladungsausgleich und die elektrochemische Leistung von HEOs untersucht.

Die Übertragung des Hochentropiekonzepts auf Elektrodenmaterialien kann neue Strategien und Technologien für das Materialdesign und die Herstellung neuartiger Verbindungen mit noch nie dagewesenen Eigenschaften liefern. Auf der Grundlage dieser Ergebnisse wird erwartet, dass diese Strategie neue Einblicke in die elektronische und strukturelle Chemie für fortschrittliche Elektrodenmaterialien eröffnen kann.

Table of Contents

1. Introduction	1
2. Fundamentals	3
2.1. Background of Lithium/Sodium-ion Batteries (LIBs/SIBs)	3
2.1.1. Composition of LIBs/SIBs	3
2.1.2. Principle of A “Rocking Chair Battery”	5
2.1.3. Layered Cathode Materials in LIBs	6
2.1.4. Layered Cathode Materials in SIBs	13
2.2. High Entropy Materials (HEMs)	18
2.2.1. Background of HEMs	18
2.2.2. Concept and Characteristics of HEMs	19
2.2.3. Entropy Stabilization	21
2.3. State of the Art	23
2.3.1. Charge Compensation Mechanisms	24
2.3.2. Crystal Structures	26
2.3.3. Applications of High Entropy Oxides (HEOs) in Battery Field	27
3. Experimental	30
3.1. Fundamentals and Measurements	30
3.1.1. X-ray Diffraction (XRD)	30
3.1.2. Scanning Electron Microscopy (SEM)	32
3.1.3. Transmission Electron Microscope (TEM)	32
3.1.4. X-ray Photoelectron Spectroscopy (XPS)	33
3.1.5. X-ray Absorption Spectroscopy (XAS)	34
3.1.6. Mössbauer Spectroscopy	34
3.1.7. Inductively Coupled Plasma (ICP) Spectroscopy	34
3.1.8. Differential Electrochemical Mass Spectrometry (DEMS)	35
3.2. Cell Testing Techniques	36

3.3. Materials Synthesis and Cell Fabrication	36
3.3.1. Nebulized Spray Pyrolysis (NSP)	36
3.3.2. Conventional Sintering	38
3.3.3. Solid state Synthesis	38
3.4. Fabrication of Cells	38
4. Spinel to Rock-Salt Transformation in High Entropy Oxides with Li Incorporation	40
4.1. Introduction	40
4.2. Results and Discussion	41
4.2.1. Powder X-ray Diffraction (PXRD)	41
4.2.2. Inductively Coupled Plasma-Optical Emission Spectroscopy (ICP-OES)	43
4.2.3. X-ray Photoelectron Spectroscopy (XPS)	44
4.2.4. Transmission Electron Microscopy (TEM)	47
4.2.5. Electrochemical Properties	49
4.3. Conclusions	51
5. Lithium Containing Layered High Entropy Oxide Structures	52
5.1. Introduction	52
5.2. Results and Discussion	53
5.2.1. Powder X-ray Diffraction (PXRD)	53
5.2.2. Microstructure	55
5.2.3. X-ray Photoelectron Spectroscopy (XPS)	59
5.2.4. Electrochemical Properties	60
5.2.5. The Effects of High Entropy	63
5.3. Conclusions	64
6. The Role of High Entropy Effects in P2-type Cathode Materials for Sodium-ion Batteries (SIBs)	65
6.1. Introduction	65
6.2. Results and Discussion	67
6.2.1. Structure and Morphology Characterization	67
6.2.2. Electrochemical Characterization	71
6.2.3. Structural Changes Studied via <i>Operando</i> X-ray Diffraction (XRD)	75
6.2.4. Gas Evolution	78
6.2.5. <i>Ex-situ</i> XRD	84
6.2.6. X-ray Photoelectron Spectroscopy (XPS)	85



6.2.7. X-ray Absorption Spectroscopy (XAS) and Inductively Coupled Plasma-Atomic Emission Spectrometry (ICP-OES)	86
6.3. Conclusion	87
7. Conclusions and Outlook	89
A. Acknowledgements	91
B. List of Abbreviations and Symbols	93
C. List of Figures	95
D. List of tables	98
E. References	99
F. Curriculum Vitae	116

Chapter 1

1. Introduction

Energy and environmental issues are two major concerns that have become widespread in the new century [1]. The continuous depletion of traditional fossil fuels such as coal and oil and the growing problem of environmental pollution are seriously affecting and limiting people's daily life and sustainability of society due to the increasing demand for energy. The development of green and renewable energy, including wind, solar, tidal and geothermal power, etc., is therefore a matter of urgency [2]. The unstable and intermittent nature of most renewable energy sources can pose a risk to the stability and security of the grid [3]. However, energy storage equipment and devices can provide some regulation and buffering function for the power grid to improve its safety and stability, so it is an important part of the new era of smart grid construction [4, 5]. In addition, the energy storage equipment is also necessary for the fast growing of the electric and hybrid vehicle industry. Therefore, the development of advanced energy storage systems is of great importance [3, 6–8].

So far, there are two main types of efficient and reliable energy storage devices: physical and chemical energy storage [9]. Physical energy storage mainly includes pumped energy storage, flywheel energy storage, etc., while chemical energy storage mainly includes batteries, capacitors and so on. Compared with other types of energy storage devices, the battery system has the characteristics of high-energy conversion efficiency, high power density and low equipment maintenance cost, which is of great concern for the energy storage market. Typically, battery systems include Nickel-Metal Hydride (Ni-MH) batteries, lead-acid (LA) batteries, flow batteries and lithium/sodium ion batteries (LIBs/SIBs) [9]. At present, LA batteries and LIBs mainly occupy the secondary battery market [10].

However, the LA batteries are being replaced by other types of batteries since they are extremely harmful to the environment, high cost and have a low energy density [9]. The new generation of electrochemical energy storage devices (LIBs, SIBs, etc.) are receiving a lot of attentions because of their surpassing advantages in energy conversion efficiency and energy/power density, environmental friendliness, and many other aspects [9, 11, 12]. For LIBs and SIBs, the energy density and cost are mainly limited by the cathode materials presently [13, 14]. In

both systems, the cathode materials are responsible for providing the detachable ions and determining the voltage of the battery system. Therefore, the cathode material decides the energy density of the entire battery system based on the relationship between the specific capacity and the average discharge voltage. This indicates that increasing the capacity and discharge voltage of the cathode material is the main way to increase the energy density of the battery system [15].

In addition, the cost of cathode materials accounts for about one-third of the cost of the whole battery system in commercialized batteries, as shown in Figure 1.1, so lowering of cathode material cost is the key to reduce the cost of the entire battery system [13, 15–17]. Based on the above analysis, the development of high-energy density, low-cost and excellent performance cathode materials is the crucial point to improve the energy density and reduce the cost of LIBs and SIBs.

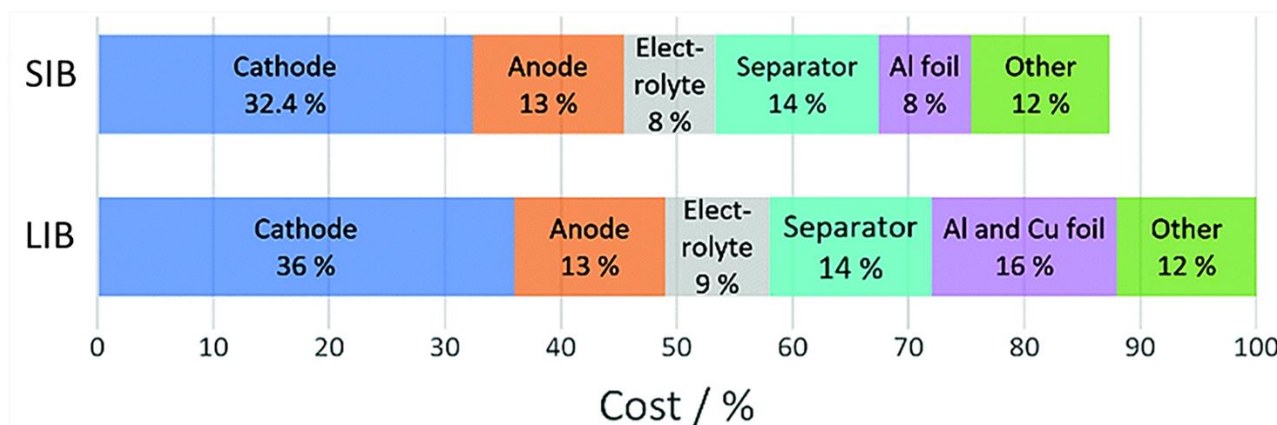


Figure 1.1: Comparison of the manufacturing costs for LIBs and Na-ion batteries SIBs. (Reproduced with permission from [16] ©2017, THE ROYAL SOCIETY OF CHEMISTRY.)

In order to improve the electrochemical performance of cathode materials, the development of new materials has been pursued, but also optimization process on known materials like elemental doping and surface coating, etc. explored. In recent years, high entropy materials (HEMs) as a new class of materials were developed to be used as electrode materials for energy storage systems. Benefitting from the high entropy effect, this kind of material displayed unexpected cycling reversibility, capacity retentions and structural stability compared to conventional compositions. In addition, the multiple possibilities of combinations of various elements and the exploration of different structures are broadening the application field and a large number of research works have been reported on the application of HEMs in energy storage devices. Therefore, HEMs are believed to propose a new strategy to next-generation high-reversibility, high-stability and long-term cycling battery systems.

This thesis is mainly to explore the synthesis and applications of different high entropy oxides (HEOs) in batteries. The terms of materials design, synthesis method, crystal structure evolutions accompanied with charge compensation and electrochemical performance of HEOs are studied. It provides solid evidence for the validation of entropy stability and the application potential of layered HEOs in LIBs and SIBs, and opens new insights into electronic and structural chemistry for advanced electrode materials.

Chapter 2

2. Fundamentals

The aim of this chapter is to introduce the fundamentals of “rocking chair battery” including LIBs and SIBs, background of high entropy materials and the application of high entropy materials in batteries. Section 2.1 covers the compositions, principle and different kinds layered structure materials as cathodes for LIBs and SIBs. Section 2.2 introduces the background of HEMs regarding definition and principle of high entropy, entropy stabilization effect and charge compensation effect. Section 2.3 introduces HEMs with different crystal structures and their applications in batteries.

2.1. Background of Lithium/Sodium-ion Batteries (LIBs/SIBs)

LIBs and SIBs have received global attentions from researchers and urgent demands for social developments as the energy storage devices play increasingly important roles in modern energy storage systems. Therefore, it is necessary to introduce the basics of LIBs and SIBs, including the composition of LIBs and SIBs (2.1.1), Principle of “rocking chair battery” (2.1.2) and the layered cathode materials for LIBs (2.1.3) and SIBs (2.1.4).

2.1.1. Composition of LIBs/SIBs

The composition of the both systems is the same to some extent, various battery structures are mainly composed of five parts: cathode electrode, anode electrode, separator, electrolyte and shell [18], four different types of batteries are shown in Figure 2.1.

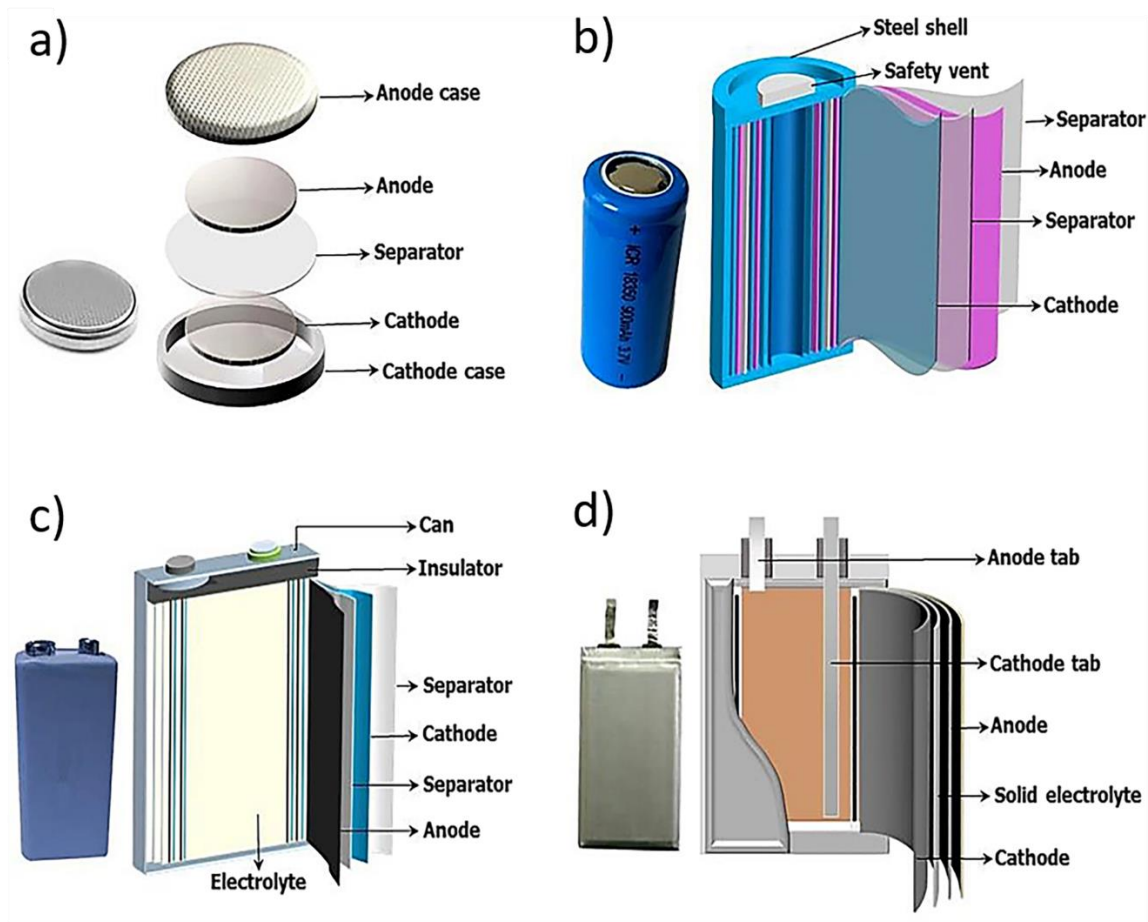


Figure 2.1: Schematic of (a) coin-type, (b) cylindrical-type, (c) prismatic-type, (d) pouch-type batteries. (Reproduced with permission from [18] ©2020, SPEINGER NATURE.)

The cathode electrode is mainly composed of lithium or sodium containing substances, such as lithium manganate (LiMn_2O_4) [19] of the spinel type, lithium cobaltate (LiCoO_2) [20] of the layered structure, ternary layered high nickel content materials ($\text{Li}(\text{Ni}_x\text{Co}_y\text{M}_{(1-x-y)})\text{O}_2$ or $\text{Li}(\text{Ni}_x\text{Co}_y\text{Al}_{(1-x-y)})\text{O}_2$) [21], layered Li-rich manganese-based cathode material ($\text{Li}(\text{Li}_{0.2}\text{Mn}_x\text{M}_{0.8-x})\text{O}_2$) [22], polyanionic types of lithium iron phosphate (LiFePO_4) [23], O3-phase and P2-phase layered manganese-based oxide ($\text{Na}(\text{Mn}_x\text{M}_{1-x})\text{O}_2$ and $\text{Na}_y(\text{Mn}_x\text{M}_{1-x})\text{O}_2$) [24], sodium vanadium phosphate ($\text{Na}_3\text{V}_2(\text{PO}_4)_3$) [25] and Prussian blue type $\text{Na}_{2-x}\text{M}(\text{Fe}(\text{CN})_6)$ [26], etc. (where the M is transition metals). Anode materials are mainly natural and synthetic graphite, lithium titanate ($\text{Li}_4\text{Ti}_5\text{O}_{12}$), hard carbon, silicon-carbon composites, etc. [27] The electrolyte consists mainly of organic solvent containing Li^+ or Na^+ salts and various additives. Usually, organic solvents include one or a combination of propylene carbonate (PC), ethylene carbonate (EC), dimethyl carbonate (DMC), methyl ethyl carbonate (EMC) and fluoroethylene carbonate (FEC), etc. The most common electrolyte salts are lithium hexafluorophosphate (LiPF_6) for LIBs, sodium hexafluorophosphate (NaPF_6) and sodium perchlorate (NaClO_4) for SIBs [28]. Separators are mainly porous insulators such as glass fiber paper or composite plastic films such as polyethylene (PE) and polypropylene (PP) [29].

2.1.2. Principle of A “Rocking Chair Battery”

The LIBs/SIBs follow the same operating principle, as shown in Figure 2.2, in which with carriers (Li^+/Na^+) constantly shuttling back and forth between the positive and negative electrode materials, accompanied by the storage and release of electrical energy [30].

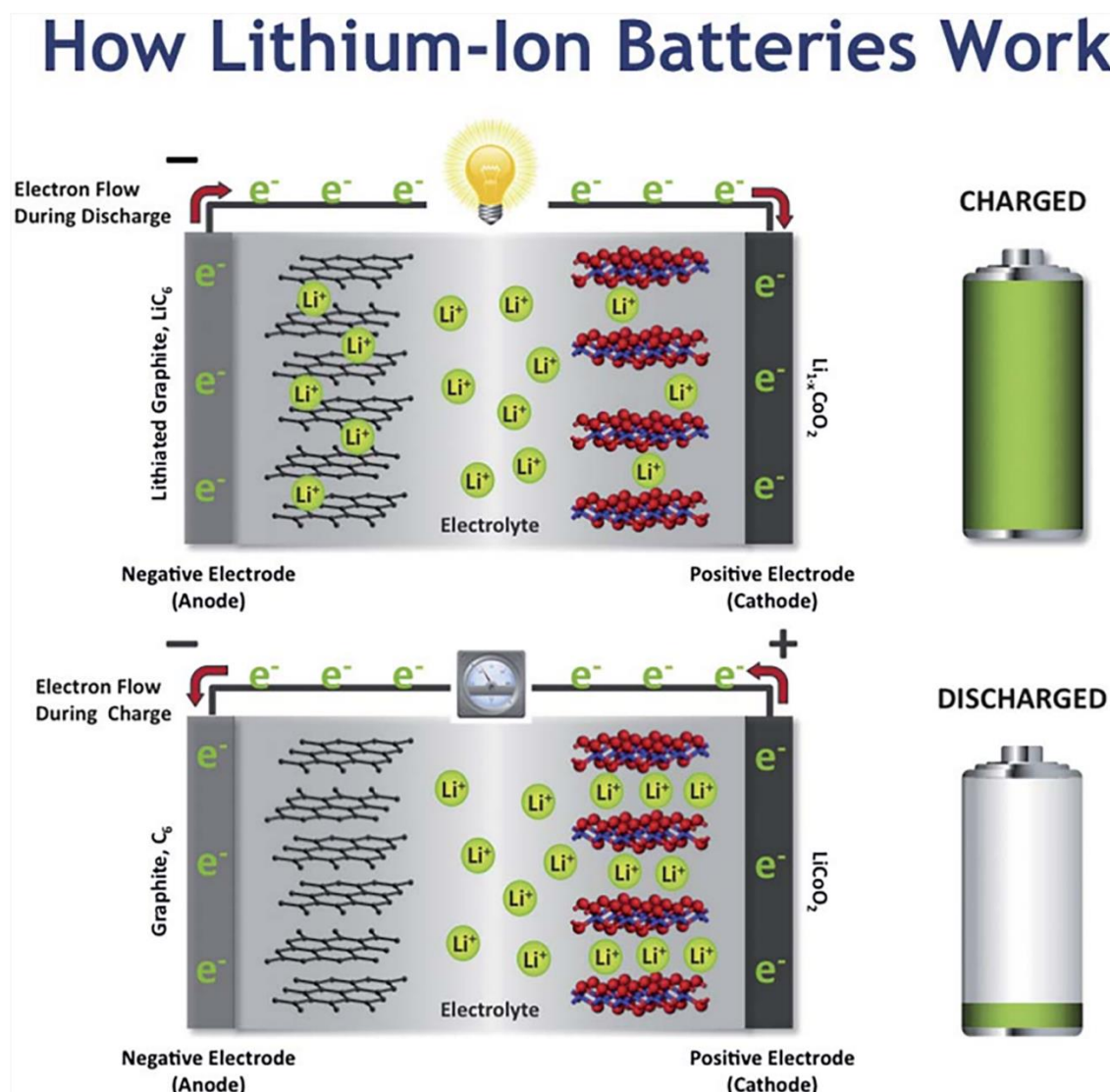
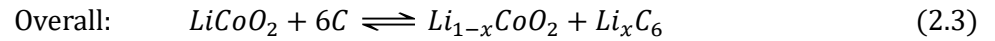
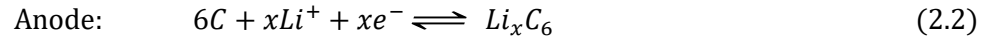
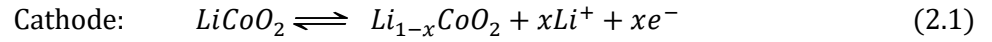


Figure 2.2: Schematic view of the principle of operation of a lithium-ion cell. (Reproduced with permission from [30] ©2012, THE ROYAL SOCIETY OF CHEMISTRY.)

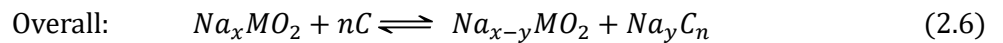
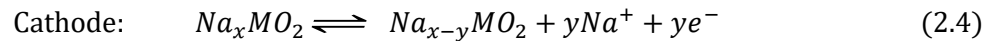
During charging, the Li^+ or Na^+ ions are extracted from the positive electrodes of oxides which contains Li^+ or Na^+ ions and enter into electrolyte, and electrons are passed through the external circuit. Meanwhile the carriers in the electrolyte are inserted into the reducible negative electrode (Equation 2.1 and 2.4), and thus enabling electrical energy to be stored. During discharging, the anode electrode releases carriers into the electrolyte and provides electrons by external circuit. Meanwhile, the cathode electrode would capture carriers and obtain electrons (Equation 2.2 and 2.5), enabling the release of electrical energy. As a result, the carriers travel forth and

back between the positive and negative terminals as they are in charged and discharged processes, therefore, these kind of batteries are called "rocking chair" battery [18].

For LIBs, take the example of the layered lithium cobalt oxide (LiCoO_2) as cathode material and the graphite as anode material [20]:



For SIBs, taking transition metal oxide (Na_xMO_2) and hard carbon as cathode and anode electrode materials as an example [31]:



2.1.3. Layered Cathode Materials in LIBs

The active lithium contained in the cathode material framework is the main source of lithium ions for the reversible de-embedding process and therefore plays a key role in the overall battery. Two-dimensional layered materials have been important in the development of lithium-ion cathode materials [27]. These densely stacked layers provide sufficient space for the reversible lithiation/delithiation process of Li^+ in "rocking-chair" LIBs.

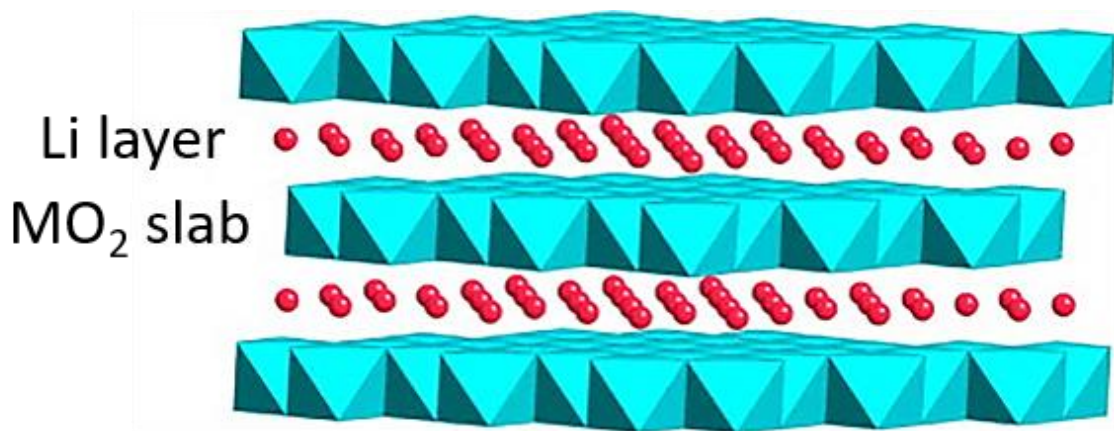


Figure 2.3: Crystal structure of layered LiMO_2 . (Reproduced with permission from [32] ©2012, ELSEVIER B.V.)

The structure of LiMO_2 , a layered oxide lithium-ion cathode material, is shown in Figure 2.3, with alternating

metal transition layers of MO_2 and octahedral LiO_6 [32, 33]. Due to the strong M-O bond, the energy of the lithium ions during movement is not sufficient to break the crystal structure of the MO_2 , which ensures that the lithium ions can only move in a parallel direction along the MO_2 layer during charging and discharging.

LiCoO₂

LiCoO₂ (LCO) that was first investigated and discovered as an intercalation cathode material for LIBs in 1980 by Prof. John B. Goodenough offers high conductivity and stable structural stability, which is the earliest and most typical commercial lithium-ion battery material [34]. It has an $\alpha\text{-NaFeO}_2$ type layered structure, in which Li^+ and Co^{3+} ions are ordered in alternating (111) planes of $R\text{-}3m$ space group and the oxygen atoms are arranged in a cubic close-packed framework stacked in an ABCABC... arrangement [35], identified as O3-type by Delmas et al. [36] This structure is mainly maintained by the octahedron formed by the oxygen ions surrounding the cation, where O^{2-} occupies position 6c and Li^+ and Co^{3+} occupy positions 3a and 3b, respectively. During the charging process, Co^{3+} is converted to Co^{4+} , accompanied by the expansion of the hexagonal lattice along the c -axis, and the structure transforms from hexagonal O3 type to monoclinic P3 type. However, to maintain the stability of the structure, only about half of the lithium ions are allowed to (de)insert. As a result, although the theoretical specific capacity of LCO is 274 mAh g^{-1} , the practical reversible capacity is only about 140 mAh g^{-1} at the upper cutoff voltage of 4.2V due to these effects. If the charging voltage is increased to 4.5V or above, more lithium ions would be extracted from crystal matrix causing oxygen losing and irreversible phase changes, which would seriously affect the stability of the material. With efforts of nearly 30 years, the reversible capacity of LCO has been improved to $\approx 185 \text{ mAh g}^{-1}$ at the upper cutoff voltage of 4.5V with practical cycling performance [35]. LCO can be prepared by solid-state sintering at high temperatures (800 °C) in an air atmosphere, and in general, excellent electrochemical properties can be obtained at low cutoff voltage. However, in order to increase its energy density, the researchers further increased the charge cutoff voltage to facilitate more lithium ions extraction and tried to suppress its structural instability by controlling material morphology, ion doping, surface coating and electrolyte modification. Mg^{2+} doping is reported to improve the electrical conductivity of the material [37], while La and Al co-doping can promote the motility of Li^+ and suppress the phase transition during charging and discharging [38]. It was also shown that coating on the surface of LCO with oxide can reduce side reactions between the material and the electrolyte and maintain good cycling stability. A recent surface treatment of LCO based on a binary mixture of Ba and Ti produced a Li-Ti-Co-O interface that effectively mitigated the degree of reaction between LCO and the electrolyte, achieving 90% capacity retention after 100 cycles at 3.0-4.5 V [39]. However, it is still facing several challenges, especially the long-term cycling stability, safety issues and high cost in battery application.

LiNiO₂

The layered-structure of LCO exists in other analogous of lithium transition metal oxides with a generic formula

of LiMO_2 in which $M = \text{V, Cr, Ni, and Fe}$. The successful application of LCO inspires a wave of efforts to explore more categories of cathode materials for LIBs, for example, lithium nickel oxide (LiNiO_2 , LNO) which has the same $\alpha\text{-NaFeO}_2$ type structure as the LCO. The LNO as a substitution of LCO not only reduces the cost but also achieves a unprecedented capacity of $>160 \text{ mAh g}^{-1}$, which benefits from a lower voltage window of LNO [40, 41]. However, LNO has not been commercially applied mainly because of many problems. (1) Complex preparation conditions. During the high temperature preparation process, Ni^{3+} is easily reduced to Ni^{2+} , which tends to lead to heterogeneous phase generation. (2) The phenomenon of cation mixing. Since the radius of Ni^{2+} (0.068 nm) and Li^+ (0.072 nm) are quite similar, Ni^{2+} partially occupies the position of Li^+ and blocks the diffusion channels of Li^+ . (3) The low thermal stability of LiNiO_2 during charging is a large risk in practical applications as well [41]. In recent years, researchers have also been actively searching for ways to optimize the preparation process and improve the stability of LNO. In order to improve the stability, the strategy of elemental doping (Al, Mg, etc.) is usually adopted to replace part of the Ni in LNO to reduce the degree of Li-Ni mixing and improve the stability of the material [42, 43]. In addition to the above strategies, it has been found that coating a protective layer of La_2O_3 or Al_2O_3 on the surface of LNO can also maintain the morphological integrity of the material during the cycling process [44, 45]. The most important is that the substitution of Co with Ni and other elements in LCO gave rise to nickel-based layered oxides ($\text{Li}(\text{Ni}_x\text{M}_{1-x})\text{O}_2$, $M=\text{Co, Mn, Al, etc.}$), achieving a great commercial success presently [41].

LiMnO₂

As another analogue to LCO, lithium manganese oxide (LiMnO_2 , LMO) was initially regarded as a promising alternative cathode material because of its low cost, environmental friendliness and large theoretical capacity of 286 mAh g^{-1} . Therefore, LiMnO_2 has been investigated as a green cathode material for sustainable energy storage device. It mainly has four crystal structures, including monoclinic, orthorhombic, tetragonal and spinel-structured LMO, but only monoclinic and orthorhombic LMO are layered structures. Typically, a direct high temperature synthesis will yield the orthorhombic ($Pm\bar{m}n$) phase with corrugated LiO_6 slabs and spinel structure while low temperature synthesis strategies, like hydrothermal approaches, will yield the layered material adopting a monoclinic phase with the $C2/m$ space group [11, 46, 47]. The respective crystal structures are shown in Figure 2.4a.

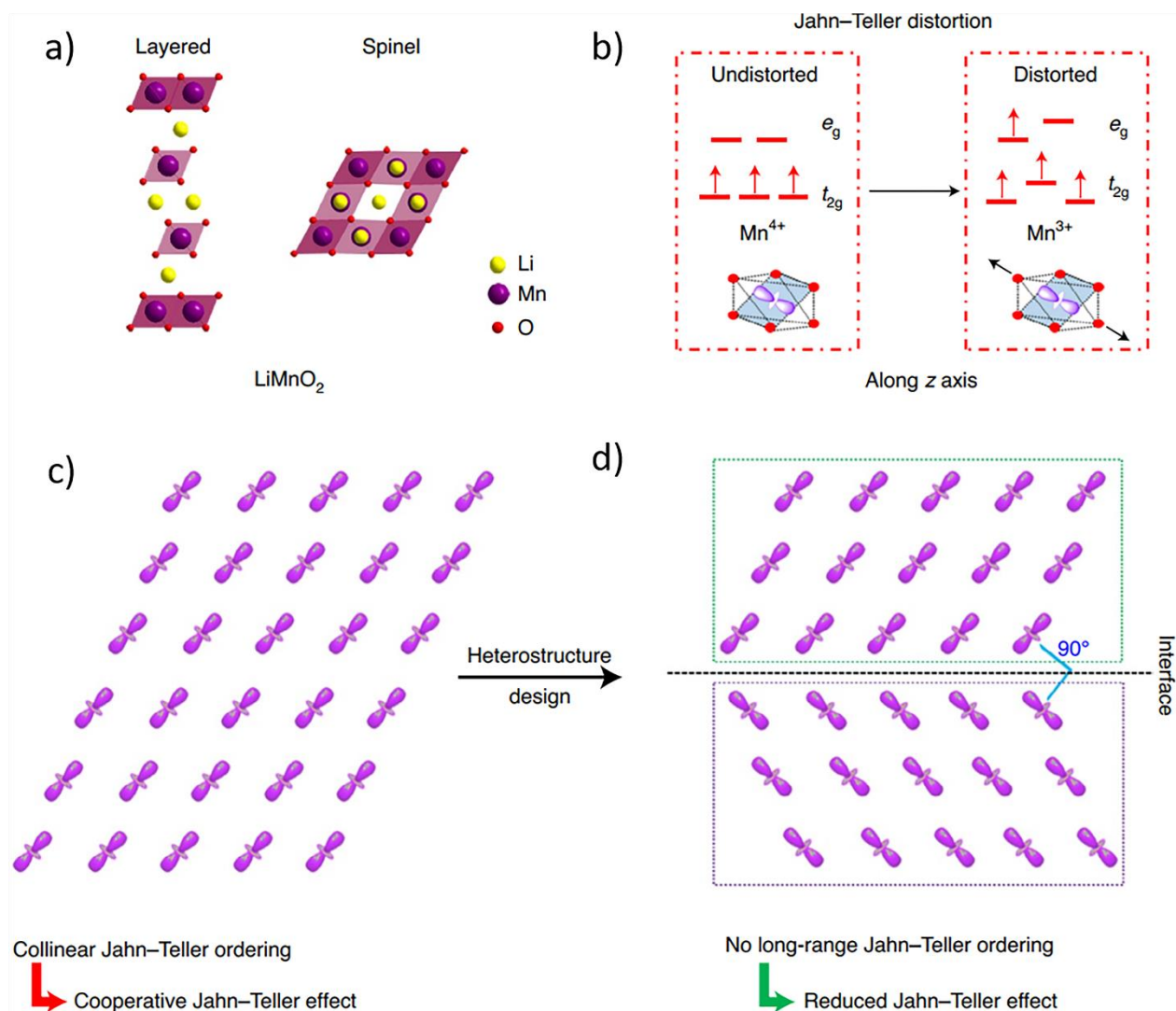


Figure 2.4: Jahn-Teller distortion correlated with orbital ordering in LiMnO_2 . (a) Crystal structures of layered and spinel LiMnO_2 . (b) Splitting of the e_g levels of d orbitals in an octahedral environment because of Jahn-Teller distortion. (c) Cooperative Jahn-Teller distortion with collinear orbital ordering. (d) Alleviated Jahn-Teller distortion with interfacial orthogonal orbital ordering. (Reproduced with permission from [46] ©2020, SPRINGER NATURE.)

The practical application of LMO cathodes in LIBs, however, has been restricted by the cooperative Jahn-Teller effect associated with high-spin Mn^{3+} , which causes severe structural degradation and rapid capacity fading [48], as a result, the actual reversible capacity is only about 190 mAh g^{-1} , considering the as large as theoretical capacity of 286 mAh g^{-1} , the actual capacity of LMO was expected to be greatly improved. As shown in Figure 2.4b, the single electron occupancy in the doubly degenerate e_g causes a local Jahn-Teller distortion with Mn-O bonds elongated along one of the octahedral axes. The orbital ordering in LMO leads to collinear Jahn-Teller ordering (Figure 2.4c-d) which results in a large volume change and a strong cooperative Jahn-Teller effect. The structural instability associated with the Jahn-Teller distortion prevents LMO from being a viable alternative to LCO because of its poor structural stability and irreversible phase transformations during charge and discharge process [46]. The main way to improve this distortion is to dope with other metals such as Al, Co, Cr, Ni, etc. On one hand, the doping of lower valence elements increased the proportion of Mn^{4+} in the original sample. On the other hand, the

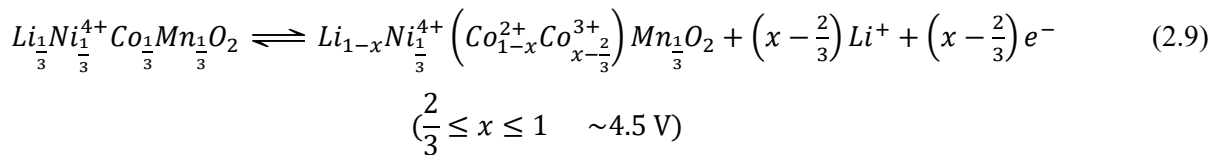
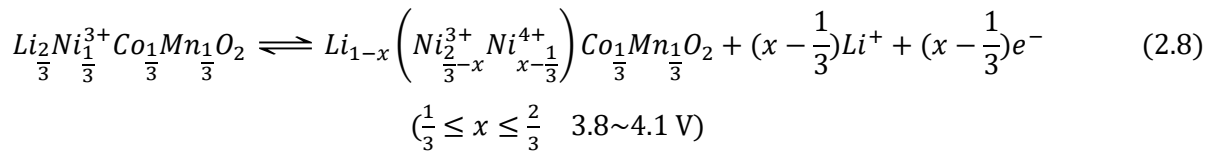
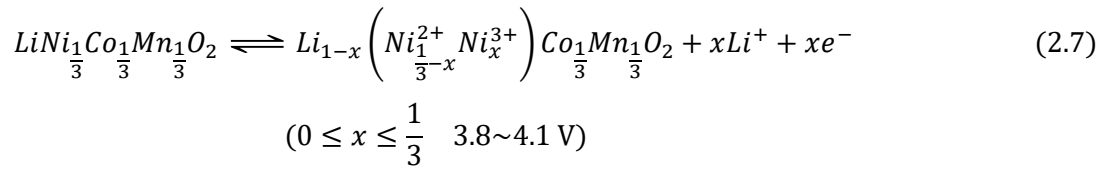
involved of elements with larger ionic radii increases the layer spacing and promotes the (de)insertion of Li ions, which with smaller ionic radii reduce the Mn-O bond length resulting in Mn³⁺ being held in octahedral positions [49]. Finally, two or more elements are generally doped to further improve the stability of the material.

Layered Li(Ni_{1-x-y}Co_yMn_x)O₂ (NCM) Cathode Materials

In the process of studying LiMO₂ layered cathode materials, Liu et al. [50] found that the lithium nickel cobalt manganese oxide (Li(Ni_{1-x-y}Co_yMn_x)O₂, 0 < x, y < 1, 0 < x+y < 1, NCM) cathode material obtained by replacing some of the Co with Ni and Mn has better cycling stability than LCO, LNO and LMO. And afterwards, Ohzuku et al. [51] found that Li(Ni_{1/3}Co_{1/3}Mn_{1/3})O₂ (NCM111) prepared in equal proportions of Ni, Co and Mn displaces excellent performance, in addition, other ratios of ternary cathode materials such as NCM 523, NCM 622 and NCM 811 have also been explored [47].

The NCM has an α-NaFeO₂ layer structure similar to that of LCO. In this structure, Mn⁴⁺ ions do not participate in redox reactions during charging and discharging, but mainly serve to stabilize the host structure. The most of the capacity is contributed by the valence change between Ni²⁺ and Ni⁴⁺, however, too much of it would lead to the Li⁺/Ni²⁺ mixing increase, which leads to the lithium ions channel be blocked by Ni²⁺, resulting in the movement of lithium ions in difficult. The introduction of Co³⁺ ions can reduce the degree of Li-Ni mixing, meanwhile, it can provide some capacity at high voltages by participating in redox reactions. But excess amount of Co will lead to shrinkage of the cell volume and affect the efficiency of lithium-ion transport. As can be seen from the above, a better performance ternary cathode material can only be found with a reasonable proportion of nickel, cobalt and manganese.

Taking NCM111 as an example, the charge/discharge electrochemical reaction equation as follows:



The redox reactions of active ions pairs of Ni²⁺/Ni³⁺ (0 ≤ x ≤ 1/3) and Ni³⁺/Ni⁴⁺ (1/3 ≤ x ≤ 2/3) usually at a potential

range of 3.8-4.1 V, as displaced as equation 2.7 and 2.8. The reaction of $\text{Co}^{3+/4+}$ ($\frac{2}{3} \leq x \leq 1$) is at the voltages of about 4.5 V. When Ni^{2+} and Co^{3+} are completely oxidized to +4, the theoretical capacity can be reach to 278 mA h g^{-1} [52]. Choi et al. [53] showed that when $x < 0.65$, the valence of O^{2-} ions in the MO_2 slabs remains unchanged; while when $x > 0.65$, the average valence of O would decrease, the lattice oxygen escapes from the structure and thus the chemical stability would be destroyed. Furthermore, the X-ray diffraction (XRD) analysis results show that the structure can keep the original lattice structure unchanged when $x < 0.77$. However, when the amount of Li^+ extraction is too high, $x > 0.77$, the appearance of a new phase can be observed. Therefore, although increasing the cut-off voltage for charging and discharging can effectively increase the specific capacity of the material, its cycling performance will be drastically reduced.

Currently, most commercial ternary cathode materials are prepared by co-precipitation of $(\text{Ni}, \text{Co}, \text{Mn})(\text{OH})_2$ or $(\text{Ni}, \text{Co}, \text{Mn})\text{CO}_3$ precursors mixed with lithium salts and then transferred into a following solid phase calcination process. For improving, doping some metal ions (Al, Fe, Cr, Ce, Mg, etc.) [24, 37, 47] in the lattice of ternary materials not only can increase the electronic and ionic conductivity and the output power density of the battery, but also improve the stability of the ternary material structure (especially the thermal stability). On the other hand, coating the surface of NCM with some metal compounds (AlF_3 , Al_2O_3 , FePO_4 , ZrO_2 , V_2O_5 , etc.) [32, 39, 44], lithium salts (Li_2MnO_3) [54] or some monomers (carbon [8], graphene [55]) of suitable thickness can physically isolate the active material from the electrolyte in the battery, which can reduce the occurrence of side reactions and inhibit the dissolution of transition metal ions in the electrolyte. At the same time, the inactive cladding layer with certain mechanical strength can also slow down the electrode material structure changing during long-term cycling [56].

Layered Li-rich Cathode Materials

As early as the end of the last century, the layered $\text{Li}_2\text{MnO}_3 \cdot \text{LiCoO}_2$ solid solution material has been found to be used as a LIBs cathode material, where Li_2MnO_3 can be written as $\text{Li}(\text{Li}_{1/3}\text{Mn}_{2/3})\text{O}_2$, which also has a layered structure with some Li replacing Mn to occupy the transition metal sites in this structure [57]. The specific discharge capacity of this electrode material can reach to 270 mAh g^{-1} or even more when charged to 4.8V owing to the involvement of the oxygen redox reaction. However, the capacity release mechanism of Li-rich materials is different from that of the LCO or ternary materials described above. With the continuous researches going on, its chemical formula can be expressed as $x\text{Li}_2\text{MnO}_3 \cdot (1-x)\text{LiMO}_2$ (M can be a single or mixed transition metal ions), so it can be seen that the composition of the lithium-rich material is diverse. A chronological evolution from the layered oxide LCO to the recent Li-rich NCM phases is shown in Figure 2.5. The different components have a very close relationship with the electrochemical performance of the lithium-rich phase, mainly in its electrochemical reaction activity, reversibility, specific capacity, cycling stability and rate retention, there are also huge differences in safety as well [58, 59].

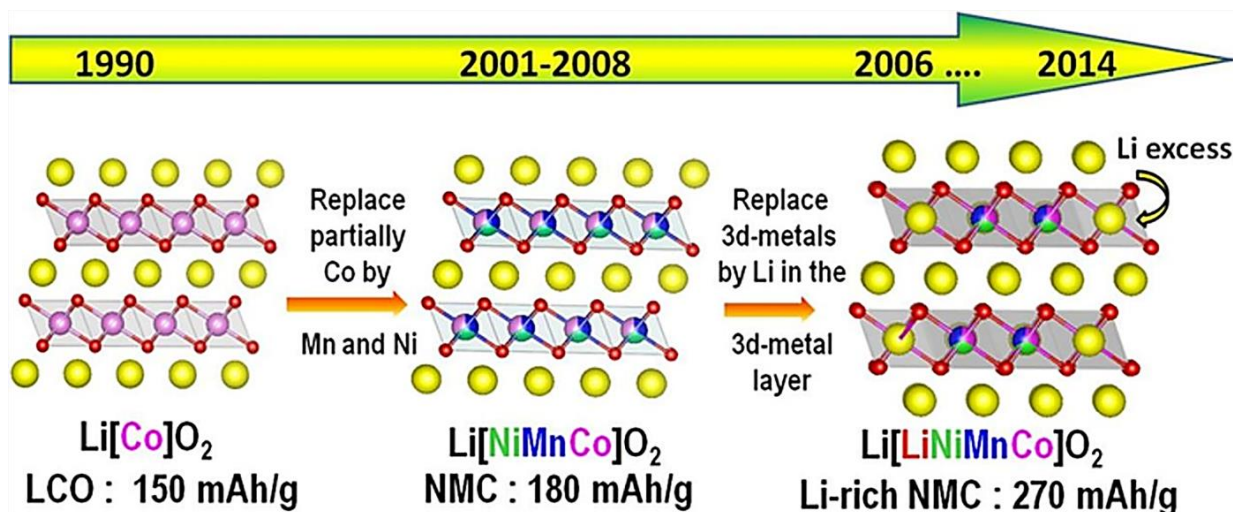


Figure 2.5: Chronological evolution of the layered oxide. (Reproduced with permission from [59] ©2015, THE ELECTROCHEMICAL SOCIETY.)

The Li_2MnO_3 (space group: $Cm/2$) and LiMO_2 (space group: $R-3m$) can be seen as homogeneous solid solution with a layered structure [57]. The layered lithium-rich phase $x\text{Li}_2\text{MnO}_3 \cdot (1-x)\text{LiMO}_2$ cathode material display a specific capacity of as high as 250 mAh g^{-1} (the actual discharge specific capacity can even exceed 300 mAh g^{-1}) and the relatively high discharge voltage enable the material an energy density of up to 1000 Wh kg^{-1} , this is a kind of the highest energy density lithium-containing cathode material known to date [60], as shown in Figure 2.6.

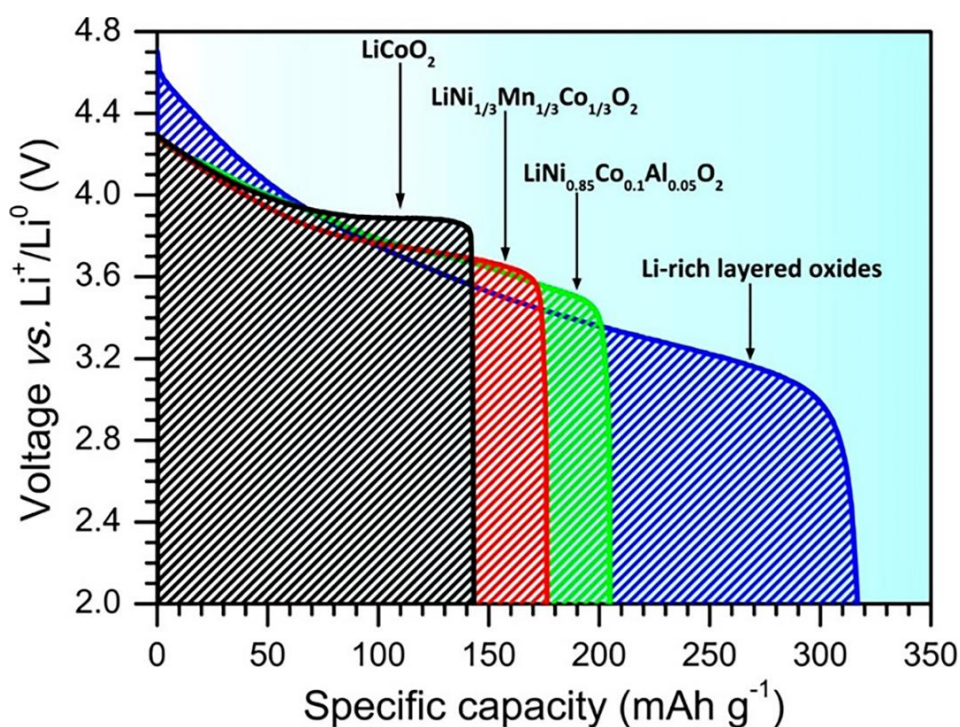


Figure 2.6: Discharge capacity in different layered oxides. (Reproduced with permission from [60] ©2017, AMERICAN CHEMICAL SOCIETY.)

During the first charge, LiMO_2 is electrochemically active below a voltage of 4.5 V and with the same mechanism as the NCM materials. However, when charged to around 4.6 V, the Li_2MnO_3 part in the structure is activated, at which point the lithium ions are excessively extracted out and the Mn in the transition metal slab enters the lithium ion layers to form the MnO_2 phase, resulting in the absence of lattice oxygen [60]. It is worth noting that this process at high voltages is usually incompletely reversible. During the subsequent discharge process some of the lithium ions are re-inserted into the Li_2MnO_3 - MnO_2 - MO_2 layer. From the reaction mechanism, it can be seen that partially deactivated Li_2MnO_3 can be used to stabilize its layered structure during charging and discharging process, resulting in reversible lithiation/delithiation of all Li^+ in the LiMO_2 structure. Furthermore, there is a trade-off in the value of x , a very high value of x implying a high content of Li_2MnO_3 leads to a low specific discharge capacity of the material. In contrast, too low of it would lead to poor cycling stability of the material [58–60]. Although higher energy densities can be achieved with Li-rich compounds theoretically, the commercial application of it is still severely limited by some drawbacks: (1) low Coulombic efficiency (CE) at initial cycle, (2) voltage plateau decaying and poor reversibility during cycling and (3) poor rate capability performance and low temperature performance [58]. Zhu et al. [61] proposed a failure mechanism that HF is generated by electrolyte decomposition at high voltage, which corrodes the electrode material. However, it is found that electrolyte additives can play a mitigating role [56], therefore, with the breakthrough of high voltage electrolyte due to improved electrolyte formulations, the high specific energy full cells based on lithium-rich phase will definitely be on an important role in the process of new energy development.

2.1.4. Layered Cathode Materials in SIBs

For sodium ion batteries, the cathode material can also be regarded as one of the key components of the SIBs and largely determines the voltage, capacity and cycling stability. In the early 1980s, researchers discovered that Na^+ could be reversibly de-embedded in the layered oxide Na_xCoO_2 , and since then, oxides, phosphates, fluorophosphates, sulfates, pyrophosphates and composite multi-ionic materials have been investigated as cathode materials. Layered oxides, tunneling oxides, multi-ionic compounds and Prussian blue materials are reported to be typical sodium ion cathode materials with promising capacity and cycling performance [62]. Although all of these materials exhibit some sodium storage properties, there are still problems of varying degrees. For example, Ni-containing layered oxides are not only expensive but also show instability in air, the water of crystallization in Prussian blue-type precursors is not easily controlled in the synthesis process, polyanionic materials, such as $\text{Na}_3\text{V}_2(\text{PO}_4)_3$, display low electronic conductivity. In comparisons, the layered structure oxides are of great interest to researchers because of their high capacity and simple synthesis process [62–64].

Structure Introduction (O-type and P-type)

Analogous to LIBs components, the layered transition metal oxides are generally written in the form Na_xMO_2 , in which M is usually composed of transition metals (Ni, Co, Mn, etc.) and doped elements, or a combination of

them. The octahedral coordination MO_6 formed by the transition metal M and O is stacked along the c-axis to form a transition metal layer, with Na^+ located between the transition metal layers. As shown in Figure 2.7, depending on the coordination environment in which the sodium ion is located, it can be divided into four main structures, P2, O3, P3 and O2 [65].

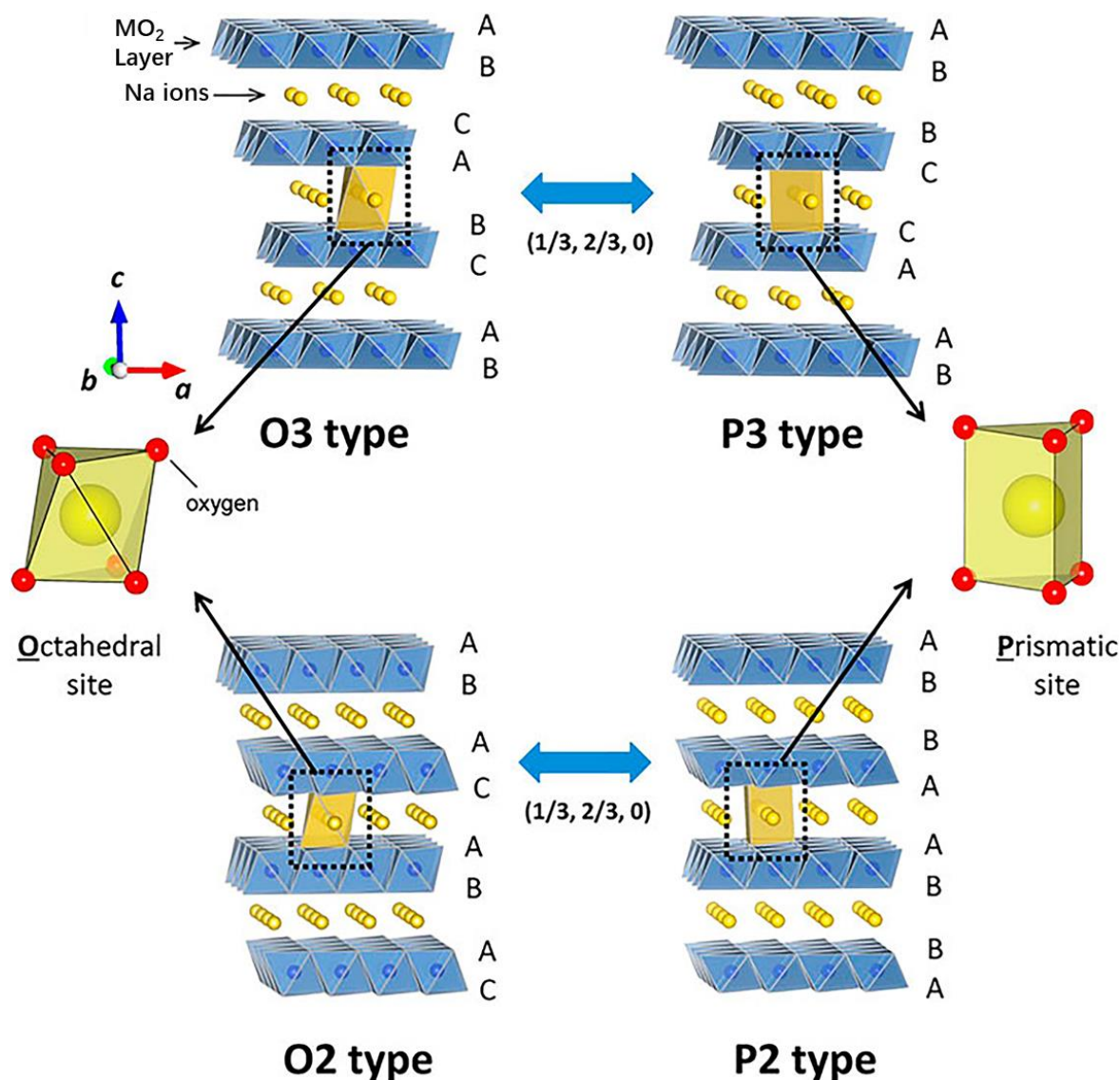


Figure 2.7: Classification of Na-M-O layered materials with sheets of edge-sharing MO_6 octahedra and phase transition processes induced by sodium extraction. (Reproduced with permission from [65] ©2020, AMERICAN CHEMICAL SOCIETY.)

O and P represent Na^+ in an octahedral and trigonal coordination environment, respectively, and 2 and 3 represent the minimum number of periods for the densest stacking arrangement of the oxygen atoms layers. Since Mn^{3+} is susceptible to Jahn-Teller deformation active, O and P in the coordination environment are generally denoted as O' and P' when the structure is distorted. The phase transformations between O3 and P3 are easily accomplished via gliding of the MO_2 layers, however, the transformations from O3 group to the O2 group and vice versa require the breaking of the M-O bonds, which is energetically more costly than gliding transformations. Therefore, cathodes typically stay within the same family (O3/P3 family or P2/O2 family) during cycling [63, 65].

Na_xCoO_2

Na_xCoO_2 materials exhibit different phase structures with different sodium contents. A large number of studies have found that the P2-type Na_xCoO_2 has the best performance compared to other types both in terms of stability and energy density [62]. Berthelot et al. [66] first studied the charge/discharge profiles of P2- $\text{Na}_{0.74}\text{CoO}_2$ in SIBs at the voltage range of 2.0-3.8 V and found that the large number of charge/discharge plateaus was closely related to the Na-vacancy ordering. And Rai et al. [67] found that the electrode material P2- $\text{Na}_{0.71}\text{CoO}_2$ has a 90% capacity retention after 90 cycles in the 2.0-3.5 V range, which also confirmed that reduced operating voltage can help to reduce phase transformations and improve stability but accompanied by a reduction in capacity. The performance of P2- Na_xCoO_2 was subsequently improved by means of ion doping, surface coating and morphology modification. However, the phase transition corresponding to the voltage plateau during charging and discharging needs to be further explored in depth [62, 63, 65].

Na_xMnO_2

Na_xMnO_2 materials have been extensively investigated because of their high specific capacity and their environmental friendliness and cost advantages. The first explanations for the phase transition process in Na_xMnO_2 materials were mainly related to the deformation of the MO_6 octahedra due to the Jahn-Teller effect of Mn^{3+} in the high spin state. The doping of lower valence ions at the Mn site to increase the proportion of Mn^{4+} is commonly used to suppress the distortion of Mn^{3+} [46]. As reported by Choi et al. [68], by studying Fe doped P2-type $\text{Na}_{0.66}(\text{Fe}_{1-x}\text{Mn}_x)\text{O}_2$ it was found that the doping of Fe^{3+} inhibits the stretching of the Mn-O bond along the z-axis direction and the optimum doping ratio was determined to be 22%, the results are shown in Figure 2.8.

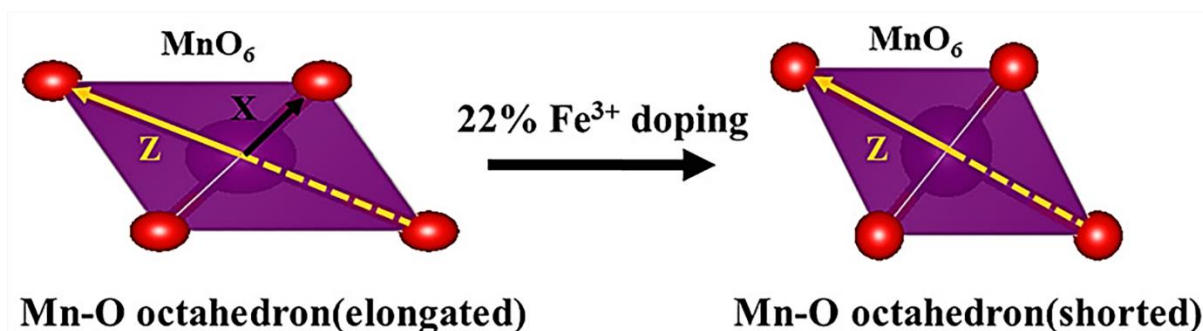


Figure 2.8: Suppression of Mn-O bond length in the Z axis by Fe substitution. (Reproduced with permission from [68] ©2018, AMERICAN CHEMICAL SOCIETY.)

Similarly, the involvement of other elements, such as Zn, Al, Ni, Mg, etc. and the surface coating with some metal oxides (Al_2O_3 and MgO e.g.) can also improve the performance of the layered Mn-based sodium ion battery cathode materials [69]. Zhang et al. [70] demonstrated a facile method to surface coat and dope P2- $\text{Na}_{0.7}\text{MnO}_2$ with a P2- $\text{Na}_{0.7}\text{Ni}_{0.33}\text{Mn}_{0.67}\text{O}_2$ layer in a single step to enhance its cycle stability, as a consequence, the coating enhances capacity retention from 62.2% to 87.7% over 50 cycles.

On the other hand, Caballero etc. [71] found that P2- $\text{Na}_{0.6}\text{MnO}_2$ materials exposed to air react spontaneously with moisture, in which case the water molecules embedded within the material cause the occurring of irreversible phase transformations, thus deteriorating the electrochemical stability. A recent study has shown that the layered-tunneled co-existing structure of the $\text{Na}_{0.6}(\text{Mn}_{1-x}\text{Cu}_x)\text{O}_2$ materials is significantly enhancing the stability in air, and the XRD spectra of the materials remained consistent with the original spectra after immersion in water [72]. All of these strategies have proven beneficial in improving material properties to some extent when tested in the SIBs, however the search for material mysteries will never be end.

Multiple Transition Metal Layered Oxide Cathodes

The previously mentioned NCM cathode materials have been developed with some success for LIBs, and this idea is valid as well when applied to SIBs, where the electrochemical performance of the material is improved by doping with two or more elements at Mn site of Na_xMnO_2 . In 2015, Li et al. [73] designed P2- $\text{Na}_{7/9}(\text{Cu}_{2/9}\text{Fe}_{1/9}\text{Mn}_{2/3})\text{O}_2$ with excellent stability in air and found that the combination of Cu and Fe inhibited the phase transition between P2-O2 during charge and discharge of the material. Wang et al. [74] showed the P2- $\text{Na}_{0.67}(\text{Ni}_{0.3-x}\text{Cu}_x\text{Mn}_{0.7})\text{O}_2$ material in 2017, and found that Cu^{2+} suppressed not only the phase transition of P2-O2 but also the ordering of sodium vacancies, thus alleviating the voltage decay during cycling, the corresponding in situ XRD spectra are shown in Figure 2.9.

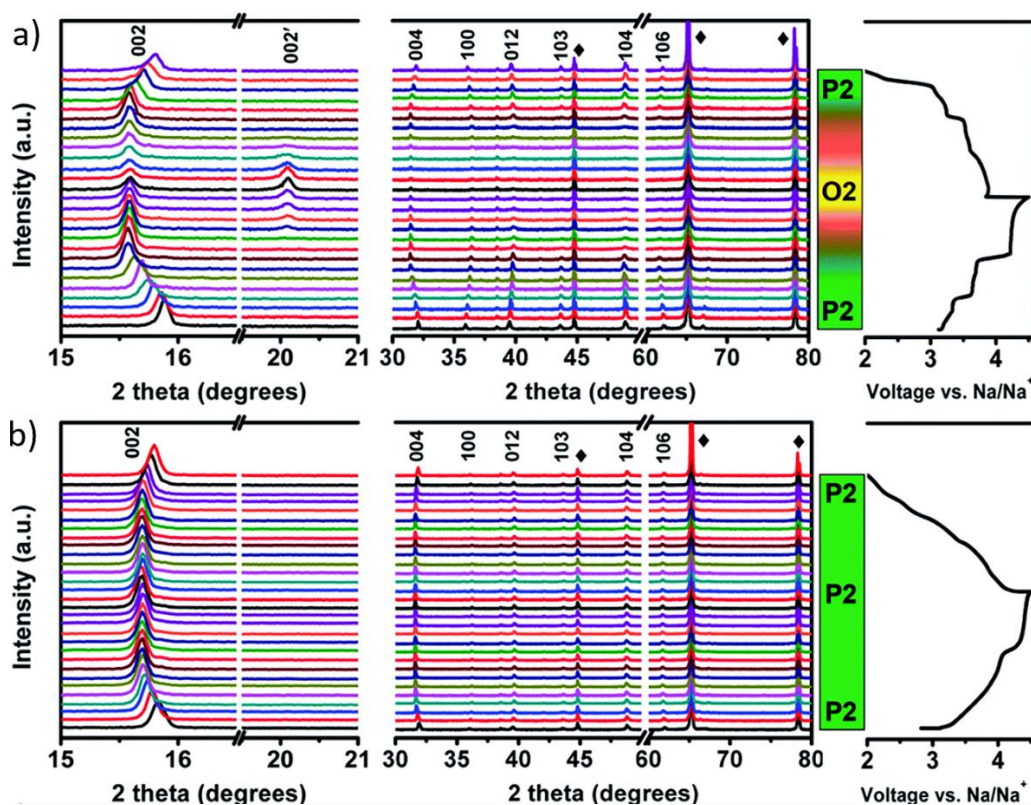


Figure 2.9: In situ XRD patterns collected during the first charge/discharge process of the (a) $\text{Na}_{0.67}(\text{Ni}_{0.3}\text{Mn}_{0.7})\text{O}_2$ and (b) $\text{Na}_{0.67}(\text{Ni}_{0.1}\text{Cu}_{0.2}\text{Mn}_{0.7})\text{O}_2$ electrodes between 2.0 and 4.5 V under a current rate of 0.1 C. (Reproduced with permission from [74] ©2013, THE ROYAL SOCIETY OF CHEMISTRY.)

Many materials have been designed by adopting a multi-element doping approach such as $\text{P2-Na}_{0.67}(\text{Mn}_{0.65}\text{Ni}_{0.15}\text{Co}_{0.2})\text{O}_2$, $\text{P2-Na}_{0.67}(\text{Mn}_{0.65}\text{Fe}_{0.2}\text{Ni}_{0.15})\text{O}_2$ and $\text{P2-Na}_{0.67}(\text{Mn}_{0.8}\text{Fe}_{0.1}\text{Ti}_{0.1})\text{O}_2$, etc. [75–77] This multi-element doping strategy does improve the electrochemical performance of SIBs over single elements, but there are still difficulties in gaining insight into the movement patterns of sodium ions and transition metal ions during the charging and discharging of these materials.

Anionic Redox Reactions

Inspired by the lithium-rich material Li_2MnO_3 ($\text{Li}(\text{Li}_{1/3}\text{Mn}_{2/3})\text{O}_2$) similarly, Na_2MnO_3 ($\text{Na}(\text{Na}_{1/3}\text{Mn}_{2/3})\text{O}_2$) has been attempted to synthesize, but not yet been achieved, this is probably because the large difference between the ionic radii of Na^+ ($r = 0.102 \text{ nm}$) and Li^+ ($r = 0.076 \text{ nm}$). However, Nazar et al. [78] successfully synthesized $\text{P2-Na}_{0.6}(\text{Li}_{0.2}\text{Mn}_{0.8})\text{O}_2$ layered materials with anionic redox reactions by adjusting the lithium/sodium/manganese ratio. Since the valence state of Mn in this material is only expressed as +4, so a plateau appearing above 4.0 V corresponds to oxidation reactions of anions (O_2^{n+}). Xu et al. [79] designed the $\text{P2-Na}_x(\text{Li}_y\text{Ni}_z\text{Mn}_{1-y-z})\text{O}_2$ material and found that the fraction of Li^+ at high voltage (4.3 V) could be removed to the diffusion channel of Na^+ from the transition metal slabs resulting in retardation of the P2-O2 phase transformation. Li et al. [80] designed a superior $\text{P2-Na}_{0.72}(\text{Li}_{0.24}\text{Ti}_{0.1}\text{Mn}_{0.6})\text{O}_2$ material that maintained a capacity of 165 mAh g^{-1} after 80 cycles in the voltage range of 1.5–4.5 V and at a current density of 10 mA g^{-1} . It demonstrated that Ti^{4+} doping can effectively alleviate the anisotropic coupling between Mn^{4+} and O_2^{n+} , suppresses the Jahn-Teller effect of Mn^{3+} , thereby stabilize the structure of the P2 phase.

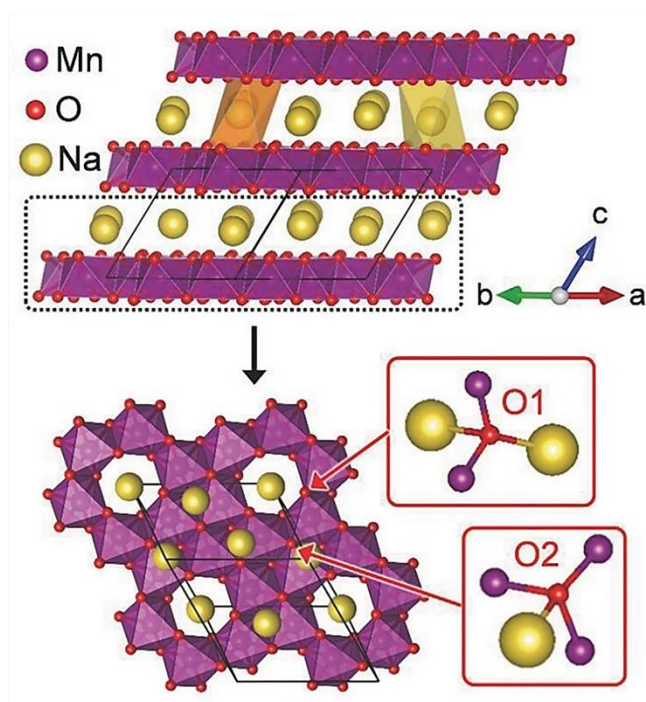


Figure 2.10: Crystal structure of $\text{Na}_2\text{Mn}_5\text{O}_7$. O coordinated by two Mn is labeled as O1, whereas O coordinated by three Mn is labeled as O2. Mn vacancies exist in the Mn layers. (Reproduced with permission from [81] ©2018, WILEY-VCH Verlag GmbH & Co. KGaA.)

In recent years, it has been found that the introduction of transition metal vacancies directly into the transition metal layer to produce non-bonded O-2p energy bands can also produce the above-mentioned sodium ion cathode materials with anionic redox. In 2018, Yamada et al. [81] designed $\text{Na}_{4/7-x}(\square_{1/7}\text{Mn}^{4+}_{6/7})\text{O}_2$ with highly reversible anionic redox, as showing in Figure 2.10. It suggested that the Na^+ between the $(\square_{1/7}\text{Mn}^{4+}_{6/7})$ layers has two different coordination environments with the adjacent O. One O is associated with two Mn, and the other O is associated with three Mn which located near to $\square_{1/7}$, leading to the creation of a non-bonded O-2p orbital providing additional capacity at high voltages.

2.2. High Entropy Materials (HEMs)

High entropy materials (HEMs) can be seen as compounds comprising several different elements in a single-phase structure and according to the Gibbs–Helmholtz equation, the large configurational entropy may result in novelty structural effects compared with conventional materials. So, the basics and core effects of HEMs are present in this section. This section describes the background of HEMs (2.2.1), concept and characteristics of high entropy alloys (HEAs) (2.2.2) and entropy stabilization effect (2.2.3).

2.2.1. Background of HEMs

A wide variety of different materials play an important role in the world and are essential for human survival and development, while the pursuit and exploration of versatile and advanced materials are the main driving forces for the development of materials science. One of the starting points of materials science is the development of functional materials with tailorable properties. Every major breakthrough in materials will bring some dramatic changes in the productivity of society [82]. In the field of traditional metallic materials, alloying strategies have mostly been limited to adding small fractions of elements as dopants in the base material to obtain new composite materials with improved properties, therefore, only a limited type of possible alloy can be developed by this method, and extensive researches in the past have proven these alloys. With the development of industrialization and technology, researchers always keep going on to explore and try to break through the chemical composition of alloys, but the aim, to find new metal materials with excellent properties, has never been changed.

There is a principle proposed by Greer et al. [83] in 1993 that the more alloying components, the higher the entropy and the better ability to form amorphous materials. According to this rule, it was expected that the alloys made from large amounts of different elements should result in the formation of amorphous ones due to the fact that the more elements involved, the lower the chance for alloys selecting viable crystal structures [83, 84]. However, the experimental results were contrary. Cantor et al. [85] experimentally found that the alloys containing 16 and 20 components in equal proportions are multiphase, crystalline and brittle both as-cast and after melt spinning. It is interesting that the above two alloys mainly consist of FCC crystal structure, especially in some areas where Cr, Mn, Fe, Co and Ni are enriched. Subsequently, a multi-element crystalline alloys, CrMnFeCoNi, with equal or near equal atomic ratio was successfully prepared and confirmed as a single-phase solid solution

structure [86]. In fact, it can be said that the high entropy does not mean high glass-forming ability, while the single-phase solid solution can be found in some high configurational entropy alloys instead. What's more, the design concept of alloys was emerged to influence the phase stability of solid solutions by precisely controlling the configurational entropy.

Although it was not defined in time, the concept of designing high configurational entropy alloys began decades ago with the development of multi-element alloys. The concept of HEAs, based on the fact that the isotropic entropy of a mixture increases with the addition of more primary elements to the alloy system, was first proposed and fully appreciated until when an article published by Yeh et al. in 2004 [87].

2.2.2. Concept and Characteristics of HEMs

The most common definition states that HEAs are a kind of alloys with 5 or more principal elements, and each element should have an atomic percentage between 5% and 35% [87]. Later, HEAs are defined as alloys with a configurational entropy value of more than $1.5R$ [88].

Usually, for a solid solution which is consisted of n kinds of elements, the configurational entropy change per mole can be calculated as:

$$\Delta S_{conf} = -R \sum_{i=1}^n c_i \ln c_i \quad (2.10)$$

Where R is the gas constant and c_i is the concentration of component i . For a given number of components (n), the configuration entropy reaches a maximum value when the all kinds of elements are with equimolar:

$$\Delta S_{conf} = -R \sum_{i=1}^n \frac{1}{n} \ln \frac{1}{n} = R \ln n \quad (2.11)$$

For a high entropy system, the ΔS_{conf} depends entirely on the number of involved elements, therefore, based on the Gibbs–Helmholtz equation (Equation 1.12), there is a competitive situation between ΔH_{mix} and ΔS_{mix} created:

$$\Delta G_{mix} = \Delta H_{mix} - T\Delta S_{mix} \quad (2.12).$$

If the contribution of $-T\Delta S_{mix}$ values to the ΔG_{mix} is sufficient or equivalent to ΔH_{mix} , entropy stabilization of crystal structure is established, and the increased configurational entropy can result in higher stability of solid solution because of the more negative ΔG_{mix} [84, 87]. Thus, when the number of components exceed a threshold value, entropy will take over the stability of the system [89, 90].

The extremely rapid development of HEAs results from their unusual properties which can be categorized in four core effects [87, 88, 91, 92]:

1) Thermodynamics: high entropy effects - high configurational entropy tends to promote the formation of stable solid solution phases

The high entropy effect can be described as that the higher mixing entropy (mainly configurational) in HEAs lowers the free energy of solid solution phases and promotes their formation at a high temperature. According to equation 1.10, the mixing entropy and the mixing enthalpy are in a competitive condition, the high mixing entropy would stabilize a phase at a sufficiently high temperature as the $T\Delta S_{\text{mix}}$ term becomes dominant and thus lowers the ΔG_{mix} . It is expected that the solid solution state with multi-principal elements which has a large ΔS_{conf} tends to be stable especially at elevated temperatures.

2) Kinetics: sluggish diffusion - kinetics of diffusion is slower than in conventional alloys and pure metals

The phase transformation and diffusion kinetics in HEAs is slower than those in conventional counterparts mainly due to the two facts. One is that the diffusion process can be considered as the continue migration of atoms from one lattice site to an empty adjacent site, however, the neighboring atoms of each lattice site in HEAs are more or less different which leads to different bonding and local energies. In the process of atomic movement, when an atom jumps into a low-energy location, it would be at a ‘trapped’ situation. In contrast, the atom jumping into a high-energy site can also increase the chance to hop back to its original site. Another fact is that phase transformations usually need cooperative diffusion of components, however, the complex composition of HEAs allows certain elements to always have relatively low activity. The combined effect of the above two realizes the slow diffusion process and the suppression of phase transformations.

3) Structure: severe lattice distortion - atoms are randomly distributed in the crystal lattice, leading to its distortion and affecting mechanical, transport and thermal properties

In a solid solution, all atoms are solute atoms that differ in atomic size from one another and occupy randomly lattice positions, thus resulting in a highly distorted multi-element lattice. It can be expected that due to this apparent difference in atomic size, there is a high degree of distortion in both crystalline and non-crystalline forms, which in turn affects their mechanical, thermal, electrical, optical and chemical behaviors.

4) Properties: cocktail effect - synergistic effect resulting from mutual interactions among composing elements, which would bring excess quantities to the average values simply predicted by the mixture rule

Since the one of HEAs system contains a variety of elements, it can be seen as a composite material at the atomic scale, and a composite effect occurs when there are multiple elements with various properties in the mixture. The ultimate properties of such materials are unpredictable, because it is not simply equal to the sum of the properties

of their principal components in themselves. In addition to the indirect effects of the various elements on the microstructure, they also exhibit a combined effect from the fundamental characteristics of the individual elements and the interactions between all of them.

The extent or even the existence of these high entropy effects was the subject of discussion in the early stages of the research, meanwhile, it can also be considered as a driving force for the study of HEMs [93, 94]. On the other hand, the above-mentioned effects are based on the most fundamental rules of thermodynamics and structural properties, and can therefore be expected to apply not only to metallic systems but also to other materials with the same design principles.

2.2.3. Entropy Stabilization

The concept of entropy stabilization in multi-component alloys has gained increasing interest in recent years, starting with the synthesis of HEAs. Since the first report on HEAs, controversial discussions on the role of configurational entropy had been ongoing, while a solid proof of entropy stabilization was still lacking [94]. Inspired by HEAs and analogues, Rost et al. [95] found the possibility to incorporate five different cations in equal atomic proportions into a single-phase oxide system and named it as an "entropy stabilized oxide" due to the clear evidence of entropy-driven structural stabilization effect. This is where the concept of entropy stabilization was first transferred to a multicomponent oxide. Recently, the family of HEMs has been emerged into a large range of materials, resulting in the development of high entropy carbides, borides, nitrides, and many other compounds [94, 96].

The configurational entropy is based entirely on the number of different elements in the single-phase structure, which can be achieved by increasing the number of elements randomly distributed on the same lattice sites. The molar configurational entropy can be calculated according to a Boltzmann-entropy-derived equation:

$$S_{\text{config}} = -R \left[\sum_{i=1}^M x_i \ln x_i \quad + \quad \sum_{j=1}^N x_j \ln x_j \right] \quad (2.13)$$

cation-site
anion-site

Where S_{config} and R are the configurational entropy and the ideal gas constant respectively, and x_i and x_j present the molar fraction of cations or anions on their respective sub lattices.

For a single anionic component, such as HEOs, the contribution of anionic site to the overall S_{config} can be considered as minor, because the anion sublattice is only occupied by oxygen. In equation 2.13, the second term for anion-sites is zero, therefore the entropy increases only related to the total number of cations adding [97]. In order to better demonstrate the contribution of different quantities of elements and molar ratios to entropy values in an N-components (N=2, 3, 4 or 5) solid solution [96], a function of the mole fraction of the Nth component is plotted in Figure 2.11a. It is clear that the S_{config} value increases significantly with the addition of more elements and reaches a maximum when all elements are present at nearly equimolar. As introduced by Murty et al. [98],

materials can be classified into “high entropy” with $S \geq 1.5R$, “medium entropy” with $1.5R > S \geq 1R$ and “low entropy” system with $S < 1R$, respectively. Empirically, it is found that the entropy-related effects occur while this value exceeds $1.5R$ and supposedly affect the material properties to varying degrees. This is due to the fact that the part of $T\Delta S_{\text{mix}}$ (presented in equation 2.12) is large enough to overcome the enthalpy change and dominate the trend in Gibbs free energy. Meanwhile, it also highlights the importance of the high temperature environment for the formation of single phase in an entropy-driven system [96, 97].

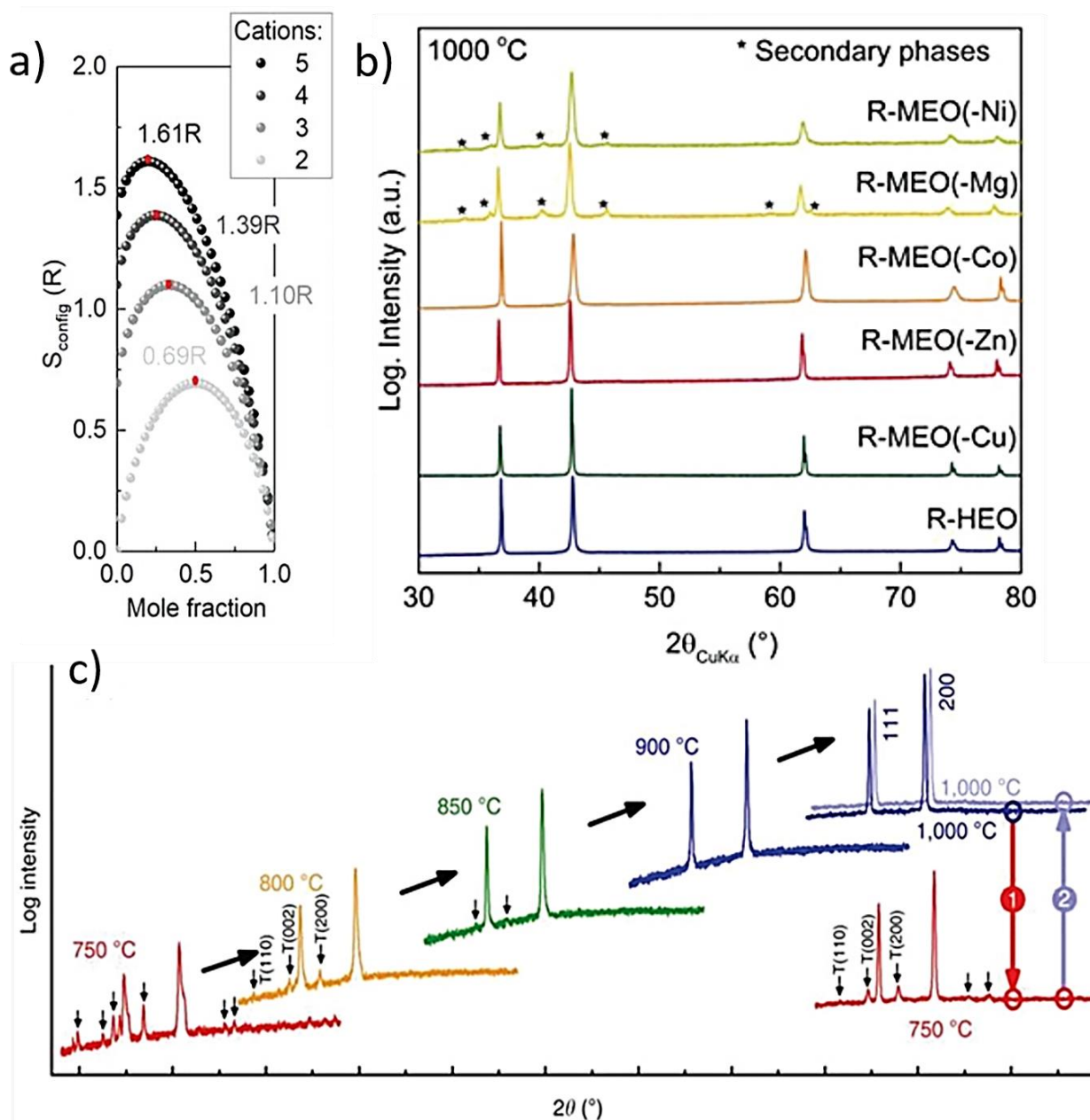


Figure 2.11: (a) dependence of configurational entropy on the number of elements, (b) XRD patterns of different types of R-MEOs and (c) reversible phase transformation as an indication of entropy stabilization effect [96]. (Reproduced with permission from (a) and (b) [96] ©2019, WILEY-VCH Verlag GmbH & Co. KGaA (c) [95]©2015, SPRINGER NATURE.)

The concept of entropy stabilization is based on the possibility of attaining a stable single-phase crystal structure

by increasing the configurational entropy of the system. It was first certified in 2015 with the obtain of a high entropy single phased (CoCuMgNiZn)O solid solution with a rock-salt structure (R-HEO) [95]. In this compound, the single ZnO and CuO are characterized as Wurtzite and Tenorite structures respectively which is far from optimal option to be rock-salt structure. However, both the structural mismatch of the composing elements and the limited solubilities of MgO-ZnO and CuO-NiO were overcome by entropy term at high temperature. Subsequently, the entropy-based material stabilization effect in R-HEO was demonstrated by a set of experiments results obtained from the heat treatment of R-HEOs at different temperatures, and showing with the reversible, entropy-driven mixing and de-mixing of phases upon increasing and decreasing temperature respectively. In details (Figure 2.11c), the de-mixing of the rock-salt structure is observed when the system is heat treated at 750 °C, and single-phase state again upon subsequent heating at 1000 °C. This reversibility strongly supports the entropy-dominated phase-stabilization concept, as at low temperatures the $T\Delta S_{\text{mix}}$ term might not be adequate to compensate for the enthalpy-driven phase separation [95, 96, 99].

Another indication of entropy-based phase stabilization effects can be observed by intentional control of the system S_{config} . As reported [96, 97], the removal of a certain cationic component from the 5-cationic R-HEOs system, as illustrated in Figure 2.11b, leads to a significant decrease in configurational entropy from the high entropy range (1.61R) to medium entropy oxides (1.39R, MEOs). This requires a higher temperature than that used for the synthesis of HEOs to compensate for their lower entropy to form a single phase. However, in some cases, such as R-MEO(-Ni) or R-MEO(-Mg), the -Ni and -Mg represent the cation removed from the parent R-HEO, it may not be possible to obtain a single-phase material even after treatment at 1000 °C due to the ΔS_{mix} term being significantly decreased.

Additionally, Mao et al. demonstrated a high-temperature (1123K) phase-stabilized spinel structure ((CoCrFeMnNi)₃O₄) which reflected a gradual shift of the observed peak due to the construction of lattice constant [100, 101]. Jiang et al. added a proof to the previous work on high-temperature phase stabilization of HEOs displaying as perovskite structure by adopting a concept of “tolerance factor” to predict the temperature-stability of these high entropy perovskite solid-solution phases [101, 102]. In addition to the above, a lot of other research works on high temperature entropy phase stabilization of HEOs, displaying fluorite [103], spinel [104], rock-salt [105, 106], amorphous [107] structure etc., have been carried out [101].

2.3. State of the Art

For HEMs, the combination of different cations and anions would result in a large number of possible components. By replacing cations or anions, their material properties such as conductivity, electrochemical stability and crystal structure can be modified easily. These tailorable properties make it suitable for a wide variety of applications. For this reason, HEMs have been utilized as catalyst for fuel cells, ceramic materials or electrode materials for LIBs/SIBs. In this thesis, the HEMs are used as a critical material to LIBs/SIBs. Here, HEMs used as electrode materials for batteries are described in detail in this section.

2.3.1. Charge Compensation Mechanisms

Following the above seminal research, a new class of HEOs was proposed, a large number of studies on different structural properties and applications of HEOs have been reported. For the typical (MgCoNiCuZn)O (named HEO_x in cited publication) components, Bérardan et al. [108, 109] reported that at least one HEO_x composition exhibits colossal dielectric constants, and confirmed a charge compensation mechanism in this system through a co-substitution by a valency 1+ and a valency 3+ element. This offers a larger possibility to develop new materials and explore potential applications by broadening phase spaces.

As reported [108], for (MgCoCuNiZn)_{1-x}Li_xO, the partial substitution of cations by Li⁺ leads to a well maintained rock-salt samples. However, the decrease in lattice parameter while Li⁺ fraction has been increased up to a certain level (x=16.6%), proves that Li⁺ can be successfully introduced into the rock-salt structure under certain restrictions. The reduction in lattice parameters suggests that Li⁺ does not occupy the insertion position, but substitutes for the +2 cations. The fact that the ionic radius of Li⁺ is larger than the average atomic radius of the other five divalent cations seems to oppose the decrease in lattice parameters appeared. This can be attributed to the formation of oxygen vacancies and the transformation of M²⁺ ions into M³⁺ which enables the partial substitution of 2+ elements by pairs of 1+ and 3+. Both of these two reasons can eventually lead to a reduction in lattice parameters, which is also the interpretation of the charge compensation effect [109].

A series of studies on these materials, such as X-ray Photoelectron Spectroscopy (XPS) and Density Functional Theory (DFT) studies [90, 110, 111], have provided a better understanding of the charge compensation mechanism. For parent HEO_x sample, all the cations are confirmed in a 2+ valence state, while the ratio of Co³⁺ increases with the amount of lithium, it can be affirmed that the charge compensation mechanism upon Li⁺ substitution involves, at least partly, the oxidation of cobalt to the 3+ state.

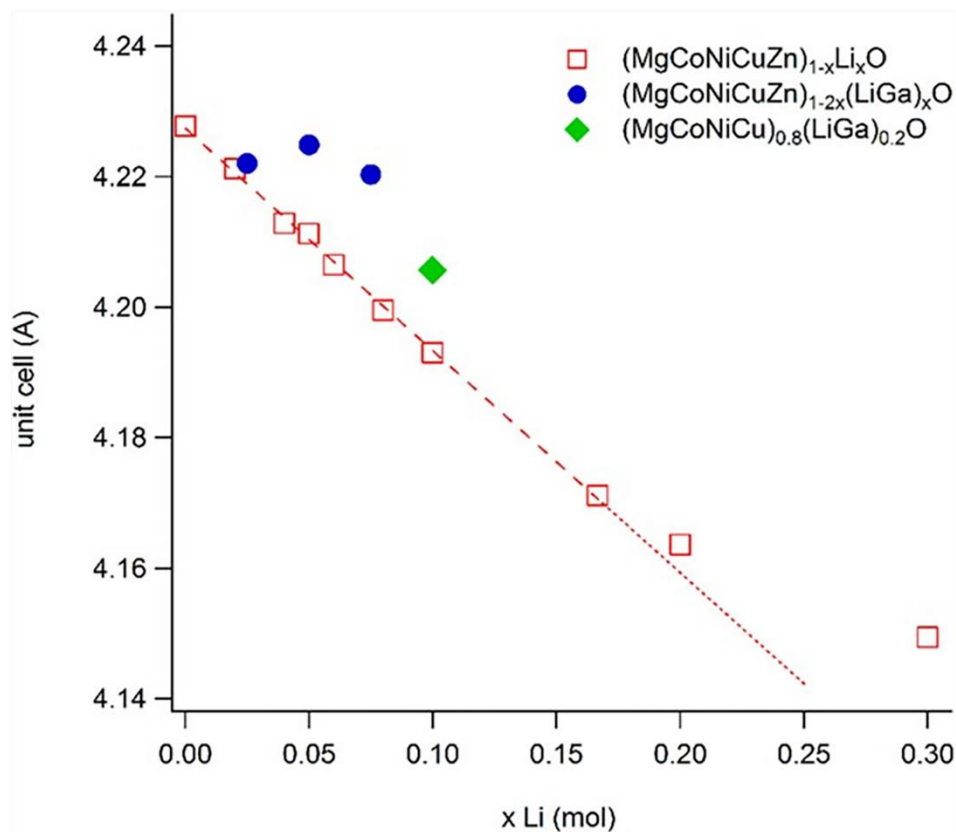


Figure 2.12: Lattice parameters for a series of compounds in the $(\text{Mg,Co,Ni,Cu,Zn})_{1-x}\text{Li}_x\text{O}$ family. (Reproduced with permission from [108] ©2016, WILEY-VCH Verlag GmbH & Co. KGaA.)

Additionally, a co-substitution with Li^+ and Ga^{3+} was performed to further confirm the presence of compensating mechanism [108]. As shown in Figure 2.12, when the x value is above 16.6%, the lattice parameter keeps decreasing but with a smaller rate, this indicates that at least two compensation mechanisms are present in the $(\text{MgCoCuNiZn})_{1-x}\text{Li}_x\text{O}$ series. When Ga^{3+} ion added, $(\text{MgCoNiCuZn})_{1-2x}(\text{LiGa})_x\text{O}$, a self-compensation mechanism between the two dopants enables the partial of 2+ elements substituted by the combination of 1+ and 3+. And the result compound, $(\text{MgCoNiCu})_{0.8}(\text{LiGa})_{0.2}\text{O}$, also crystallizes into a pure phase but with slightly smaller lattice parameter than the pristine sample, which confirms that a divalent cation can be completely substituted by a charge balanced combination of +1 and +3 or larger than +3 cations. Another content of charge compensation mechanism might correspond to the oxygen defects formation [108, 112]. By comparing samples with different lithium content, additional small peaks of oxygen in XPS results can be assigned to hydroxides or a kind of oxygen atoms with subsurface defects [108, 113, 114]. Therefore, the role of oxygen in the compensation mechanism cannot be ruled out.

To conclude, in addition to the large number of combinations of 2+ cations, which could lead to many different physical properties and potential applications, the various possible substitutions of 1+ elements or the co-substitution of 1+ and 3+ (or >3+) elements further expand the phase space of these materials to a large number of possible compositions. This opens up a new field of research into functional oxide materials, so such materials are not only limited to rock-salt structural oxides, but are extended to a wider range of different crystalline forms [108].

2.3.2. Crystal Structures

Considering of only one sub-lattice for cations in rock-salt structure [95], as shown in Figure 2.13a, R-HEOs was the main high entropy oxide of interest for the initial study. For the same reason, the range of HEOs was then extended to include a high entropy fluorite structure [115], as shown in Figure 2.13b. However, in comparison to single sub-lattice in the rock-salt and fluorite structure, spinel [104] or perovskite [102, 116, 117] structure based HEOs possess two different cation sub-lattices, with a general formulation of AB_2O_4 or ABO_3 . This permits the presence of trivalent cations to increase the range of valence changes, thus increasing the reversibility in the lithiation/delithiation process [118]. The formation of single-phase perovskite-based HEO (PE-HEO), fluorite-based HEO (F-HEO) and spinel-based HEO (SP-HEO) materials provides guidance for extending this design concept to structures with multiple cation sites as well. Representatively, the X-ray diffraction of single-phase PE-HEOs with 6 and 10 cation is shown in Figure 2.13c. The 6-cation PE-HEO, $(Gd_{0.2}La_{0.2}Nd_{0.2}Sm_{0.2}Y_{0.2})MnO_3$, provides evidence to stabilize multiple cations only at the A-site in an orthorhombic structure, correspondingly, the 10-cation one, $(Gd_{0.2}La_{0.2}Nd_{0.2}Sm_{0.2}Y_{0.2})(Co_{0.2}Cr_{0.2}Fe_{0.2}Mn_{0.2}Ni_{0.2})O_3$, exhibits a more chemically complex HEO, in which the A and B sites are occupied by five different assignable cations respectively, and all constituent elements are uniformly distributed on their respective positions [117].

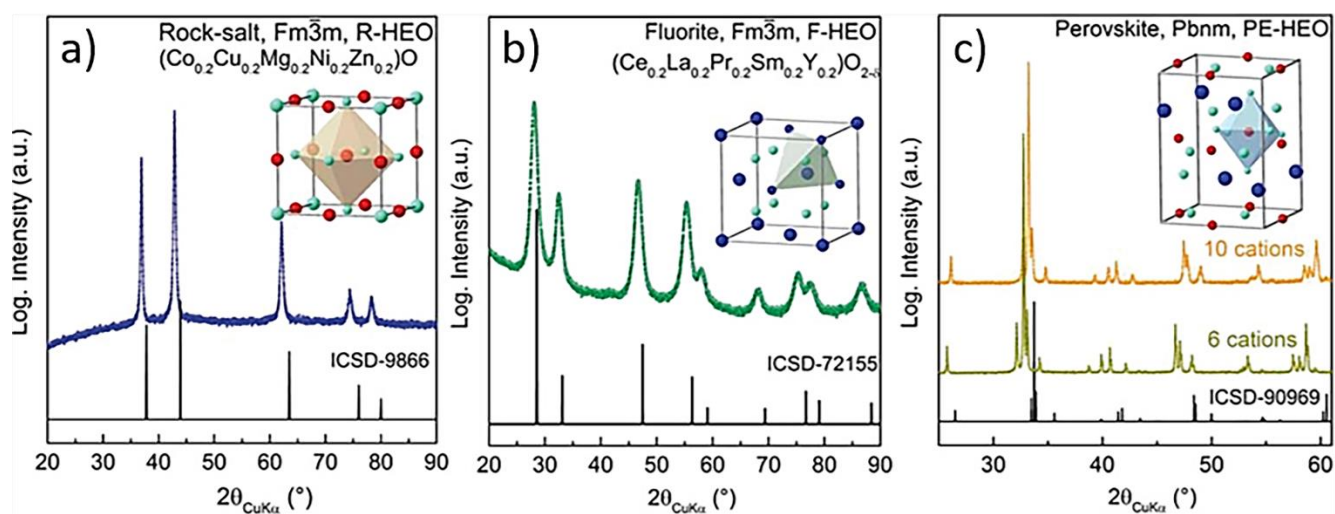


Figure 2.13: XRD patterns of HEO systems: (a) R-HEO, (b) F-HEO and (c) PE-HEOs. (Reproduced with permission from [96] ©2019, WILEY-VCH Verlag GmbH & Co. KGaA.)

It is worth noting that the local structure of HEOs is an important factor affecting the configuration entropy since any type of clustering or separation of elements would reduce the number of possible microstates and thus lowering the overall entropy [96, 98]. This means that in any type of structure or at any cation sites in these structures, it is required that the elements should be uniformly distributed in the lattice and exhibit the same local chemical environment [96].

2.3.3. Applications of High Entropy Oxides (HEOs) in Battery Field

As the main component in energy storage devices, different types of electrode materials that can be used in batteries have been a hot research topic in the field of materials in the past decades. Among them, metal oxides as electrode materials have received a lot of attention in recent years due to their high energy density and high specific capacity. In recent years, HEOs as a new class of oxide materials, have been explored as lithium and sodium ion electrolytes and electrode materials, which have attracted much attention due to their unique entropy stability and cation tailoring ability [90, 96, 119–121].

Following the pioneering experience on the researching of HEO, Bérardan et al. made initial attempts on electrochemical properties of this materials [109]. It was reported that 30% Li-doped (CoCuMgNiZn)O shows a much higher ion conductivity of 10^{-3} S cm^{-1} than that of pristine HEO (10^{-8} S cm^{-1}) at room temperature. This promising property, incorporating sufficient ions into the HEO structure causing a good conductivity, makes them a new potential material applied for lithium-based batteries, and it is inspired that more studies on the performance of HEMs in electrochemical energy storage devices are worthwhile [109, 119].

High Entropy Oxides as Anode Materials in Lithium-ion Batteries (LIBs)

Conversion type transition metal oxides (TMOs) as active anode materials with higher theoretical capacity compared to standard graphite anodes since the 1990s for LIBs are widely explored, however, both the suffering from a low initial CE and severely solid structures transformation resulting in fast capacity decay limit their application in long-life batteries [122, 123]. Recently, the entropy-stabilized metal oxides are widely studied and used as anode materials for LIBs due to their excellent structural stability and ionic conductivity. In 2018, a rock-salt (CoCuMgNiZn)O was first reported by Sarkar et al. [97] as an anode electrode material in a half coin cell, showing a good cycling performance that without capacity fading after 500 cycles (Figure 2.14a). The phenomenon of an increase in capacity over cycling is a typical conversion-type electrode and can be attributed to activation processes in electrode materials [97, 124, 125]. However, as can be seen in Figure 2.14b, the 4-cation systems with lower configurational entropy by excluding a specific element from (CoCuMgNiZn)O show faster capacity decay and poor cycling stability compared with that of 5-cation HEO. In order to compare "high entropy materials" and "medium entropy materials" further, the CEs for the first 50 cycles are depicted in Figure 2.14c. It can be seen that only the "high entropy material" shows a stable behavior, this shows severe side reactions which reduce the efficiency when the entropy stabilization of the active material is not adequate. It can be concluded that benefitting from the stabilization effect of entropy, the higher configurational entropy of the 5-cation system looks more favorable to maintain structural stability, storage capacity retention and cyclic stability.

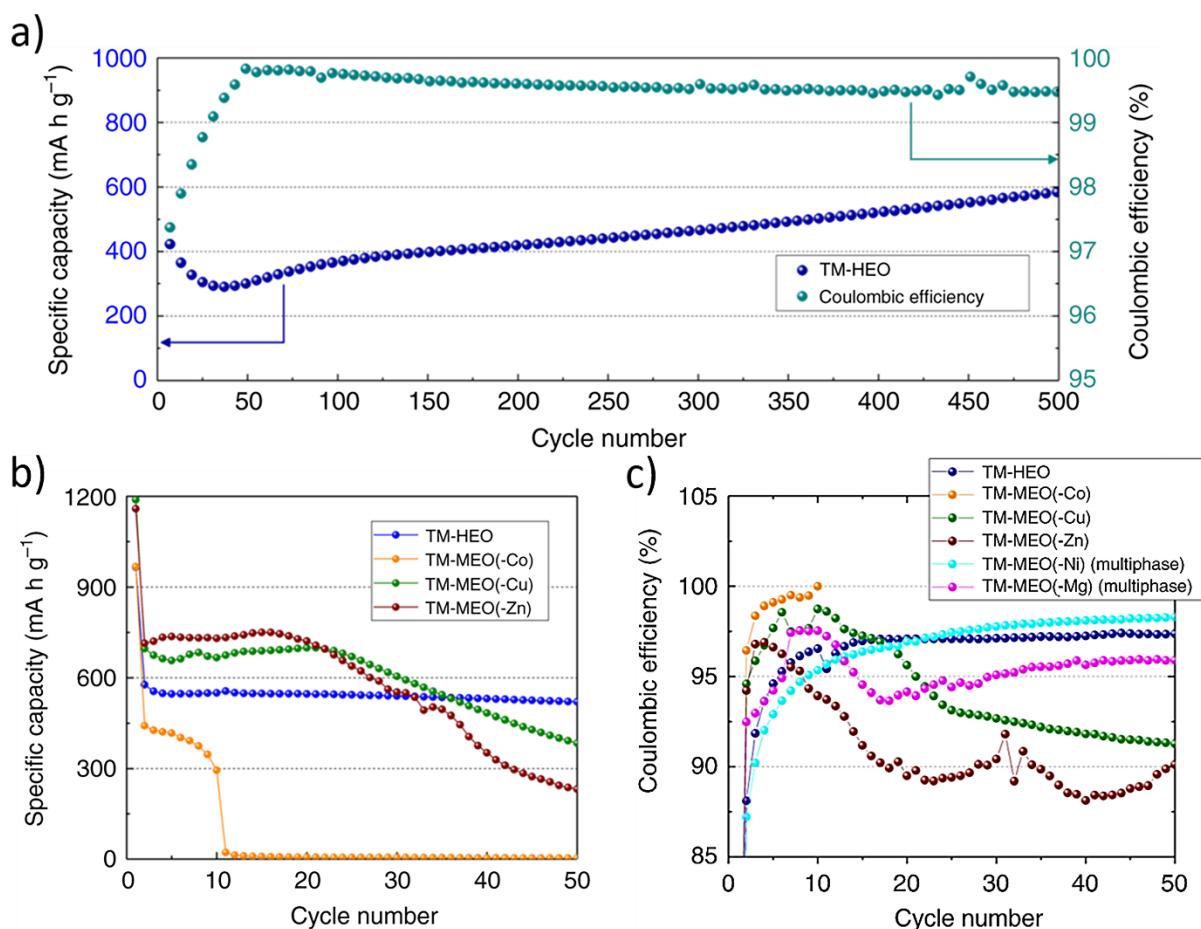


Figure 2.14: (a) Long-term cycling stability of the calcined HEO at 200 mA g⁻¹ together with the corresponding coulombic efficiency, (b) comparison of the different medium and high entropy oxides under investigation, (c) Coulombic efficiency vs. cycle number for all the tested electrode materials at 50 mA g⁻¹. (Reproduced with permission from [97] ©2019, SPRINGER NATURE.)

Typically, lithium metal foil as a counter electrode in half-cell testing can provide sufficient or excess lithium, but the limited lithium content and lithium ions reversible efficiency in full-cell testing are key factors in full-cell performance. The performance of (CoCuMgNiZn)O as anode in a full cell was evaluated by Wang et al., with Li(Ni_{1/3}Co_{1/3}Mn_{1/3})O₂ as the cathode material [126]. It is found that such cells delivered an initial specific capacity of 446 mA h g⁻¹ at 120 mA g⁻¹, as well as 300 mA h g⁻¹ and 256 mA h g⁻¹ maintained after 50 and 100 cycles, respectively. Such good performance of rock-salt type HEOs as anode have thus stimulated the further developments and studying on other types of HEOs. In a relevant study, a spinel (Mg_{0.2}Ti_{0.2}Zn_{0.2}Cu_{0.2}Fe_{0.2})₃O₄ as an anode materials in a half cell LIB was reported by Chen et al. [127] It delivered a high reversible specific capacity of 504 mA h g⁻¹ at 100mA g⁻¹ after 300 cycles and an excellent 96.2% capacity retention (272 mA h g⁻¹) at a high current density of 2000 mA g⁻¹ after 800 cycles. Yan et al. [128] synthesized a different HEO, [(BiNa)_{0.2}(LaLi)_{0.2}(CeK)_{0.2}Ca_{0.2}Sr_{0.2}]TiO₃, with a perovskite structure via a conventional sold-state method. As an anode material in half LIB, it provides an initial discharge capacity of 125.9 mAh g⁻¹ and with no decay after 300 cycles, the charge compensation mechanism and unique entropy stabilization of the A-site in the perovskite structure can be attributed as the main reasons.

HEOs as Cathode Materials in Lithium/Sodium-ion Batteries (LIBs/SIBs)

HEMs can be used not only as anode materials for LIBs/SIBs, but also as cathode materials, and thus are attracting increasing attention for their outstanding properties and wide range of applications. Wang et al. [129] prepared a high entropy Li-containing oxyfluoride (LHEOF), $\text{Li}_x(\text{Co}_{0.2}\text{Mg}_{0.2}\text{Cu}_{0.2}\text{Ni}_{0.2}\text{Zn}_{0.2})\text{OF}_x$, by adding additional halide (LiF) to R-HEO via a simple high energy ball milling method. Due to the involvement of fluorine, the operating potential of LHEOF is increased to ~ 3.4 V compared to 1.0 V for R-HEO, and thus the synthesized LHEOF was adopted as an active cathode material in LIBs. Resulting from the high entropy stabilization, it shows significantly improved capacity retention performance compared to LiNiOF over 300 cycles. Additionally, a new HEO with layered O3 type, $\text{Na}(\text{Ni}_{0.12}\text{Cu}_{0.12}\text{Mg}_{0.12}\text{Fe}_{0.15}\text{Co}_{0.15}\text{Mn}_{0.1}\text{Ti}_{0.1}\text{Sn}_{0.1}\text{Sb}_{0.04})\text{O}_2$, was synthesized by Zhao et al. [130] via solid-state reaction as cathode in SIBs. This HEO delivers a long cycling stability at different current densities, for example, around 83% of capacity retention after 500 cycles at 3.0 C and approximately 80% of that at 5.0 C. A proposed mechanism can be adopted to explain that the entropy stabilization on the host substrate is beneficial in promoting the formation of layered O3-type structures to a great extent, resulting in the better rate performance as well as long-life cycling stability. Very recently, a high entropy P2-type layered sodium TMO, $\text{Na}_{0.6}(\text{Ti}_{0.2}\text{Mn}_{0.2}\text{Co}_{0.2}\text{Ni}_{0.2}\text{Ru}_{0.2})\text{O}_2$, was designed and prepared by Yang et al. [131] It is determined by with a cathode electrode material in SIBs and exhibits a good capacity of 68 mA h g^{-1} at a super high current density of $15\,000 \text{ mA g}^{-1}$ (86 C) benefiting from the high entropy composition. The excellent rate performance of it mainly results from (1) the mitigation of the ordering of Na^+ /vacancy caused by a random distribution of cations in the TM slabs and (2) the formation of a permeable low barrier diffusion framework. The outstanding rate performance and the potential for further improvements in long-term cycling stability provide plenty of opportunities for further research along this direction.

Chapter 3

3. Experimental

This chapter gives a short introduction to the characterization techniques and experimental processes adopted in this work. Brief descriptions regarding the basic principles of these experimental techniques and samples preparation for characterizations (3.1), cell testing techniques (3.2) and the processes of sample synthesis and cells fabrications (3.3) are given in each section. If not stated otherwise, the experiments were carried out by the author of this study.

3.1. Fundamentals and Measurements

A combination of different characterization methods is an effective way to study the properties of samples from multiple perspectives. Some of the general characterization methods used for battery materials are presented in this section. The methods include X-ray diffraction (XRD), electron microscopy, inductively coupled plasma (ICP), X-ray photoelectron spectroscopy (XPS) and electrochemical techniques.

3.1.1. X-ray Diffraction (XRD)

X-ray diffraction (XRD) is one of the most important tools to determine the crystalline phases and lattice parameters of many kinds of materials, such as fluids, powders, pellets, etc. Usually, the properties and functions of materials are highly related to crystal structures and their subtle differences. Therefore, the XRD technique has been regarded as an essential means in materials research, analysis and development.

The Bragg equation [132],

$$n\lambda = 2d \sin \theta \quad (3.1),$$

is the basis to understand XRD which gives a relationship between the various parameters of the crystal. In this equation, n is an integer, λ is the characteristic wavelength of the incident X-rays, d is the spacing between the planes in the atomic lattice, and θ is the angle between the incident and the planes where the X-ray photons are diffracted.

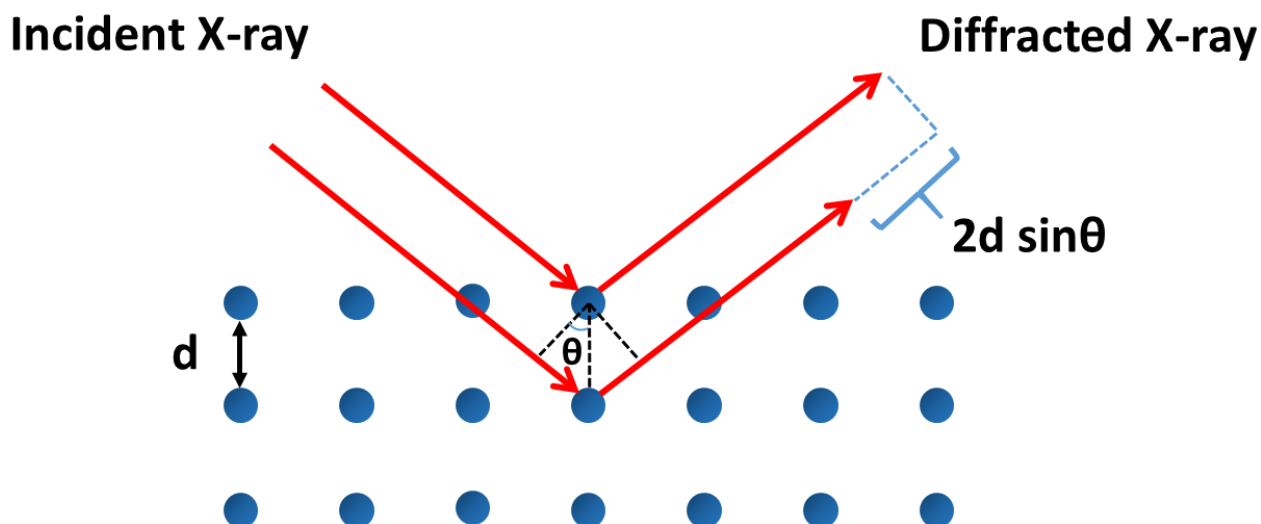


Figure 3.1: Illustration of X-ray diffraction defined by Bragg's law.

To better understand the principle, the geometry of XRD measurement is schematically shown in Figure 3.1. The constructive interference occurs only when the path difference ($d\sin\theta$) is a multiple ($n=1, 2\dots$) of the adopted wavelength (λ) of X-ray beam. Since the λ value in measurement is known and the angles at which constructive interference occurs are measured, the distance between lattice planes of samples can be determined by using the Bragg equation. As results, the measurements can be reflected as a so called diffractogram, in which X-ray intensity on the y-axis versus the angle 2θ on the x-axis are presented. The phase quantifications can be performed by Rietveld analysis by using the some supporting software, such as TOPAS, Fullprof, Jade, etc. The quality of the Rietveld fit is usually measured by the weighted profile R-factor (R_{wp}).

Operando XRD is a kind of time-resolved XRD technique to obtain crystallization information or structure evolution under a condition that dynamically changes over time [133]. No doubt that the operando technique is also the effective method for dynamic electrochemical process in different working states of electrode materials, to identify phase transitions, lattice constant changes, and crystal evolutions [134]. Therefore, in order to design and develop novel materials, the chemical and physical changes in a large number of reported works have been investigated and analyzed through the operando XRD technique.

In this thesis, the structure and phase purity of all as-prepared HEO materials were examined by powder X-ray diffraction (PXRD).

The experiments were performed using two different X-ray diffractometers. All measurements using the Bruker D8 Advance diffractometer with a Cu-K α radiation source ($\lambda = 1.54056 \text{ \AA}$) and a STOE Stadi P diffractometer with a Ga-Jet X-ray source using Ga-K β radiation ($\lambda = 1.20793 \text{ \AA}$) were measured by the author of this thesis. Operando studies and Rietveld refinement were performed with the help of Dr. Qingsong Wang and Dr. Simon Schweidler, respectively (both KIT).

3.1.2. Scanning Electron Microscopy (SEM)

Scanning electron microscopy (SEM) is an extensively used surface analytical technique, it can offer clear, large area and high-resolution images of target samples. What's more, the SEM equipped with energy-dispersive X-ray spectroscopy (EDX or EDS) can determine the atomic composition and distribution.

In SEM systems, the focused electron beam carries large kinetic energy in the range of 1-20 keV, and this energy is dissipated as various of signals generated by the interactions between electrons and sample. The signals include secondary electrons (SEs), backscattered electrons (BSEs), diffracted backscattered electrons (EBSDs), photons, visible light and heat. The SEM images are constructed by detecting the SEs and BSEs. BSEs are the primary electron beam and are generated by reflecting back after elastic interactions between the beam and the deeper areas of samples. However, secondary electrons come from the atoms of the samples, they are a result of inelastic interactions between the electron beam and samples. Usually, BSEs illustrate contrasts in composition in multiphase samples and SEs show morphology and topography on samples [135].

All SEM measurements were performed by the author of this thesis on a ZEISS Gemini Leo 1530 equipped with an Oxford EDX detector. The powder samples for each SEM experiment were prepared by coating them with Au using a sputter coater (30 s, 30 mA) to improve conductivity.

3.1.3. Transmission Electron Microscope (TEM)

The transmission electron microscope (TEM) is built similar with an optical microscope however electrons are used instead of visible light. Since the wavelength of the electron is much lower than that of visible light and the resolution of optical instruments are highly related to the wavelength of the used probe, therefore, the resolution of TEM is thousands time higher than that of an optical microscope [136].

The image signals of TEM are generated by transmitted electrons detecting. The accelerated electrons with an energy of 200-300 keV are targeted to samples, the transmitted electrons are detected and focused via an objective and aperture lens systems and projected onto an electronic image device to obtain a magnified image of the sample. In order to capture transmitted signals, the sample is required thin enough ($< 200 \text{ nm}$) [136, 137].

SEM can also be fitted with detectors to capture the transmitted electrons to get outstanding image resolution, this scanning mode with the transmitted signal collection is generally named scanning transmission electron microscopy (STEM). In addition, the TEM equipped with EDX, selected area electron diffraction (SAED) and

electron energy loss spectroscopy (EELS) can also be possible to characterize the elemental composition and, crystallographic phases.

TEM measurements were conducted on powder samples dispersed on a lacey carbon-coated copper grid in this thesis. TEM measurements were carried out by Kai Wang, Ziming Ding, and Xiaohui Huang working in Prof. Dr. Christian Kübel's Group (all KIT). Data analysis was done by the author with the help of the above-mentioned scientists. The samples were loaded onto an FEI double tilt holder. TEM, SAED and STEM-EDX data were collected using an FEI Titan 80-300 microscope equipped with a CEOS image spherical aberration corrector, a HAADF STEM detector (Fischione model 3000), EDAX SUTW EDX detector and a Tridiem Gatan image filter. The microscope was operated at an accelerating voltage of 300 kV.

3.1.4. X-ray Photoelectron Spectroscopy (XPS)

X-ray photoelectron spectroscopy (XPS) is a kind of widely used quantitative technique for revealing the information of the elemental composition, chemical and electronic state to a depth of 1-10 nm of materials.

In typical XPS measurement, some electrons at specific bound states can be excited by irradiated a sample with X-rays of sufficient energy which result in a fact that the photoelectron breaks away from the nuclear attraction of the element. Once these excited electrons escape from the sample and enter the vacuum, they can be collected by an electron analyzer which is used to measure their kinetic energy [138, 139]. Each prominent energy peak on the spectrum corresponds to a specific element, thus identifying the elements contained in the sample. In addition, the area of each peak is proportional to the number of atoms present for each element, so the amount of each element in the sample can be determined by calculating the area of correspond peak. What's more, core level shift is important information for determining the valence states of elements [140].

XPS measurements were measured and analyzed either by Dr. Raheleh Azmi (KIT) or by Dr. Thomas Diemant and Dr. Guruprakash Karkera at the Helmholtz Institute Ulm (HIU). The final figures were prepared and analyzed by the author of this study, using Casaxps software with the help of Dr. Qingsong Wang (KIT).

XPS measurements at KIT were performed on a K-Alpha+ instrument (Thermo Fisher Scientific) with a monochromatic Al-K α X-ray source (1486.6 eV) and 400 μ m spot size. The K-Alpha+ charge compensation system was applied to prevent localized charge buildup during analysis using 8 eV electrons and low-energy Ar ions. Data acquisition and processing were carried out using the Thermo Advantage software [145]. The spectra were fitted with one or more Voigt profiles. The binding energies are reported with respect to the C 1s peak of hydrocarbons at 285.0 eV. XPS measurements at HIU were performed on a Specs XPS system with a Phoibos 150 energy analyser using monochromatic Al K α radiation (1486.6 eV), a take-off angle of 45° and pass energies of 30 and 90 eV at the analyser for detail and survey spectra, respectively. The samples were kept under Ar while transferring from the glovebox to the XPS system to avoid contamination.

3.1.5. X-ray Absorption Spectroscopy (XAS)

X-ray absorption spectroscopy (XAS) is a method to characterize the chemical nature and environment of atoms in molecules, the X-ray energies provided by synchrotron sources are particularly applicable to elements with redox activity [140]. Since each core electron has a well-defined binding energy, the photoelectric effect occurs at specific X-ray photon energies.

X-ray absorption spectra of any materials can be characterized by sudden increases in absorption at these specific X-ray photon energies. The abrupt increases in absorption are called absorption edges, which can be named according to the electron that is excited. It is known as the K-edge when the photoelectron originates from a 1s core level, and an L-edge when the ionization is from a 2s or 2p electron [140, 141].

The K-edge spectrum is divided into two regions, the extended X-ray absorption fine structure (EXAFS) region referring to structure well above the absorption edge, and the X-ray absorption near edge structure (XANES) region, which provides detailed information about the oxidation state and local geometric information [141, 142]. The K-edge absorption edge energy increases with increasing oxidation state. The higher the oxidation state of the metal, the more positive the overall charge of the atom, and therefore more energy is required to excite an electron from an orbital [140].

XAS measurements and analysis for 3-NTMO₂, 5-NTMO₂, and 7-NTMO₂ were performed by Dr. Ahmad Omar in Leibniz Institute for Solid State and Materials Research (IFW), Dresden. XANES at the Mn K-edge was performed at the beamline P65 of PETRA III extension of DESY (Hamburg, Germany) in transmission setup. The electrode was prepared using carbon paper as the current collector, and the mass loading of the active material was around 12 mg cm⁻². Customized coin cells with Kapton windows were prepared using the same electrolyte as the laboratory electrochemical measurements, which were then connected with an eightfold coin cell holder [143] coupled with a Bio-Logic potentiostat. The cells were cycled at 0.1C (1 C = 200 mA g⁻¹) in the voltage range of 1.5-4.6 V vs. Na⁺/Na. Appropriate metallic foils were used for calibration. The obtained data was analysed by Dr. Qingsong Wang and the author of the study by using the DEMETER package [144].

3.1.6. Mössbauer Spectroscopy

Mössbauer spectroscopy can be used to study the chemical environment and oxidation state of Fe. In Chapter 5, ⁵⁷Fe Mössbauer spectroscopy was performed in transmission geometry using a spectrometer with a moving source of ⁵⁷Co in a Rh matrix and a triangular velocity variation. The isomer shift is given relative to bcc-Fe at room temperature. Mössbauer spectroscopy was performed and analyzed by Dr. Abhishek Sarkar (KIT).

3.1.7. Inductively Coupled Plasma (ICP) Spectroscopy

The inductively coupled plasma-optical emission spectroscopy (ICP-OES, iCAP 7600DUO from Thermo Fisher Scientific, Waltham, MA, USA) is an effective technique for elemental composition determined. Experimentally

for Chapter 4, Chapter 5 and Chapter 6, about 10 mg of the respective powder samples (weighing accuracy ± 0.05 mg) were dissolved in 6 mL of hydrochloric acid, 2 mL of nitric acid, and 4 mL of sulfuric acid at 513 K for 35 min in a microwave oven (Speedwave Xpert from Berghof). Analysis was accomplished using four different calibration solutions and an internal standard (Sc). Two or three major wavelengths of elements were used for calculation. The oxygen content was probed by the method of carrier gas hot extraction (CGHE) using a commercial oxygen/nitrogen analyzer TC600. The oxygen concentration was calibrated with the certified standard KED 1025, a steel powder from ALPHA, and the calibration was verified using a commercial powder. The calibration range was close to the sample concentration. The standards and the samples were weighed with a mass in the range from 1 to 3 mg in Sn crucibles (9-10 mm). Then, 5 mg of graphite were added and wrapped. Combined with a Sn pellet (~200 mg), they were placed into a Ni crucible. The package was loaded in an outgassed (5800 W) high temperature graphite crucible. The measurements were conducted at 5000 W. Evolving CO₂ and CO were swept out by helium as inert carrier gas and measured via infrared detectors.

In Chapter 6, the Mn contents in the electrolyte filled separators were determined in another way. Each electrolyte filled separator was immersed in 5 ml DMC inside a glove box. The Mn containing aliquots from solutions were then diluted by a factor of 100 with doubly-distilled deionized (DD-DI) water, and the Mn concentrations of the resulting solutions were determined by ICP-OES.

ICP-OES measurements were measured either by Dr. Thomas Bergfeldt (KIT) or with the help of Dr. Qingsong Wang. The data were analyzed by the author of this study with help of Mr. David Stenzel and Dr. Qingsong Wang (both KIT).

3.1.8. Differential Electrochemical Mass Spectrometry (DEMS)

Differential electrochemical mass spectrometry (DEMS) is an analytical technique that combines electrochemical half-cell experimentation with mass spectrometry. It can be used to identify the gaseous or volatile electrochemical reactants, one method to achieve this is to oxidize carbonaceous species to CO₂, which is quantitatively detected in a mass spectrometer meanwhile [145, 146].

The gas evolution of the cathode materials in Chapter 6 during the electrochemical cycling was studied by DEMS. In detail, a customized cell using a cathode (\varnothing 30 mm, ~ 3.5 mg cm⁻² areal loading) was charged/discharged in the voltage range of 1.5-4.6 V vs. Na⁺/Na at 20 mA g⁻¹. The specific current was calculated based on the cathode active material. A hole (\varnothing 4 mm) in the center of the cathode allowed gas flow. GF/D glass microfiber (\varnothing 40 mm) and Na metal (\varnothing 30 mm,) were used as separator and anode, respectively. 800 μ L electrolyte was used in this measurement, and the compositions of electrolyte is 1.0 mol L⁻¹ NaClO₄ in a 1:1:1 vol ratio of EC, DMC and PC solution and with FEC (5% in volume). During electrochemical cycling, a constant stream of He (purity 6.0) carrier gas (2.5 mL min⁻¹) was passed through the cell. The extracted gas mixture was analyzed using a mass spectrometer (Omni Star GSD 320, Pfeiffer Vacuum GmbH). DEMS was measured and analyzed by Mr. Sören L. Dreyer (KIT).

3.2. Cell Testing Techniques

Cyclic voltammetry (CV) and galvanostatic cycling are two standard analytical methods used for electrochemical performance determination in this study. The brief introduction and test parameters for each technique are described in this section. The CV technique can be used to study the complete performance of a system via recording information on the electrochemical behavior [147]. The results are present through sweeping the potential over time with a set rate in the cut-off potential window and recording the current varying versus potential [147, 148].

In CV curves, if there are no changes on the position of the maximum current peaks regard to their potential with the scan rate varying, and the heights of the anodic and cathodic peaks appear to be equal, it can be said that the redox process occurring is reversible [149]. Galvanostatic cycling is another technique to investigate battery materials. For the test, a constant current determined by the capacity of the electrode material is applied to electrode, until to a defined potential range are reached. In this process, the potential variation over time is recorded [147, 150].

CV measurements in this thesis were performed by using a Bio-logic potentiostat (VMP3). Depending on the different purposes of the tests, the voltage ranges were set to both 2.0-4.5 V and 0.1-3.0 V versus Li^+/Li for studies in Chapter 4, 2.5-4.5 V versus Li^+/Li in Chapter 5, and 2.5-4.6 V and 1.5-4.6 V versus Na^+/Na in Chapter 6, respectively. The sweep rate in each work was 0.1 mV s^{-1} . Galvanostatic cycling measurements were performed by using Arbin battery test system (BT-2000) or Land CT2001A battery test system (Wuhan LAND Electronic Co. Ltd., China) at room temperature. The specific capacity was calculated based on the mass of active material, and the applied voltage ranges are same with those used in CV tests.

3.3. Materials Synthesis and Cell Fabrication

There are a lot of different advanced techniques adopted for synthetic battery materials. This section briefly describes the materials preparation methods what used in this thesis, including nebulized spray pyrolysis (NSP), conventional sintering and solid-state method. And the details of cells fabrication are also present in this section.

3.3.1. Nebulized Spray Pyrolysis (NSP)

Generally, most of oxide materials are synthesized by using either conventional solid-state reactions [151, 152] or solution-based techniques [71, 153]. However, time consuming procedures are involved for solid-state reactions to repeat milling procedures and thermal treatments [151, 152]. The solution-based methods usually require the complex agents/components resulting in large amounts of residues after synthesis, post-calcining and even inevitable grinding [71, 153]. Recently, a new method, NSP, was successfully adopted to prepare Al doped lithium lanthanum zirconium oxide ($\text{Li}_{7-3x}(\text{La}_3\text{Zr}_2\text{Al}_x)\text{O}_{12}$) which shows the advantages that thermolysis and

annealing occur simultaneously resulting in the formation of nanocrystalline powders [154]. The NSP method with the experimental setup is shown in Figure 3.3.

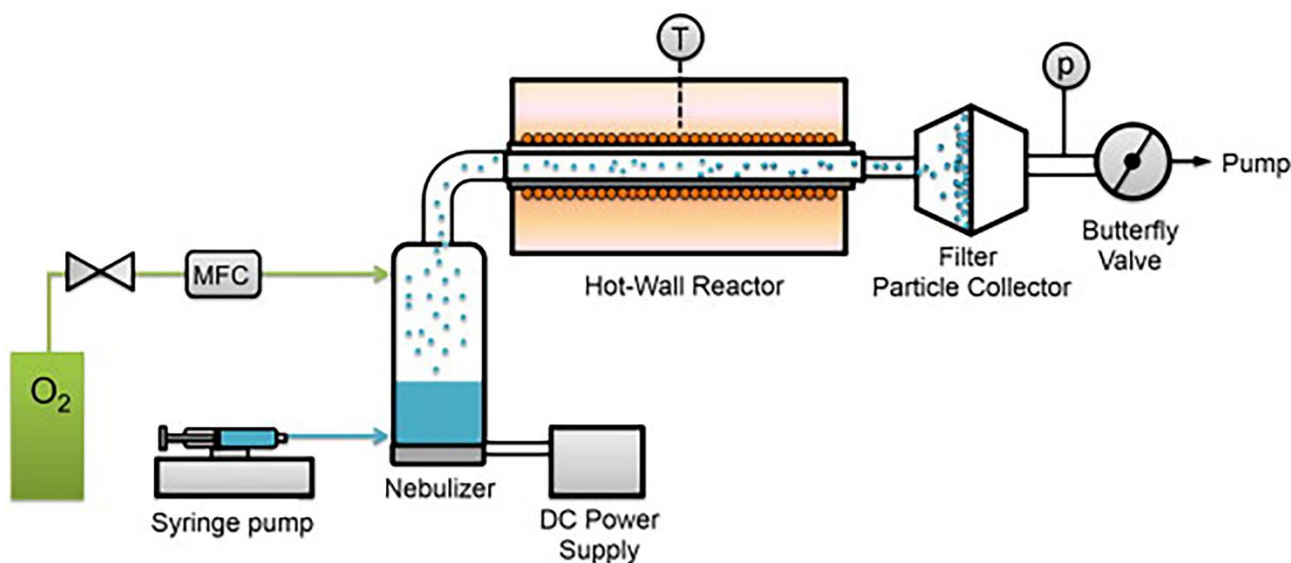


Figure 3.2: Nebulized spray pyrolysis experimental setup [154]. (Reproduced with permission from [154] ©2014 Elsevier B.V.)

The precursor solution was continually delivered into a nebulizer container with a constant level by a syringe pump. The solution mist was carried into the hot-wall reactor by flowing gas controlled by a mass flow controller (MFC). The process pressure in the whole system is maintained at a constant value (900 mbar) which is achieved and enable to be adjusted by using a Baratron absolute pressure gauge and a vacuum pump. Nanoparticles were synthesized at a set temperature and collected by a glass fiber filter paper placed inside a collection unite. In order to prevent water vapor condensation on the filter, the collector should be kept heating above 100 °C by external heating tape [154].

The NSP process provides shorter processing times compared to other techniques (e.g., solid-state reaction, sol-gel, etc.) and flexibility regarding composition and phase formation. Furthermore, it can be used to produce even compositionally complex systems (containing substantially more than two elements) at a high yield [154]. This method allows the production of nanocrystalline powders either directly in the desired crystal structure and phase composition [155] or as a precursor for further heat treatments.

The NSP method were applied in Chapter 4 and Chapter 5 for preparing target HEOs. In Chapter 4, the products were synthesized with gradually increasing lithium contents ($x = 0, 0.2, 0.4, 0.6, 0.8,$ and 1), namely $\text{Li}_x(\text{NiFeMnCrCo})_y\text{O}_z$, $\text{Li}_x(\text{NiFeMnCrMg})_y\text{O}_z$, and $\text{Li}_x(\text{NiFeMnZnMg})_y\text{O}_z$. To this end, equimolar solutions of the respective metal salts were prepared from $\text{Ni}(\text{NO}_3)_2 \cdot 6\text{H}_2\text{O}$ (Alfa Aesar, 98%), $\text{Fe}(\text{NO}_3)_3 \cdot 9\text{H}_2\text{O}$ (abcr GmbH, 98%), $\text{Mn}(\text{NO}_3)_2 \cdot 3\text{H}_2\text{O}$ (abcr GmbH, 98%), $\text{Cr}(\text{NO}_3)_3 \cdot 9\text{H}_2\text{O}$ (abcr GmbH, 99%), $\text{Co}(\text{NO}_3)_2 \cdot 6\text{H}_2\text{O}$ (abcr GmbH, 99%), $\text{Mg}(\text{NO}_3)_2 \cdot 6\text{H}_2\text{O}$ (Sigma Aldrich, 99%), $\text{Zn}(\text{NO}_3)_2$ (Riedel-de Haën), and LiNO_3 (Alfa Aesar, 99%). The resultant precursor solutions were transformed into fine droplets by an ultrasonic nebulizer and further transported using flowing nitrogen through a hot-wall reactor (1050 °C). The particles were collected on filter paper maintained at

120 °C in order to prevent water vapor condensation on the deposited powders. In Chapter 5, the as-synthesized materials via NSP method were applied as precursor for next step heat treatment. Similarly, nitrate salts of the respective metals (LiNO_3 , $\text{Co}(\text{NO}_3)_2 \cdot 6\text{H}_2\text{O}$, $\text{Ni}(\text{NO}_3)_2 \cdot 6\text{H}_2\text{O}$, $\text{Mn}(\text{NO}_3)_2 \cdot 4\text{H}_2\text{O}$, $\text{Zn}(\text{NO}_3)_2 \cdot 6\text{H}_2\text{O}$, $\text{Fe}(\text{NO}_3)_3 \cdot 9\text{H}_2\text{O}$, $\text{Al}(\text{NO}_3)_3 \cdot 6\text{H}_2\text{O}$, NaNO_3 ; Sigma-Aldrich) were adopted to prepare starting solution for NSP process.

3.3.2. Conventional Sintering

Sintering can result in high-strength bonds and crystalline structure formation or reconstruction. Generally, the atmosphere, temperature and duration time need to be controlled precisely in order to provide a ceramic material with particular characteristics. For conventional sintering, it is the simplest technique which involves heating of a designed precursors at an ambient atmosphere without applying any external pressure [156, 157].

All of precursors present in Chapter 5 were synthesized by NSP method firstly. Then, all collected powder was further calcined at 900 °C for 12 h with a heating speed of 5 °C min⁻¹ and cooled down, to obtain eventually layered cathode materials.

3.3.3. Solid state Synthesis

Owing to the benefits of cost-efficiency, process simplicity and accurate stoichiometric ratios, solid-state method is one of the most often applied synthesis process in industrial manufacturing [157]. In a typical approach of the method, the starting materials, including the transition metal and Li/Na nitrates, acetates, oxides, etc., are blend by ball milling or other mixers [158]. And then, the mixture is calcined at an appropriate temperature for a few hours until the electrode material is successfully prepared.

In Chapter 6, three P2-type cathode electrode materials in this paper, $\text{Na}_{0.67}(\text{Mn}_{0.55}\text{Ni}_{0.21}\text{Co}_{0.24})\text{O}_2$, $\text{Na}_{0.67}(\text{Mn}_{0.45}\text{Ni}_{0.18}\text{Co}_{0.24}\text{Ti}_{0.1}\text{Mg}_{0.03})\text{O}_2$ and $\text{Na}_{0.67}(\text{Mn}_{0.45}\text{Ni}_{0.18}\text{Co}_{0.18}\text{Ti}_{0.1}\text{Mg}_{0.03}\text{Al}_{0.04}\text{Fe}_{0.02})\text{O}_2$ were synthesized via a simple solid-state reaction. In the first step, stoichiometric amounts of the precursors Na_2CO_3 (Acros Organics 99.95%), MgO (abcr GmbH 99.5%), Al_2O_3 (Alfa Aesar 99.5%), TiO_2 (Alfa Aesar 99.5%), Mn_3O_4 (abcr GmbH 97%), Fe_3O_4 (Alfa Aesar 97%), Co_3O_4 (Alfa Aesar 99%), and NiO (Alfa Aesar 99%) were thoroughly mixed by ball milling at 400 rpm for 2h and pressed into pellets under pressure of 5 t. After that, the pellets were heated up to 500 °C for 2 h and calcined at 900 °C for 12 h. The final product was obtained by cooling naturally to room temperature and directly kept into an Ar-filled glovebox to prevent any further air exposure.

3.4. Fabrication of Cells

Electrodes for cell testing were prepared by doctor blading (100 μm slit size) slurry on Al foil (Gelion LIB Co., Ltd.) and Cu foil (MTI Corporation). The slurry contained 70 wt.% of HEO as active material, 20 wt.% Super C65 carbon black additive (TIMCAL Ltd.), and 10 wt.% polyvinylidene fluoride binder (PVDF, Solef5130, Solvay) dissolved in N-methyl-2-pyrrolidone (NMP, Sigma Aldrich). The resultant electrodes were dried in a

vacuum at 120 °C for 12 h, followed by punching out circular disks of diameter in 13 mm. Usually the active material loading is of 1.5-2.5 mg cm⁻², the specific capacity was calculated on the basis of the active material mass. Cells were assembled in an Ar-filled glovebox and tested using CR2032 coin cells. Li and Na metal foil (Gelon LIB Co., Ltd.) were used as counter electrode, glass microfiber filter paper (GF/C, Whatman) as separator. It is note that, the compositions of electrolyte applied for LIBs and SIBs are different more or less, 1 M LiPF₆ in a 3:7 weight mixture of EC: ethyl methyl carbonate (EMC) was used as electrolyte (LP57, BASF SE) for LIBs testing, while the electrolyte used for SIBs was 1.0 mol L⁻¹ NaClO₄ in a 1:1:1 vol ratio of EC, DMC and PC solution and with FEC (5% in volume).

In addition, a kind of special cells were utilized for *operando* XRD analysis, customized CR2032 coin cells with Kapton windows in Ø 4 mm on each side were used for carrying out the measurements. The active material loading is 2.5-3 mg cm⁻² which is higher than that for Galvanostatic charging and discharging and CV testing, in order to obtain stronger signal of XRD diffraction.

Chapter 4

4. Spinel to Rock-Salt Transformation in High Entropy Oxides with Li Incorporation

The majority of the results presented in this chapter have been published in Electrochem [159]. The experimental work was carried out jointly by Junbo Wang and David Stenzel. The manuscript was organized and written by Junbo Wang and David Stenzel together under the guidance of Dr. Ben Breitung and all other co-authors. Co-authors contributed by helping with certain characterization methods, providing valuable discussions, and reviewing the article draft for the peer-reviewed publication process.

4.1. Introduction

A recent finding by Bérardan et al. on the subject of $(\text{NiCuZnMgCo})_{1-x-y}\text{Ga}_y\text{A}_x\text{O}$ (with $\text{A} = \text{Li}, \text{Na}, \text{K}$) showed that introducing monovalent elements into a divalent structure, a formation of oxygen vacancies can appear, which are created by a charge compensation mechanism, resulting in a decrease in lattice parameters and the possibility of ionic conductivity occurring [109]. Lately, HEOs have been shown to have potential as conversion, intercalation, and insertion materials for application in LIBs and SIBs [96, 97, 126, 130, 160–162]. Nevertheless, the role of monovalent Li in an oxide crystal structure and the reaction of the other incorporated elements upon addition of Li is not clear yet.

While the lithiation mechanism for binary or ternary oxide systems has been investigated extensively, the lithiation processes appearing in HEOs are still very unclear, because the complex nature of a HEO system, as the presence of many different metal ions, complicates a detailed analysis. However, the presence of different metal ions that may result in different properties can be analyzed in detail via a combination of many different techniques. Investigations into the evolution of the crystal structure in conventional transition-metal oxides during the lithiation/delithiation process provide valuable insights into the lithiation mechanism and help in postulating theories about the observed structural changes [97]. An example for a well-investigated structural change during lithiation, either by chemical or electrochemical means, is the transition of Co_3O_4 from a spinel phase into a rock-

salt phase. The spinel compound converts into a partially ordered rock-salt compound (LiCo_3O_4), which occurs by Li^+ insertion into octahedral 16c Wyckoff sites, leading to a shift of Co^{3+} from the tetragonal 8a sites into adjacent octahedral 16c site [163–166].

In this chapter, I replaced systematically the ions and analyzed what changes appear in a series of materials with similar components and structures. The effect of Li incorporation on the lattice structure of spinel-type materials $(\text{NiFeMnCrCo})_x\text{O}_y$, $(\text{NiFeMnCrMg})_x\text{O}_y$, and $(\text{NiFeMnZnMg})_x\text{O}_y$ was studied. The Li content was gradually increased by tailoring the amount of precursor used in the synthesis via NSP method and the exact atomic percent of the Li was measured by ICP-OES. The addition of monovalent ions to a mixed $\text{M}^{2+}/\text{M}^{3+}$ (spinel) or M^{2+} (rock-salt, with $\text{M} = \text{metal}$) phase requires charge compensation and, depending on the Li concentration, may lead to phase transformation. To gather information about the charge compensation mechanism, elements that are known to exhibit multiple oxidation states were substituted out in a stepwise approach by elements that exhibit a single distinct oxidation state ($\text{Co}^{2+/3+} \rightarrow \text{Mg}^{2+}$ and $\text{Cr}^{3+/6+} \rightarrow \text{Zn}^{2+}$). The oxidation states of the elements were individually analyzed and connected to the structural transition. This study investigates the importance of including certain metal elements in HEOs and their combinational effects, a concept known as the “cocktail effect.” It offers a supplementary parameter that can be used through chemical composition of HEOs to control their functional properties and further widening the possibilities offered by this new class of materials. In addition, the redox behavior of $\text{Li}_x(\text{NiFeMnCrCo})_y\text{O}_z$ in LIB cells has been tested to assess the overall application potential in the battery field.

4.2. Results and Discussion

In the present work, the spinel to rock-salt phase transformation with increasing Li concentration in HEOs was investigated. Such transition is relatively well-known for simple oxides and has been the subject of many studies. The employed HEOs were prepared via the NSP method, allowing the incorporation of lithium without any additional chemical or electrochemical post-treatment steps. The Li content was gradually increased, while keeping the ratio of the other metals constant. In particular, three different HEOs were prepared, namely $\text{Li}_x(\text{NiFeMnCrCo})_y\text{O}_z$ (HEO-1), $\text{Li}_x(\text{NiFeMnCrMg})_y\text{O}_z$ (HEO-2), and $\text{Li}_x(\text{NiFeMnZnMg})_y\text{O}_z$ (HEO-3), and the amount of lithium stepwise increased ($x = 0, 0.2, 0.4, 0.6, 0.8, 1$) for every composition. Upon lithiation, different structures and oxidation states were expected to evolve, as the monovalent Li^+ ions in mixed-valence spinel or rock-salt systems must be compensated for in order to maintain charge neutrality.

4.2.1. Powder X-ray Diffraction (PXRD)

The structural transition was investigated by means of PXRD. Figure 4.1 shows PXRD patterns of the as-prepared materials, revealing the change from spinel to rock-salt structure with increasing Li content. The elements highlighted in the respective formulas represent those that were replaced by others during the course of this study. For HEO-1 (Figure 4.1a), the relative intensity of the (220), (311), (422), and (511) reflections are found to

Figure 4.1b shows PXRD patterns obtained for HEO-2, where Co has been substituted by Mg. XPS (later explained in detail, Figure 4.3) showed that the non-lithiated HEO-1 contained mainly Co^{2+} . In contrast, in the lithiated state, Co^{2+} is oxidized to Co^{3+} . By replacing $\text{Co}^{2+/3+}$ with Mg^{2+} , the charge compensation associated with the Co redox is eliminated. Therefore, some changes in phase transformation behavior can be anticipated. In fact, a comparison of the (311) and (222) reflection intensities of HEO-1 and HEO-2 for $x = 0.4$ revealed some differences among the materials that both the intensity decreasing of (311) and increasing of (222) for HEO-2 are more pronounced than those for HEO-1. This in turn suggests larger changes in structure or form factor for HEO-2, most probably because of differences in the overall charge compensation mechanism. Moreover, when Cr is replaced by Zn (HEO-3, Figure 4.1c), the full transition to the rock-salt structure is already evident for $x = 0.4$. This finding demonstrates that the transition occurs at lower Li concentrations if the average charge of the metal ions involved is reduced ($\text{Co}^{2+/3+} \rightarrow \text{Mg}^{2+}$ and $\text{Cr}^{3+/6+} \rightarrow \text{Zn}^{2+}$).

4.2.2. Inductively Coupled Plasma-Optical Emission Spectroscopy (ICP-OES)

ICP-OES was used to analyze the stoichiometries of chemical compositions. Figure 4.2 shows the corresponding data for the HEO-1 with different Li contents. While the theoretical metal to oxygen ratio of spinel-type M_3O_4 materials is 0.75, the relative cation concentration increases when a rock-salt phase of general formula M_1O_1 is formed. This trend was indeed observed in the data, where a maximum of 0.9 was achieved.

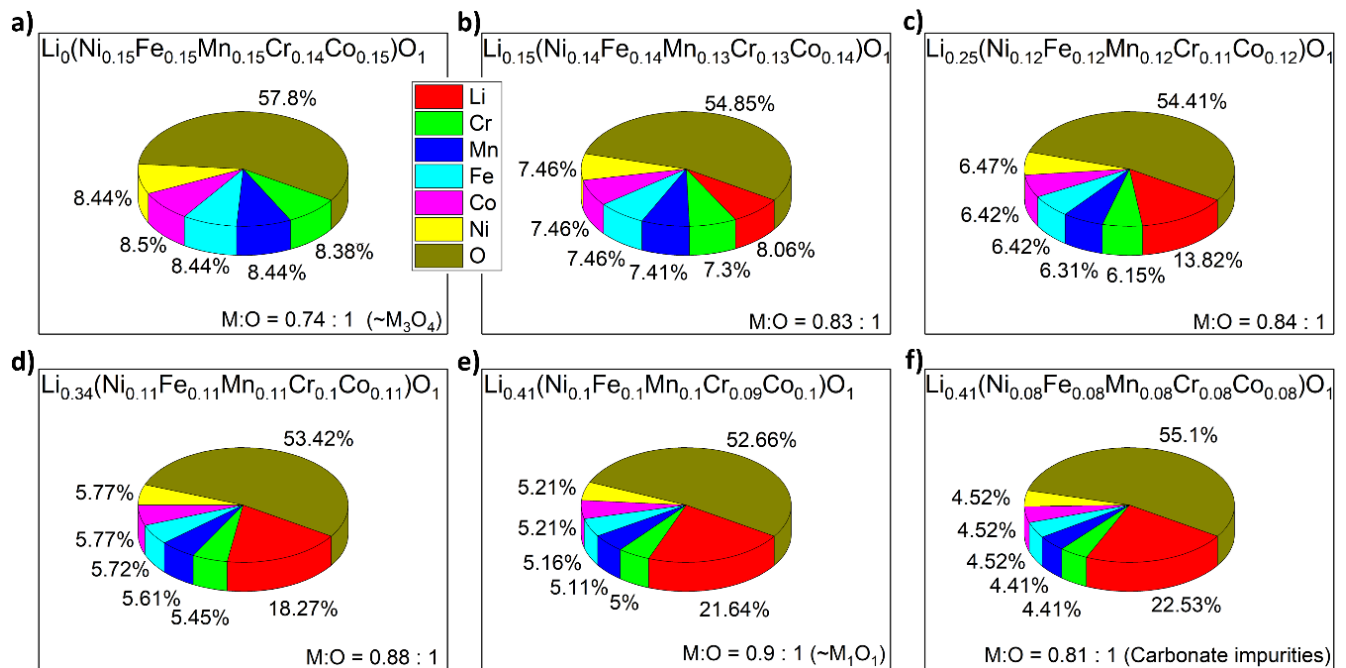


Figure 4.2: ICP-OES of HEO-1 with different Li contents. All numbers are given in units of at.%. Increasing M:O ratio indicates transition from spinel to rock-salt phase. Excess oxygen is due to Li_2CO_3 formation. ICP-OES data for HEO-2 follow the same trend, but show the highest M:O ratios for lower Li contents (Table 4.1).

Based on the ICP-OES results, the stoichiometries of the compounds were calculated, details can be found in Table 4.1. The excess amount of oxygen at high Li contents ($x > 0.8$) can be explained by the formation of Li_2CO_3 . The formation of carbonate surface species is well-known for LIB cathode materials (e.g., NCM) [167, 168]. Note that Li_2O and other Li-containing impurities undergo reactions with H_2O and CO_2 in the ambient atmosphere. The presence of carbonates was also confirmed by XPS shown in below.

Table 4.1: Stoichiometry of HEO-1 and HEO-2 with different Li contents from ICP-OES analysis.

	Normalized to O (exact)	Metal to oxygen ratio (exact)	Normalized to metals other than Li (rounded)
HEO-1	$\text{Li}_0(\text{Ni}_{0.15}\text{Fe}_{0.15}\text{Mn}_{0.15}\text{Cr}_{0.14}\text{Co}_{0.15})\text{O}_1$	0.74:1 ($\sim\text{M}_3\text{O}_4$, spinel)	$\text{Li}_0\text{M}_1\text{O}_{1.4}$
	$\text{Li}_{0.15}(\text{Ni}_{0.14}\text{Fe}_{0.14}\text{Mn}_{0.13}\text{Cr}_{0.13}\text{Co}_{0.14})\text{O}_1$	0.83:1	$\text{Li}_{0.2}\text{M}_1\text{O}_{1.5}$
	$\text{Li}_{0.25}(\text{Ni}_{0.12}\text{Fe}_{0.12}\text{Mn}_{0.12}\text{Cr}_{0.11}\text{Co}_{0.12})\text{O}_1$	0.84:1	$\text{Li}_{0.4}\text{M}_1\text{O}_{1.7}$
	$\text{Li}_{0.34}(\text{Ni}_{0.11}\text{Fe}_{0.11}\text{Mn}_{0.11}\text{Cr}_{0.10}\text{Co}_{0.11})\text{O}_1$	0.88:1	$\text{Li}_{0.6}\text{M}_1\text{O}_{1.9}$
	$\text{Li}_{0.41}(\text{Ni}_{0.10}\text{Fe}_{0.10}\text{Mn}_{0.10}\text{Cr}_{0.09}\text{Co}_{0.10})\text{O}_1$	0.90:1 ($\sim\text{M}_1\text{O}_1$, rock-salt)	$\text{Li}_{0.8}\text{M}_1\text{O}_2$
	$\text{Li}_{0.41}(\text{Ni}_{0.08}\text{Fe}_{0.08}\text{Mn}_{0.08}\text{Cr}_{0.08}\text{Co}_{0.08})\text{O}_1$	0.81:1 (carbonate impurities)	$\text{Li}_1\text{M}_1\text{O}_{2.5}$
HEO-2	$\text{Li}_0(\text{Ni}_{0.14}\text{Fe}_{0.14}\text{Mn}_{0.14}\text{Cr}_{0.14}\text{Mg}_{0.14})\text{O}_1$	0.70:1 ($\sim\text{M}_3\text{O}_4$, spinel)	$\text{Li}_0\text{M}_1\text{O}_{1.4}$
	$\text{Li}_{0.15}(\text{Ni}_{0.14}\text{Fe}_{0.13}\text{Mn}_{0.13}\text{Cr}_{0.13}\text{Mg}_{0.14})\text{O}_1$	0.82:1	$\text{Li}_{0.2}\text{M}_1\text{O}_{1.5}$
	$\text{Li}_{0.25}(\text{Ni}_{0.12}\text{Fe}_{0.12}\text{Mn}_{0.12}\text{Cr}_{0.12}\text{Mg}_{0.12})\text{O}_1$	0.85:1	$\text{Li}_{0.4}\text{M}_1\text{O}_{1.7}$
	$\text{Li}_{0.35}(\text{Ni}_{0.11}\text{Fe}_{0.11}\text{Mn}_{0.11}\text{Cr}_{0.11}\text{Mg}_{0.11})\text{O}_1$	0.90:1 ($\sim\text{M}_1\text{O}_1$, rock-salt)	$\text{Li}_{0.6}\text{M}_1\text{O}_{1.8}$
	$\text{Li}_{0.39}(\text{Ni}_{0.10}\text{Fe}_{0.10}\text{Mn}_{0.10}\text{Cr}_{0.10}\text{Mg}_{0.10})\text{O}_1$	0.89:1	$\text{Li}_{0.8}\text{M}_1\text{O}_2$
	$\text{Li}_{0.44}(\text{Ni}_{0.08}\text{Fe}_{0.08}\text{Mn}_{0.08}\text{Cr}_{0.08}\text{Mg}_{0.08})\text{O}_1$	0.84:1 (carbonate impurities)	$\text{Li}_{1.1}\text{M}_1\text{O}_{2.5}$

4.2.3. X-ray Photoelectron Spectroscopy (XPS)

XPS was conducted to gain insights into the chemical states of the elements. Co in the non-lithiated HEO-1 was present as 87% Co^{2+} of total, from the characteristic Co^{2+} satellite peak at 786.4 eV. In contrast, for $\text{Li}_x(\text{NiFeMnCrCo})\text{O}$ ($x = 1$), Co was in the oxidation state +3 (Figure 4.3a) [169–173]. As expected, Mg ions with a measured binding energy of Mg 1s 1303.4 and 1303.7 eV in non-lithiated and lithiated HEO-2 respectively, can be attributed to the Mg^{2+} state (Figure 4.3b) [174, 175]. Identification of the Ni oxidation state solely on the basis of the Ni 2p peak is challenging [169–173, 176–179]. However, overlap of all Ni 2p spectra (Figure 4.4d) of HEO-1 and HEO-2 revealed only minor differences among the lithiated and non-lithiated materials. Moreover, the spectra could be fitted with a multiplet set of Ni^{2+} ions according to the deconvolution approach presented in ref [170] (Figure 4.3c). Therefore, the oxidation state of Ni ions in HEO-1 and HEO-2 is attributed to Ni^{2+} in both lithiated and non-lithiated states. The Cr ions in non-lithiated HEO-1 and HEO-2 are present in Cr^{3+} state, however, the ions were partially oxidized to Cr^{6+} for the lithiated material. While Cr^{3+} showed multiplet splitting (Figure

4.3d), Cr^{6+} has an empty valence band and thus a sharp single peak at 579.9 eV emerged (Figure 4.3d) [173, 180, 181]. According to the fitting results, in the lithiated HEO-1 and HEO-2 ($x = 1$), 50 and 80% of total Cr, respectively, were present as Cr^{6+} . The increased Cr^{6+} fraction in HEO-2 is a direct result of the ceased $\text{Co}^{2+/3+}$ redox couple, since the single charge of Li has to be compensated elsewhere.

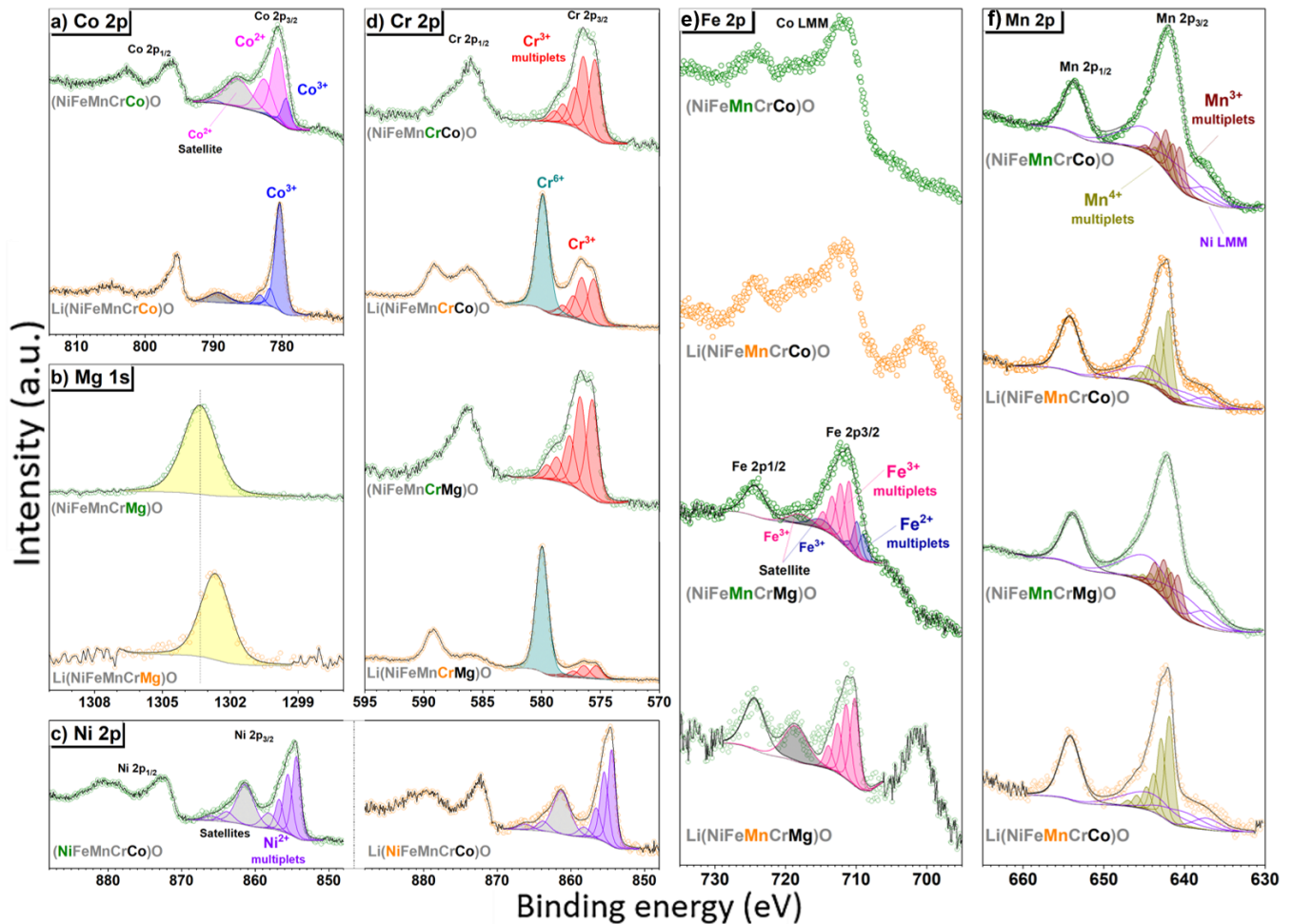


Figure 4.3: XPS spectra of (a) Co for HEO-1, (b) Mg for HEO-2, (c) Ni for HEO-1, (d) Cr, (e) Fe and (f) Mn for HEO-1 and HEO-2 in the non-lithiated ($x = 0$) and lithiated states ($x = 1$).

The Fe 2p spectra of HEO-1 in Figure 4.3e were not deconvoluted because of overlapping with the Co LMM Auger on the higher binding energy side of Fe 2p_{3/2}. For HEO-2, peak fitting indicated the presence of Fe²⁺ (30%) and Fe³⁺ (70%) in the non-lithiated material and only Fe³⁺ in the lithiated material [173, 182].

Moreover, inspection of the C 1s spectra of HEO-1 and HEO-2 (Figure 4.4b) revealed a new, intense peak emerging at 290 eV after lithiation. This peak coincides with an increase in intensity in the O 1s spectrum at 531.5 eV (Figure 4.4a) and thus can be attributed to the formation of Li₂CO₃. This result agrees with previous related findings [35]. Additionally, Figure 4.4e and Figure 4.4f reveal that the Zn ions in HEO-3 (with Zn 2p_{3/2} and Zn LMM binding energies of 1021.6 and 497.6 eV, respectively) are in the oxidation state +2.

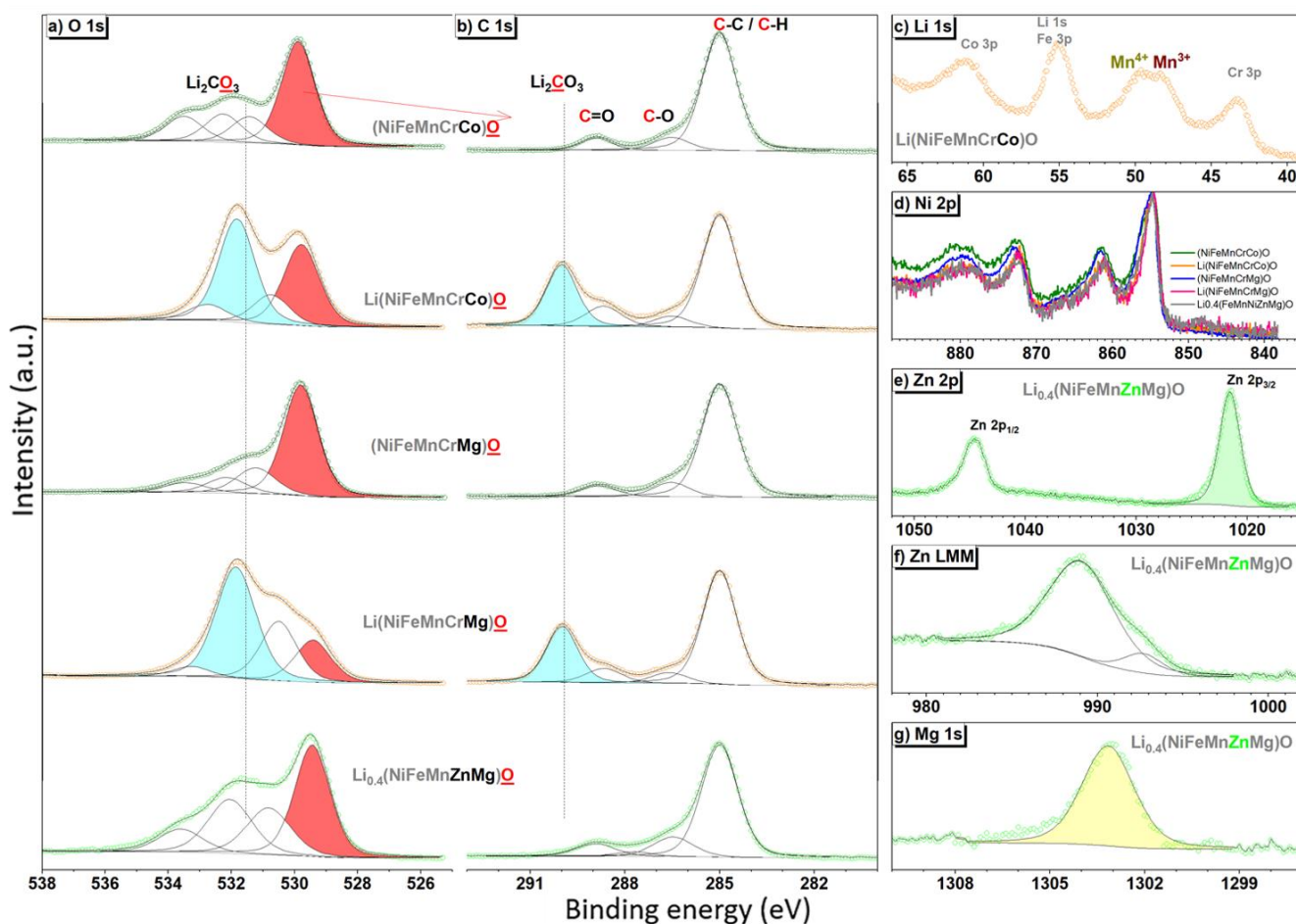


Figure 4.4: XPS spectra of the (a) O 1s, (b) C 1s, (c) Li 1s, (d) Ni 2p, (e) Zn 2p, (f) Zn LMM, and (g) Mg 1s core level regions for HEO-1 (with $x = 0$ and 1), HEO-2 (with $x = 0$ and 1), and HEO-3 (with $x = 0.4$).

Because of intense multiplet splitting of Mn in the 2p data, usually the Mn 3s and 3p peaks are used to determine the oxidation state [170, 171, 173, 183]. However, such analysis was hampered by the overlap of photoelectron peaks of Mg, Zn, Li, Fe, and Cr. Nevertheless, from the Mn 3p spectrum of the lithiated HEO-1 in Figure 4.4c, the occurrence of peaks centered at 47.8 and 49.6 eV is apparent. This in turn suggests the presence of at least two different Mn species [183]. Upon lithiation, the higher binding energy component emerged clearly, indicating Mn^{4+} contribution, whereas the lower binding energy peak in the Mn 3p spectrum suggests mixed $\text{Mn}^{2+/3+}$ state (the binding energy is higher than that normally found for Mn^{2+} and lower than for Mn^{3+}) [183]. The commonly observed multiplet splitting in Mn 2p [170, 171, 173] and the overlap with the Ni LMM Auger line led to a large number of peaks in the fitting procedure. Following the fitting approach developed for battery cathode materials as presented in refs [170, 171], the Mn 2p spectra for the non-lithiated HEO-1 and HEO-2 (Figure 4.3f) could be fitted successfully assuming Mn^{3+} and Mn^{4+} multiplets. The fraction of Mn^{4+} in both of these materials was calculated to be $\sim 30\%$. However, it increased to 90% for the lithiated HEO-1 and 100% for the lithiated HEO-2 (i.e., the Mn 2p peak could be fitted assuming only Mn^{4+} multiplets).

Table 4.2: Metal oxidation states and the corresponding fractions for HEO-1 and HEO-2 in the non-lithiated ($x = 0$) and lithiated states ($x = 1$) from XPS analysis.

	Ni	Fe	Mn	Cr	Co	Mg
(NiFeMnCrCo)O	Ni ²⁺	Not quantified	~70% Mn ³⁺ ~30% Mn ⁴⁺	~100% Cr ³⁺	~87% Co ²⁺ ~13% Co ³⁺	-
Li(NiFeMnCrCo)O	Ni ²⁺	Not quantified	~10% Mn ³⁺ ~90% Mn ⁴⁺	50% Cr ³⁺ 50% Cr ⁶⁺	100% Co ³⁺	-
(NiFeMnCrMg)O	Ni ²⁺	~30% Fe ²⁺ ~70% Fe ³⁺	~70% Mn ³⁺ ~30% Mn ⁴⁺	~100% Cr ³⁺	-	Mg ²⁺
Li(NiFeMnCrMg)O	Ni ²⁺	100% Fe ³⁺	100% Mn ⁴⁺	20% Cr ³⁺ 80% Cr ⁶⁺	-	Mg ²⁺

In summary, it is concluded that the lithiation of HEO-1 and HEO-2 leads to total or partial oxidation of Co, Mn, Fe, and Cr, whereas Ni, Zn (in HEO-3), and Mg remain in their initial oxidation state (details in Table 4.2).

4.2.4. Transmission Electron Microscopy (TEM)

TEM measurements were conducted to examine the materials' morphology and to probe the distribution of elements in the crystal structure. Note that non-uniform distribution would decrease the configurational entropy, thereby hinting at phase separation. Figure 4.5 shows high-resolution TEM micrographs of the non-lithiated and lithiated HEO-1. In both cases, the particles, which consist of small crystallites, are of spherical shape, with sizes ranging from the nanometer to the micrometer length scale. Moreover, EDX in STEM mode of the same samples confirmed the uniform elemental distributions (Figure 4.6).

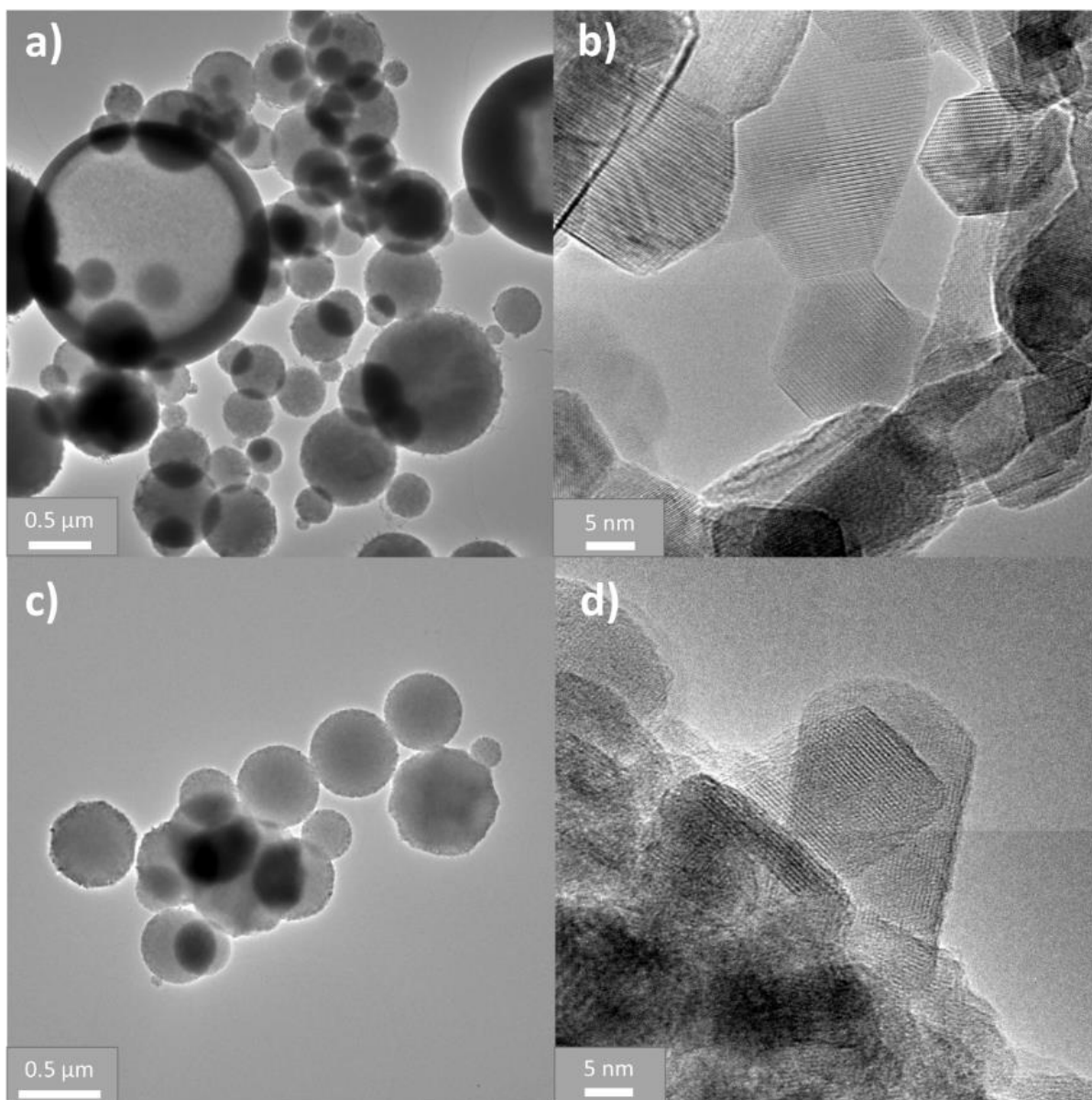


Figure 4.5: TEM micrographs at different magnifications of HEO-1 (a) and (b) in the non-lithiated ($x = 0$) and (c) and (d) lithiated states ($x = 1$).

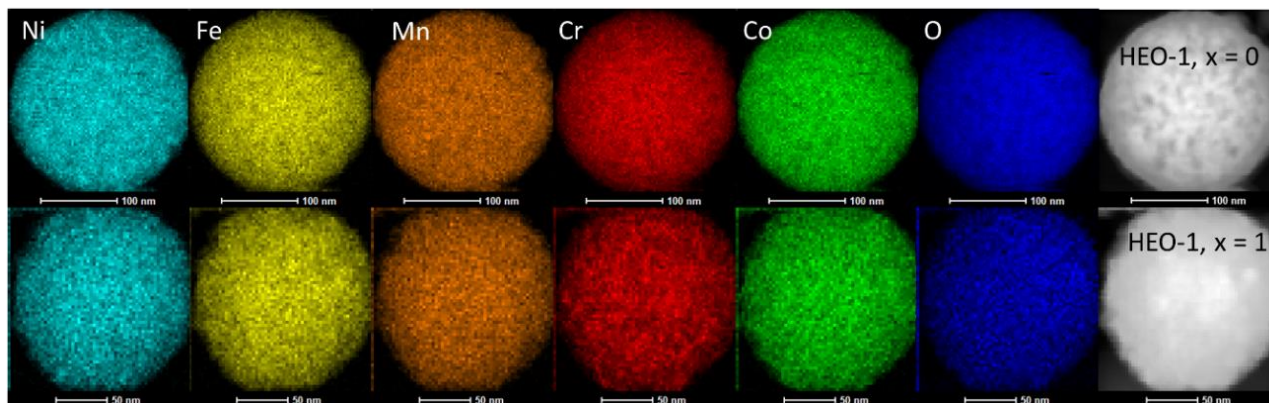


Figure 4.6: STEM-EDX mapping of HEO-1 in the non-lithiated ($x = 0$) and lithiated states ($x = 1$).

4.2.5. Electrochemical Properties

Cyclic voltammetry was performed to learn about the redox behaviors of HEO-1 (Figure 4.7) as a function of Li content in the voltage ranges of 2.0-4.5 V and 0.1-3.0 V vs. Li⁺/Li. To this end, tape-cast electrodes were assembled in coin cells and cycled against Li metal as counter electrode. The sweep rate was set to 0.1 mV/s. Figure 4.7a shows the CV curves of the initial cycle for the low-voltage region. The reduction potential was found to gradually increase with increasing Li concentration until the rock-salt phase was formed. Related to the structure conversion, from spinel to rock-salt with increasing Li content, this behavior differs from that of simple oxides. For example, rock-salt CoO and spinel Co₃O₄ have been shown to exhibit reduction potentials of 0.58 V and 0.85 V versus Li⁺/Li, respectively [184]. Overall, this result seems to be due to the increased oxidation state of metals in the rock-salt structure (high Li content), as shown in the section on XPS above.

As can be seen from Figure 4.7a, the reduction potentials are 0.25 V for $x = 0$, 0.37 V for $x = 0.2$, 0.44 V for $x = 0.4$, 0.52 V for $x = 0.6$, 0.61 V for $x = 0.8$, and 0.59 V for $x = 1$. Except for the increase in x from 0.8 to 1, the reduction potential increased in a stepwise manner by 80-120 mV. Figure 4.7b shows the CV curves of the initial cycle for the high-voltage region. As somewhat expected, the spinel-type HEO-1 materials showed minor redox activity above 3.5 V. However, for the highly lithiated rock-salt structure HEO-1 with $x \geq 0.8$, two pairs of oxidation/reduction peaks were observed. This result indicates that, after the transition to rock-salt phase, Li can be extracted from the lattice, leading to (partially) reversible redox behavior (CV curves in Figure 4.7c). However, whether or not this is directly connected to the structure or the Li concentration cannot be comprehensively concluded at this stage; further research is clearly required to answer this question. Nevertheless, the strong increase in specific current coincides with the structural changes detected by XRD.

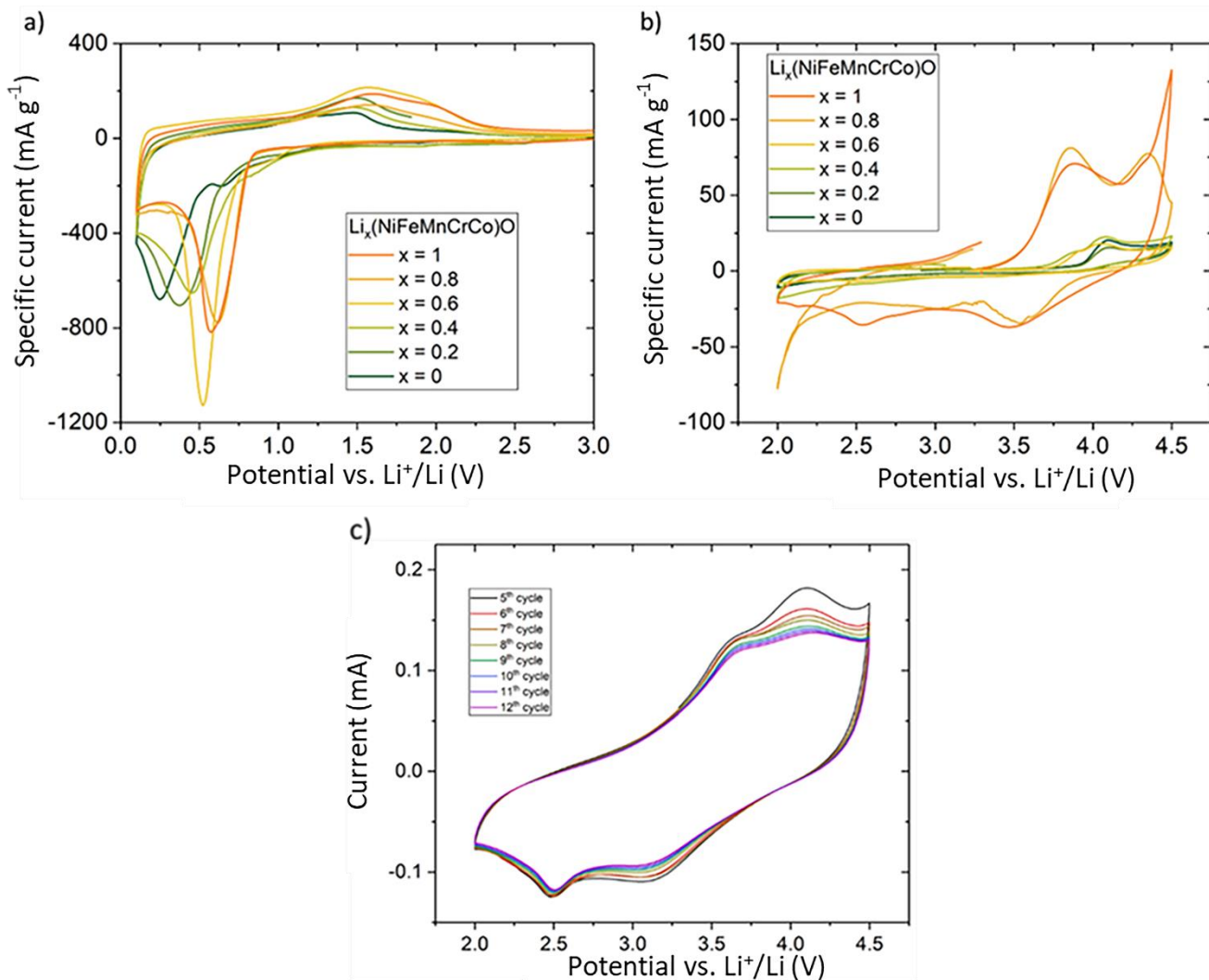


Figure 4.7: Cyclic voltammograms for HEO-1 with different Li contents in the voltage range of (a) 0.1-3.0 V and (b) 2.0-4.5 V versus Li⁺/Li. Note that only the initial cycle is shown for clarity. (c) The 5th to 12th cycles of HEO-1 (with x = 1) in the voltage range of 2.0-4.5 V versus Li⁺/Li.

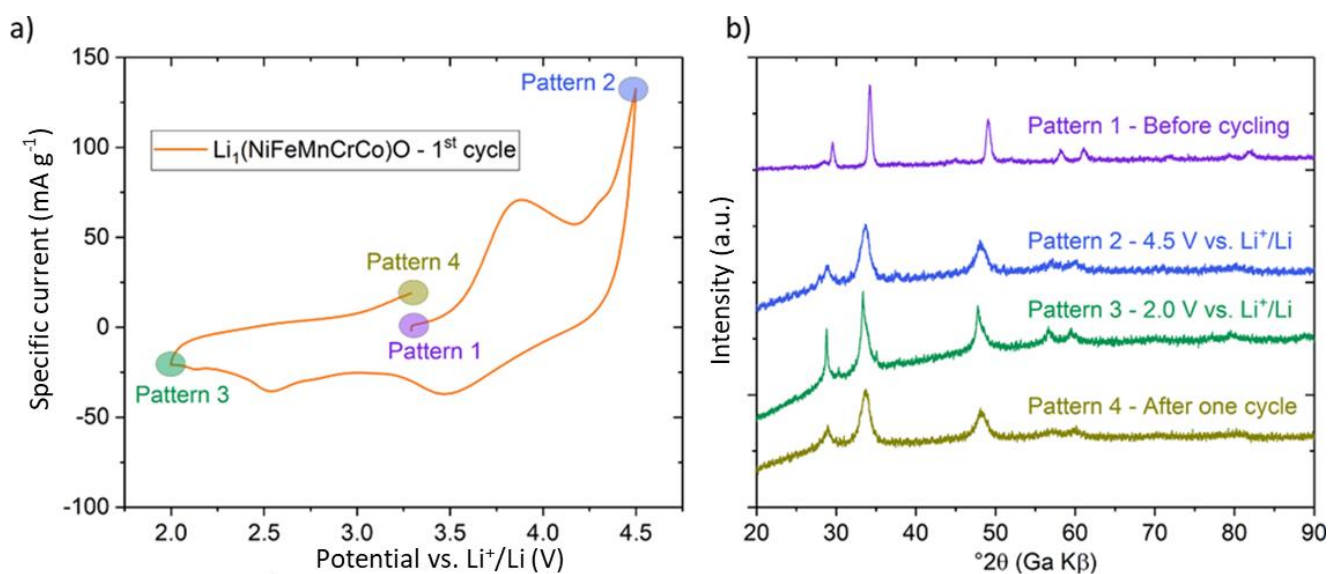


Figure 4.8: Structural changes during lithiation/delithiation of HEO-1 (with x = 1). a) Representative cyclic voltammogram and b) PXRD patterns obtained at different lithiation/delithiation states.

Lithiated HEO-1 ($x = 1$) was further studied to determine whether structural changes occur in the initial cycle. To this end, the electrodes were extracted from the cells after reaching 4.5 V, 2.0 V, and after the first cycle (denoted by colored circles in Figure 4.8a) and probed using PXRD. As can be seen from Figure 4.8b, all patterns show the characteristic of rock-salt reflections, thus indicating that the lattice structure is retained. However, some changes in reflection broadening are apparent and deserve more study.

4.3. Conclusions

The Cocktail effect as a driving force for the study and main reason for the different properties of HEMs, it is worth being investigated and explored. Therefore, studies of compositions adjustments and charge compensation were elaborated in this chapter, involving analysis of the structure and the representation of oxidation states, as well as the effects of different compositions through stepwise controlling Li content and replacing different single elements in precise.

In this chapter, three different HEOs were analyzed regarding the phase transformation from spinel to rock-salt with incorporation of monovalent Li ions during synthesis. Charge compensation was found to be accompanied by full or partial oxidation of some of the elements (note that, interestingly, the Ni^{2+} did not change oxidation state during chemical lithiation). When oxidation was not possible, the spinel-type HEO transformed into a rock-salt phase of lower average charge. Hence, this transition can be tailored by replacing the multivalent elements (e.g., $\text{Co}^{2+/3+} \rightarrow \text{Mg}^{2+}$ and $\text{Cr}^{3+/6+} \rightarrow \text{Zn}^{2+}$) present in the lattice. Moreover, the formation of surface carbonate and chromate species in the rock-salt structure HEOs was observed via XPS. Their formation seems to be associated with excess Li when exceeding a certain threshold concentration. Electrochemical testing using cyclic voltammetry revealed increasing redox activity with increasing Li content. In particular, the lithiated rock-salt HEOs deserve further investigation into their performance as negative and positive electrode materials in rechargeable LIBs.

Precise tuning of material compositions in this work to control and edit the structure of materials and the oxidation states of elements may expand different physical properties and potential applications, this is also a good illustration of the Cocktail effect of HEMs. In this way, various combinations and substitutions of different elements further extend the phase space of these materials to a tremendous number of possible compositions. What's more, the combined effects and tailorable properties of the individual elements and the interactions between all of them are therefore offering new ideas to study and develop other materials with the same design principles as well.

Chapter 5

5. Lithium Containing Layered High Entropy Oxide Structures

The majority of the results presented in this chapter have been published in Scientific Reports [185]. The experimental work was mainly carried out by Junbo Wang. The manuscript was organized by Junbo Wang under the guidance of Dr. Ben Breitung and all other co-authors. Co-authors contributed by supporting with certain characterization methods, providing valuable discussions, and reviewing the article draft.

5.1. Introduction

Recently, the utilization of the high entropy concept for oxide materials has been enjoying rising popularity [96, 99, 108, 109, 115, 186–188]. The materials can be tailored with regard to their elemental composition, which leads to property changes due to the interactions of the different elements. The configurational entropy is solely based on the number of different elements that incorporated in a single-phase structure, (e.g., different species on the cationic sublattice) and can be calculated using a Boltzmann-entropy-derived equation (Equation 2.11).

The layered materials used as cathode materials for LIBs are facing the problems that the capacity is limited due to oxygen loss and irreversible structural transformation in the partially delithiated layered structure cathodes when the extracted amount of Li^+ is above 50% [189–191]. This topic was started since the consideration that the crystal structure might be stabilized with the entropy stabilization, achieving more Li^+ delithiation and structural conversion suppressing.

In this work, a new class of layered high entropy materials is reported, namely L-HEOs, comprising five different equimolar and homogeneously distributed cations. This kind of layered materials crystallizing in the layered $R\text{-}3m$ space group (Delafossite $\alpha\text{-NaFeO}_2$ -type structure) are known especially for their capability of reversible intercalation of Li^+ ions. This characteristic made them become the most prominent cathode materials for current Li-ion battery technology, such as LCO and NCM [21, 47, 192, 193]. However, other areas are also in the focus

of both academy and industry. For example, Delafossite-type materials can be used as semiconductors in solar cells, as catalysts for the photoelectrochemical reduction of CO₂ as well as for thermoelectric and lighting applications [194–199].

The L-HEOs were prepared by the NSP method and subsequent high-temperature annealing. Specifically, five different compounds were successfully produced, namely, Li(NiCoMnAlZn)₁O₂, Li(NiCoMnAlFe)₁O₂ and Li_{0.8}Na_{0.2}(NiCoMnAlFe)₁O₂, with the metal ions present in equimolar proportions. The materials were characterized in detail, especially regarding the formation of solid-solution phases. Possible entropic effects and the application of Hume Rothery's second rules for solid solutions are discussed near the end of this chapter for better understanding of the high entropy concept [200].

5.2. Results and Discussion

The L-HEOs were synthesized using a stepwise approach. In order to compare the structure and the structural evolution when incorporating more elements, two materials were prepared first using the same synthesis procedure. Then, additional elements were added in a stepwise manner and the obtained materials were characterized. All materials contain the metals in equimolar ratios.

5.2.1. Powder X-ray Diffraction (PXRD)

The study started from a typical NCM cathode material used for Li-ion battery applications, namely Li(NiCoMn)₁O₂ (see Figure 5.1a). Then, Al was added, forming Li(NiCoMnAl)₁O₂, before entering into the high entropy region with 5 or more different elements on the same cationic sublattice.

All samples showed a well-developed layered structure of α -NaFeO₂ type (space group $R\bar{3}m$, $Z = 3$, Figure 5.1b), which can be seen from the clear splitting of the (018) and (110) reflections [201] in the XRD patterns in Figure 5.1a. Alternating layering of metal and lithium layers occurred in all cases, with the metals and Li occupying the octahedral sites in the cubic close-packed oxygen lattice, in which the Li⁺ and metals occupy the Wyckoff $3b$ and $3a$ sites respectively [202]. A possible intermixing and unit cell parameters were considered by using Rietveld refinement analysis, the statistical results are shown in Figure 5.1c and Table 5.1.

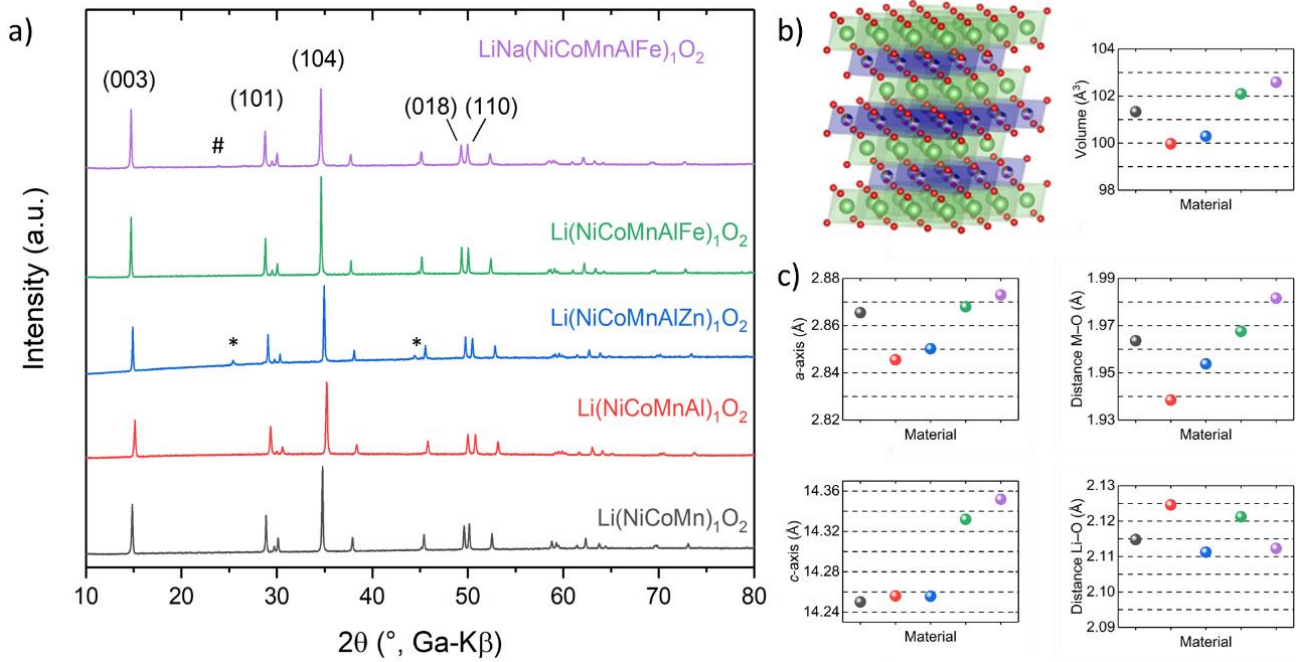


Figure 5.1: (a) XRD patterns for the different compounds, with secondary phases denoted by asterisks and number signs. (b) Crystal structure of $\alpha\text{-NaFeO}_2$. Green spheres represent lithium, red spheres oxygen and multi-colored spheres the positions of the statistically distributed metal cations. (c) Lattice parameters from Rietveld refinement analysis (color scheme as in panel a).

Upon addition of Al to $\text{Li}(\text{NiCoMn})_1\text{O}_2$, the reflections shifted to larger 2θ values, thus indicating a smaller unit cell. This result coincides with the smaller ionic radius of Al^{3+} (0.54 \AA) than low-spin Ni^{2+} (0.69 \AA), Ni^{3+} (0.56 \AA) and Co^{3+} (0.55 \AA) [203]. This is also evident from the decreasing a -axis parameter (Figures 5.1c), from 2.865(1) \AA for $\text{Li}(\text{NiCoMn})_1\text{O}_2$ to 2.845(1) \AA for $\text{Li}(\text{NiCoMnAl})_1\text{O}_2$. Note that the a -axis is strongly affected by the ionic radius of the respective metals [204], Al^{3+} adding results in a strong decrease in unit-cell volume (V_{cell}) due to the relationship between V_{cell} and a ($V_{\text{cell}} = a^2 \cdot c \cdot (\sin 60^\circ)$), from 101.333(9) \AA^3 for $\text{Li}(\text{NiCoMn})_1\text{O}_2$ to 99.97(9) \AA^3 for $\text{Li}(\text{NiCoMnAl})_1\text{O}_2$.

By adding Zn, an increase in a -axis parameter and unit-cell volume as well as the formation of a secondary phase was observed and which is denoted by an asterisk in Figure 5.1a. The latter phase can most probably be assigned to a spinel-type structure, similar to ZnAl_2O_4 . It is noted that the spinel-type oxides are known to form high entropy structures when suitable ions are incorporated [104, 205]. Therefore, a large number of possible compositions is conceivable (i.e., $\text{Zn}(\text{M}_1\text{M}_2\text{M}_3\text{M}_4\text{M}_5)_2\text{O}_4$, with $\text{M} = \text{Zn, Fe, Co, Ni}$ and/or Mn). In addition, Zn could be replaced by one or more (different) metal ions. Rietveld refinement assuming the presence of spinel revealed a ZnAl_2O_4 content of 9-10%. This value has to be taken with care, though, since we doubt that the reflection stems from “pure” ZnAl_2O_4 . To further support our hypothesis, high-resolution TEM (HR-TEM) and SAED measurements were performed, which also indicated the presence of a distorted ZnAl_2O_4 -type spinel structure (Figure 5.3e and Figure 5.3f).

Moreover, the addition of Zn led to an increase in the transition metal to oxygen distance compared with $\text{Li}(\text{NiCoMnAl})_1\text{O}_2$, thereby corroborating its incorporation into the lattice. However, the position of the 104 reflection changed only slightly compared to that of $\text{Li}(\text{NiCoMnAl})_1\text{O}_2$. Hence, it seems that Zn was only partially

incorporated. This result emphasizes the importance of choosing suitable elements to maintain a single-phase structure.

Substituting Fe for Zn in $\text{Li}(\text{NiCoMnAlZn})_1\text{O}_2$ led to an increase in lattice parameters, which again indicates successful incorporation into the crystal structure. In addition, the material was single phase, with the reflections shifted toward smaller angles. It is worth mentioning that the a -axis lattice parameter values for $\text{Li}(\text{NiCoMnAlFe})_1\text{O}_2$ are similar to those of $\text{Li}(\text{NiCoMn})_1\text{O}_2$, nevertheless, based on the ionic radii, the unit cell was expected to increase. The partial replacement of Li^+ with Na^+ ($\text{LiNa}(\text{NiCoMnAlFe})_1\text{O}_2$), which has a considerably larger ionic radius (0.76 \AA vs 1.02 \AA), had a direct effect on the lattice parameters (increase in a , c and V , shown in Figure 5.1c).

Table 5.1: Statistical result of Li/M mixing from Rietveld refinement analysis, the values are given in fractions of 1.

Compositions	Lithium site			Metal site	
	Li	Na	Metal	Li	Metal
$\text{Li}(\text{NiCoMn})\text{O}_2$	0.96	0	0.04	0.15	0.85
$\text{Li}(\text{NiCoMnAl})\text{O}_2$	0.968	0	0.032	0.27	0.73
$\text{Li}(\text{NiCoMnAlZn})\text{O}_2$	0.965	0	0.035	0.26	0.74
$\text{Li}(\text{NiCoMnAlFe})\text{O}_2$	0.966	0	0.034	0.25	0.75
$\text{Li}_{0.8}\text{Na}_{0.2}(\text{NiCoMnAlFe})\text{O}_2$	0.8	0.2	0	0.11	0.89

For all L-HEOs, some Li/M cation mixing was apparent (Table 5.1). In particular, the Al-containing materials showed a relatively higher degree of mixing, with the exception of $\text{LiNa}(\text{NiCoMnAlFe})_1\text{O}_2$ most likely due to the presence of Na^+ .

5.2.2. Microstructure

SEM and TEM measurements were performed to gain more insights into the structure and the elemental distribution. Figure 5.2 shows similar SEM micrographs, these particles were agglomerated into larger aggregates, revealing particle sizes around $1 \mu\text{m}$ or below. It can be observed that the $\text{Li}(\text{NiCoMn})_1\text{O}_2$ consist of sphere-like particles with a homogeneous distribution. However, the morphology of other more-elements samples are more complex.

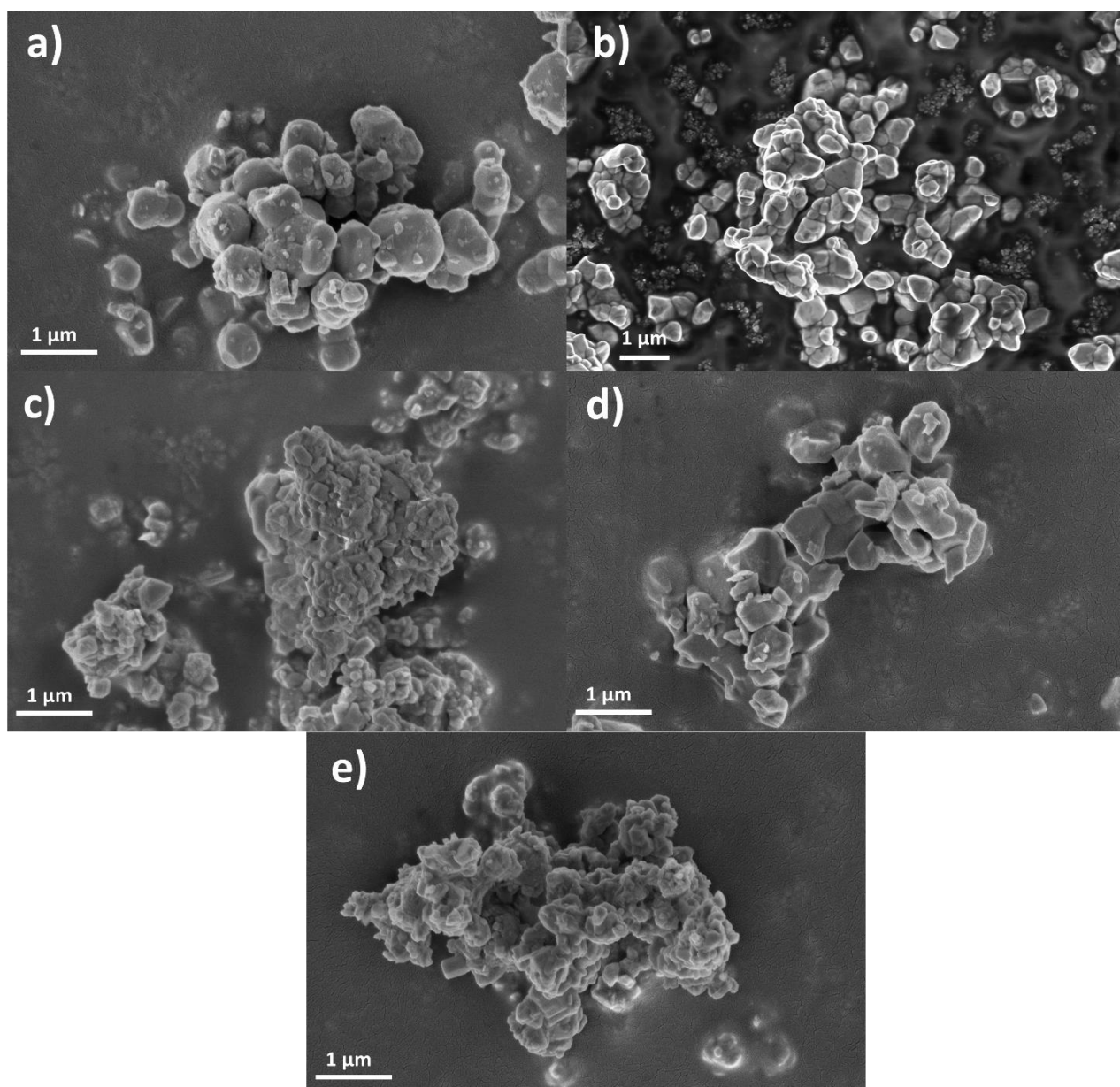


Figure 5.2: SEM micrographs of (a) $\text{Li}(\text{NiCoMn})_1\text{O}_2$, (b) $\text{Li}(\text{NiCoMnAl})_1\text{O}_2$, (c) $\text{Li}(\text{NiCoMnAlZn})_1\text{O}_2$, (d) $\text{Li}(\text{NiCoMnAlFe})_1\text{O}_2$ and (e) $\text{LiNa}(\text{NiCoMnAlFe})_1\text{O}_2$.

Figure 5.3a-c shows HR-TEM micrographs and SAED patterns for the different L-HEOs. The particles appear to be highly crystalline, irrespective of the composition and, for $\text{Li}(\text{NiCoMnAlZn})_1\text{O}_2$, where a secondary phase was observed by XRD, a single-phase particle was probed. The Debye-Scherrer rings match the XRD data shown in Figure 5.1a. The (003) lattice planes were also clearly detected by HR-TEM. Overall, the electron microscopy results confirm the layered structure of L-HEOs as well as the incorporation of elements into the Li_xMO_2 lattice. Figure 5.3d presents results from EDX analysis of $\text{LiNa}(\text{NiCoMnAlFe})_1\text{O}_2$ due to the most elements involving. The mapping indicates uniform distribution of all elements. No agglomeration or segregation of single elements or secondary phases were observed. This means that the largest possible configurational entropy can be expected.

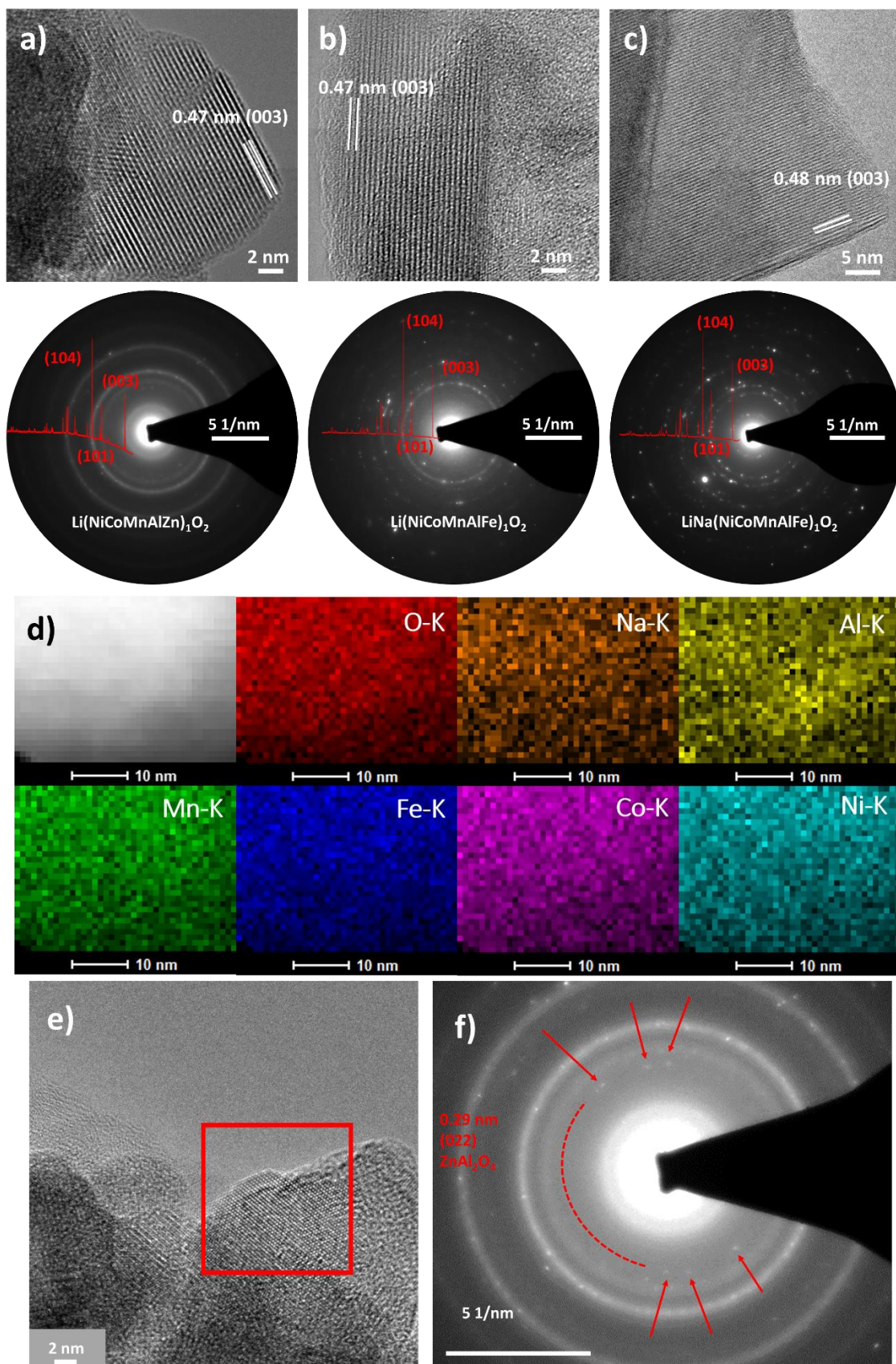


Figure 5.3: TEM of (a) $\text{Li}(\text{NiCoMnAlZn})_1\text{O}_2$, (b) $\text{Li}(\text{NiCoMnAlFe})_1\text{O}_2$ and (c) $\text{LiNa}(\text{NiCoMnAlFe})_1\text{O}_2$. The HR-TEM micrographs emphasize the high degree of crystallinity and the SAED patterns corroborate the XRD results. d) High-resolution EDX mapping of $\text{LiNa}(\text{NiCoMnAlFe})_1\text{O}_2$. (e) HR-TEM and (f) SAED measurements of $\text{Li}(\text{NiCoMnAlZn})_1\text{O}_2$, indicating the presence of a distorted ZnAl_2O_4 -type spinel structure.

In order to probe the distribution of elements over a larger sample area and to exclude clustering of elements, SEM/EDX measurements were performed. Figure 5.4a shows elemental heat maps obtained on a μm -size agglomerate of $\text{LiNa}(\text{NiCoMnAlFe})_1\text{O}_2$ particles, this is consistent with the TEM results. The intensity of the $K\alpha$ signals is shown on the scale between 1 and 10 au. The maps demonstrate that the elements are uniformly distributed. Areas of lower intensity result from lower sample thicknesses. The relatively lower intensity of the Na map is due to its low elemental weight and the respective interactions during EDX analysis.

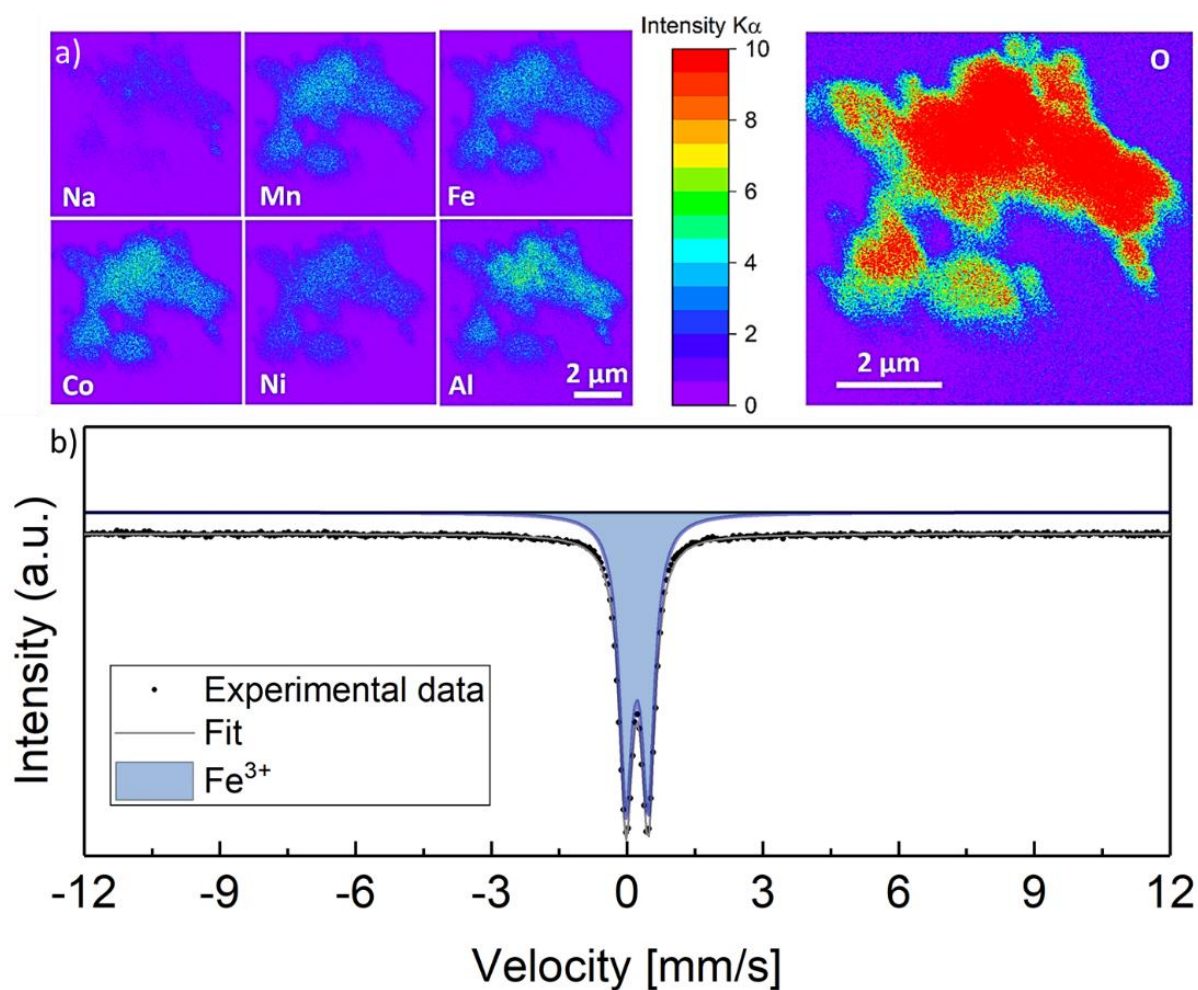


Figure 5.4: (a) Elemental heat maps of a μm -sized agglomerate and (b) Mössbauer spectroscopy of $\text{LiNa}(\text{NiCoMnAlFe})_1\text{O}_2$.

$\text{LiNa}(\text{NiCoMnAlFe})_1\text{O}_2$ was further used to study the chemical environment and oxidation state of Fe by Mössbauer spectroscopy. This particular material was chosen for the same reason that it contains the largest number of different elements, including Fe needed for Mössbauer spectroscopy. The spectrum shown in Figure 5.4b was fitted by a quadrupole doublet with an average quadrupole splitting of 0.492 mm s^{-1} . The isomer shift (0.34 mm s^{-1}) suggests the presence of Fe^{3+} . No other components were found, which would be indicative of different oxidation states and/or magnetic interactions and therefore inhomogeneities. Overall, the Mössbauer data demonstrate that the Fe^{3+} ions have a uniform chemical environment in the entire sample (approx. 150 mg) and, combined with the EDX results, they provide evidence of homogenous ion distribution and solid-solution state in the Li_xMO_2 lattice.

5.2.3. X-ray Photoelectron Spectroscopy (XPS)

XPS was used to determine the oxidation state(s) of metals on the surface of the L-HEOs. In Figure 5.5a, the main Ni $2p_{3/2}$ peaks of $\text{Li}(\text{NiCoFeMnAl})_1\text{O}_2$ and $\text{LiNa}(\text{NiCoFeMnAl})_1\text{O}_2$ are shown in magenta and their pronounced Ni $2p$ satellite in cyan. According to the presented deconvolution, based on previous publications on NCM materials, Ni ions were identified as Ni^{2+} [171, 206]. The Co ions in both $\text{Li}(\text{NiCoFeMnAl})_1\text{O}_2$ and $\text{LiNa}(\text{NiCoFeMnAl})_1\text{O}_2$ showed a minor contribution of Co^{2+} , according to the low intensity peak detected around 785.5 eV that is considered a characteristic satellite of Co^{2+} ions (shown in blue in Figure 5.5b) [171, 206]. The majority of Co ions were identified as Co^{3+} (shown in dark yellow). Quantitatively, the ratio of $\text{Co}^{2+}/\text{Co}_{\text{total}}$ was determined as 30% and 24% for $\text{Li}(\text{NiCoFeMnAl})_1\text{O}_2$ and $\text{LiNa}(\text{NiCoFeMnAl})_1\text{O}_2$, respectively.

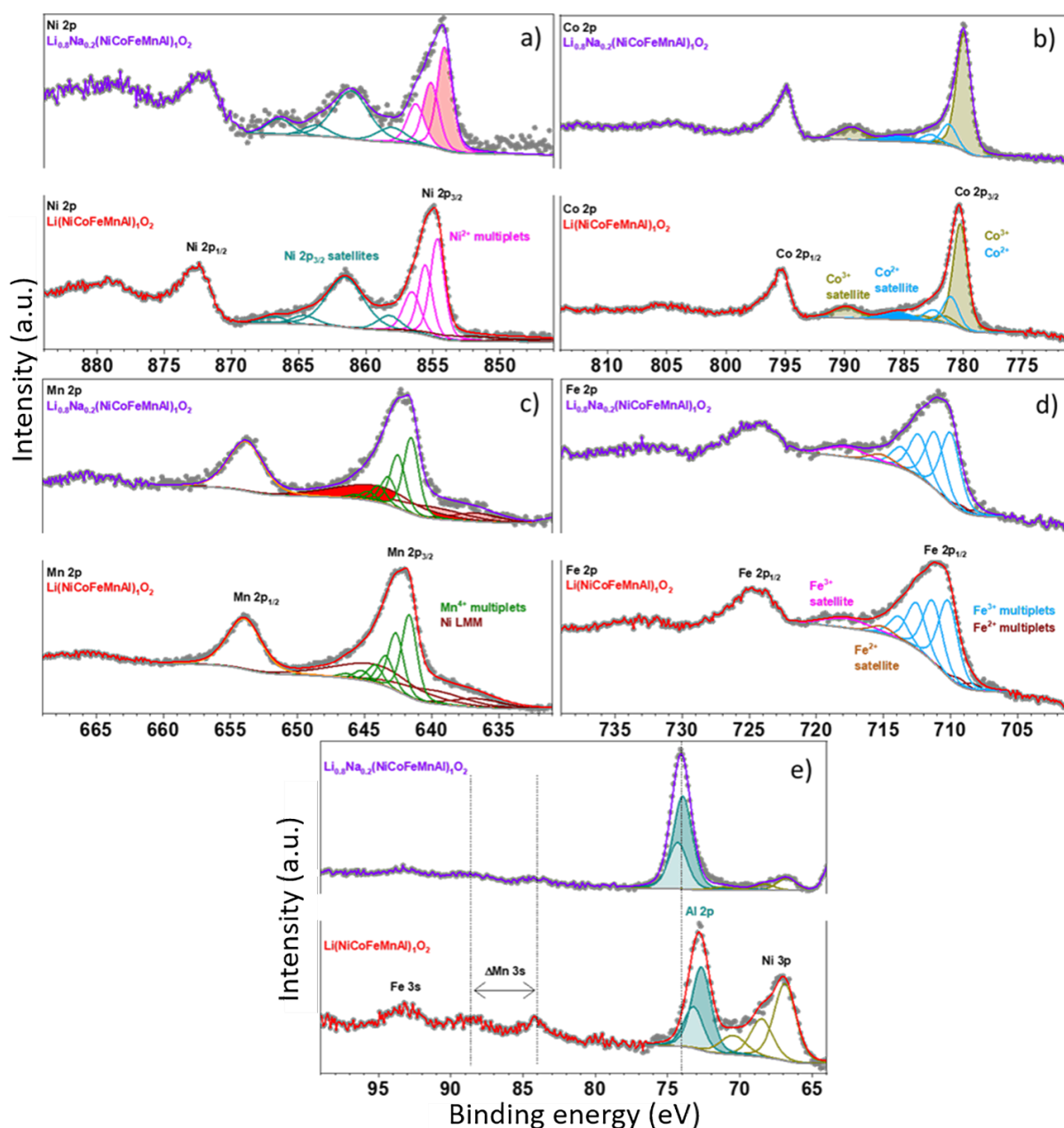


Figure 5.5: XPS of $\text{Li}(\text{NiCoMnAlFe})_1\text{O}_2$ and $\text{LiNa}(\text{NiCoMnAlFe})_1\text{O}_2$. The (a) Ni, (b) Co, (c) Mn, (d) Fe and (e) detailed spectra are shown.

As shown in Figure 5.5c, The Mn 2p_{3/2} spectra could be deconvoluted with a Mn⁴⁺ multiplet structure (green color) and including the Ni LMM Auger contribution (in dark brown color) [171, 206]. This deconvolution is the base of assignment of the 4+ state to Mn ions in L-HEOs. According to the presented multiplet splitting, the deconvolution of the Fe 2p_{3/2} spectra and the specified satellite structure, shown in blue in Figure 5.5d. The Fe ions were identified mainly as Fe³⁺ and the contribution of the Fe²⁺ state was negligible due to its less than 8% of total Fe ions which is explainable for surfaces under air and fitting difficulties because of overlapping peaks [173, 182]. The Al 2p and the Al 2s spectra of L-HEOs overlapped with the Ni 3p spectra and Ni 3s. Our attempt to properly deconvolute the Al 2p spectra resulted in the peak fitting shown in Figure 5.5e. The binding energy of Al 2p_{3/2} was 72.8 and 74 eV for Li(NiCoFeMnAl)₁O₂ and LiNa(NiCoFeMnAl)₁O₂, respectively. The differences in the binding energy of Al can be explained by the diverging cation mixing of the respective materials. Additionally, the very oxophilic nature of Al might result in the formation of oxide species on the surface, which are a bit different, depending on the composition of the layered structure [207].

5.2.4. Electrochemical Properties

Recently, Zhao et al. showed for Na-ion batteries that the high entropy concept is beneficial for achieving stable cell capacities [208]. Because NCM-type materials are common cathodes for Li-ion batteries, in the present work, the L-HEO structures were tested regarding the possibility to reversibly intercalate/extract Li ions (Figure 5.6).

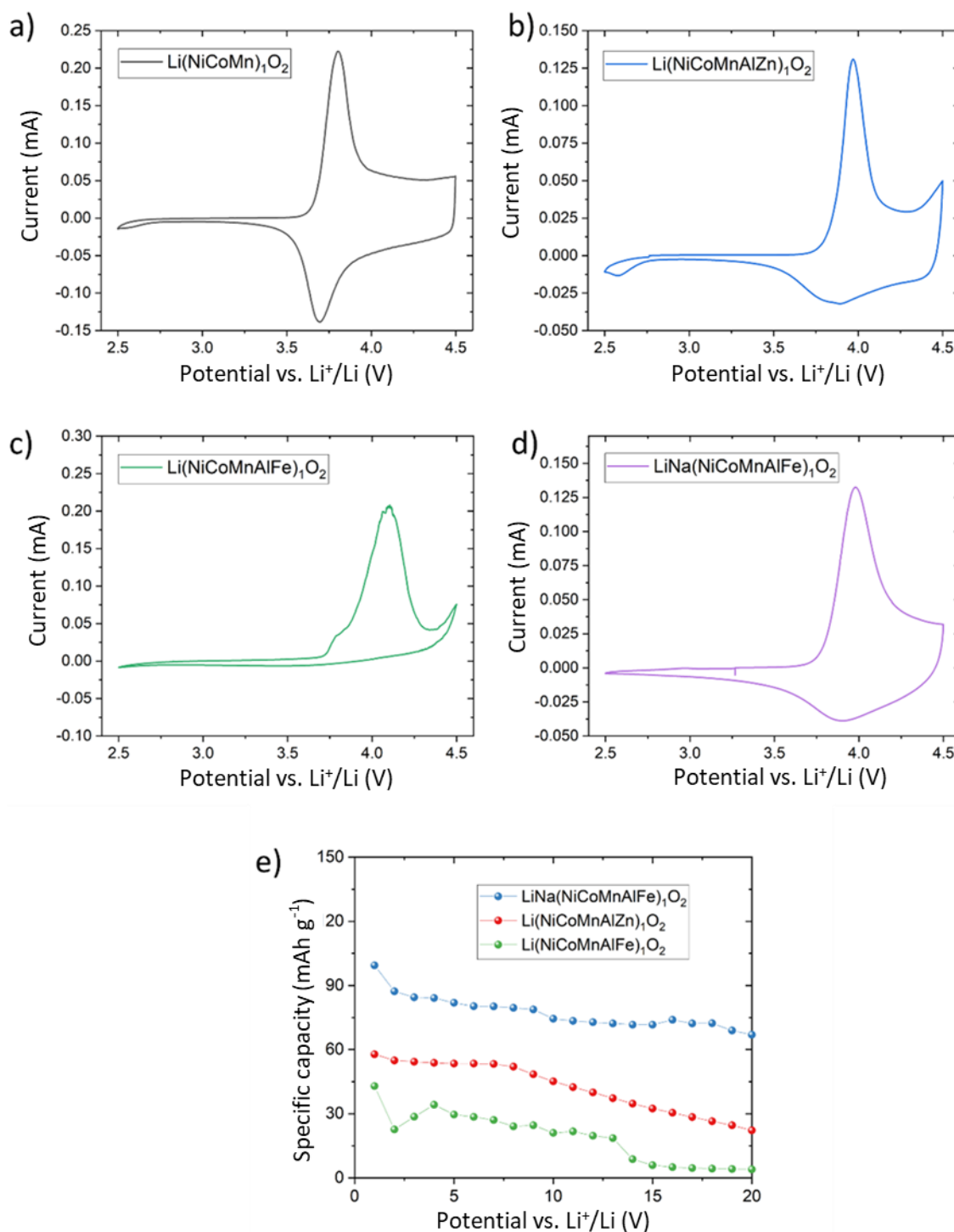


Figure 5.6: Cyclic voltammetry and charge/discharge profiles of as prepared (a) Li(NiCoMn)₁O₂, (b) Li(NiCoMnAlZn)₁O₂, (c) Li(NiCoMnAlFe)₁O₂ and (d) LiNa(NiCoMnAlFe)₁O₂. (e) Specific discharge capacity of LiNa(NiCoMnAlFe)₁O₂, Li(NiCoMnAlZn)₁O₂ and Li(NiCoMnAlFe)₁O₂ from galvanostatic cycling experiments.

Figure 5.6a-d shows cyclic voltammetric curves at a sweep rate of 0.1 mV/s. The Li(NiCoMn)₁O₂ data revealed an oxidation peak around 3.8 V which is in agreement with literature and the potential increased to 4.0 V for Li(NiCoMnAlZn)₁O₂. However, when substituting Fe³⁺ for Zn²⁺ (Li(NiCoMnAlFe)₁O₂), it increased even further to 4.1 V, despite the fact that the Al³⁺ content remained unchanged. Although this material did not show high reversibility, the increase in oxidation potential clearly demonstrates that either the incorporated elements or the

configurational entropy or both exert a strong effect on the electrochemical behavior, which also validates the tailoring ability. Interestingly, when some of the Li was replaced with Na ($\text{LiNa}(\text{NiCoMnAlFe})_1\text{O}_2$), both the specific capacity increased by a factor of more than two (Figure 5.6e) and the reversibility improved considerably compared to $\text{Li}(\text{NiCoMnAlFe})_1\text{O}_2$. The oxidation potential dropped by only 100 mV to 4.0 V (Figure 5.6c and d), which seems promising for the development of high-energy-density cathode materials. However, most of the materials showed reasonable redox activity, but the specific capacities achieved are not yet satisfactory (Figure 5.6e), probably because that in the quest to maximise entropy, the equimolar ratio of the elements leads to a severe reduction in the proportion of redox active elements (e.g., Ni and Co).

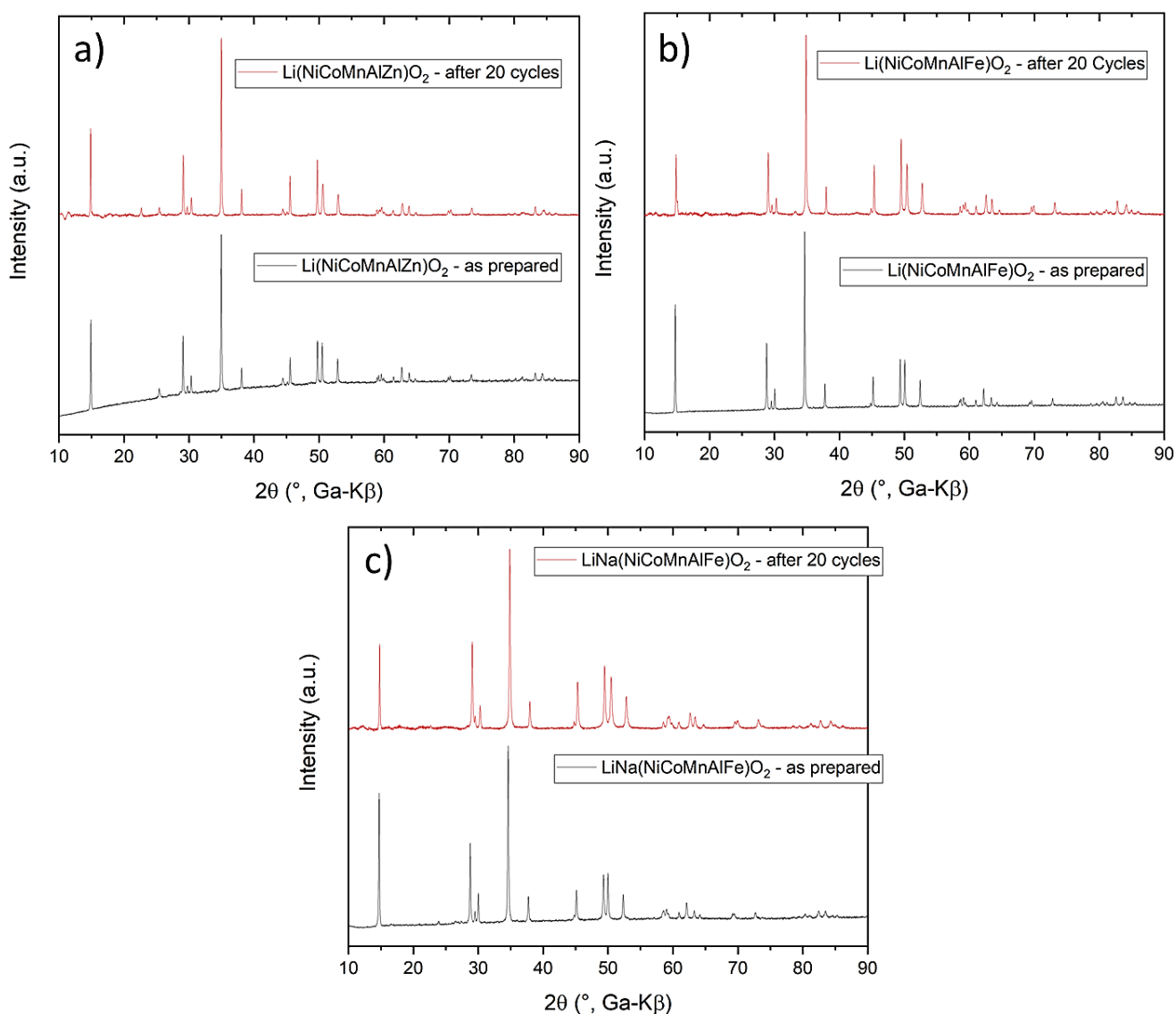


Figure 5.7: XRD patterns of (a) $\text{Li}(\text{NiCoMnAlZn})_1\text{O}_2$, (b) $\text{Li}(\text{NiCoMnAlFe})_1\text{O}_2$ and (c) $\text{LiNa}(\text{NiCoMnAlFe})_1\text{O}_2$ recorded before and after electrochemical cycling.

In order to learn about the structural stability upon electrochemical cycling, the L-HEO materials were probed using XRD before and after 20 cycles (Figure 5.7). The layered structure was clearly preserved for all of the materials, thus indicating good stability with cycling. Only for $\text{Li}(\text{NiCoMnAlZn})_1\text{O}_2$, a small reflection appeared

around 23°. What is more striking is the change in intensity ratio between the 003 and 104 reflections. The low ratio of 003/104 reflections reflect a high the cation mixing after several round cycles, if the reflections do show about the same intensity, the cation mixing is low. For cycled $\text{Li}(\text{NiCoMnAlFe})_1\text{O}_2$ and $\text{LiNa}(\text{NiCoMnAlFe})_1\text{O}_2$, the 003 reflection showed decreased intensity, suggesting increased cation mixing, which in turn may help explain the capacity fading shown in Figures 5.6e.

Taken together, the data in Figure 5.6 and Figure 5.7 demonstrate the versatility of the high entropy approach—small changes in composition strongly affect the electrochemical characteristics, including cycling performance and stability. The reason for the enhanced performance of $\text{LiNa}(\text{NiCoMnAlFe})_1\text{O}_2$ may well be that the larger Na^+ ions somewhat widen the diffusion channels which are blocked otherwise due to cation disorder [209]. As somewhat expected, the L-HEO material with the lowest degree of cation mixing showed the best cyclability and delivered the largest specific capacities. This suggests that, in principle, it should be possible to design next-generation L-HEOs for battery applications [97, 161, 208]. Nevertheless, the issue of cation mixing remains to be resolved and the specific capacities need to be increased still [202, 210, 211]. Overall, the impact of entropy stabilization on the cycling performance is largely unclear and is an interesting question for future studies. Common (non-HEO) cathode intercalation materials can only be delithiated to a certain extent to prevent irreversible structural changes [212, 213]. This reduces the amount of usable Li and therefore limits the specific capacity. Overall, it would be exciting to see if L-HEO materials with a large entropy stabilization allow for higher degrees of delithiation by more effectively stabilizing the layered structure.

5.2.5. The Effects of High Entropy

The question if “only” a high entropy or an entropy stabilization is apparent can be discussed in part using the Hume-Rothery’s second rule for solid-solution formation [212]. The latter can be understood as a description under which precondition elements can form a solid solution. The rule states that the ionic radius of the incorporated elements should not differ by more than about 15% and that the crystal structures, valences and electronegativities should be similar. The type of crystal structure of the L-HEO materials synthesized here is Delafossite $\alpha\text{-NaFeO}_2$. Many of the individual elements may show comparable stable structures in the respective lattice type ($\alpha\text{-LiAlO}_2$, LiCoO_2 , LiNiO_2 , LiFeO_2 , except for Mn and Zn). Therefore, the first precondition seems to be fulfilled for 4 out of 6 of the tested elements. Other preconditions are similar ionic radii and electronegativities.

Table 5.2: Valence, ionic radius and electronegativity for different elements [214, 215].

	Co^{3+}	Ni^{2+}	Ni^{3+}	Al^{3+}	Fe^{3+}	Mn^{4+}	Zn^{2+}	Li^+	Na^+
Ionic radius (Å)	0.55	0.69	0.56	0.54	0.55	0.53	0.74	0.76	1.02
Electronegativity	1.693	1.367	1.695	1.513	1.651	1.912	1.336	1.009	1.024

Table 5.2 shows the respective values. As is evident, these characteristics are similar for the trivalent transition metal ions. It is known that in NCM materials, Mn is present in the oxidation state 4+, thereby partially reducing Ni to 2+. The size of Mn^{4+} is also similar, which helps explain its successful incorporation into a single-phase structure. The radius of Zn^{2+} differs quite significantly and is more similar in radius to Li^+ . The discrepancy in Zn^{2+} radius and the differences in structure as explained above seem to increase the mixing enthalpy too much, such that the entropy cannot compensate it and therefore no single-phase material is formed. Nevertheless, XRD and TEM indicate that some of the Zn^{2+} ions are incorporated into the material, so entropy stabilization and the formation of a single-phase structure may be apparent until a certain threshold concentration in the structure is reached. Formation of a single phase at higher temperatures may be possible, but the accompanying Li loss prevents such studies. Despite its even larger radius and discrepancy in valence and electronegativity, Li^+ is successfully incorporated, since it is an integral part of the layered $R-3m$ structure. In summary, application of the Hume-Rothery rules to these systems indicates good miscibility of elements for $Li(NiCoMnAlFe)_1O_2$ and $LiNa(NiCoMnAlFe)_1O_2$. In these systems, high entropy is clearly apparent, but entropy stabilization might be questionable. The $Li(NiCoMnAlZn)_1O_2$ material showed the presence of side phases, most probably due to the different characteristics of Zn^{2+} . Therefore, the stabilizing role of entropy remains elusive for these layered materials and the term “high entropy” (referring to high configurational entropy) rather than “entropy stabilized” has been applied in the present work [216].

5.3. Conclusions

In this work, a new class of layered high entropy oxide materials, namely L-HEOs, has been synthesized. The incorporated elements were found to be virtually equimolar and, more importantly, uniformly distributed on the nanometer and micrometer levels. Moreover, reversible Li^+ intercalation/extraction into/from the L-HEOs was demonstrated, but the specific capacities achieved were relatively low (when compared to state-of-the-art cathode materials). The question if these materials are entropy-stabilized toward to electrochemical properties cannot be clearly answered due to non-optimal solutions for synthetic methods resulting in unsatisfactory performance. Nevertheless, given the broad application area of layered materials and the benefits arising from the high entropy approach (e.g., versatility in composition), L-HEOs may pave the way for new strategies.

Chapter 6

6. The Role of High Entropy Effects in P2-type Cathode Materials for Sodium-ion Batteries (SIBs)

The majority of the results presented in this chapter have been submitted to the peer-reviewed publication. The experimental work was carried out by Junbo Wang. The manuscript was organized and written by Junbo Wang under the guidance of Dr. Qingsong Wang, Dr. Ben Breitung and all other co-authors. Co-authors contributed by supporting with gas evolution testing, certain characterization methods, providing valuable discussions, and reviewing the article draft.

6.1. Introduction

Over the last decades, SIBs have received increasing attention as energy storage devices for a wide range of applications, particularly for grid-scale renewable energy storage [217, 218]. This has been driven by the exponential growth of global energy demand and the increasing societal demands toward sustainability [219]. Compared to the widely used LIBs, SIBs are a viable alternatives thanks to their lower cost and abundant resources [220, 221]. Studies on cathode materials for SIBs have been extensively focused on layered oxides, Na_xTMO_2 (TM= transition metal), which offer high theoretical capacities [222, 223].

Layered transition metal (TM) oxides are generally classified based on the TMO_2 layer stacking and the alkali coordination, into different types such as O3, P3, P2, and O2, based on the scheme by Delmas et al. in the early 1980s [36]. According to the proposed definition, the “O” and “P” represent the surrounding environment of alkali ions, “octahedral” and “prismatic”, respectively. The numbers “2” and “3” stand for the repeat oxygen packing are ABBAABBA... and ABCABC... [36, 62, 63].

The crystallographic nature of Na-based layered oxides is different from Li-based ones. Li^+ ions are found to be favored in the octahedral sites, and the Li-based layered oxides prefer to crystallize in the O3-type structure in most cases [36]. While Na-based layered oxides commonly exist as two main structures, O3- and P2-type phases

with Na⁺ ions preferably occupying the octahedral (O) or prismatic (P) sites. Theoretically, the high energy barrier of the O3 structure inhibits the diffusion of Na⁺ ions, leading to a complex phase transition during the sodiation/desodiation process [224]. In comparison, the P2-type structure to the open Na⁺ diffusion pathways in a trigonal prismatic environment resulting in a faster ion diffusion. This is highly beneficial for energy storage as it leads to a higher reversible capacity and better rate ability than the O3-phase [225–228]. However, in these layered oxides, unfavorable phase transitions often occurs between P- and O- type structures (caused by layer gliding or TM migration) during charge-discharge cycles, which hinders the cycling performance [62, 217, 225]. The phase transition of P2 to O2 appears at high charging potential (> 4.2 V) when the Na⁺ ions are extracted from the layer, resulting in energetically unstable prismatic sites. Such stacking transformation is usually not fully reversible, which leads to non-uniform electrochemical reactions in the electrode, resulting in poor rate performance and cycling life [63, 229]. As an essential constitution of P2-type materials, the element Mn plays a critical role. In the discharging (sodiation) process, Mn ions ideally remain in the +4 state and are electrochemically inert above 2.0 V, which can help effectively maintaining the structural stability. However, when the electrode material undergoes a further discharging process (below 2.0 V), the reduction of Mn⁴⁺ occurs and is continuously forming the unfavorable Jahn–Teller active Mn³⁺ [223, 23, 231]. This leads to an increase in lattice distortion, the decomposition of active materials, and even results in the appearance of new (impurity) phases, ultimately causing a decrease in electrochemical performances [231–233]. Therefore, effective strategies for the rational design of the P2-cathode, to reduce unwanted phase changes and deterioration of Mn during cycling and to achieve a high-performance Na-based cathode materials, are crucial for the eventually commercial applications [232, 234].

The concept of high entropy in multi-component metal alloys, reported a few years ago, has opened up new possibilities for materials design and synthesis [85]. In short, it can be presumed that as various elements are incorporated in a single-phase structure, the resulted large configurational entropy may have caused an entropy-driven structural stabilization effect [95, 97]. As electrode material for SIBs, a high entropy O3-type material was reported by Zhao et al. in 2019, showing very good performance in long life cycles at different charge/discharge rates [130]. Recently, Yang et al. reported a multiprincipal component P2-type oxide for Na-ion batteries, in which the high entropy concept was introduced and exhibited the improved cycling performance has been achieved [131]. Despite all these examples, this is still only the beginning of applying the high entropy concept in layered materials for energy storage devices, and the role of entropy stabilization still deserves to be further explored.

In this chapter, in the light of the high entropy concept, three different P2-type Na-ion compositions with varying configurational entropy were synthesized as cathode materials for SIBs, by a simple solid-state reaction method. According to the configurational entropy values (calculated by equation 2.13), Na_{0.67}(Mn_{0.55}Ni_{0.21}Co_{0.24})O₂, Na_{0.67}(Mn_{0.45}Ni_{0.18}Co_{0.24}Ti_{0.1}Mg_{0.03})O₂ and Na_{0.67}(Mn_{0.45}Ni_{0.18}Co_{0.18}Ti_{0.1}Mg_{0.03}Al_{0.04}Fe_{0.02})O₂ are defined as low, medium and high entropy oxides and specifically denoted as 3-NTMO₂, 5-NTMO₂ and 7-NTMO₂ in this section, respectively. The Mn in all materials is fixed to 4+ by tuning the metal ratio to rule out the Jahn-Teller effect in the initial state. The effects of entropy on the cycling stability, capacity and voltage retention, and specific energy

at two different cut-off voltages are discussed in detail. *Operando*/post-mortem XRD and DEMS characterizations were particularly used to gain comprehensive insights into the structural stability and the structural evolution between different samples with distinctive configurational entropy values upon cycling. XPS, XAS, and ICP-OES were applied to investigate the evolution of Mn under the different configurational entropy environments. As observed in this study, 7-NTMO₂ with the highest configurational entropy demonstrated the high structural stability and the alleviation of Mn dissolution upon cycling. The high-entropy design strategy provides valuable guidance for achieving an improved performance of SIBs and even further accomplishing innovations in materials design.

6.2. Results and Discussion

6.2.1. Structure and Morphology Characterization

The collected XRD data and corresponding Rietveld refinement on 3-NTMO₂, 5-NTMO₂, and 7-NTMO₂ are shown in Figure 6.1. All three patterns were refined according to the $P6_3/mmc$ space group with the ideal P2-type stacking, by assuming the random distributing of the involved metal elements in the TM layers [235, 236].

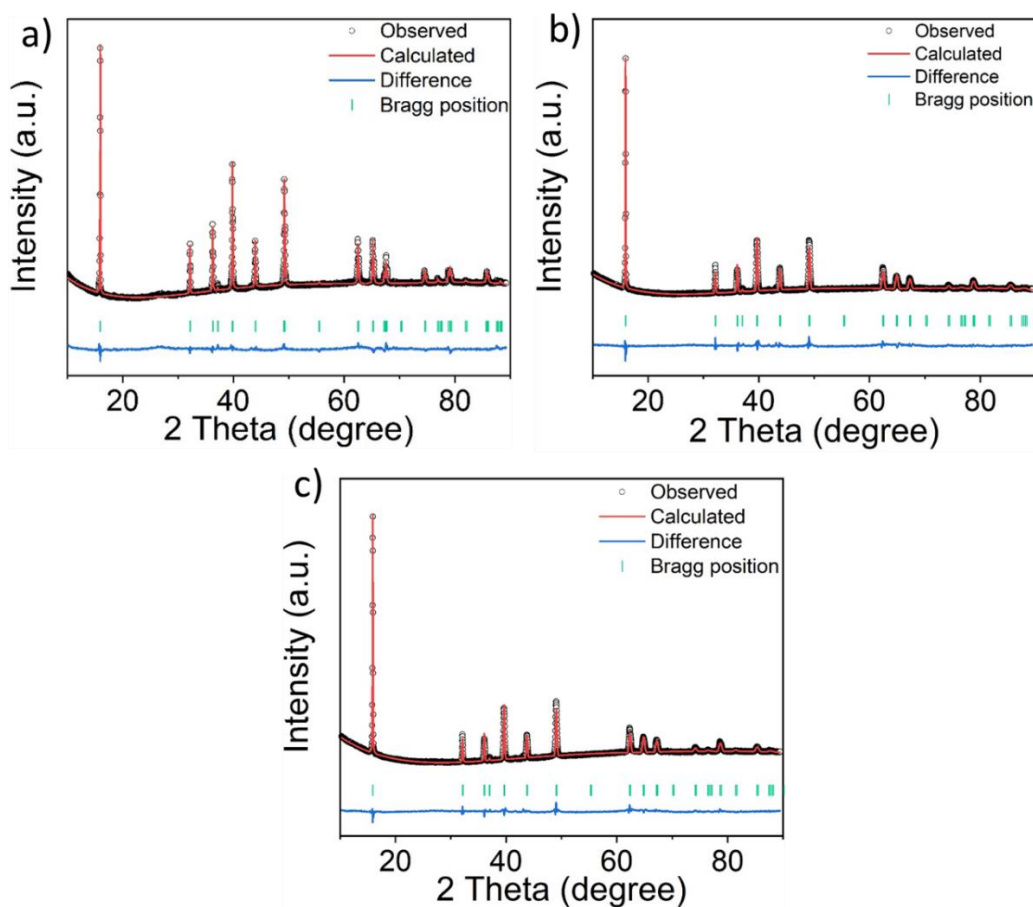


Figure 6.1: X-ray diffraction patterns and Rietveld refinements of the as-prepared (a) 3-NTMO₂, (b) 5-NTMO₂ and (c) 7-NTMO₂ powders. The experimental (calculated) data and the residual discrepancy is shown in black (red) and blue, respectively.

The detailed refinement data regarding agreement factor (R_{wp} and R_p) and lattice parameters are shown in Table 6.1. A larger lattice parameter c is calculated for 7-NTMO₂ (11.1542(5) Å), which would enable a lower diffusion barrier for Na⁺ ions than in the case of 3-NTMO₂ ($c = 11.1343(4)$ Å) and 5-NTMO₂ ($c = 11.1443(6)$ Å).

Table 6.1: Refinement errors and detailed crystallographic parameters of three samples

	3-NTMO ₂	5-NTMO ₂	7-NTMO ₂
$a = b/\text{Å}$	2.8607(1)	2.8729(1)	2.8781(1)
$c/\text{Å}$	11.1343(4)	11.1443(6)	11.1542(5)
$V/\text{Å}^3$	78.910(4)	79.587(5)	79.876(4)
R_p (%)	1.19	1.35	1.26
R_{wp} (%)	1.56	1.99	1.73

The stoichiometric compositions were determined by ICP, as shown in Table 6.2, the atomic ratios of all elements are in good agreement with the designed compositions. This suggests the absence of component loss during the sample preparation process. The configurational entropy values were calculated to be 0.99R, 1.34R, and 1.52R for 3-NTMO₂, 5-NTMO₂, and 7-NTMO₂, respectively.

Table 6.2: Overview of the ICP-OES results of the synthesized materials

Composition	Composition and ICP-OES results
Na _{0.67} (Mn _{0.55} Ni _{0.21} Co _{0.24})O ₂	Na _{0.6510} (Mn _{0.5336} Ni _{0.2058} Co _{0.2293})O ₂
Na _{0.67} (Mn _{0.45} Ni _{0.18} Co _{0.24} Ti _{0.1} Mg _{0.03})O ₂	Na _{0.6666} (Mn _{0.4467} Ni _{0.1817} Co _{0.2340} Ti _{0.0933} Mg _{0.0254})O ₂
Na _{0.67} (Mn _{0.45} Ni _{0.18} Co _{0.18} Ti _{0.1} Mg _{0.03} Al _{0.04} Fe _{0.02})O ₂	Na _{0.6649} (Mn _{0.4433} Ni _{0.1806} Co _{0.1763} Ti _{0.0947} Mg _{0.026} Al _{0.037} Fe _{0.016})O ₂

In order to obtain more insights into the structure of the as-prepared materials, the morphology and elemental distribution were gained by SEM and TEM. As demonstrated in Figure 6.2 and Figure 6.3, all these three samples exhibit similar morphological features. The powder samples are composed of irregular plate-shape bulk particles with a particle size between 1 μm and 3 μm, where nano-sized particles cover a portion of the large microparticles.

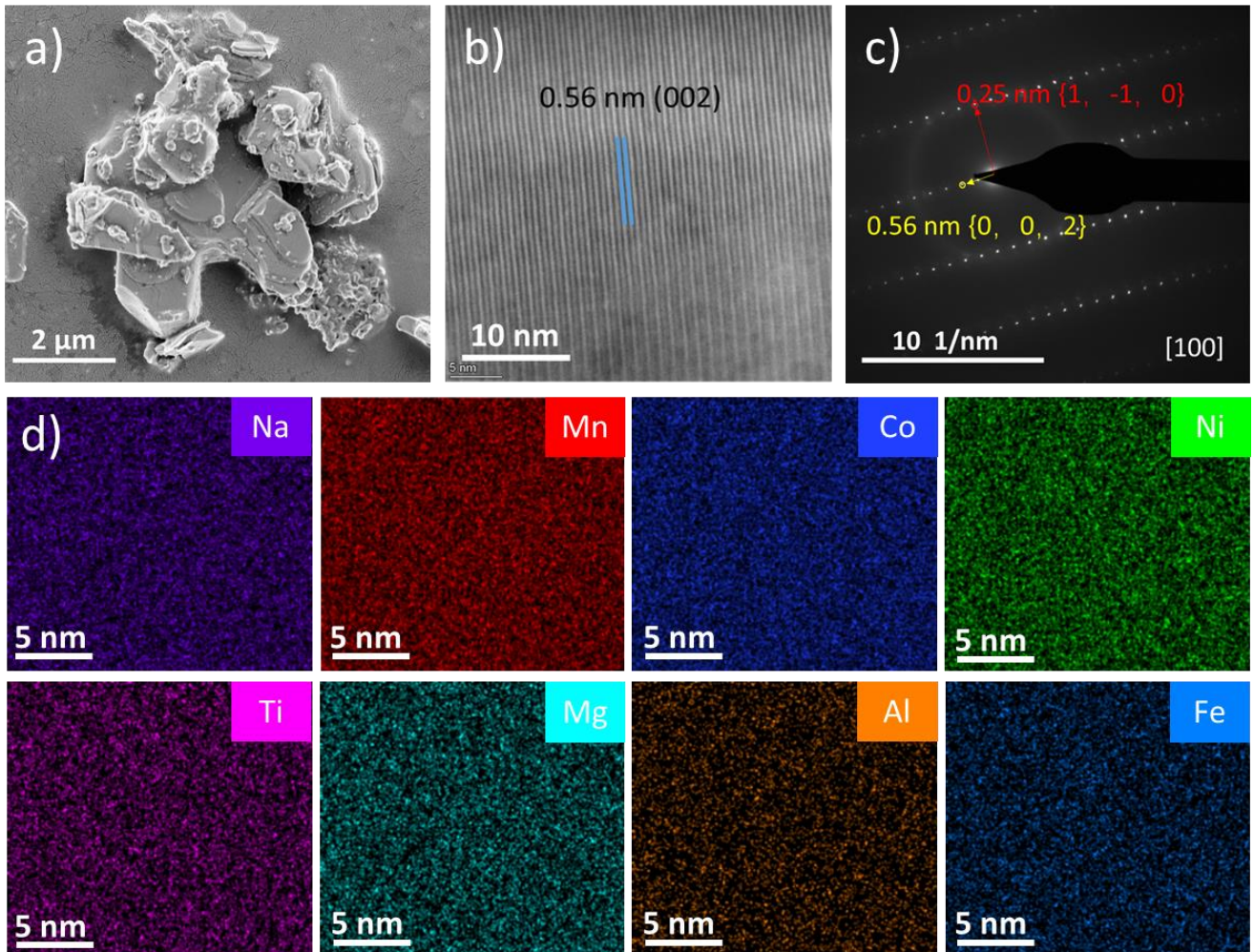


Figure 6.2: Results of the morphological analysis of 7-NTMO₂. (a) SEM image, (b) STEM, (c) SAED along the direction of [100] and (d) high-resolution EDX mapping.

Here, the 7-NTMO₂ is exemplified described that the crystal particles are highly crystallinity with an interplanar distance of spacing of 0.56 nm between adjacent lattice stripes, corresponding to the spacing value of the (002) plane in the P2 phase (Figure 6.2b). Figure 6.2c displays the SAED patterns of 7-NTMO₂ are viewed along the [100] direction. It contains only one set of diffraction spots, which can be perfectly indexed into the P2 structure and confirm the XRD results. The corresponding elemental mapping (Figure 6.2d) from EDX analysis indicates that is no significant agglomeration or segregation of single elements or secondary phases. Furthermore, all elements are uniformly distributed at the nanoscale level. In contrast, the morphological results of 5-NTMO₂ and 3-NTMO₂ are shown in Figure 6.3.

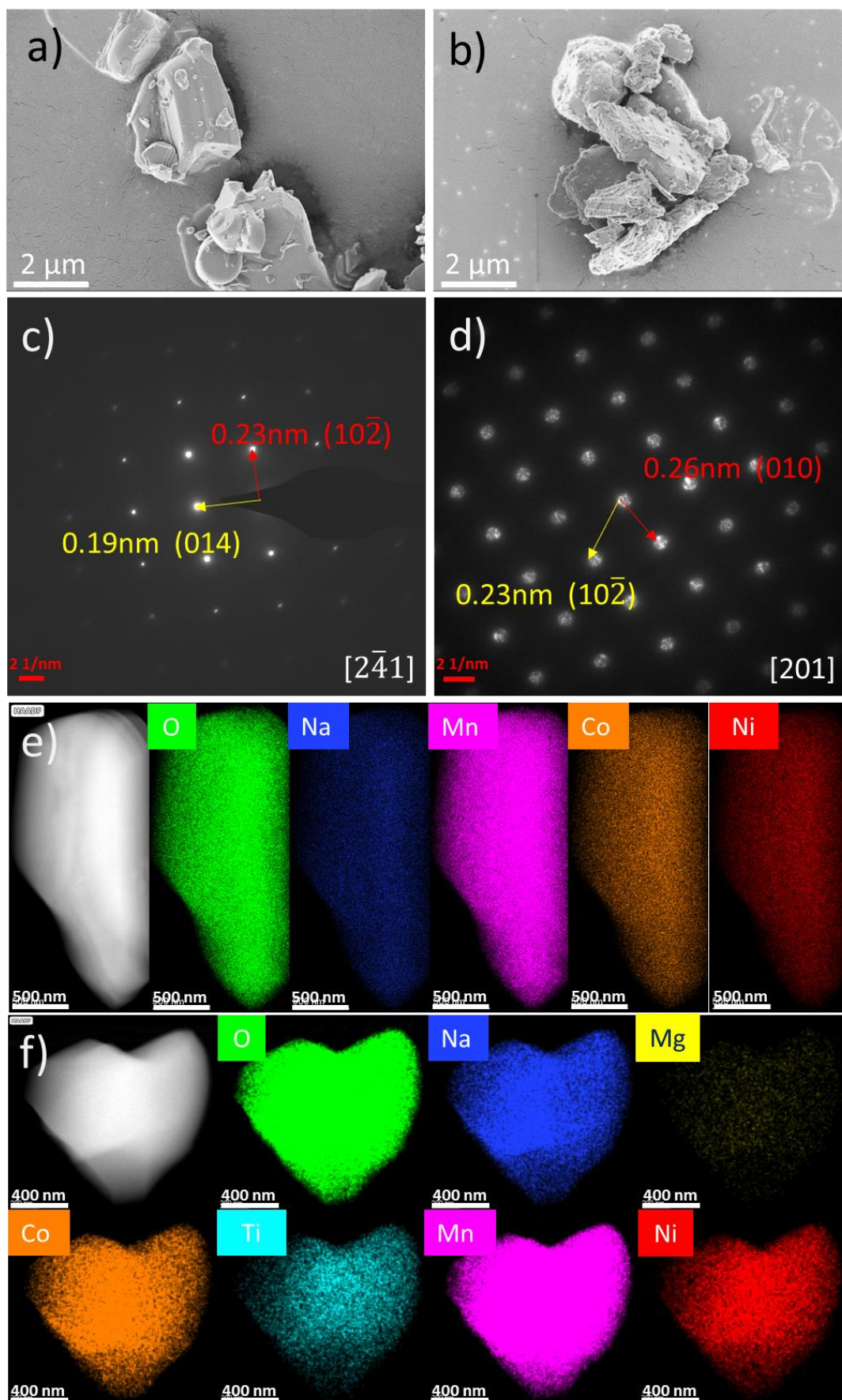


Figure 6.3: (a) and (b) SEM images, (c) and (d) SAED patterns along the direction of $[2\bar{4}1]$ and $[201]$, and (e) and (f) the HR-TEM micrograph and high-resolution EDX mapping for 3-TNMO₂ and 5-TNMO₂, respectively.

6.2.2. Electrochemical Characterization

In this work, all voltages are reported vs. Na^+/Na . The CV results of electrodes with 3-NTMO₂, 5-NTMO₂ and 7-NTMO₂ are shown in Figure 6.4. The materials surveyed in the voltage range between 1.5 V and 4.6 V with a scan rate of 0.1 mV s^{-1} , to observe the evolutions of the peaks located at 4.2 V associated with both the phase transition and the deep extraction of Na^+ caused by oxygen oxidization or oxygen release which contribute a part of capacity at above 4.2 V [229, 230, 236, 237]. When charged above 4.2 V, a further decrease of the sodium content in the P2 layered structure leads to an energetically favored misalignment of oxygen atoms along the *c*-axis, and part of the capacity is attributed to oxygen activities [230, 232, 238, 239]. Therefore, in the initial two cycles, the oxidation reaction peaks located at around 4.3 V shift towards lower potential and show a decrease in intensity.

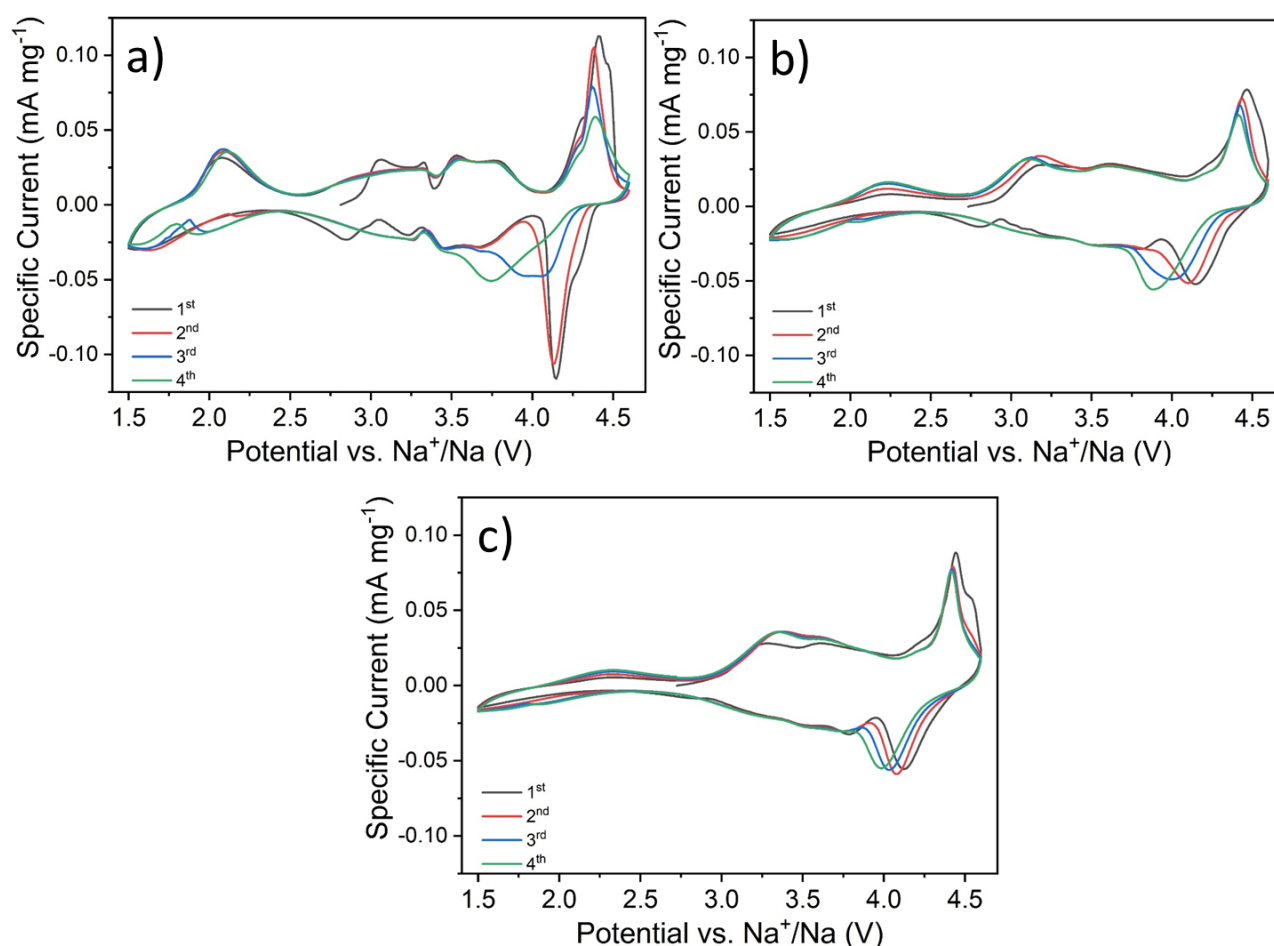


Figure 6.4: Cyclic voltammograms of (a) 3-NTMO₂, (b) 5-NTMO₂ and (c) 7-NTMO₂ at a scan rate of 0.1 mV s^{-1} in the voltage range of 1.5-4.6 V.

Shifts of different strengths for the redox peaks above 3.5 V are observed for these three electrode materials. The changes are most pronounced for 3-NTMO₂, which demonstrates that the structure of this material changes more during the redox processes than for 5-NTMO₂ and 7-NTMO₂. 3-NTMO₂ exhibits intense phase transitions during

initial cycling processes (see further the section on *operando* XRD). In the following cycles, the potential of reduction reaction decreases significantly to 3.7 V in the 4th cycle. For the 5-NTMO₂ electrode, intensity degradation and position change of redox peak at 4.3 V are not so pronounced than those of 3-NTMO₂, which can be explained by improved structural stability and lower polarization. Compared to 3-NTMO₂ and 5-NTMO₂, the 7-NTMO₂ electrode exhibits good reversibility at the high potential range (3.8-4.6 V) during the entire testing process. In the low voltage range (about 2.2 V), the clearly identifiable peaks for the 3-NTMO₂ electrode correspond to Mn^{3+/4+} transitions. The Jahn–Teller distortion active Mn³⁺ at a high Na⁺ content state may induce a phase transition from P2 to P2' (space group *Cmcm* and/or *C2/n*) as reported by Benoit et al. and Ivana Hasa et al. [238, 240, 241] This leads to the partial dissolution of Mn ions and capacity fading. As shown in Figure 6.4a, the intensities and the polarization of the Mnⁿ⁺ redox reaction peaks increase gradually with successive cycling scans of 3-NTMO₂, which suggests that the involved Mnⁿ⁺ redox reaction increase correspondingly with an unfavorable structural stability [230, 242]. This behavior is less pronounced for 5-NTMO₂, as seen from the initial intensity of the peak at the 1st cycle and the subsequent variation of profiles. For the 7-NTMO₂ electrode, the intensity of the Mnⁿ⁺ redox reaction peaks change minimally during 4 cycles. These results demonstrate the good reversibility of the high entropy material 7-NTMO₂ compared to the other two P2 materials.

Galvanostatic cycling was carried out for further investigation of the electrochemical performance. As an activation process, the 1st cycle is performed at a rate of 0.05C. Charge-discharge profiles of the 2nd, 5th, 10th, 20th and 50th cycles at a rate of 0.5C in two different potential ranges are analyzed (Figure 6.5a-c and Figure 6.6a-c). The electrochemical properties of electrodes were characterized at a voltage range of 2.6-4.6 V (Figure 6.5) so that the formation of Mn³⁺ can be ruled out. The 3-NTMO₂ shows a discharge capacity of 115 mA h g⁻¹ at the 2nd cycle, which is slightly higher than that of 5-NTMO₂ (113 mA h g⁻¹) and 7-NTMO₂ (102 mA h g⁻¹) because of a higher percentage of active elements involved. Usually, extended plateaus starting at around 4.2 V indicate the occurrence of two-phase reactions (the P2-O2 phase transition) during charging processes (Figure 6.5a-b) [74, 230, 242, 243]. For 7-NTMO₂, a smooth charging slope without plateau indicates a facile extraction of sodium ions with high structural stability [63, 131, 234].

Capacity loss and voltage decay can be observed upon battery cycling for all these three materials to different degrees. As shown in Figure 6.5a, a sharp voltage drop is evident in the charge/discharge profile of 3-NTMO₂. The midpoint voltage (MPV) of the discharge decreases from 3.72 V at the 2nd cycle to 3.23 V at the 50th cycle. The sharp drop is consistent with the sharp intensity decrease and the shift of the reduction peaks to lower potentials in the above CV result. In contrast, the MPV dropped from 3.78 V to 3.51 V and from 3.78 V to 3.67 V in 5-NTMO₂ and 7-NTMO₂, respectively. Therefore, 7-NTMO₂ demonstrates the best discharge voltage retention.

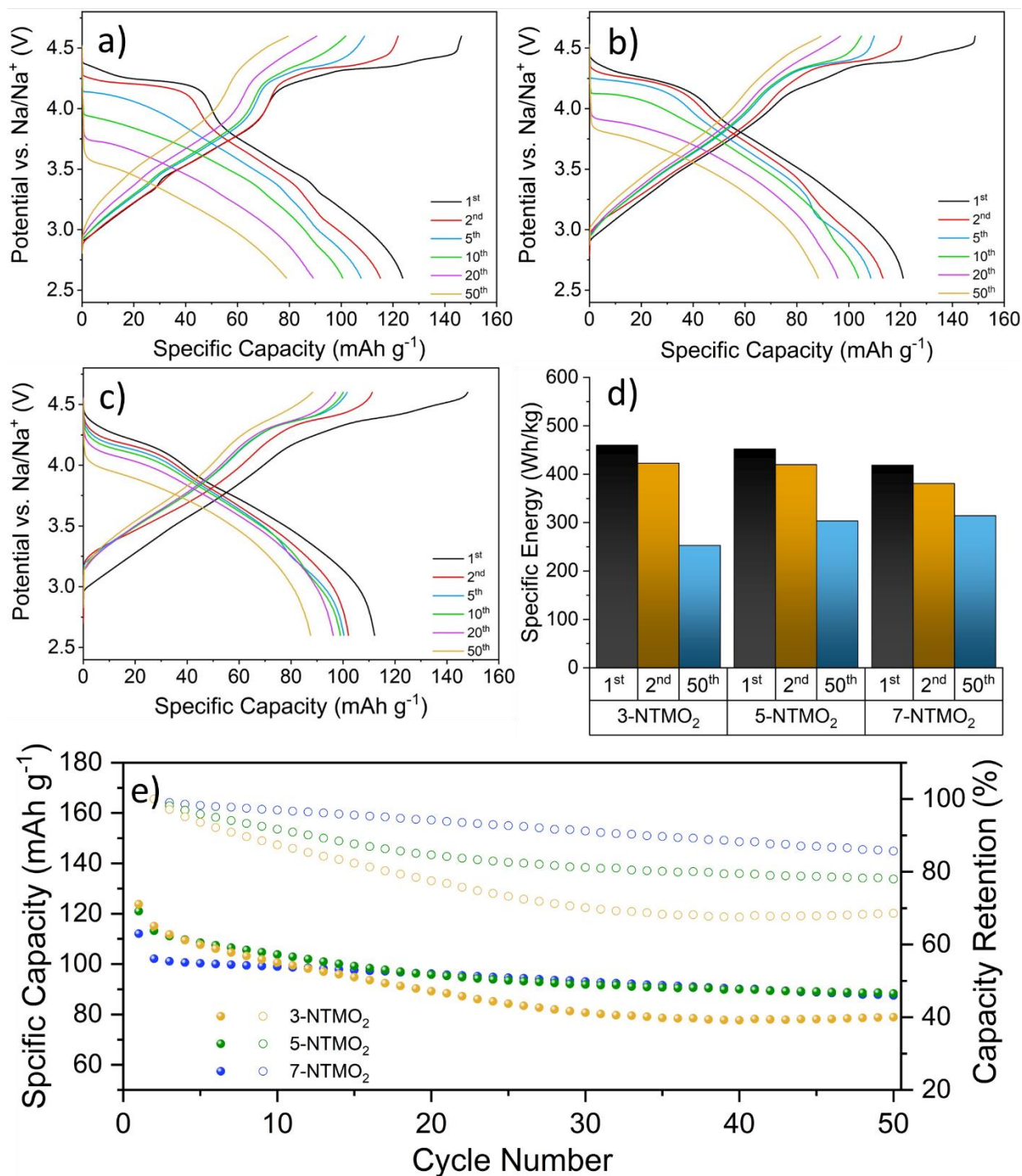


Figure 6.5: Charge-discharge curves of (a) 3-NTMO₂, (b) 5-NTMO₂ and (c) 7-NTMO₂. (d) Comparison of discharge energy at the 1st, 2nd and 50th cycle. (e) Cycling performance and capacity retention at 0.5 C for 50 cycles. All tests are operated at potential window of 2.5-4.6V at 0.5C at room temperature.

Figure 6.5e shows the cycling performance of the materials at 0.5C. Although a higher initial capacity is displayed, the 3-NTMO₂ and 5-NTMO₂ electrodes show obvious decays in the first 15 cycles. After that, the trend towards lower specific capacity is not mitigated for 3-NTMO₂, while it is more moderate for 5-NTMO₂. In contrast, the 7-NTMO₂ electrode exhibits superior cycling stability in the whole test. Ultimately, at the 50th cycle, capacity recoveries of 69%, 78% and 86% was obtained for 3-NTMO₂, 5-NTMO₂, and 7-NTMO₂, respectively. In addition,

the voltage decays and capacity losses are detrimental to the specific energy of active materials. Translating these capacity values into gravimetric energy densities with a theoretical Na metal anode (Figure 6.5d), the 2nd discharge provided a specific energy of 423 W h kg⁻¹, 420 W h kg⁻¹, and 381 W h kg⁻¹, and the 50th cycle resulted in specific energies of 253 W h kg⁻¹, 303 W h kg⁻¹, and 314 W h kg⁻¹ for 3-NTMO₂, 5-NTMO₂, and 7-NTMO₂, respectively.

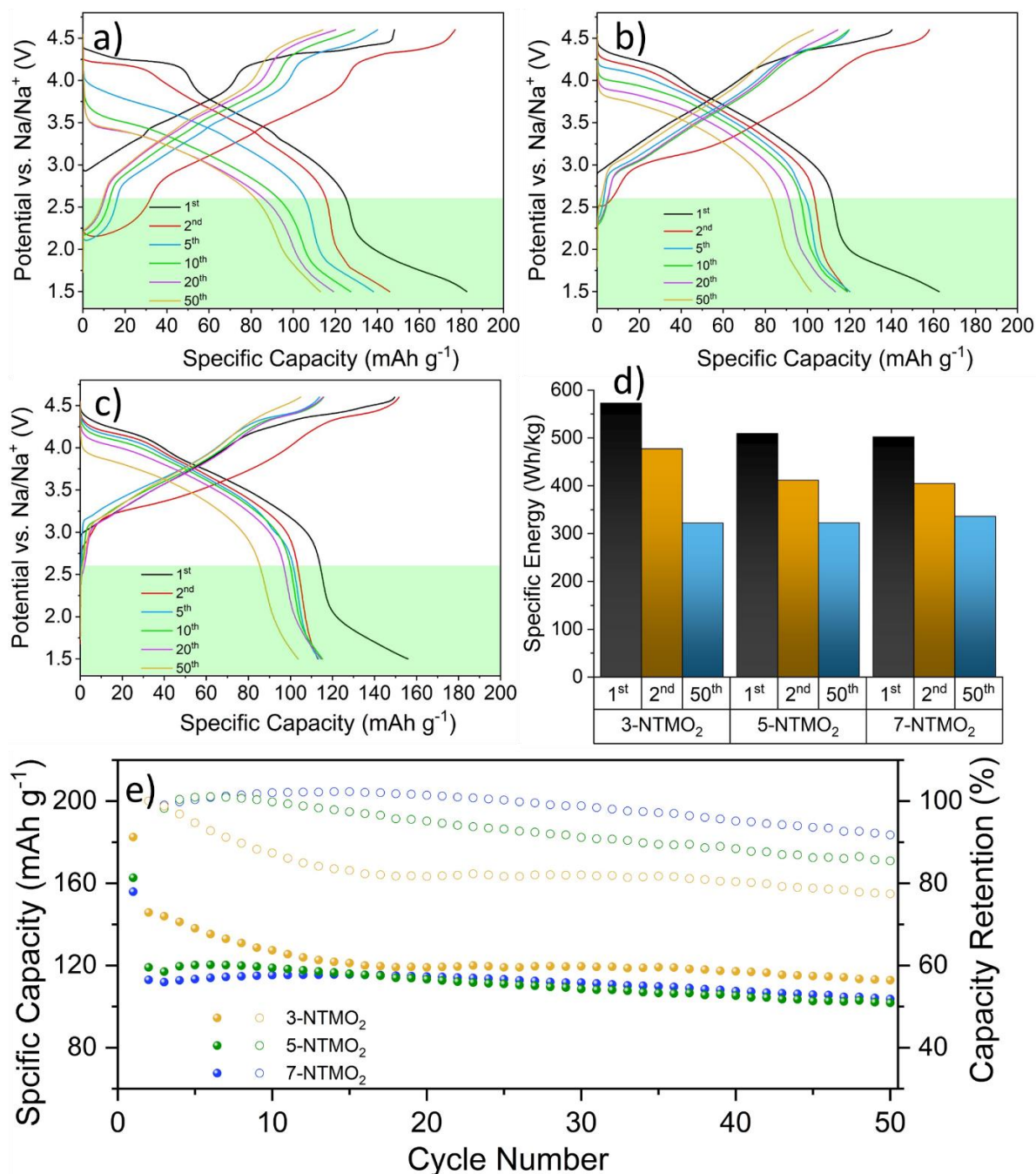


Figure 6.6: Charge–discharge curves of (a) 3-NTMO₂, (b) 5-NTMO₂ and (c) 7-NTMO₂. (d) Comparison of discharge energy at the 1st, 2nd and 50th cycle. (e) Cycling performance and capacity retention at 0.5 C for 50 cycles. All tests are operated at potential window of 1.5–4.6 V at 0.5C at room temperature.

Figure 6.6 shows the charge/discharge profiles in the voltage range of 1.5-4.6 V. A broader potential range was chosen to reveal the influence of structural rearrangement in a broader potential range involving $\text{Mn}^{\text{n+}}$ redox reaction on the electrochemical performance [75, 76, 230].

The disproportionation reactions of Mn^{3+} ions can produce soluble Mn^{2+} ions leading to a steady loss of the active materials. After the second cycle, the charge capacity is 146, 119, and 113 mA h g^{-1} for 3-NTMO₂, 5-NTMO₂, and 7-NTMO₂, respectively. The large differences in the initial discharge capacities (of which are 31, 6, and 11 mA h g^{-1}) are attributed to the insertion of Na^+ below 2.6 V. This intercalation of Na^+ ions reaches the theoretical Na^+ intercalation limit at which the oxidation states of the active elements are partially in a low valence state. This will be discussed in XPS analysis part later in more detail. Compared to the cycling between 2.6-4.6 V, the reduction reaction of the $\text{Mn}^{4+}/\text{Mn}^{3+}$ pairs emerge at around 2.2 V (highlighted by green boxes in Figure 6.6a-c) in the discharge process. The slopes are steeper for 5-NTMO₂ and 7-NTMO₂ than for 3-NTMO₂, indicating the less active $\text{Mn}^{\text{n+}}$ redox reaction. For the 3-NTMO₂ sample, the values of voltage decay and capacity loss between 1.5 V and 4.6 V are higher than in the narrow potential window (2.6-4.6 V, Figure 6.5). Although good reversibility was observed between the 20th and the 50th cycles, the severe potential polarization and performance degradation compared to the initial cycles cannot be ignored. These results suggest that the disproportionation of Mn at a discharged state may have had a significant effect on the electrode material in the early cycles [244, [245]. As shown in Figure 6.6e, a similar trend of capacity degradations is observed as that displayed in the range of 2.6-4.6 V. However, the cell with the 3-NTMO₂ electrode can deliver a higher capacity (113 mA h g^{-1}) after 50 cycles, than 5-NTMO₂ and 7-NTMO₂. This is likely due to the higher discharge capacities caused by the reduction reactions of the $\text{Mn}^{4+}/\text{Mn}^{3+}$ pair. Nevertheless, the fast capacity fading leads to a low-capacity retention of 62% for 3-NTMO₂ (Figure 6.6e). In contrast, the 5-NTMO₂ and 7-NTMO₂ electrodes display slower fading with remaining capacities of 102 and 104 mA h g^{-1} after 50 cycles, corresponding to of 86% and 92% capacity retention, respectively. Accordingly, the specific discharge energy at the 2nd cycle is 477, 411 and 405 W h kg^{-1} for 3-NTMO₂, 5-NTMO₂ and 7-NTMO₂, respectively, while decreasing to 322, 322 and 336 Wh kg^{-1} at the 50th cycle (Figure 6.6d). These results show that 7-NTMO₂ features much-improved capacity and voltage retention as a result of improved structure stability both in higher voltages and below 2.6 V, demonstrating the high entropy approach can effectively enhance the cycling stability.

6.2.3. Structural Changes Studied via *Operando* X-ray Diffraction (XRD)

The severe loss of charge storage capacity observed during the 1st and 2nd cycle can likely be attributed to phase transitions, which were studied by *operando* XRD investigation. X-ray diffractograms were collected in the potential window of 1.5-4.6 V, and the corresponding 2D contour maps are shown in Figure 6.7. For 3-NTMO₂ (Figure 6.7a), the (002) reflection located at 12.2° continuously shifts upon changing to lower 2θ angles from the open-circuit voltage (OCV) to about 4.35 V. This gradual shift is an indication of a “solid-solution” reaction, during which the change in composition induces a continuous modification of the structural parameters but in the same crystallographic structure [246]. The growth of the *c*-axis lattice parameter is caused by the increase in

repulsion between two adjacent oxygen layers with the Na⁺ extraction. Beyond 4.35 V, the (002) reflection started shifting to higher diffraction angles (with a maximum of 14.5°), accompanied by a new phase formation within the high voltage region of 4.35-4.6 V. This new phase is defined as the so-called O2 stacking “Z”-phase induced by the sliding of MO₂ slabs into an octahedral coordination environment [246, 247]. As a result, the migration of transition metal layers may disturb the long-range ordering of the crystal structure. This behavior corresponds to the sharp oxidation peak occurring at about 4.3 V in the first charging process, as seen during cyclic voltammetry. Additionally, the X-ray diffractograms collected at the high voltage charged state show some new peaks with low intensity between 12.4° and 14.5°. This suggests the loss of long-range order along the *c*-axis [246, 248, 249]. Likewise, an O2-type structure with octahedral vacancies in the Na⁺ layer was reported for Na_{2/3}(Ni_{1/3}Mn_{2/3})O₂ at a deep charged state [249, 250].

During the discharge process, instead of a fast shift of the (002) reflection to smaller 2θ angles, the new Z-phase with O2 stacking persists and returns only gradually back to P2 phase upon discharging to 3.8 V, and finally recovers to the initial position after discharging to 3.1 V. With the further intercalation of Na⁺ ions, the (002) reflection continues to shift to higher 2θ angles, in alignment with a reduction of the *c*-axis lattice parameter, until the cell is discharged to the cut-off voltage of 1.5 V.

During the 2nd cycle, the intensity of the (002) reflection peak is drastically decreased compared to the region above 4.2 V at the 1st cycle. Nevertheless, the P2 (002) reflection at 12.2° shifted to higher diffraction angles with the appearance of the O2 (002) reflection at 13.3° during charging. Moreover, the phase transition region extends to a wider range from 4.35 V to the charge cutoff voltage and subsequently to 2.14 V, reflecting poor reversibility. The appearance of the Z-phase is also observed for 5-NTMO₂ when charged to 4.36 V (Figure 6.7b), but the shift to higher diffraction angles is suppressed (with a maximum of 14.2°). During the 2nd cycle, the reflection of the Z phase is still found in the deeply charged state, but the main reflection of the P2 phase remains at its original position. This result indicates that for the 5-NTMO₂ electrode during the second cycle, the solid-solution and phase transition reactions occur simultaneously (not just the phase transition).

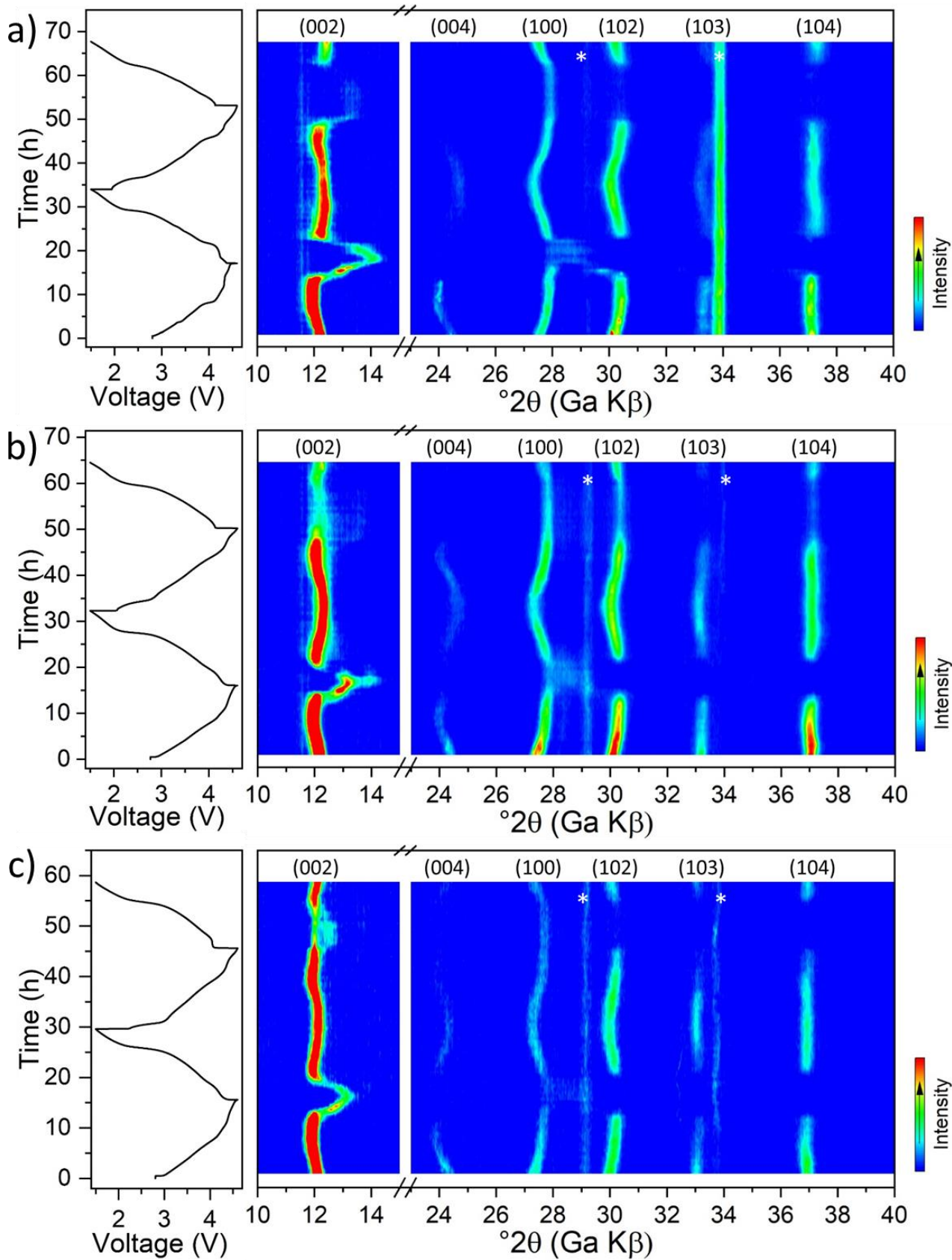


Figure 6.7: *Operando* XRD contour maps of the initial two complete cycles for electrodes with (a) 3-NTMO₂, (b) 5-NTMO₂ and (c) 7-NTMO₂. The corresponding charge-discharge profiles are shown on the left side.

Unlike 3-NTMO₂ and 5-NTMO₂, the structural evolution of 7-NTMO₂ is slightly different when it was charged above 4.35 V (Figure 6.7c). The P2 (002) reflection only shifts slightly to higher angles (with a maximum of 13.1°). The continuity of the diffraction peak shifting and the low shift variations indicate optimal maintenance of crystal structure [237]. A solid-solution reaction mechanism during the full charge/discharge process in the voltage range of 2.5-4.6 V has been demonstrated which is also supported by CV and galvanostatic cycling data. Accordingly, the 7-NTMO₂ displays good structure reversibility upon the entire Na⁺ insertion/extraction process, as concluded both from the electrochemical properties by comparing voltage and capacity retentions and from the analysis of lattice changes via operando XRD. It is confirmed that the high entropy approach is an effective strategy for inhibiting the P2-O2 phase transition and plays an important role in maintaining high reversible capacities and mitigating the potential drop.

6.2.4. Gas Evolution

For an overview of gas evolution in SIBs, the reader is referred to the extensive study of Zhang et al. [251] The gas evolution behavior of the cathode materials was studied via DEMS. For this purpose, cells were cycled at a specific current of 20 mA g⁻¹ in the customized DEMS setup for two consecutive cycles. Figure 6.8 and Figure 6.12 show the correlation between the voltage profiles and the gas evolution rates for the most prominently evolved gases, hydrogen (H₂, *m/z* = 2) and carbon dioxide (CO₂, *m/z* = 44). The origin of these gases can be inferred from the analogy with the gas evolution in LIBs, where CO₂ can originate either from the chemical oxidation of the electrolyte involving the release of lattice oxygen, or from electrochemical electrolyte oxidation or, mainly during the first cycle, from surface carbonates [168, 239, 252]. As the released oxygen in the case of layered oxide cathode materials for LIBs is highly reactive in nature, it is rarely detected directly as molecular oxygen, but instead indirectly as the reaction product CO₂ [253, 254]. In this work, the same observation is made, and elemental oxygen is detected only below the quantification limit, while large amounts of CO₂ are clearly produced. H₂ is formed by the reduction of trace amounts of water and alcohols at the anode. Its release at high potentials is usually explained by the formation of protonic species as byproducts of electrolyte oxidation reactions at the cathode and their subsequent migration to the anode, where they are reduced [255].

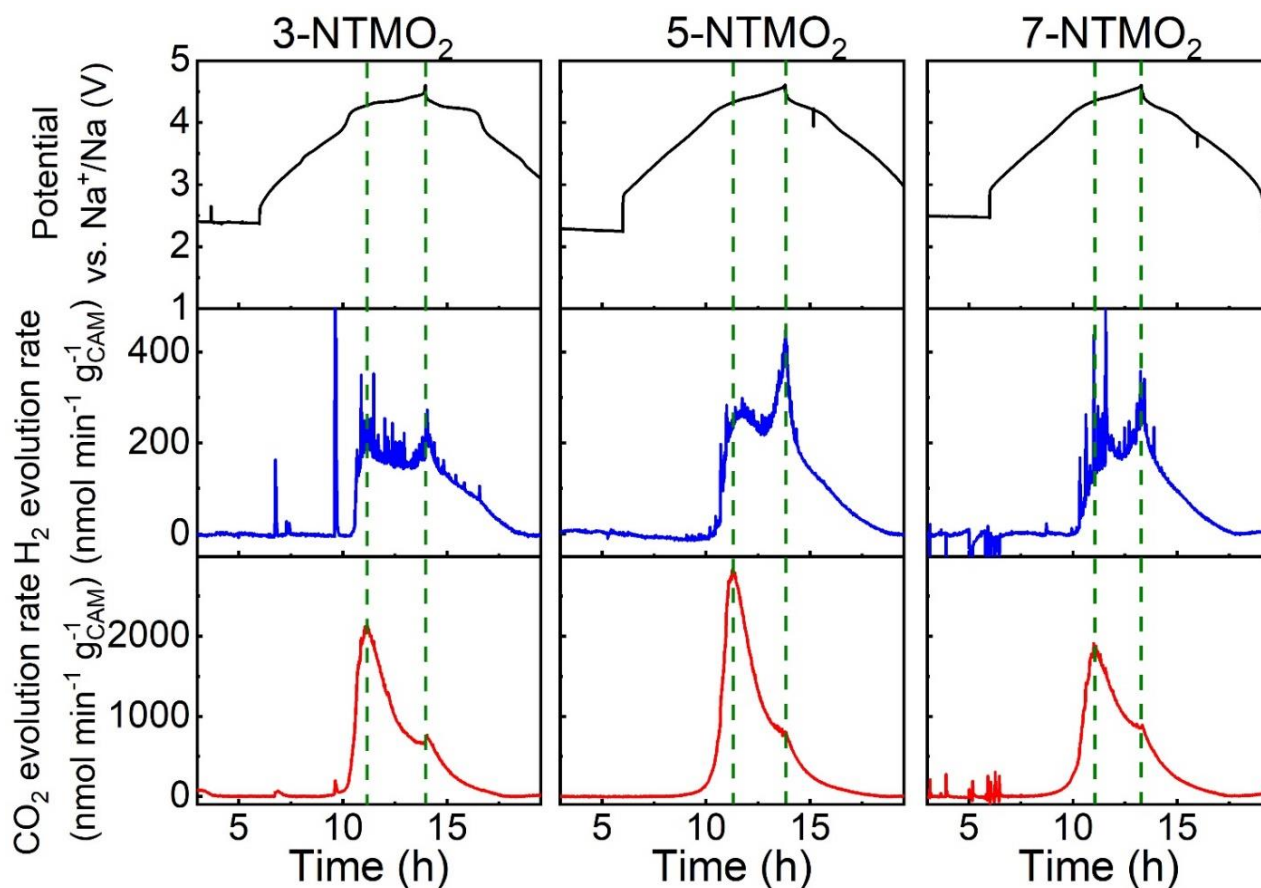


Figure 6.8: Carbon dioxide and hydrogen evolution rate characterized by differential electrochemical mass spectrometry during the first cycle of 3-NTMO₂, 5-NTMO₂ and 7-NTMO₂ cathodes vs. Na metal.

In the first cycle, all three materials show strong gas evolution (Figure 6.8). The highest evolution rate of carbon dioxide was not located as expected at the highest voltage but during the P2-O2 phase transition at the 4.3 V plateau. It should be noted that residual carbonates can often explain a large part of gas evolution in the initial cycle [239]. While no carbonate bands are visible in Fourier transform infrared spectroscopy (FTIR) spectra of the materials (Figure 6.9), suggesting a carbonate-free surface. A similar shoulder can also be observed in the H₂ evolution rates, suggesting electrolyte oxidation as the origin of the gas evolution.

As the gas release is irreversible, the dQ/dV plots do not show a corresponding cathodic peak during discharge. In detailed, the dQ/dV plots (Figure 6.10) also show an irreversible shoulder at around 4.3 V. For the first charge process, 3-NTMO₂ shows a strong peak at 4.35 V with two small shoulders which was resulted from the phase transition of P2 and O2 [256], the similar peaks occur in the case of 5-NTMO₂ and 7-NTMO₂ as well. However, this peak changes greatly upon consecutive cycling. For 3-NTMO₂, the peak at the 2nd cycle shifts to a lower intensity and accompanied by weakened but noticeable shoulder peaks. Yet, for 5-NTMO₂ and 7-NTMO₂, the intensities and locations of this peak show tinier variation but with vanishing shoulder peaks, suggesting the better structure stability and cycling reversibility than 3-NTMO₂. From dQ/dV analysis it is clear the influence of different compositions with variable configurational entropies on the voltage-capacity profiles of NTMO₂ electrodes.

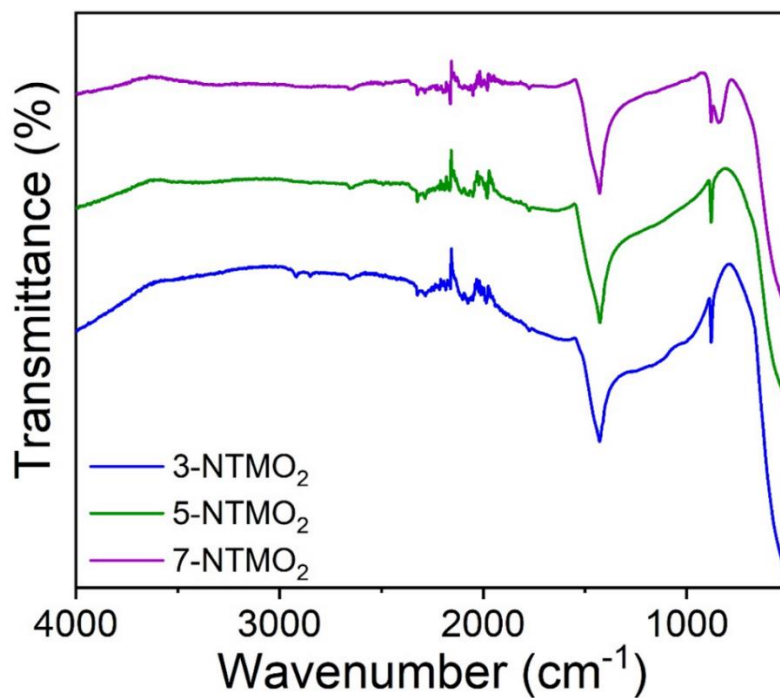


Figure 6.9: Fourier transform infrared spectra of as prepared 3-NTMO₂, 5-NTMO₂ and 7-NTMO₂ powder samples.

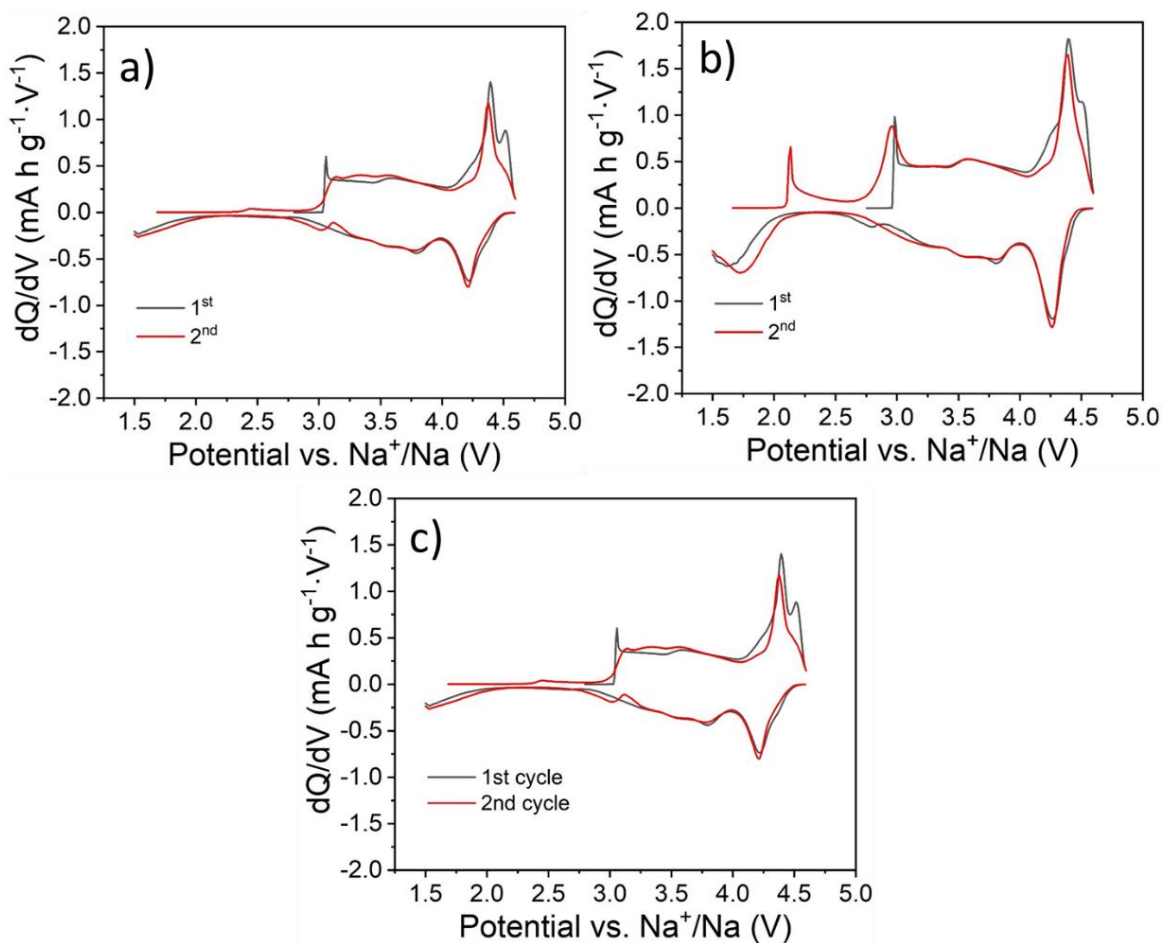


Figure 6.10: Differential capacity vs. potential (dQ/dV) curves for the first two cycles of (a) 3-NTMO₂, (b) 5-NTMO₂ and (c) 7-NTMO₂. Cells were measured at 0.05C at room temperature.

From these results, it can be concluded that significant amounts of lattice oxygen are released at around 4.3 V during the phase transition, which reacts with electrolyte to form carbon dioxide via chemical oxidation. A similar observation has been made for Mn-rich cathode materials for LIBs and was confirmed by isotope labeling experiments [257]. For the P2-type cathode active material $\text{Na}_{0.78}(\text{Li}_{0.25}\text{Ni}_{0.75})\text{O}_2$, isotope labelling also confirmed a substantial loss of lattice oxygen by electrolyte oxidation to CO_2 , but at a potential of 5.0 V [258]. As for these materials, the intensive gas evolution in the first cycle may indicate the presence of anion redox in the investigated materials, which has been reported for various SIB cathode materials [259, 260]. The presence, extent, and reversibility of anion redox is beyond the scope of this work and will be investigated in a follow-up study.

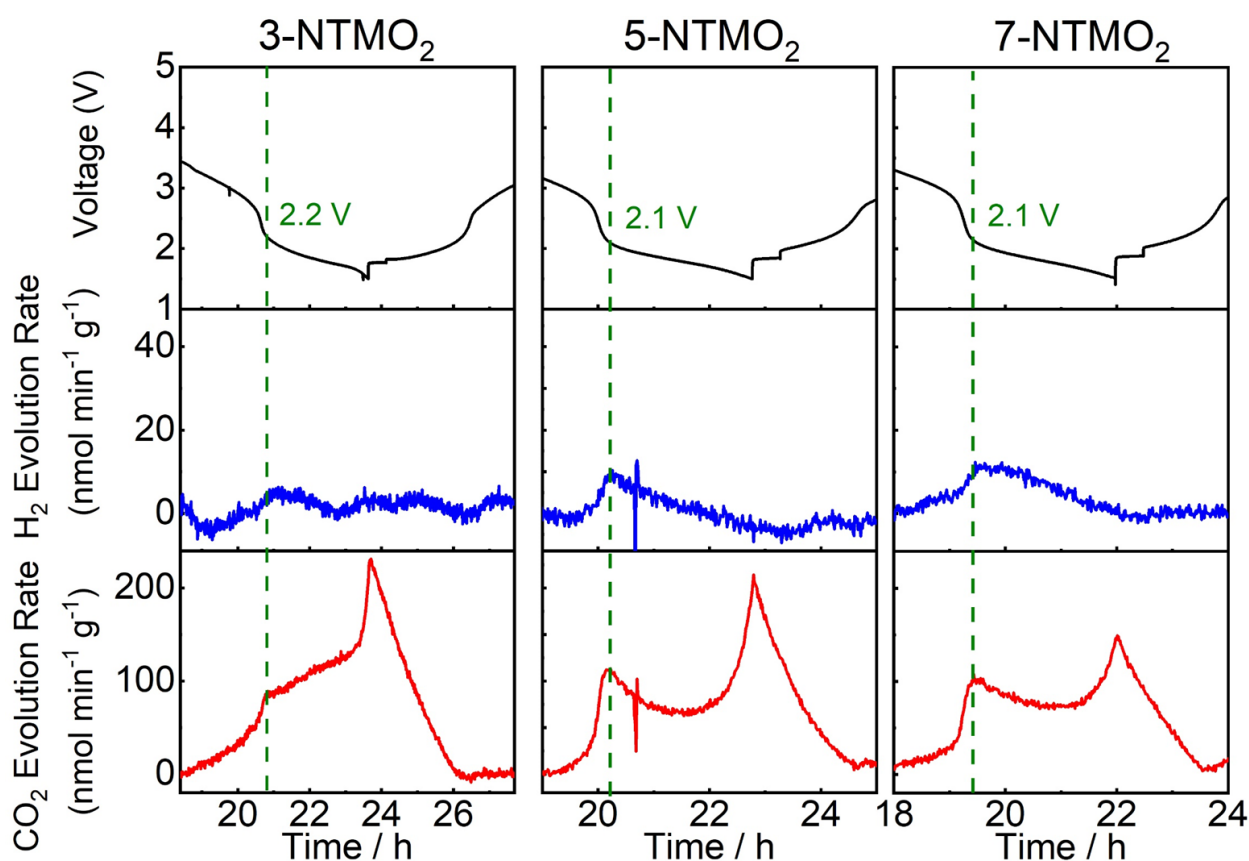


Figure 6.11: Carbon dioxide and hydrogen evolution rate characterized by differential electrochemical mass spectrometry during the first discharging of 3-NTMO₂, 5-NTMO₂ and 7-NTMO₂ cathodes vs. Na metal.

At lower potentials toward the end of discharge (Figure 6.11), additional CO_2 evolution, but almost no H_2 evolution, is observed. Because two peaks are visible, one after the fast voltage drop from 3.0 V to 2.0 V and another at the end of discharge below 1.8 V, two different mechanisms can be assumed. By applying constant voltage steps, the peaks can be deconvoluted. The first peak coincides with the $\text{Mn}^{4+/3+}$ redox reaction and the associated anisotropic volume change and Mn disproportionation. The gas evolution may be attributed to the solid electrolyte interphase (SEI) and cathode-SEI (cSEI) damage caused by Mn^{2+} [261]. Continuous CO_2 evolution is observed at potentials lower 1.7 V vs. Na^+/Na , which can most likely be explained by the reduction of FEC at the cathode side, which has been reported to occur from 1.8 V vs. Li^+/Li under CO_2 evolution [262]. The observation

of increasing steady state currents at the end of each constant voltage step supports an electrochemical reaction pathway, e.g., the FEC reduction.

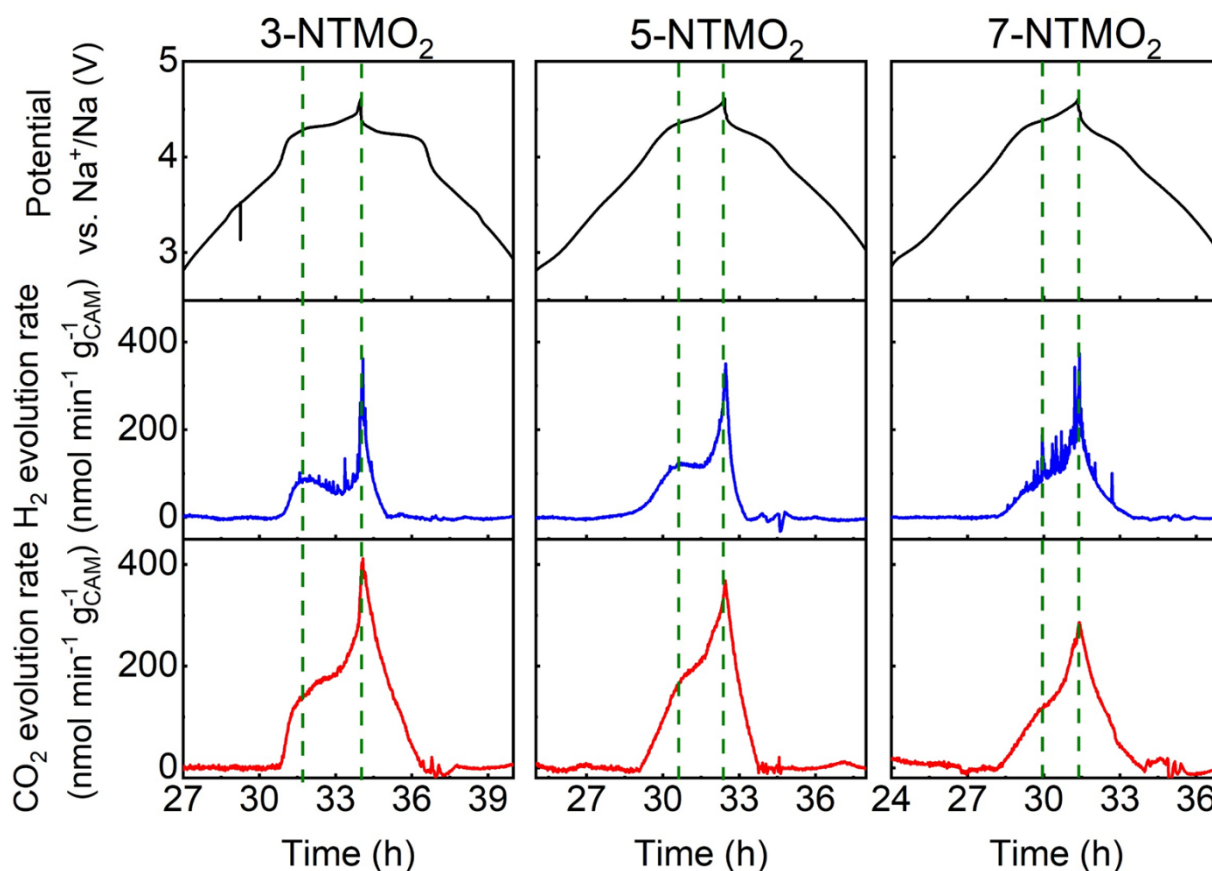


Figure 6.12: Gas evolution characterized by differential electrochemical mass spectrometry during the 2nd cycle.

The gas evolution at higher voltages during the second cycle is highlighted in Figure 6.12. Here, a distinct difference in behavior can be observed for different materials. As the length of the voltage plateau decreases, the gas evolution profiles also change, with 3-NTMO₂ having both the most distinct plateau and gas evolution shoulder. In the dQ/dV plot (Figure 6.10), 3-NTMO₂ is also the only material that still exhibit an irreversible shoulder at 4.3 V in the second cycle. Figure 6.13a shows the carbon dioxide evolution as a function of the voltage and Figure 6.13b shows a comparison of all materials' carbon dioxide evolution during the second charge as a function of the specific charge capacity. However, due to the steep voltage profiles between 3.8 V and 4.2 V, the initial voltage of the gas evolution cannot be determined precisely. Here, an exponential trend is observed according to the LIBs [263]. Previously, it was shown that significant electrochemical oxidation of the electrolyte in LIBs only occurs above 5.0 V vs. Li/Li⁺, corresponding to 4.67 V vs. Na/Na⁺ [239]. From the observed onset of gas evolution already around 4.0 V vs. Na/Na⁺, and the distinct shoulder peak in the H₂ evolution of 3-NTMO₂ (Figure 6.8 and Figure 6.12), it can be concluded that mostly chemical oxidation takes place, caused by the irreversible loss of lattice oxygen [257].

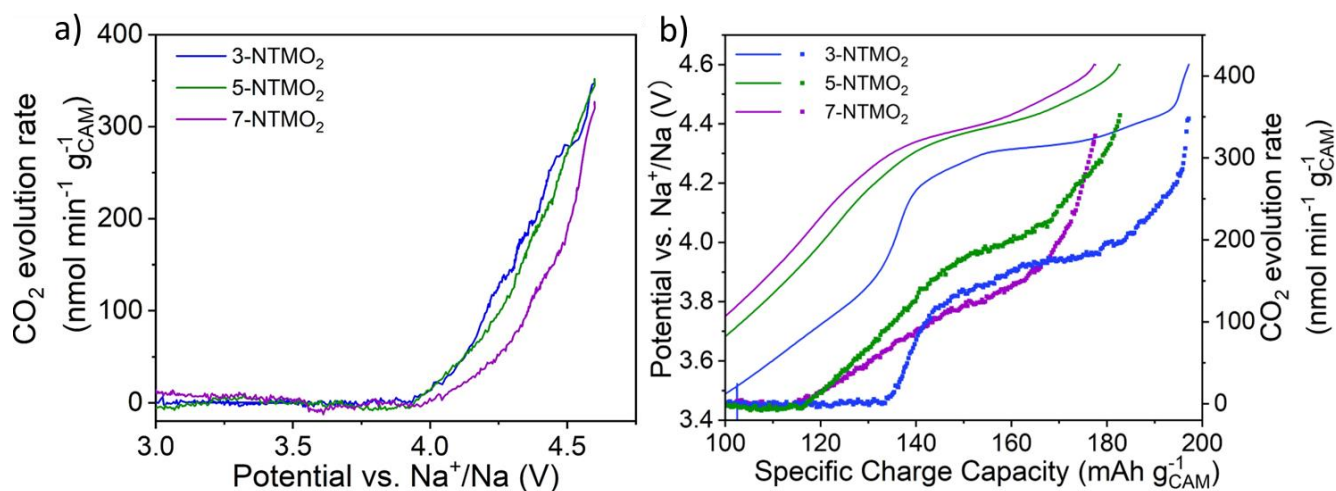


Figure 6.13: (a) Carbon dioxide evolution rate as a function of voltage and (b) Carbon dioxide evolution rates and voltage as a function of charge capacity in the 2nd cycle.

Table 6.3: Summary of obtained DEMS data.

Material	1 st cycle	1 st cycle	2 nd cycle	2 nd cycle	2 nd cycle	1 st cycle	1 st cycle	2 nd cycle	2 nd cycle
	Charge capacity (mAh/g)	Discharge capacity (mAh/g)	Charge capacity (mAh/g)	Discharge capacity (mAh/g)		Coulombic efficiency (%)	total H ₂ (μmol/g)	total CO ₂ (μmol/g)	total H ₂ (μmol/g)
7-NTMO ₂	146	172	178	177	99.4	54	300	26	36
5-NTMO ₂	156	177	183	178	97.3	76	380	27	45
3-NTMO ₂	160	191	197	189	95.9	60	315	20	57

Table 6.3 summarizes the specific capacities and total amounts of gasses released for all three materials. It can be concluded that increased CO₂ evolution due to the enhanced release of lattice oxygen explains, at least in part, the higher irreversible capacity and lower capacity retention during long-term cycling (Figure 6.6e) of 3-NTMO₂ compared to both 5-NTMO₂ and 7-NTMO₂. While the lattice oxygen release depends on the degree of desodiation and thus on the charge capacity, the difference in gas evolution is not observed at the end of charge, but when the plateau is reached around 4.3 V. At the same time, the main charge capacity difference is due to charging at low potentials between 1.5 V and 2.6 V.

In summary, the DEMS analysis shows that the gas evolution behavior changes with the increasing configurational entropy of the cathode materials and that the total amount of gas evolved is reduced. Since the lattice oxygen is the major source of oxygen, increasing in configurational entropy reduces the detrimental release of lattice oxygen, partially explaining the better material performance.

6.2.5. *Ex-situ* XRD

To further understand the structural evolutions upon long-term cycling and verify the superior structural stability of 7-NTMO₂, *ex-situ* XRD was performed for both prior to cycling and after the 50th cycle in the discharged state (Figure 6.14).

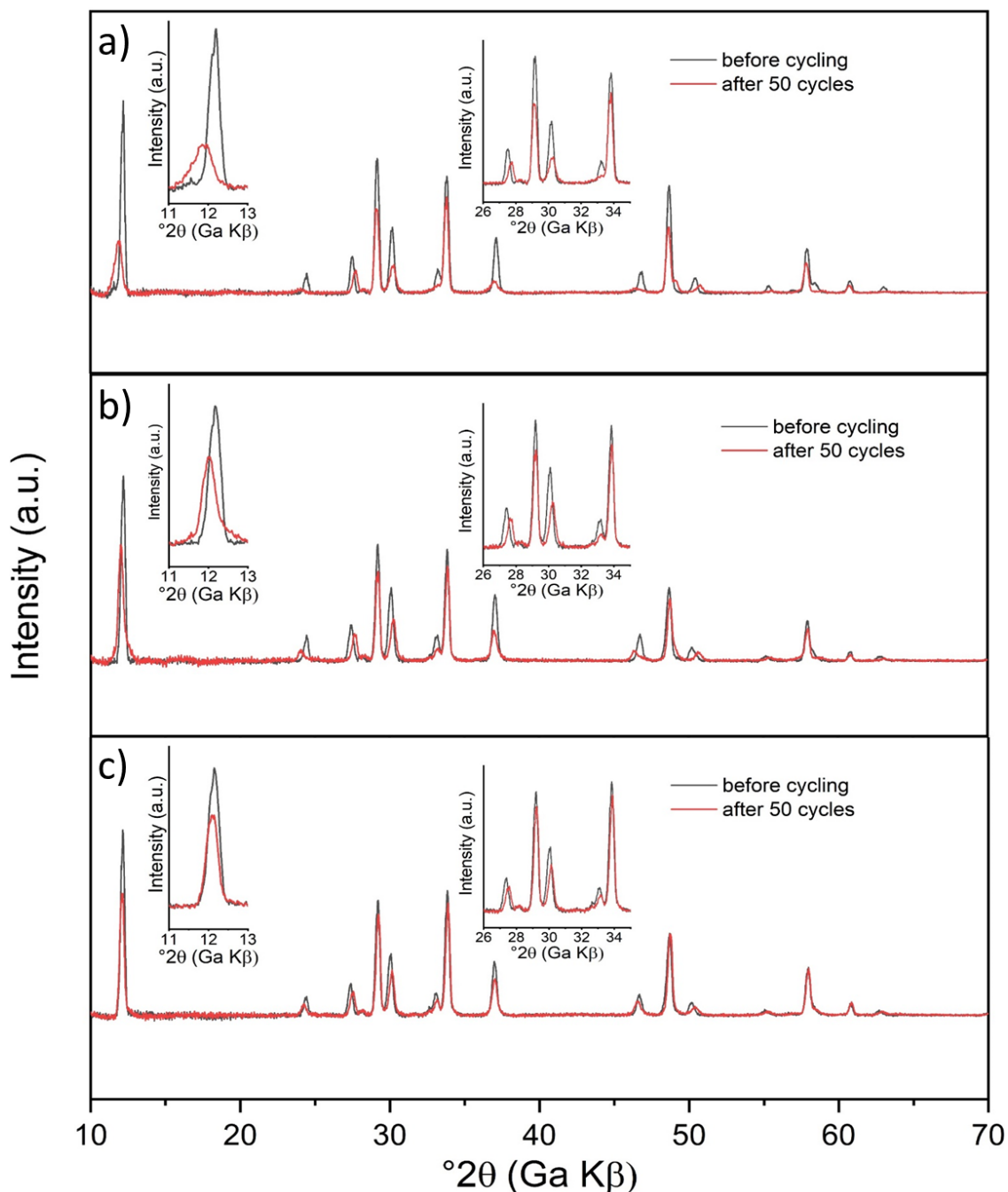


Figure 6.14: *Ex-situ* X-ray diffractograms of (a) 3-NTMO₂, (b) 5-NTMO₂ and (c) 7-NTMO₂ in the pristine and discharged state after 50 cycles, respectively.

The main reflections of all cathode materials can still be assigned to the P2 structures. However, different degrees of degradation are evident from the data. For 3-NTMO₂ (Figure 6.14a), the XRD pattern depicts a large shift of

the (002) and the (004) reflections toward lower angles. The increased *c*-axis lattice parameter suggests that irreversible expansion of the material along the direction perpendicular to the plane of the Na⁺ layers, thus suggesting incomplete sodiation [249, 264]. Note that incomplete sodiation as a result of deteriorated diffusion kinetics could be due to the TM dissolution, leading to a change in chemical environment of the oxygen atoms [264]. The issue of Mn dissolution was investigated by ICP-OES and will be discussed later.

In comparison, the reflection shifts are much less pronounced for 5-NTMO₂ (Figure 6.14b). Particularly, the 7-NTMO₂ electrode (Figure 6.14c) displays the best structural stability over 50 cycles. Moreover, the full-width at half-maximum (FWHM) of the (002) and (004) reflections of 3-NTMO₂ after cycling increased more obviously than for 5-NTMO₂ and 7-NTMO₂. This increase of FWHM indicates a decrease in crystallinity of the material during cycling, which is often associated with the loss of Na⁺ intercalation sites and irreversibility [264, 265].

6.2.6. X-ray Photoelectron Spectroscopy (XPS)

XPS was also employed to analyze and compare the surface chemistry information of the different cathode materials. Figure 6.15 shows the Mn 2p spectra for 3-NTMO₂, 5-NTMO₂ and 7-NTMO₂ prior to cycling and after 50 cycles in the discharged state.

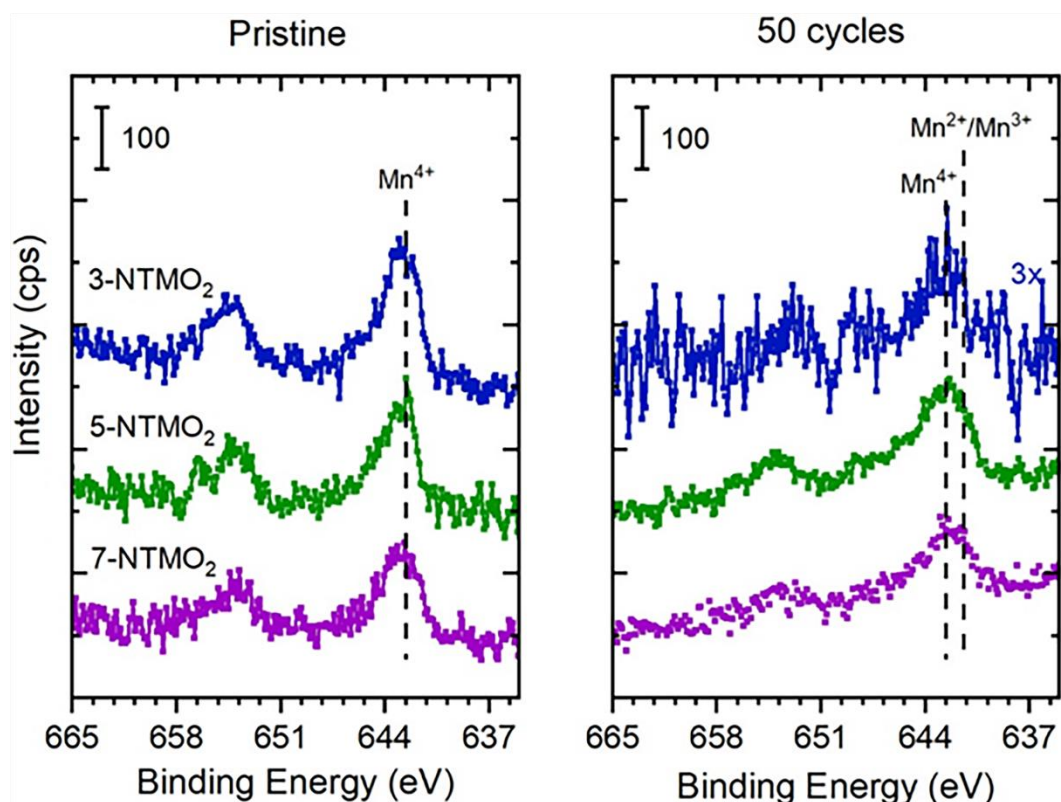


Figure 6.15: X-ray photoelectron spectra in the Mn 2p region measured on the surface of pristine electrodes and after 50 cycles for 3-NTMO₂, 5-NTMO₂ and 7-NTMO₂.

The spectra of the pristine materials show a main peak doublet at 642.6 eV (Mn 2p_{3/2}) and 654.3 eV (Mn 2p_{1/2}), which can be attributed to Mn⁴⁺, consistent with the materials design. The spectra of the cycled electrodes show

a decrease in peak intensity for all three samples, which is most pronounced for 3-NTMO₂. For the Mn 2p spectra after cycling, a broadening of the features to lower binding energy is apparent, which points to the existence of lower-valence Mn ions (i.e., Mn³⁺/Mn²⁺). The broadening is most significant for 3-NTMO₂ while it is less pronounced for 5-NTMO₂ and 7-NTMO₂. In general, a lower Mn³⁺ content leads to a lower level of Mn dissolution and improvement in cycling stability. The existence of Mn³⁺ in the cathode is the main reason for Mn dissolution and associated loss of active material [231]. It has been confirmed that these phase transitions are irreversible, and undoubtedly, they would be the main contributor to the fast capacity fading. In the next step, the change of the Mn oxidation state and its dissolution into electrolyte was further investigated and the results of this study are discussed in the following part.

6.2.7. X-ray Absorption Spectroscopy (XAS) and Inductively Coupled Plasma- Optical Emission Spectrometry (ICP-OES)

As discussed above, the Mnⁿ⁺ redox for the larger voltage window (up to 1.5V) results in unfavorable Mn dissolution, and therefore, to a decrease in capacity. In order to gain more information about the changes in oxidation state of Mn during cycling, XAS was performed in transmission mode for all three cathode materials. It is expected that the overall Mn oxidation state is reduced during the dissolution process. The XANES region of the collected Mn *K*-edge normalized spectra are shown in Figure 6.16. Figure 6.16a-c depict the spectra at OCV prior to cycling and after the initial cycle in the first discharged state for electrodes with 3-NTMO₂, 5-NTMO₂ and 7-NTMO₂, respectively. The insets display the first derivative of the spectra in order to highlight the shift in the oxidation state of Mn ions. A clear shift of the Mn edge to lower energy can be observed for 3-NTMO₂ (inset in Figure 6.16a), showing the overall decrease in Mn ions oxidation state compared to the pristine state. Contrastingly, there is no perceptible change in the XANES spectra of 7-NTMO₂, as can be seen from the nearly overlapping plots of the first derivative of the Mn edge.

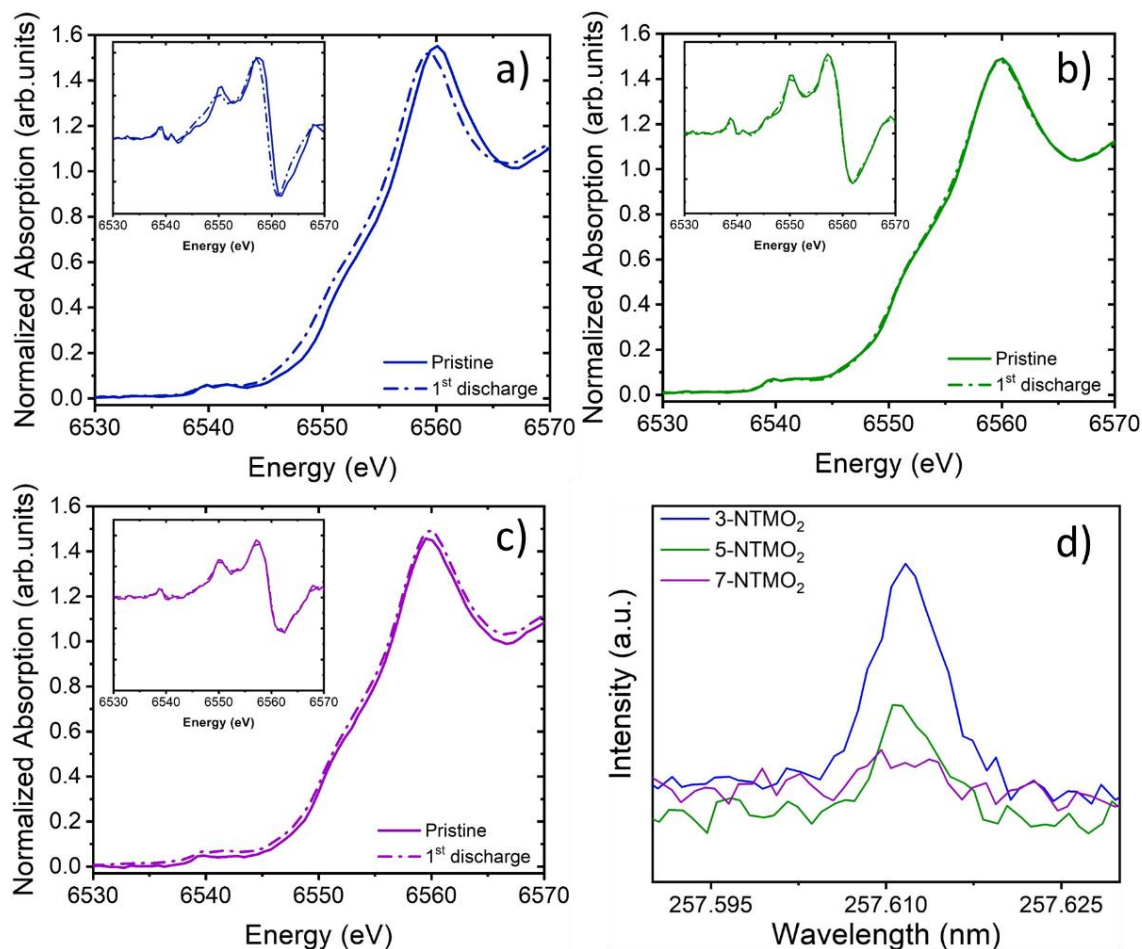


Figure 6.16: X-ray absorption spectra collected at the Mn K-edge at open circuit voltage before cycling and at the first discharged state for (a) 3-NTMO₂, (b) 5-NTMO₂ and (c) 7-NTMO₂. The insets show the first derivative of the spectra. (d) Comparison of dissolution of Mn ions in electrolyte characterized by ICP-OES.

To quantitatively investigate the degrees of Mn dissolution, ICP-OES was used to quantitatively investigate the degree of Mn dissolution into the electrolyte. After 50 cycles between 1.5 V and 4.6 V, the electrolyte was collected from the coin cells. The results in Figure 6.16d demonstrates that the amount of dissolution of Mn progressively decreases progressively from 3-NTMO₂ to 7-NTMO₂, i.e., with increasing configurational entropy. It is worth noting that the ICP-OES results are consistent with the XPS analysis of the final oxidation state of Mn after 50 cycles. Hence, it is likely that the stronger Mn dissolution is a contributing factor to the poor cycling stability of 3-NTMO₂. In addition, these results confirm that 7-NTMO₂ with the highest configurational entropy shows much improved structural stability.

6.3. Conclusion

Three different layered P2-type oxides, defined as low, medium and high entropy oxides, were successfully designed, synthesized via a solid-state method, and investigated as cathode materials for SIBs. The high entropy 7-NTMO₂ shows superior reversibility during sodiation/desodiation in both potential windows of 2.6-4.6 V and 1.5-4.6 V. In contrast, a fast capacity fading was observed in case of low entropy 3-NTMO₂ and a moderate decay

for the medium entropy 5-NTMO₂. By using a combination of *operando* XRD and *ex-situ* XRD, it is found that all materials tend to undergo a solid-solution reaction after several cycles, accompanied by a weakening of the phase transition reaction. The high configurational entropy is beneficial to alleviate the phase transition and maintain the structural stability. Furthermore, DEMS analysis reveals a decrease in gas release with an increase in configurational entropy. At the same time, the disproportionation reaction of Mn³⁺ at low potentials, leading to the formation of soluble Mn²⁺, is suppressed in 7-NTMO₂, as proven by means of XPS and XAS measurements and confirmed by ICP-OES characterization of electrolytes in cycled cells. The contributions of the high entropy effect to improve electrochemical performance has attracted increasing attention. Here further compelling and encouraging evidence is provided for demonstrating the potential of high entropy materials for electrochemical energy storage applications.

Chapter 7

7. Conclusions and Outlook

HEMs as a new class of materials have attracted a lot of attentions in recent years due to their application potential in energy storage systems. Exploring the performance and mechanism of their high entropy properties in electrochemical behavior is and will continue to be an important topic in the future. This thesis aims to explore the application of HEMs as promising cathode materials in LIBs/SIBs. It not only includes the investigation of charge compensation of HEOs that accompanied the phase transition process, but also provides new development strategies for layered cathode materials.

In Chapter 4, the Cocktail effect of HEMs that precise tuning of material compositions to control and edit the structure of materials and the oxidation states of elements is illustrated. In this work, three different HEOs, initially in the form of as spinel structures, were designed and synthesized with the NSP method by adjusting the compositions stepwise. The phase transformation of spinel to rock-salt and the change in oxidation states of monovalent Li ions incorporated elements during synthesis were analyzed by XRD and XPS measurements. As confirmed and calculated by EDX in STEM mode and ICP-OES results of the exemplified samples, all elements are uniformly distributed in particles and the stoichiometries of those are well in consistent with the design conditions. In addition, charge compensation was found to be associated with complete or partial oxidation of some elements. When oxidation is not possible, the spinel-type HEOs will transform into a rock-salt phase with lower average charge. Therefore, this transition can be tailored to some extent by replacing the multivalent elements present in the lattice, such as $\text{Co}^{2+/3+}$ to Mg^{2+} and $\text{Cr}^{3+/6+}$ to Zn^{2+} . In addition, cyclic voltammetry experiments with HEO-1 revealed the increasing electrochemical activity with increasing Li content, which suggests the lithiated rock-salt HEOs are worth to be further studied in their performance as anode and cathode materials for LIBs. Overall, the tailorable properties of HEMs are emphasized in this section that various combinations and substitutions of different individual elements extend the phase space of materials to a tremendous number of possible compositions. It offers new ideas to study and develop many other materials with the same design principles as well.

The concept of high entropy has also been applied to another type of cathode materials. In Chapter 5, a new class of layered HEOs has been synthesized and used as cathode materials in LIBs. Similar to Chapter 4, the incorporated elements were designed as equimolar and were uniformly distributed on the nanometer and micrometer levels which were also confirmed by EDX analysis. The electrochemical behavior of reversible lithiation/delithiation was demonstrated, but the specific capacities achieved were relatively low. Although the contributions of entropy stabilization towards electrochemical properties could not be well demonstrated, the strategy of introducing the concept of high entropy into layered cathode materials may still be a promising way to find new materials.

Inspired by the experience of applying the concept of high entropy in layered HEOs as cathode materials for LIBs, an attempt was also made to introduce the high entropy strategy in layered P2 type materials used for SIBs. In Chapter 6, three different P2-type layered oxides defined as low, medium and high entropy oxides were designed, synthesized by a solid-state method and investigated as cathode materials. The 7-NTMO₂ shows improved reversibility during the sodiation/desodiation processes in both potential windows of 2.6-4.6 V and 1.5-4.6 V. In contrast, a rapid decrease in capacity in the case of 3-NTMO₂ and a weaker degradation trend in 5-NTMO₂ were observed. Studying by using a combination of *operando* XRD and *ex-situ* XRD, it was found that the materials tend to undergo a solid-solution reaction after several rounds of cycling, which is accompanied by the weakening in the degree of phase transition reaction. The high configurational entropy is beneficial to mitigate the phase transition and maintain structural stability. Additionally, DEMS analysis shows that an increase in configurational entropy reduces the gas release, thus partially explains the better electrochemical performance of 7-NTMO₂. At the same time, the disproportioning of Mn³⁺ at low potentials, leading to the formation of soluble Mn²⁺, is suppressed in 7-NTMO₂, as proven by means of XPS and XAS measurements and confirmed by ICP-OES characterization of electrolytes for quantification of Mn dissolution.

The concept of HEMs and the contribution of the high entropy effect to electrochemical performance have been reported in numerous publications; this work provides more solid and convincing evidence to support these views. In addition, this work provides new insights for new classes of materials and confidence in the application of high-entropy materials for energy storage systems. Given the broad range of applications for many different types of materials and the advantages that arise from the high entropy approach (e.g., versatility in composition), HEMs could pave the way for new strategies for highly reversible and stable next-generation battery systems.

A. Acknowledgements

First of all, I would like to express my sincere gratitude to Prof. Dr.-Ing. Horst Hahn giving me the chance to join his group. This international group provides the best conditions for research, a strong academic atmosphere and platforms to present each individual themselves. I got great improvement in instrument operation, problem-solving and oral presentation skills and learned a lot of knowledge about energy storage devices and materials science in this group. In addition, I also have fond memories of the good relations between colleagues, the spontaneous sharing of desserts, the BBQ to see colleagues off and the whole INT outing and hiking activities.

Dr. Ben Breitung, as the main supervisor to my PhD work, provided very often and effective communications and discussions with me regarding different problems during my whole PhD study. I cannot imagine how can I finish this work without his help and suggestions. He is not only a supervisor but also a friend who was always able to offer a new perspective that opens my mind and guide me in a new direction when I was confused. Not only in terms of research works, but the most important is that his positive and pleasant attitudes towards life and getting along with others has profoundly influenced my attitude towards my future career blueprint.

I also would like to thank Dr. Qingsong Wang, who introduced me to join this battery group and provided a lot of supports in daily life and my whole PhD research works. With his help and close working together, I got fast and great improvement during the first year of my PhD. Especially, I would like to express my gratitude for his great help in manuscript organization and revision for Chapter 4.

Furthermore, I would like to appreciate several co-workers, colleagues and friends during the past three years. Kai Wang, Ziming Ding and Xiaohui Huang contributed the whole cooperation works of TEM measurements in this thesis. Dr. Abhishek Sarkar and Dr. Simon Schweidler always gave suggestions and comments on XRD measurement and analysis patiently. Additionally, I also thank Dr. Raheleh Azmi, Dr. Guruprakash Karkera, Dr. Ahmad Omard, Dr. Thomas Diemant and Sören Lukas Dreyer for performing XPS, XAS, DEMS measurements and deep discussions for this thesis. Moreover, Dr. Parvathy Anitha Sukkurji, Dr. Yanjiao Ma, Ruby Singh, David Stenzel, Ibrahim Issac and Yanyan Cui shall be appreciated as they shared a lot of experimental experience and skills in instruments using and synthesis processes, even though some of them have left the group.

I would like to thank my supervisor during my MSc, Professor Haining Zhang, for his great support in the development of my laboratory skills, academic logic and study abroad during my MSc. I also thank my home country China and the Chinese Scholarship Council (CSC) for the valuable opportunity to study abroad and financial support.

For my parents, my father is a truck driver and my mother accompanies him on his travels all the time. Before going to university, although they didn't have enough time or the ability to support me educationally, I remember that they would always bring me local specialties after returning from a trip and support me financially on my trips, which show me how rich and colorful the world is from afar. Eleven and a half years have passed since I left my parents after high school to pursue my studies far away from home, subsequently came to a foreign country and now I have graduated with my PhD, I am really grateful to my parents for their support in all the decisions I have made. Although they were ordinary and not highly educated, their work experience in different locations

made them the best educators for me in terms of their quest to expand horizons and highly intelligent way of dealing with people.

In addition, I would like to thank all my relatives and friends who have expressed their concern and support for me. But the thing I regret the most is that I cannot get to see my grandmother one last time as I was far away, I will always remember the scene when I shared chocolate with her before I left the home country.

Last but not least, I would like to thank my girlfriend, now wife-to-be, for being with me for 11 years, for sharing happy time and staying with me when I was down, and for being able to say yes to my proposal during my PhD research, which made my life so much richer. Past is not involved, the rest of the life please enlighten.

B. List of Abbreviations and Symbols

BSE	Backscattered electron
CE	Coulombic efficiency
CGHE	Carrier gas hot extraction
cSEI	Cathode solid electrolyte interphase
CV	Cyclic voltammetry
DD-DI	Doubly-distilled deionized
DEMS	Differential electrochemical mass spectrometry
DFT	Density functional theory
DMC	Dimethyl carbonate
EBS	Diffacted backscattered electron
EC	Ethylene carbonate
EDX	Energy-dispersive X-ray spectroscopy
EMC	Methyl ethyl carbonate
FEC	Fluoroethylene carbonate
FEI	Field electron and ion company
F-HEO	Fluorite-based High entropy oxide
FTIR	Fourier-transform infrared spectroscopy
FWHM	Full-width at half-maximum
GF/C	Glass microfiber filter pape
HEA	High entropy alloy
HEM	High entropy material
HEO	High entropy oxide
HR-TEM	High-resolution Transmission Electron Microscope
ICP	Inductively Coupled Plasma
ICP-OES	Inductively Coupled Plasma-Optical Emission Spectroscopy
LA	Lead-acid
LCO	Lithium cobalt oxide, LiCoO_2
LHEOF	High entropy Li-containing oxyfluoride
LIB	Lithium-ion battery
LLZO	Lithium lanthanum zirconium oxide
LMO	Lithium manganese oxide, LiMnO_2
LNO	Lithium nickel oxide, LiNiO_2
M	Metal
MEO	Medium entropy oxide
MFC	Mass flow controller

MPV	Midpoint voltage
NCM	Lithium nickel cobalt manganese oxide, $\text{LiNi}_{1-x-y}\text{Co}_y\text{Mn}_x\text{O}_2$
Ni-MH	Nickel-Metal Hydride
NMP	N-methyl-2-pyrrolidone
NSP	Nebulized spray pyrolysis
OCV	Open circuit voltage
PC	Propylene carbonate
PC	Propylene carbonate
PE	Polyethylene
PE-HEO	Perovskite-based HEO
PP	Polypropylene
PVDF	Polyvinylidene difluoride binder
PXRD	Powder X-ray diffraction
R-HEO	Rock-salt structure HEO
R_{wp}	Weighted profile R-factor
SAED	Selected-area electron diffraction
S_{config}	Configurational entropy
SE	Secondary electron
SEI	Solid electrolyte interphase
SEM	Scanning electron microscopy
SIB	Sodium-ion battery
SP-HEO	Spinel-based HEO
STEM	Scanning transmission electron microscopy
TEM	Transmission Electron Microscope
TMO	Transition metal oxide
V_{cell}	Unit-cell volume
XANES	X-ray absorption near edge structure
XAS	X-ray absorption spectroscopy
XPS	X-ray photoelectron spectroscopy
XRD	X-ray diffraction

C. List of Figures

Figure 1.1: Comparison of the manufacturing costs for LIBs and Na-ion batteries SIBs.	2
Figure 2.1: Schematic of (a) coin-type, (b) cylindrical-type, (c) prismatic-type, (d) pouch-type batteries.	4
Figure 2.2: Schematic view of the principle of operation of a lithium-ion cell.	5
Figure 2.3: Crystal structure of layered LiMO_2	6
Figure 2.4: Jahn-Teller distortion correlated with orbital ordering in LiMnO_2 . (a) Crystal structures of layered and spinel LiMnO_2 . (b) Splitting of the e_g levels of d orbitals in an octahedral environment because of Jahn-Teller distortion. (c) Cooperative Jahn-Teller distortion with collinear orbital ordering. (d) Alleviated Jahn-Teller distortion with interfacial orthogonal orbital ordering.	9
Figure 2.5: Chronological evolution of the layered oxide.	12
Figure 2.6: Discharge capacity in different layered oxides.	12
Figure 2.7: Classification of Na-Me-O layered materials with sheets of edge-sharing MeO_6 octahedra and phase transition processes induced by sodium extraction.	14
Figure 2.8: Suppression of Mn-O bond length in the Z axis by Fe substitution.	15
Figure 2.9: In situ XRD patterns collected during the first charge/discharge process of the (a) $\text{Na}_{0.67}\text{Ni}_{0.3}\text{Mn}_{0.7}\text{O}_2$ and (b) $\text{Na}_{0.67}\text{Ni}_{0.1}\text{Cu}_{0.2}\text{Mn}_{0.7}\text{O}_2$ electrodes between 2.0 and 4.5 V under a current rate of 0.1 C.	16
Figure 2.10: Crystal structure of $\text{Na}_2\text{Mn}_3\text{O}_7$. O coordinated by two Mn is labeled as O1, whereas O coordinated by three Mn is labeled as O2. Mn vacancies exist in the Mn layers.....	17
Figure 2.11: (a) dependence of configurational entropy on the number of elements, (b) XRD patterns of different types of R-MEOs and (c) reversible phase transformation as an indication of entropy stabilization effect.....	22
Figure 2.12: Lattice parameters for a series of compounds in the $(\text{Mg,Co,Ni,Cu,Zn})_{1-x}\text{Li}_x\text{O}$ family.....	25
Figure 2.13: XRD patterns of HEO systems: (a) R-HEO, (b) F-HEO and (c) PE-HEOs.	26
Figure 2.14: (a) long-term cycling stability of the calcined HEO at 200 mA g^{-1} together with the corresponding coulombic efficiency, (b) comparison of the different medium and high entropy oxides under investigation, (c) Coulombic efficiency vs. cycle number for all the tested electrode materials at 50 mA g^{-1}	28
Figure 3.1: Illustration of X-ray diffraction defined by Bragg's law.....	31
Figure 3.2: Nebulized spray pyrolysis experimental setup.....	37
Figure 4.1: PXRD patterns of (a) HEO-1, (b) HEO-2, and (c) HEO-3 with different Li contents. Transition from spinel to rock-salt phase occurs with increasing lithium concentration.	42
Figure 4.2: ICP-OES of HEO-1 with different Li contents. All numbers are given in units of at.%. Increasing M:O ratio indicates transition from spinel to rock-salt phase. Excess oxygen is due to Li_2CO_3 formation. ICP-OES data for HEO-2 follow the same trend, but show the highest M:O ratios for lower Li contents (Table 4.1).	43
Figure 4.3: XPS spectra of (a) Co for HEO-1, (b) Mg for HEO-2, (c) Ni for HEO-1, (d) Cr, (e) Fe and (f) Mn for HEO-1 and HEO-2 in the non-lithiated ($x = 0$) and lithiated states ($x = 1$).	45

Figure 4.4: XPS spectra of the (a) O 1s, (b) C 1s, (c) Li 1s, (d) Ni 2p, (e) Zn 2p, (f) Zn LMM, and (g) Mg 1s core level regions for HEO-1 (with x = 0 and 1), HEO-2 (with x = 0 and 1), and HEO-3 (with x = 0.4).	46
Figure 4.5: TEM micrographs at different magnifications of HEO-1 (a) and (b) in the non-lithiated (x = 0) and c) and d) lithiated states (x = 1).	48
Figure 4.6: STEM-EDX mapping of HEO-1 in the non-lithiated (x = 0) and lithiated states (x = 1).	48
Figure 4.7: Cyclic voltammograms for HEO-1 with different Li contents in the voltage range of (a) 0.1-3.0 V and (b) 2.0-4.5 V versus Li ⁺ /Li. Note that only the initial cycle is shown for clarity. (c) The 5th to 12th cycles of HEO-1 (with x = 1) in the voltage range of 2.0-4.5 V versus Li ⁺ /Li.	50
Figure 4.8: Structural changes during lithiation/delithiation of HEO-1 (with x = 1). a) Representative cyclic voltammogram and b) PXRD patterns obtained at different lithiation/delithiation states.....	50
Figure 5.1: (a) XRD patterns for the different compounds, with secondary phases denoted by asterisks and number signs. (b) Crystal structure of α -NaFeO ₂ . Green spheres represent lithium, red spheres oxygen and multi-colored spheres the positions of the statistically distributed metal cations. (c) Lattice parameters from Rietveld refinement analysis (color scheme as in panel a).	54
Figure 5.2: SEM micrographs of (a) Li(NiCoMn) ₁ O ₂ , (b) Li(NiCoMnAl) ₁ O ₂ , (c) Li(NiCoMnAlZn) ₁ O ₂ , (d) Li(NiCoMnAlFe) ₁ O ₂ and (e) LiNa(NiCoMnAlFe) ₁ O ₂	56
Figure 5.3: TEM of (a) Li(NiCoMnAlZn) ₁ O ₂ , (b) Li(NiCoMnAlFe) ₁ O ₂ and (c) LiNa(NiCoMnAlFe) ₁ O ₂ . The HR-TEM micrographs emphasize the high degree of crystallinity and the SAED patterns corroborate the XRD results. d) High-resolution EDX mapping of LiNa(NiCoMnAlFe) ₁ O ₂ . (e) HR-TEM and (f) SAED measurements of Li(NiCoMnAlZn) ₁ O ₂ , indicating the presence of a distorted ZnAl ₂ O ₄ -type spinel structure.....	57
Figure 5.4: (a) Elemental heat maps of a μ m-sized agglomerate and (b) Mössbauer spectroscopy of LiNa(NiCoMnAlFe) ₁ O ₂	58
Figure 5.5: XPS of Li(NiCoMnAlFe) ₁ O ₂ and LiNa(NiCoMnAlFe) ₁ O ₂ . The (a) Ni, (b) Co, (c) Mn, (d) Fe and (e) detailed spectra are shown.....	59
Figure 5.6: Cyclic voltammetry and charge/discharge profiles of as prepared (a) Li(NiCoMn) ₁ O ₂ , (b) Li(NiCoMnAlZn) ₁ O ₂ , (c) Li(NiCoMnAlFe) ₁ O ₂ and (d) LiNa(NiCoMnAlFe) ₁ O ₂ . (e) Specific discharge capacity of LiNa(NiCoMnAlFe) ₁ O ₂ , Li(NiCoMnAlZn) ₁ O ₂ and Li(NiCoMnAlFe) ₁ O ₂ from galvanostatic cycling experiments.....	61
Figure 5.7: XRD patterns of (a) Li(NiCoMnAlZn) ₁ O ₂ , (b) Li(NiCoMnAlFe) ₁ O ₂ and (c) LiNa(NiCoMnAlFe) ₁ O ₂ recorded before and after electrochemical cycling.	62
Figure 6.1: X-ray diffraction patterns and Rietveld refinements of the as-prepared (a) 3-NTMO ₂ , (b) 5-NTMO ₂ and (c) 7-NTMO ₂ powders. The experimental (calculated) data and the residual discrepancy is shown in black (red) and blue, respectively.	67
Figure 6.2: Results of the morphological analysis of 7-NTMO ₂ . (a) SEM image, (b) STEM, (c) SAED along the direction of [100] and (d) High-resolution EDX mapping.	69

Figure 6.3: (a) and (b) SEM images, (c) and (d) SAED patterns along the along the direction of [241] and [201], and (e) and (f) the HR-TEM micrograph and high-resolution EDX mapping for 3-TNMO ₂ and 5-TNMO ₂ , respectively.....	70
Figure 6.4: Cyclic voltammograms of (a) 3-NTMO ₂ , (b) 5-NTMO ₂ and (c) 7-NTMO ₂ at a scan rate of 0.1 mV s ⁻¹ in the voltage range of 1.5-4.6 V.....	71
Figure 6.5: Charge-discharge curves of (a) 3-NTMO ₂ , (b) 5-NTMO ₂ and (c) 7-NTMO ₂ . (d) Comparison of discharge energy at the 1 st , 2 nd and 50 th cycle. (e) Cycling performance and capacity retention at 0.5 C for 50 cycles. All tests are operated at potential window of 2.5-4.6V at 0.5C at room temperature.	73
Figure 6.6: Charge–discharge curves of (a) 3-NTMO ₂ , (b) 5-NTMO ₂ and (c) 7-NTMO ₂ . (d) Comparison of discharge energy at the1 st , 2 nd and 50 th cycle. (e) Cycling performance and capacity retention at 0.5 C for 50 cycles. All tests are operated at potential window of 1.5-4.6V at 0.5C at room temperature.	74
Figure 6.7: <i>Operando</i> XRD contour maps of the initial two complete cycles for electrodes with (a) 3-NTMO ₂ , (b) 5-NTMO ₂ and (c) 7-NTMO ₂ . The corresponding charge-discharge profiles are shown on the left side.	77
Figure 6.8: Carbon dioxide and hydrogen evolution rate characterized by differential electrochemical mass spectrometry during the first cycle of 3-NTMO ₂ , 5-NTMO ₂ and 7-NTMO ₂ cathodes vs. Na metal.	79
Figure 6.9: Fourier transform infrared spectra of as prepared 3-NTMO ₂ , 5-NTMO ₂ and 7-NTMO ₂ powder samples.	80
Figure 6.10: Differential capacity vs. potential (dQ/dV) curves for the first two cycles of (a) 3-NTMO ₂ , (b) 5-NTMO ₂ and (c) 7-NTMO ₂ . Cells were measured at 0.05C at room temperature.....	80
Figure 6.11: Carbon dioxide and hydrogen evolution rate characterized by differential electrochemical mass spectrometry during the first discharging of 3-NTMO ₂ , 5-NTMO ₂ and 7-NTMO ₂ cathodes vs. Na metal.	81
Figure 6.12: Gas evolution characterized by differential electrochemical mass spectrometry during the 2 nd cycle.	82
Figure 6.13: (a) Carbon dioxide evolution rate as a function of voltage and (b) Carbon dioxide evolution rates and voltage as a function of charge capacity in the 2 nd cycle.	83
Figure 6.14: <i>Ex-situ</i> X-ray diffractograms of (a) 3-NTMO ₂ , (b) 5-NTMO ₂ and (c) 7-NTMO ₂ in the pristine and discharged state after 50 cycles, respectively.....	84
Figure 6.15: X-ray photoelectron spectra in the Mn 2p region measured on the surface of pristine electrodes and after 50 cycles for 3-NTMO ₂ , 5-NTMO ₂ and 7-NTMO ₂	85
Figure 6.16: X-ray absorption spectra collected at the Mn K-edge at open circuit voltage before cycling and at the first discharged state for (a) 3-NTMO ₂ , (b) 5-NTMO ₂ and (c) 7-NTMO ₂ . The insets show the first derivate of the spectra. (d) Comparison of dissolution of Mn ions in electrolyte characterized by ICP-OES.	87

D. List of tables

Table 4.1: Stoichiometry of HEO-1 and HEO-2 with different Li contents from ICP-OES analysis.	44
Table 4.2: Metal oxidation states and the corresponding fractions for HEO-1 and HEO-2 in the non-lithiated ($x = 0$) and lithiated states ($x = 1$) from XPS analysis.	47
Table 5.1: Statistical result of Li/M mixing from Rietveld refinement analysis, the values are given in fractions of 1.	55
Table 5.2: Valence, ionic radius and electronegativity for different elements.	63
Table 6.1: Refinement errors and detailed crystallographic parameters of three samples	68
Table 6.2: Overview of the ICP-OES results of the synthesized materials	68
Table 6.3: Summary of obtained DEMS data.	83

E. References

- [1] A. Demirbas, “Potential applications of renewable energy sources, biomass combustion problems in boiler power systems and combustion related environmental issues,” *Prog. Energy Combust. Sci.*, vol. 31, no. 2, pp. 171–192, 2005.
- [2] J. Chow, R. J. Kopp, and P. R. Portney, “Energy Resources and Global Development,” *Science.*, vol. 302, no. 5650, pp. 1528–1531, 2003.
- [3] P. Duffy, C. Fitzpatrick, T. Conway, and R. P. Lynch, “Energy Sources and Supply Grids - The Growing Need for Storage,” *Royal Society of Chemistry*, vol. 2019-Janua, no. 46, 2019.
- [4] M. Broussely, C. Delmas, C. Poullerie, F. Perton, and J. P. Pe, “Effect of magnesium substitution on the cycling behavior of lithium nickel cobalt oxide,” *J. Power Sources*, vol. 96, pp. 293–302, 2001.
- [5] M. A. Basit, S. Dilshad, R. Badar, and S. M. Sami ur Rehman, “Limitations, challenges, and solution approaches in grid-connected renewable energy systems,” *Int. J. Energy Res.*, vol. 44, no. 6, pp. 4132–4162, 2020.
- [6] X. Li, “A review on energy management, operation control and application methods for grid battery energy storage systems,” *CSEE J. Power Energy Syst.*, vol. PP, no. 99, pp. 1–15, 2019.
- [7] S. Wicki and E. G. Hansen, “Clean energy storage technology in the making: An innovation systems perspective on flywheel energy storage,” *J. Clean. Prod.*, vol. 162, pp. 1118–1134, 2017.
- [8] B. Dunn, H. Kamath, and J. M. Tarascon, “Electrical energy storage for the grid: A battery of choices,” *Science.*, vol. 334, no. 6058, pp. 928–935, 2011.
- [9] T. M. I. Mahlia, T. J. Saktisahdan, A. Jannifar, M. H. Hasan, and H. S. C. Matseelar, “A review of available methods and development on energy storage; Technology update,” *Renew. Sustain. Energy Rev.*, vol. 33, pp. 532–545, 2014.
- [10] M. R. Lukatskaya, B. Dunn, and Y. Gogotsi, “Multidimensional materials and device architectures for future hybrid energy storage,” *Nat. Commun.*, vol. 7, 2016.
- [11] A. Vlad, N. Singh, C. Galande, and P. M. Ajayan, “Design Considerations for Unconventional Electrochemical Energy Storage Architectures,” *Adv. Energy Mater.*, vol. 5, no. 19, 2015.
- [12] J. W. Choi and D. Aurbach, “Promise and reality of post-lithium-ion batteries with high energy densities,” *Nat. Rev. Mater.*, vol. 1, 2016.
- [13] C. Vaalma, D. Buchholz, M. Weil, and S. Passerini, “The demand for lithium-ion batteries (LIBs) has been increasing since their commercialization in 1991 and their widespread use in portable electronics,” *Nat. Rev. Mater.*, vol. 3, p. 18013, 2018.
- [14] H. R. Yao, Y. You, Y. X. Yin, L. J. Wan, and Y. G. Guo, “Rechargeable dual-metal-ion batteries for advanced energy storage,” *Phys. Chem. Chem. Phys.*, vol. 18, no. 14, pp. 9326–9333, 2016.
- [15] Y. You and A. Manthiram, “Progress in High-Voltage Cathode Materials for Rechargeable Sodium-Ion Batteries,” *Adv. Energy Mater.*, vol. 8, no. 2, 2018.

-
- [16] N. Ortiz-Vitoriano, N. E. Drewett, E. Gonzalo, and T. Rojo, "High performance manganese-based layered oxide cathodes: Overcoming the challenges of sodium ion batteries," *Energy Environ. Sci.*, vol. 10, no. 5, pp. 1051–1074, 2017.
- [17] Y. Kim, K. H. Ha, S. M. Oh, and K. T. Lee, "High-capacity anode materials for sodium-ion batteries," *Chem. - A Eur. J.*, vol. 20, no. 38, pp. 11980–11992, 2014.
- [18] T. Chen *et al.*, "Applications of Lithium-Ion Batteries in Grid-Scale Energy Storage Systems," *Trans. Tianjin Univ.*, vol. 26, no. 3, pp. 208–217, 2020.
- [19] M. M. Thackeray and K. Amine, "LiMn₂O₄ spinel and substituted cathodes," *Nat. Energy*, vol. 6, no. 5, p. 566, 2021.
- [20] J. B. Goodenough and K. S. Park, "The Li-ion rechargeable battery: A perspective," *J. Am. Chem. Soc.*, vol. 135, no. 4, pp. 1167–1176, 2013.
- [21] S. T. Myung *et al.*, "Nickel-Rich Layered Cathode Materials for Automotive Lithium-Ion Batteries: Achievements and Perspectives," *ACS Energy Lett.*, vol. 2, no. 1, pp. 196–223, 2017.
- [22] J. R. Croy, M. Balasubramanian, K. G. Gallagher, and A. K. Burrell, "Review of the U.S. Department of Energy's 'deep Dive' Effort to Understand Voltage Fade in Li- and Mn-Rich Cathodes," *Acc. Chem. Res.*, vol. 48, no. 11, pp. 2813–2821, 2015.
- [23] W. Dreyer, J. Jamnik, C. Gohlke, R. Huth, J. Moškon, and M. Gaberšček, "The thermodynamic origin of hysteresis in insertion batteries," *Nat. Mater.*, vol. 9, no. 5, pp. 448–453, 2010.
- [24] P. F. Wang, Y. You, Y. X. Yin, and Y. G. Guo, "Layered Oxide Cathodes for Sodium-Ion Batteries: Phase Transition, Air Stability, and Performance," *Adv. Energy Mater.*, vol. 8, no. 8, 2018.
- [25] S. Chen *et al.*, "Challenges and Perspectives for NASICON-Type Electrode Materials for Advanced Sodium-Ion Batteries," *Adv. Mater.*, vol. 29, no. 48, pp. 1–21, 2017.
- [26] J. Song *et al.*, "Removal of interstitial H₂O in hexacyanometallates for a superior cathode of a sodium-ion battery," *J. Am. Chem. Soc.*, vol. 137, no. 7, pp. 2658–2664, 2015.
- [27] Y. Huang *et al.*, "Electrode Materials of Sodium-Ion Batteries toward Practical Application," *ACS Energy Lett.*, vol. 3, no. 7, pp. 1604–1612, 2018.
- [28] H. Che *et al.*, "Electrolyte design strategies and research progress for room-temperature sodium-ion batteries," *Energy Environ. Sci.*, vol. 10, no. 5, pp. 1075–1101, 2017.
- [29] S. S. Zhang, "A review on the separators of liquid electrolyte Li-ion batteries," *J. Power Sources*, vol. 164, no. 1, pp. 351–364, 2007.
- [30] M. M. Thackeray, C. Wolverton, and E. D. Isaacs, "Electrical energy storage for transportation - Approaching the limits of, and going beyond, lithium-ion batteries," *Energy Environ. Sci.*, vol. 5, no. 7, pp. 7854–7863, 2012.
- [31] K. M. Abraham, "How Comparable Are Sodium-Ion Batteries to Lithium-Ion Counterparts?," *ACS Energy Lett.*, vol. 5, no. 11, pp. 3544–3547, 2020.
- [32] B. Xu, D. Qian, Z. Wang, and Y. S. Meng, "Recent progress in cathode materials research for advanced lithium ion batteries," *Mater. Sci. Eng. R Reports*, vol. 73, no. 5–6, pp. 51–65, 2012.

-
- [33] W. Zhang *et al.*, “Two-Dimensional Layered Oxide Structures Tailored by Self-Assembled Layer Stacking via Interfacial Strain,” *ACS Appl. Mater. Interfaces*, vol. 8, no. 26, pp. 16845–16851, 2016.
- [34] K. Mizushima, P. C. Jones, P. J. Wiseman, and J. B. Goodenough, “ Li_xCoO_2 ($0 < x \leq 1$): A NEW CATHODE MATERIAL FOR BATTERIES OF HIGH ENERGY DENSITY,” *Solid State Ionics*, vol. 3–4, pp. 171–174, 1981.
- [35] Y. Lyu *et al.*, “An Overview on the Advances of LiCoO_2 Cathodes for Lithium-Ion Batteries,” *Adv. Energy Mater.*, vol. 11, no. 2, 2021.
- [36] K. S. Suranat *et al.*, “Structure classification and properties of the layered oxides,” *Neuroscience*, vol. 1, no. 1, pp. iii–vii, 1980.
- [37] A. Liu, J. Li, R. Shunmugasundaram, and J. R. Dahn, “Synthesis of Mg and Mn Doped LiCoO_2 and Effects on High Voltage Cycling,” *J. Electrochem. Soc.*, vol. 164, no. 7, pp. A1655–A1664, 2017.
- [38] Q. Liu *et al.*, “Approaching the capacity limit of lithium cobalt oxide in lithium ion batteries via lanthanum and aluminium doping,” *Nat. Energy*, vol. 3, no. 11, pp. 936–943, 2018.
- [39] B. Hu *et al.*, “Reversible phase transition enabled by binary Ba and Ti-based surface modification for high voltage LiCoO_2 cathode,” *J. Power Sources*, vol. 438, no. August, p. 226954, 2019.
- [40] P. Kalyani and N. Kalaiselvi, “Various aspects of LiNiO_2 chemistry: A review,” *Sci. Technol. Adv. Mater.*, vol. 6, no. 6, pp. 689–703, 2005.
- [41] F. Kong *et al.*, “Kinetic Stability of Bulk LiNiO_2 and Surface Degradation by Oxygen Evolution in LiNiO_2 -Based Cathode Materials,” *Adv. Energy Mater.*, vol. 9, no. 2, 2019.
- [42] A. Gupta, W. D. Chemelewski, C. Buddie Mullins, and J. B. Goodenough, “High-Rate Oxygen Evolution Reaction on Al-Doped LiNiO_2 ,” *Adv. Mater.*, vol. 27, no. 39, pp. 6063–6067, 2015.
- [43] S. Muto *et al.*, “Effect of Mg-doping on the degradation of LiNiO_2 -based cathode materials by combined spectroscopic methods,” *J. Power Sources*, vol. 205, pp. 449–455, 2012.
- [44] P. Mohan and G. P. Kalaigan, “Electrochemical performance of La_2O_3 -coated layered LiNiO_2 cathode materials for rechargeable lithium-ion batteries,” *Ionics*, vol. 19, no. 6, pp. 895–902, 2013.
- [45] M. G. Kim and J. Cho, “Air stable Al_2O_3 -coated Li_2NiO_2 cathode additive as a surplus current consumer in a Li-ion cell,” *J. Mater. Chem.*, vol. 18, no. 48, pp. 5880–5887, 2008.
- [46] X. Zhu *et al.*, “ LiMnO_2 cathode stabilized by interfacial orbital ordering for sustainable lithium-ion batteries,” *Nat. Sustain.*, vol. 4, no. 5, pp. 392–401, 2021.
- [47] F. Schipper, E. M. Erickson, C. Erk, J.-Y. Shin, F. F. Chesneau, and D. Aurbach, “Review—Recent Advances and Remaining Challenges for Lithium Ion Battery Cathodes,” *J. Electrochem. Soc.*, vol. 164, no. 1, pp. A6220–A6228, 2017.
- [48] H. Y. Asl and A. Manthiram, “Reining in dissolved transition-metal ions,” *Science*, vol. 369, no. 6500, pp. 140–141, 2020.
- [49] X. M. Wu, R. X. Li, S. Chen, Z. Q. He, and M. F. Xu, “Comparative study of Co, Cr and Al-doped LiMnO_2 prepared by ion exchange,” *Bull. Mater. Sci.*, vol. 31, no. 2, pp. 109–113, 2008.

-
- [50] Z. Liu, A. Yu, and J. Y. Lee, "Synthesis and characterization of $\text{LiNi}_{1-x-y}\text{Co}_x\text{Mn}_y\text{O}_2$ as the cathode materials of secondary lithium batteries," *J. Power Sources*, vol. 81–82, pp. 416–419, 1999.
- [51] T. Ohzuku and Y. Makimura, "Layered Lithium Insertion Material of $\text{LiCo}_{1/3}\text{Ni}_{1/3}\text{Mn}_{1/3}\text{O}_2$ for Lithium-Ion Batteries," pp. 642–643, 2001.
- [52] J. Kasnatscheew *et al.*, "Learning from Overpotentials in Lithium Ion Batteries: A Case Study on the $\text{LiNi}_{1/3}\text{Co}_{1/3}\text{Mn}_{1/3}\text{O}_2$ (NCM) Cathode," *J. Electrochem. Soc.*, vol. 163, no. 14, pp. A2943–A2950, 2016.
- [53] J. Choi and A. Manthiram, "Role of Chemical and Structural Stabilities on the Electrochemical Properties of Layered $\text{LiNi}_{1/3}\text{Mn}_{1/3}\text{Co}_{1/3}\text{O}_2$ Cathodes," *J. Electrochem. Soc.*, vol. 152, no. 9, p. A1714, 2005.
- [54] J. Li, Y. Xu, X. Li, and Z. Zhang, " Li_2MnO_3 stabilized $\text{LiNi}_{1/3}\text{Co}_{1/3}\text{Mn}_{1/3}\text{O}_2$ cathode with improved performance for lithium ion batteries," *Appl. Surf. Sci.*, vol. 285, no. PARTB, pp. 235–240, 2013.
- [55] Y. H. Ding *et al.*, "Co-precipitation synthesis and electrochemical properties of graphene supported $\text{LiMn}_{1/3}\text{Ni}_{1/3}\text{Co}_{1/3}\text{O}_2$ cathode materials for lithium-ion batteries," *Nanotechnology*, vol. 24, no. 37, 2013.
- [56] X. Zuo, C. Fan, J. Liu, X. Xiao, J. Wu, and J. Nan, "Effect of tris(trimethylsilyl)borate on the high voltage capacity retention of $\text{LiNi}_{0.5}\text{Co}_{0.2}\text{Mn}_{0.3}\text{O}_2$ /graphite cells," *J. Power Sources*, vol. 229, pp. 308–312, 2013.
- [57] K. Numata, C. Sakaki, and S. Yamanaka, "Synthesis and characterization of layer structured solid solutions in the system of LiCoO_2 - Li_2MnO_3 ," *Solid State Ionics*, vol. 117, no. 3–4, pp. 257–263, 1999.
- [58] J. Zheng *et al.*, "Li- and Mn-Rich Cathode Materials: Challenges to Commercialization," *Adv. Energy Mater.*, vol. 7, no. 6, 2017.
- [59] P. Rozier and J. M. Tarascon, "Review—Li-Rich Layered Oxide Cathodes for Next-Generation Li-Ion Batteries: Chances and Challenges," *J. Electrochem. Soc.*, vol. 162, no. 14, pp. A2490–A2499, 2015.
- [60] B. Qiu, M. Zhang, Y. Xia, Z. Liu, and Y. S. Meng, "Understanding and Controlling Anionic Electrochemical Activity in High-Capacity Oxides for Next Generation Li-Ion Batteries," *Chem. Mater.*, vol. 29, no. 3, pp. 908–915, 2017.
- [61] Y. Zhu *et al.*, "Failure mechanism of layered lithium-rich oxide/graphite cell and its solution by using electrolyte additive," *J. Power Sources*, vol. 317, pp. 65–73, 2016.
- [62] Y. Lyu *et al.*, "Recent advances in high energy-density cathode materials for sodium-ion batteries," *Sustain. Mater. Technol.*, vol. 21, pp. 1–21, 2019.
- [63] J. Zhang, W. Wang, W. Wang, S. Wang, and B. Li, "Comprehensive Review of P2-Type $\text{Na}_{2/3}\text{Ni}_{1/3}\text{Mn}_{2/3}\text{O}_2$, a Potential Cathode for Practical Application of Na-Ion Batteries," *ACS Appl. Mater. Interfaces*, 2019.
- [64] C. Zhao, Y. Lu, L. Chen, and Y. S. Hu, "Ni-based cathode materials for Na-ion batteries," *Nano Res.*, vol. 12, no. 9, pp. 2018–2030, 2019.
- [65] T. Hosaka, K. Kubota, A. S. Hameed, and S. Komaba, "Research Development on K-Ion Batteries," *Chem. Rev.*, vol. 120, no. 14, pp. 6358–6466, 2020.
- [66] R. Berthelot, D. Carlier, and C. Delmas, "Electrochemical investigation of the P2- Na_xCoO_2 phase diagram," *Nat. Mater.*, vol. 10, no. 1, pp. 74–80, 2011.
- [67] A. K. Rai, L. T. Anh, J. Gim, V. Mathew, and J. Kim, "Electrochemical properties of Na_xCoO_2 ($x \sim 0.71$) cathode for rechargeable sodium-ion batteries," *Ceram. Int.*, vol. 40, no. 1 PART B, pp. 2411–2417, 2014.

- [68] J. U. Choi, Y. J. Park, J. H. Jo, L. Y. Kuo, P. Kaghazchi, and S. T. Myung, "Unraveling the Role of Earth-Abundant Fe in the Suppression of Jahn-Teller Distortion of P'2-Type $\text{Na}_{2/3}\text{MnO}_2$: Experimental and Theoretical Studies," *ACS Appl. Mater. Interfaces*, vol. 10, no. 48, pp. 40978–40984, 2018.
- [69] J. Y. Hwang, S. T. Myung, J. U. Choi, C. S. Yoon, H. Yashiro, and Y. K. Sun, "Resolving the degradation pathways of the O3-type layered oxide cathode surface through the nano-scale aluminum oxide coating for high-energy density sodium-ion batteries," *J. Mater. Chem. A*, vol. 5, no. 45, pp. 23671–23680, 2017.
- [70] J. Zhang and D. Y. W. Yu, "Stabilizing $\text{Na}_{0.7}\text{MnO}_2$ cathode for Na-ion battery via a single-step surface coating and doping process," *J. Power Sources*, vol. 391, no. February, pp. 106–112, 2018.
- [71] A. Caballero, L. Hernán, J. Morales, L. Sánchez, J. Santos Peña, and M. A. G. Aranda, "Synthesis and characterization of high-temperature hexagonal P2- $\text{Na}_{0.6}\text{MnO}_2$ and its electrochemical behaviour as cathode in sodium cells," *J. Mater. Chem.*, vol. 12, no. 4, pp. 1142–1147, 2002.
- [72] T. R. Chen *et al.*, " Cu^{2+} Dual-Doped Layer-Tunnel Hybrid $\text{Na}_{0.6}\text{Mn}_{1-x}\text{Cu}_x\text{O}_2$ as a Cathode of Sodium-Ion Battery with Enhanced Structure Stability, Electrochemical Property, and Air Stability," *ACS Appl. Mater. Interfaces*, vol. 10, no. 12, pp. 10147–10156, 2018.
- [73] Y. Li *et al.*, "Air-Stable Copper-Based P2- $\text{Na}_{7/9}\text{Cu}_{2/9}\text{Fe}_{1/9}\text{Mn}_{2/3}\text{O}_2$ as a New Positive Electrode Material for Sodium-Ion Batteries," *Adv. Sci.*, vol. 2, no. 6, pp. 1–7, 2015.
- [74] L. Wang *et al.*, "Copper-substituted $\text{Na}_{0.67}\text{Ni}_{0.3-x}\text{Cu}_x\text{Mn}_{0.7}\text{O}_2$ cathode materials for sodium-ion batteries with suppressed P2-O2 phase transition," *J. Mater. Chem. A*, vol. 5, no. 18, pp. 8752–8761, 2017.
- [75] D. Yuan *et al.*, "Synthesis and electrochemical behaviors of layered $\text{Na}_{0.67}[\text{Mn}_{0.65}\text{Co}_{0.2}\text{Ni}_{0.15}]\text{O}_2$ microflakes as a stable cathode material for sodium-ion batteries," *J. Mater. Chem. A*, vol. 1, no. 12, pp. 3895–3899, 2013.
- [76] D. Yuan *et al.*, "P2-type $\text{Na}_{0.67}\text{Mn}_{0.65}\text{Fe}_{0.2}\text{Ni}_{0.15}\text{O}_2$ Cathode Material with High-capacity for Sodium-ion Battery," *Electrochim. Acta*, vol. 116, pp. 300–305, 2014.
- [77] X. Sun *et al.*, " $\text{Na}[\text{Ni}_{0.4}\text{Fe}_{0.2}\text{Mn}_{0.4-x}\text{Ti}_x]\text{O}_2$: A cathode of high capacity and superior cyclability for Na-ion batteries," *J. Mater. Chem. A*, vol. 2, no. 41, pp. 17268–17271, 2014.
- [78] E. De La Llave *et al.*, "Improving Energy Density and Structural Stability of Manganese Oxide Cathodes for Na-Ion Batteries by Structural Lithium Substitution," *Chem. Mater.*, vol. 28, no. 24, pp. 9064–9076, 2016.
- [79] X. Xu *et al.*, "Identifying the Critical Role of Li Substitution in P2- $\text{Na}_x(\text{Li}_y\text{Ni}_x\text{Mn}_{1-y-z})\text{O}_2$ (0 less than x, y, z less than 1) Intercalation Cathode Materials for High Energy Na-ion Batteries," *Chem. Mater.*, vol. 2, 2014.
- [80] C. Li, C. Zhao, B. Hu, W. Tong, M. Shen, and B. Hu, "Unraveling the Critical Role of Ti Substitution in P2- $\text{Na}_x\text{Li}_y\text{Mn}_{1-y}\text{O}_2$ Cathodes for Highly Reversible Oxygen Redox Chemistry," *Chem. Mater.*, vol. 32, no. 3, pp. 1054–1063, 2020.
- [81] B. Mortemard de Boisse *et al.*, "Highly Reversible Oxygen-Redox Chemistry at 4.1 V in $\text{Na}_{4/7-x}[\square_{1/7}\text{Mn}_{6/7}]\text{O}_2$ (\square : Mn Vacancy)," *Adv. Energy Mater.*, vol. 8, no. 20, 2018.
- [82] K. Biswas, "High entropy materials," vol. 113, no. 9. 2017.

-
- [83] A. Lindsay Greer, "Confusion by design," *Nature*, vol. 366, no. 366, pp. 303–304, 1993.
- [84] Y. Zhang, *High-Entropy Materials-A Brief Introduction*, vol. 113, no. 9. 2019.
- [85] B. Cantor, I. T. H. Chang, P. Knight, and A. J. B. Vincent, "Microstructural development in equiatomic multicomponent alloys," *Mater. Sci. Eng. A*, vol. 375–377, no. 1-2 SPEC. ISS., pp. 213–218, 2004.
- [86] B. Cantor, "Multicomponent and high entropy alloys," *Entropy*, vol. 16, no. 9, pp. 4749–4768, 2014.
- [87] J. W. Yeh *et al.*, "Nanostructured high-entropy alloys with multiple principal elements: Novel alloy design concepts and outcomes," *Adv. Eng. Mater.*, vol. 6, no. 5, pp. 299-303+274, 2004.
- [88] J. W. Yeh, "Recent progress in high-entropy alloys," *Ann. Chim. Sci. des Mater.*, vol. 31, no. 6, pp. 633–648, 2006.
- [89] C. Toher, C. Oses, D. Hicks, and S. Curtarolo, "Unavoidable disorder and entropy in multi-component systems," *npj Comput. Mater.*, vol. 5, no. 1, pp. 10–12, 2019.
- [90] Y. Ma *et al.*, "High-entropy energy materials: Challenges and new opportunities," *Energy Environ. Sci.*, vol. 14, no. 5, pp. 2883–2905, 2021.
- [91] M. H. Tsai and J. W. Yeh, "High-entropy alloys: A critical review," *Mater. Res. Lett.*, vol. 2, no. 3, pp. 107–123, 2014.
- [92] J. W. Yeh, Y. L. Chen, S. J. Lin, and S. K. Chen, "High-Entropy Alloys – A New Era of Exploitation," *Mater. Sci. Forum*, vol. 560, pp. 1–9, 2007.
- [93] E. J. Pickering and N. G. Jones, "High-entropy alloys: a critical assessment of their founding principles and future prospects," *Int. Mater. Rev.*, vol. 61, no. 3, pp. 183–202, 2016.
- [94] D. B. Miracle and O. N. Senkov, "A critical review of high entropy alloys and related concepts," *Acta Mater.*, vol. 122, pp. 448–511, 2017.
- [95] C. M. Rost *et al.*, "Entropy-stabilized oxides," *Nat. Commun.*, vol. 6, 2015.
- [96] A. Sarkar *et al.*, "High-Entropy Oxides: Fundamental Aspects and Electrochemical Properties," *Adv. Mater.*, vol. 31, no. 26, 2019.
- [97] A. Sarkar *et al.*, "High entropy oxides for reversible energy storage," *Nat. Commun.*, vol. 9, no. 1, 2018.
- [98] B. S. Murty, J. W. Yeh, and S. Ranganathan, "A Brief History of Alloys and the Birth of High-Entropy Alloys," *High Entropy Alloy.*, no. 2008, pp. 1–12, 2014.
- [99] A. Sarkar *et al.*, "Nanocrystalline multicomponent entropy stabilised transition metal oxides," *J. Eur. Ceram. Soc.*, vol. 37, no. 2, pp. 747–754, 2017.
- [100] A. Mao, F. Quan, H. Z. Xiang, Z. G. Zhang, K. Kuramoto, and A. L. Xia, "Facile synthesis and ferrimagnetic property of spinel (CoCrFeMnNi)₃O₄ high-entropy oxide nanocrystalline powder," *J. Mol. Struct.*, vol. 1194, pp. 11–18, 2019.
- [101] A. Salián and S. Mandal, "Entropy stabilized multicomponent oxides with diverse functionality—a review," *Crit. Rev. Solid State Mater. Sci.*, pp. 1–52, 2021.
- [102] S. Jiang *et al.*, "A new class of high-entropy perovskite oxides," *Scr. Mater.*, vol. 142, pp. 116–120, 2018.
- [103] K. Chen *et al.*, "A five-component entropy-stabilized fluorite oxide," *J. Eur. Ceram. Soc.*, vol. 38, no. 11, pp. 4161–4164, 2018.

-
- [104] J. Dąbrowa *et al.*, “Synthesis and microstructure of the (Co,Cr,Fe,Mn,Ni)₃O₄ high entropy oxide characterized by spinel structure,” *Mater. Lett.*, vol. 216, pp. 32–36, 2018.
- [105] W. Hong, F. Chen, Q. Shen, Y. H. Han, W. G. Fahrenholtz, and L. Zhang, “Microstructural evolution and mechanical properties of (Mg,Co,Ni,Cu,Zn)O high-entropy ceramics,” *J. Am. Ceram. Soc.*, vol. 102.
- [106] H. Chen *et al.*, “Entropy-stabilized metal oxide solid solutions as CO oxidation catalysts with high-temperature stability,” *J. Mater. Chem. A*, vol. 6, no. 24, pp. 11129–11133, 2018.
- [107] J. Zhang, X. Zhang, Y. Li, Q. Du, X. Liu, and X. Qi, “High-entropy oxides 10La₂O₃-20TiO₂-10Nb₂O₅-20WO₃-20ZrO₂ amorphous spheres prepared by containerless solidification,” *Mater. Lett.*, vol. 244, pp. 167–170, 2019.
- [108] D. Bérardan, S. Franger, D. Dragoë, A. K. Meena, and N. Dragoë, “Colossal dielectric constant in high entropy oxides,” *Phys. Status Solidi - Rapid Res. Lett.*, vol. 10, no. 4, pp. 328–333, 2016.
- [109] D. Bérardan, S. Franger, A. K. Meena, and N. Dragoë, “Room temperature lithium superionic conductivity in high entropy oxides,” *J. Mater. Chem. A*, vol. 4, no. 24, pp. 9536–9541, 2016.
- [110] Z. Rak *et al.*, “Charge compensation and electrostatic transferability in three entropy-stabilized oxides: Results from density functional theory calculations,” *J. Appl. Phys.*, vol. 120, no. 9, 2016.
- [111] N. Osenciat *et al.*, “Charge compensation mechanisms in Li-substituted high-entropy oxides and influence on Li superionic conductivity,” *J. Am. Ceram. Soc.*, vol. 102, no. 10, pp. 6156–6162, 2019.
- [112] R. Dedryvère, S. Laruelle, S. Grugeon, P. Poizot, D. Gonbeau, and J. M. Tarascon, “Contribution of X-ray Photoelectron Spectroscopy to the Study of the Electrochemical Reactivity of CoO toward Lithium,” *Chem. Mater.*, vol. 16, no. 6, pp. 1056–1061, 2004.
- [113] M. C. Biesinger, L. W. M. Lau, A. R. Gerson, and R. S. C. Smart, “Resolving surface chemical states in XPS analysis of first row transition metals, oxides and hydroxides: Sc, Ti, V, Cu and Zn,” *Appl. Surf. Sci.*, vol. 257, no. 3, pp. 887–898, 2010.
- [114] J. C. Dupin, D. Gonbeau, P. Vinatier, and A. Levasseur, “Systematic XPS studies of metal oxides, hydroxides and peroxides,” *Phys. Chem. Chem. Phys.*, vol. 2, no. 6, pp. 1319–1324, 2000.
- [115] R. Djenadic *et al.*, “Multicomponent equiatomic rare earth oxides,” *Mater. Res. Lett.*, vol. 5, no. 2, pp. 102–109, 2017.
- [116] Y. Sharma *et al.*, “Single-crystal high entropy perovskite oxide epitaxial films,” *Phys. Rev. Mater.*, vol. 2, no. 6, pp. 1–6, 2018.
- [117] A. Sarkar *et al.*, “Rare earth and transition metal based entropy stabilised perovskite type oxides,” *J. Eur. Ceram. Soc.*, vol. 38, no. 5, pp. 2318–2327, 2018.
- [118] T. X. Nguyen, J. Patra, J. K. Chang, and J. M. Ting, “High entropy spinel oxide nanoparticles for superior lithiation-delithiation performance,” *J. Mater. Chem. A*, vol. 8, no. 36, pp. 18963–18973, 2020.
- [119] A. Amiri and R. Shahbazian-Yassar, “Recent progress of high-entropy materials for energy storage and conversion,” *J. Mater. Chem. A*, vol. 9, no. 2, pp. 782–823, 2021.
- [120] M. Fu, X. Ma, K. Zhao, X. Li, and D. Su, “High-entropy materials for energy-related applications,” *iScience*, vol. 24, no. 3, p. 102177, 2021.

-
- [121] Y. Chen *et al.*, “Opportunities for High-Entropy Materials in Rechargeable Batteries,” *ACS Mater. Lett.*, vol. 3, no. 2, pp. 160–170, 2021.
- [122] X. Guo *et al.*, “Nanostructured graphene-based materials for flexible energy storage,” *Energy Storage Mater.*, vol. 9, no. June, pp. 150–169, 2017.
- [123] C. M. Park, J. H. Kim, H. Kim, and H. J. Sohn, “Li-alloy based anode materials for Li secondary batteries,” *Chem. Soc. Rev.*, vol. 39, no. 8, pp. 3115–3141, 2010.
- [124] C. Ding *et al.*, “A bubble-template approach for assembling Ni-Co oxide hollow microspheres with an enhanced electrochemical performance as an anode for lithium ion batteries,” *Phys. Chem. Chem. Phys.*, vol. 18, no. 37, pp. 25879–25886, 2016.
- [125] P. Poizot, S. Laruelle, S. Grugeon, L. Dupont, and J. Tarascon, “Nano-sized transition-metal oxides,” *Nature*, vol. 407, no. September, 2000.
- [126] Q. Wang *et al.*, “High entropy oxides as anode material for Li-ion battery applications: A practical approach,” *Electrochem. commun.*, vol. 100, no. February, pp. 121–125, 2019.
- [127] H. Chen, N. Qiu, B. Wu, Z. Yang, S. Sun, and Y. Wang, “A new spinel high-entropy oxide ($\text{Mg}_{0.2}\text{Ti}_{0.2}\text{Zn}_{0.2}\text{Cu}_{0.2}\text{Fe}_{0.2}$) $_3\text{O}_4$ with fast reaction kinetics and excellent stability as an anode material for lithium ion batteries,” *RSC Adv.*, vol. 10, no. 16, pp. 9736–9744, 2020.
- [128] J. Yan *et al.*, “A high-entropy perovskite titanate lithium-ion battery anode,” *J. Mater. Sci.*, vol. 55, no. 16, pp. 6942–6951, Jun. 2020.
- [129] Q. Wang *et al.*, “Multi-anionic and -cationic compounds: New high entropy materials for advanced Li-ion batteries,” *Energy Environ. Sci.*, pp. 0–28, 2019.
- [130] C. Zhao, F. Ding, Y. Lu, L. Chen, and Y. S. Hu, “High-Entropy Layered Oxide Cathodes for Sodium-Ion Batteries,” *Angew. Chemie - Int. Ed.*, vol. 59, no. 1, pp. 264–269, 2020.
- [131] L. Yang *et al.*, “Multiprincipal Component $\text{P2-Na}_{0.6}(\text{Ti}_{0.2}\text{Mn}_{0.2}\text{Co}_{0.2}\text{Ni}_{0.2}\text{Ru}_{0.2})\text{O}_2$ as a High-Rate Cathode for Sodium-Ion Batteries,” *JACS Au*, vol. 1, no. 1, pp. 98–107, 2021.
- [132] C. G. Pope, “X-ray diffraction and the bragg equation,” *J. Chem. Educ.*, vol. 74, no. 1, pp. 129–131, 1997.
- [133] N. Pienack and W. Bensch, “In-situ-Verfolgung der Bildung kristalliner Feststoffe,” *Angew. Chemie*, vol. 123, no. 9, pp. 2062–2083, 2011.
- [134] X. Wei, X. Wang, Q. An, C. Han, and L. Mai, “Operando X-ray Diffraction Characterization for Understanding the Intrinsic Electrochemical Mechanism in Rechargeable Battery Materials,” *Small Methods*, vol. 1, no. 5, pp. 1–13, 2017.
- [135] W. Zhou, R. Apkarian, Z. L. Wang, and D. Joy, “Fundamentals of scanning electron microscopy (SEM),” *Scanning Microsc. Nanotechnol. Tech. Appl.*, pp. 1–40, 2007.
- [136] D. B. Williams and C. B. Carter, “Transmission electron microscopy: A textbook for materials science,” 2009.
- [137] M. Khan, “THE TRANSMISSION ELECTRON MICROSCOPE,” 2012.
- [138] R. R. Mather, “Surface modification of textiles by plasma treatments,” 2009.

-
- [139] C. S. Fadley, "X-ray photoelectron spectroscopy: Progress and perspectives," *J. Electron Spectros. Relat. Phenomena*, vol. 178–179, no. C, pp. 2–32, 2010.
- [140] J. Yano and V. K. Yachandra, "X-ray absorption spectroscopy," *Photosynth. Res.*, vol. 102, no. 2, pp. 241–254, 2009.
- [141] J. E. Penner-Hahn, "X-ray absorption spectroscopy in coordination chemistry," *Coord. Chem. Rev.*, vol. 190–192, pp. 1101–1123, 1999.
- [142] M. L. Baker, M. W. Mara, J. J. Yan, K. O. Hodgson, B. Hedman, and E. I. Solomon, "K- and L-edge X-ray absorption spectroscopy (XAS) and resonant inelastic X-ray scattering (RIXS) determination of differential orbital covalency (DOC) of transition metal sites," *Coord. Chem. Rev.*, vol. 345, pp. 182–208, 2017.
- [143] M. Herklotz *et al.*, "A novel high-throughput setup for in situ powder diffraction on coin cell batteries," *J. Appl. Crystallogr.*, vol. 49, pp. 340–345, 2016.
- [144] B. Ravel and M. Newville, "ATHENA, ARTEMIS, HEPHAESTUS: Data analysis for X-ray absorption spectroscopy using IFEFFIT," *J. Synchrotron Radiat.*, vol. 12, no. 4, pp. 537–541, 2005.
- [145] A. A. Abd-El-Latif *et al.*, "Insights into electrochemical reactions by differential electrochemical mass spectrometry," *TrAC - Trends Anal. Chem.*, vol. 70, pp. 4–13, 2015.
- [146] H. Baltruschat, "Differential electrochemical mass spectrometry," *J. Am. Soc. Mass Spectrom.*, vol. 15, no. 12, pp. 1693–1706, 2004.
- [147] M. S. Palagonia, C. Erinmwingbovo, D. Brogioli, and F. La Mantia, "Comparison between cyclic voltammetry and differential charge plots from galvanostatic cycling," *J. Electroanal. Chem.*, vol. 847, 2019.
- [148] M. Chatti *et al.*, "ELECTROCHEMICAL METHODES-Fundamentals and Applications, *Journal of Chemical Education*, vol. 60, no. 1, A25, 1983.
- [149] N. Aristov and A. Habekost, "Cyclic Voltammetry - A Versatile Electrochemical Method Investigating Electron Transfer Processes," *World J. Chem. Educ. Vol. 3, 2015, Pages 115-119*, vol. 3, no. 5, pp. 115–119, 2015.
- [150] V. S. Bagotsky, "Electrochemical Research Techniques," *Fundam. Electrochem. Second Ed.*, pp. 191–215, 2005.
- [151] H. Buschmann *et al.*, "Structure and dynamics of the fast lithium ion conductor 'Li₇La₃Zr₂O₁₂,'" *Phys. Chem. Chem. Phys.*, vol. 13, no. 43, pp. 19378–19392, 2011.
- [152] A. Kuhn, J.-Y. Choi, L. Robben, F. Tietz, M. Wilkening, and P. Heitjans, "Li Ion Dynamics in Al-Doped Garnet-Type Li₇La₃Zr₂O₁₂ Crystallizing with Cubic Symmetry Solid Electrolytes / Garnets / Lithium Ion Dynamics / NMR / Spin-Lattice Relaxation," *Z. Phys. Chem*, vol. 226, pp. 525–537, 2012.
- [153] I. Kokal, M. Somer, P. H. L. Notten, and H. T. Hintzen, "Sol-gel synthesis and lithium ion conductivity of Li₇La₃Zr₂O₁₂ with garnet-related type structure," *Solid State Ionics*, vol. 185, no. 1, pp. 42–46, 2011.
- [154] R. Djenadic *et al.*, "Nebulized spray pyrolysis of Al-doped Li₇La₃Zr₂O₁₂ solid electrolyte for battery applications," *Solid State Ionics*, vol. 263, pp. 49–56, 2014.

-
- [155] R. Djenadic, M. Botros, and H. Hahn, "Is Li-doped MgAl_2O_4 a potential solid electrolyte for an all-spinel Li-ion battery?," *Solid State Ionics*, vol. 287, pp. 71–76, 2016.
- [156] M. S. M. Ghazali, M. S. Shaifudin, W. R. W. Abdullah, W. M. I. W. M. Kamaruzzaman, M. F. M. Fekeri, and M. A. Zulkifli, "Conventional Sintering Effects on the Microstructure and Electrical Characteristics of Low-Voltage Ceramic Varistor," *Sinter. Technol. - Method Appl.*, 2018.
- [157] J. Li, M. Zhang, D. Zhang, Y. Yan, Z. Li, and Z. Nie, "Effect of sintering conditions on electrochemical properties of $\text{LiNi}_{0.8}\text{Co}_{0.1}\text{Mn}_{0.1}\text{O}_2$ as cathode material," *Int. J. Electrochem. Sci.*, vol. 15, no. 3, pp. 1881–1892, 2020.
- [158] Y. Xi, Y. Liu, D. Zhang, S. Jin, R. Zhang, and M. Jin, "Comparative study of the electrochemical performance of $\text{LiNi}_{0.5}\text{Co}_{0.2}\text{Mn}_{0.3}\text{O}_2$ and $\text{LiNi}_{0.8}\text{Co}_{0.1}\text{Mn}_{0.1}\text{O}_2$ cathode materials for lithium ion batteries," *Solid State Ionics*, vol. 327, no. June, pp. 27–31, 2018.
- [159] J. Wang *et al.*, "Spinel to Rock-Salt Transformation in High Entropy Oxides with Li Incorporation," *Electrochem*, vol. 1, no. 1, pp. 60–74, 2020.
- [160] Q. Wang *et al.*, "Multi-anionic and -cationic compounds: new high entropy materials for advanced Li-ion batteries," *Energy Environ. Sci.*, pp. 17–19, 2019.
- [161] N. Qiu, H. Chen, Z. Yang, S. Sun, Y. Wang, and Y. Cui, "A high entropy oxide ($\text{Mg}_{0.2}\text{Co}_{0.2}\text{Ni}_{0.2}\text{Cu}_{0.2}\text{Zn}_{0.2}\text{O}$) with superior lithium storage performance," *J. Alloys Compd.*, vol. 777, pp. 767–774, Mar. 2019.
- [162] B. Breitung *et al.*, "Gassing Behavior of High-Entropy Oxide Anode and Oxyfluoride Cathode Probed Using Differential Electrochemical Mass Spectrometry," *Batter. Supercaps*, pp. 1–10, 2020.
- [163] M. M. Thackeray, S. D. Baker, K. T. Adendorff, and J. B. Goodenough, "Lithium insertion into Co_3O_4 : A preliminary investigation," *Solid State Ionics*, vol. 17, no. 2, pp. 175–181, 1985.
- [164] K. M. Nam *et al.*, "Syntheses and characterization of wurtzite CoO, rocksalt CoO, and spinel Co_3O_4 nanocrystals: Their interconversion and tuning of phase and morphology," *Chem. Mater.*, vol. 22, no. 15, pp. 4446–4454, 2010.
- [165] J. Charlotte Li, K. He, E. A. Stach, and D. Su, "Comparison of Co_3O_4 and CoO Nanoparticles as Anodes for Lithium-ion Batteries," *Microsc. Microanal.*, vol. 21, no. S3, pp. 477–478, 2015.
- [166] J. Li *et al.*, "Kinetic Phase Evolution of Spinel Cobalt Oxide during Lithiation," *ACS Nano*, vol. 10, no. 10, pp. 9577–9585, 2016.
- [167] R. Jung *et al.*, "Effect of Ambient Storage on the Degradation of Ni-Rich Positive Electrode Materials (NMC811) for Li-Ion Batteries," *J. Electrochem. Soc.*, vol. 165, no. 2, pp. A132–A141, 2018.
- [168] T. Hatsukade, A. Schiele, P. Hartmann, T. Brezesinski, and J. Janek, "Origin of Carbon Dioxide Evolved during Cycling of Nickel-Rich Layered NCM Cathodes," *ACS Appl. Mater. Interfaces*, vol. 10, no. 45, pp. 38892–38899, 2018.
- [169] C. R. Mariappan *et al.*, "High electrochemical performance of 3D highly porous $\text{Zn}_{0.2}\text{Ni}_{0.8}\text{Co}_2\text{O}_4$ microspheres as an electrode material for electrochemical energy storage," *CrystEngComm*, vol. 20, no. 15, pp. 2159–2168, 2018.

-
- [170] R. Azmi, M. Masoumi, H. Ehrenberg, V. Trouillet, and M. Bruns, "Surface analytical characterization of $\text{LiNi}_{0.8-y}\text{Mn}_y\text{Co}_{0.2}\text{O}_2$ ($0 \leq y \leq 0.4$) compounds for lithium-ion battery electrodes," *Surf. Interface Anal.*, vol. 50, no. 11, pp. 1132–1137, 2018.
- [171] R. Azmi, V. Trouillet, M. Strafela, S. Ulrich, H. Ehrenberg, and M. Bruns, "Surface analytical approaches to reliably characterize lithium ion battery electrodes," *Surf. Interface Anal.*, vol. 50, no. 1, pp. 43–51, Jan. 2018.
- [172] V. Kumar *et al.*, "Pseudocapacitance of Mesoporous Spinel-Type MCo_2O_4 (M = Co, Zn, and Ni) Rods Fabricated by a Facile Solvothermal Route," *ACS Omega*, vol. 2, no. 9, pp. 6003–6013, Sep. 2017.
- [173] M. C. Biesinger, B. P. Payne, A. P. Grosvenor, L. W. M. Lau, A. R. Gerson, and R. S. C. Smart, "Resolving surface chemical states in XPS analysis of first row transition metals, oxides and hydroxides: Cr, Mn, Fe, Co and Ni," *Appl. Surf. Sci.*, vol. 257, no. 7, pp. 2717–2730, 2011.
- [174] E. Diler, B. Lescop, S. Rioual, G. Nguyen Vien, D. Thierry, and B. Rouvellou, "Initial formation of corrosion products on pure zinc and MgZn_2 examined by XPS," *Corros. Sci.*, vol. 79, pp. 83–88, 2014.
- [175] V. K. Mittal, P. Chandramohan, S. Bera, M. P. Srinivasan, S. Velmurugan, and S. V. Narasimhan, "Cation distribution in $\text{Ni}_x\text{Mg}_{1-x}\text{Fe}_2\text{O}_4$ studied by XPS and Mössbauer spectroscopy," *Solid State Commun.*, vol. 137, no. 1–2, pp. 6–10, 2006.
- [176] M. C. Biesinger, B. P. Payne, L. W. M. Lau, A. Gerson, and R. S. C. Smart, "X-ray photoelectron spectroscopic chemical state Quantification of mixed nickel metal, oxide and hydroxide systems," *Surf. Interface Anal.*, vol. 41, no. 4, pp. 324–332, Apr. 2009.
- [177] A. P. Grosvenor, M. C. Biesinger, R. S. C. Smart, and N. S. McIntyre, "New interpretations of XPS spectra of nickel metal and oxides," *Surf. Sci.*, vol. 600, no. 9, pp. 1771–1779, May 2006.
- [178] B. P. Payne, M. C. Biesinger, and N. S. McIntyre, "Use of oxygen/nickel ratios in the XPS characterisation of oxide phases on nickel metal and nickel alloy surfaces," *J. Electron Spectros. Relat. Phenomena*, vol. 185, no. 5–7, pp. 159–166, 2012.
- [179] M. C. Biesinger, L. W. M. Lau, A. R. Gerson, and R. S. C. Smart, "The role of the Auger parameter in XPS studies of nickel metal, halides and oxides," *Phys. Chem. Chem. Phys.*, vol. 14, no. 7, pp. 2434–2442, 2012.
- [180] B. P. Payne, M. C. Biesinger, and N. S. McIntyre, "X-ray photoelectron spectroscopy studies of reactions on chromium metal and chromium oxide surfaces," *J. Electron Spectros. Relat. Phenomena*, vol. 184, no. 1–2, pp. 29–37, Feb. 2011.
- [181] M. C. Biesinger, C. Brown, J. R. Mycroft, R. D. Davidson, and N. S. McIntyre, "X-ray photoelectron spectroscopy studies of chromium compounds," *Surf. Interface Anal.*, vol. 36, no. 12, pp. 1550–1563, 2004.
- [182] A. P. Grosvenor, B. A. Kobe, M. C. Biesinger, and N. S. McIntyre, "Investigation of multiplet splitting of Fe 2p XPS spectra and bonding in iron compounds," *Surf. Interface Anal.*, vol. 36, no. 12, pp. 1564–1574, 2004.

-
- [183] J. Töpfer, A. Feltz, D. Gräf, B. Hackl, L. Raupach, and P. Weissbrodt, “Cation Valencies and Distribution in the Spinel NiMn₂O₄ and M_zNiMn_{2-z}O₄ (M = Li, Cu) Studied by XPS,” *Phys. Status Solidi*, vol. 134, no. 2, pp. 405–415, Dec. 1992.
- [184] M. V. Reddy, G. Prithvi, K. P. Loh, and B. V. R. Chowdari, “Li storage and impedance spectroscopy studies on Co₃O₄, CoO, and CoN for Li-ion batteries,” *ACS Appl. Mater. Interfaces*, vol. 6, no. 1, pp. 680–690, 2014.
- [185] J. Wang *et al.*, “Lithium containing layered high entropy oxide structures,” *Sci. Rep.*, vol. 10, no. 1, pp. 1–13, 2020.
- [186] Q. Wang *et al.*, “Multi-anionic and -cationic compounds: New high entropy materials for advanced Li-ion batteries,” *Energy Environ. Sci.*, vol. 12, no. 8, pp. 2433–2442, 2019.
- [187] C. Oses, C. Toher, and S. Curtarolo, “High-entropy ceramics,” *Nat. Rev. Mater.*, vol. 5, no. 4, pp. 295–309, 2020.
- [188] Y. Zhang, “High-Entropy Materials,” *Springer Singapore*, 2019.
- [189] Y. Furushima, C. Yanagisawa, T. Nakagawa, Y. Aoki, and N. Muraki, “Thermal stability and kinetics of delithiated LiCoO₂,” *J. Power Sources*, vol. 196, no. 4, pp. 2260–2263, 2011.
- [190] S. Zhang, J. Ma, Z. Hu, G. Cui, and L. Chen, “Identifying and Addressing Critical Challenges of High-Voltage Layered Ternary Oxide Cathode Materials,” *Chem. Mater.*, vol. 31, no. 16, pp. 6033–6065, 2019.
- [191] C. M. Julien and A. Mauger, “Lithium-Ion Batteries,” 2020.
- [192] L. de Biasi, B. Schwarz, T. Brezesinski, P. Hartmann, J. Janek, and H. Ehrenberg, “Chemical, Structural, and Electronic Aspects of Formation and Degradation Behavior on Different Length Scales of Ni-Rich NCM and Li-Rich HE-NCM Cathode Materials in Li-Ion Batteries,” *Adv. Mater.*, vol. 31, no. 26, p. 1900985, Jun. 2019.
- [193] N. Yabuuchi and T. Ohzuku, “Novel lithium insertion material of LiCo_{1/3}Ni_{1/3}Mn_{1/3}O₂ for advanced lithium-ion batteries,” *J. Power Sources*, vol. 119–121, pp. 171–174, 2003.
- [194] J. Gu *et al.*, “Mg-Doped CuFeO₂ Photocathodes for Photoelectrochemical Reduction of Carbon Dioxide,” *J. Phys. Chem. C*, vol. 117, no. 24, pp. 12415–12422, Jun. 2013.
- [195] W. C. Sheets *et al.*, “Silver delafossite oxides,” *Inorg. Chem.*, vol. 47, no. 7, pp. 2696–2705, 2008.
- [196] Y. Jin and G. Chumanov, “Solution synthesis of pure 2H CuFeO₂ at low temperatures,” *RSC Adv.*, vol. 6, no. 31, pp. 26392–26397, 2016.
- [197] U. Kang *et al.*, “Photosynthesis of formate from CO₂ and water at 1% energy efficiency via copper iron oxide catalysis,” *Energy Environ. Sci.*, vol. 8, no. 9, pp. 2638–2643, 2015.
- [198] M. S. Prévot, Y. Li, N. Guijarro, and K. Sivula, “Improving charge collection with delafossite photocathodes: a host–guest CuAlO₂/CuFeO₂ approach,” *J. Mater. Chem. A*, vol. 4, no. 8, pp. 3018–3026, 2016.
- [199] M. S. Prévot, N. Guijarro, and K. Sivula, “Enhancing the Performance of a Robust Sol-Gel-Processed p-Type Delafossite CuFeO₂ Photocathode for Solar Water Reduction,” *ChemSusChem*, vol. 8, no. 8, pp. 1359–1367, 2015.

-
- [200] F. Otto, Y. Yang, H. Bei, and E. P. George, "Relative effects of enthalpy and entropy on the phase stability of equiatomic high-entropy alloys," *Acta Mater.*, vol. 61, no. 7, pp. 2628–2638, 2013.
- [201] P. Zhou *et al.*, "Stable layered Ni-rich $\text{LiNi}_{0.9}\text{Co}_{0.07}\text{Al}_{0.03}\text{O}_2$ microspheres assembled with nanoparticles as high-performance cathode materials for lithium-ion batteries," *J. Mater. Chem. A*, vol. 5, no. 6, pp. 2724–2731, 2017.
- [202] X. Zhang, W. J. Jiang, A. Mauger, Qilu, F. Gendron, and C. M. Julien, "Minimization of the cation mixing in $\text{Li}_{1+x}(\text{NMC})_{1-x}\text{O}_2$ as cathode material," *J. Power Sources*, vol. 195, no. 5, pp. 1292–1301, 2010.
- [203] M. Bianchini, M. Roca-Ayats, P. Hartmann, T. Brezesinski, and J. Janek, "There and Back Again—The Journey of LiNiO_2 as a Cathode Active Material," *Angew. Chemie Int. Ed.*, vol. 58, no. 31, pp. 10434–10458, Jul. 2019.
- [204] A. O. Kondrakov *et al.*, "Anisotropic Lattice Strain and Mechanical Degradation of High- and Low-Nickel NCM Cathode Materials for Li-Ion Batteries," *J. Phys. Chem. C*, vol. 121, no. 6, pp. 3286–3294, 2017.
- [205] A. Mao, H. Z. Xiang, Z. G. Zhang, K. Kuramoto, H. Zhang, and Y. Jia, "A new class of spinel high-entropy oxides with controllable magnetic properties," *J. Magn. Magn. Mater.*, vol. 497, p. 165884, 2020.
- [206] R. Azmi, M. Masoumi, H. Ehrenberg, V. Trouillet, and M. Bruns, "Surface analytical characterization of $\text{LiNi}_{0.8-y}\text{Mn}_y\text{Co}_{0.2}\text{O}_2$ ($0 \leq y \leq 0.4$) compounds for lithium-ion battery electrodes," *Surf. Interface Anal.*, vol. 50, no. 11, pp. 1132–1137, Nov. 2018.
- [207] L. Dahéron *et al.*, "Possible Explanation for the Efficiency of Al-Based Coatings on LiCoO_2 : Surface Properties of $\text{LiCo}_{1-x}\text{Al}_x\text{O}_2$ Solid Solution," *Chem. Mater.*, vol. 21, no. 23, pp. 5607–5616, Dec. 2009.
- [208] C. Zhao, F. Ding, Y. Lu, L. Chen, and Y.-S. Hu, "High-Entropy Layered Oxide Cathodes for Sodium-Ion Batteries," *Angew. Chemie Int. Ed.*, vol. 17, no. 11, p. 955, Nov. 2019.
- [209] Z. Xue *et al.*, "Sodium Doping to Enhance Electrochemical Performance of Overlithiated Oxide Cathode Materials for Li-Ion Batteries via Li/Na Ion-Exchange Method," *ACS Appl. Mater. Interfaces*, vol. 10, no. 32, pp. 27141–27149, 2018.
- [210] A. Abdellahi, A. Urban, S. Dacek, and G. Ceder, "The Effect of Cation Disorder on the Average Li Intercalation Voltage of Transition-Metal Oxides," *Chem. Mater.*, vol. 28, no. 11, pp. 3659–3665, 2016.
- [211] D. Li, Y. Sasaki, K. Kobayakawa, and Y. Sato, "Morphological, structural, and electrochemical characteristics of $\text{LiNi}_{0.5}\text{Mn}_{0.4}\text{M}_{0.1}\text{O}_2$ ($\text{M} = \text{Li}, \text{Mg}, \text{Co}, \text{Al}$)," *J. Power Sources*, vol. 157, no. 1, pp. 488–493, 2006.
- [212] L. De Biasi, A. O. Kondrakov, H. Geßwein, T. Brezesinski, P. Hartmann, and J. Janek, "Between Scylla and Charybdis: Balancing among Structural Stability and Energy Density of Layered NCM Cathode Materials for Advanced Lithium-Ion Batteries," *J. Phys. Chem. C*, vol. 121, no. 47, pp. 26163–26171, 2017.
- [213] S. C. Yin, Y. H. Rho, I. Swainson, and L. F. Nazar, "X-ray/neutron diffraction and electrochemical studies of lithium De/Re-intercalation in $\text{Li}_{1-x}\text{Co}_{1/3}\text{Ni}_{1/3}\text{Mn}_{1/3}\text{O}_2$ ($x = 0 \rightarrow 1$)," *Chem. Mater.*, vol. 18, no. 7, pp. 1901–1910, 2006.

- [214] K. Li and D. Xue, “Estimation of electronegativity values of elements in different valence states,” *J. Phys. Chem. A*, vol. 110, no. 39, pp. 11332–11337, 2006.
- [215] R. D. Shannon, “Revised effective ionic radii and systematic studies of interatomic distances in halides and chalcogenides,” *Acta Crystallogr. Sect. A*, vol. 32, no. 5, pp. 751–767, Sep. 1976.
- [216] A. Sarkar, B. Breitung, and H. Hahn, “High entropy oxides: The role of entropy, enthalpy and synergy,” *Scr. Mater.*, vol. 187, pp. 43–48, 2020.
- [217] J. Y. Hwang, S. T. Myung, and Y. K. Sun, “Sodium-ion batteries: Present and future,” *Chem. Soc. Rev.*, vol. 46, no. 12, pp. 3529–3614, 2017.
- [218] C. Delmas, “Sodium and Sodium-Ion Batteries: 50 Years of Research,” *Adv. Energy Mater.*, vol. 8, no. 17, 2018.
- [219] J. M. Tarascon, “Na-ion versus Li-ion Batteries: Complementarity Rather than Competitiveness,” *Joule*, vol. 4, no. 8, pp. 1616–1620, 2020.
- [220] V. Palomares, M. Casas-Cabanas, E. Castillo-Martínez, M. H. Han, and T. Rojo, “Update on Na-based battery materials. A growing research path,” *Energy Environ. Sci.*, vol. 6, no. 8, pp. 2312–2337, 2013.
- [221] C. Delmas, D. Carlier, and M. Guignard, “The Layered Oxides in Lithium and Sodium-Ion Batteries: A Solid-State Chemistry Approach,” *Adv. Energy Mater.*, vol. 11, no. 2, 2021.
- [222] M. H. Han, E. Gonzalo, G. Singh, and T. Rojo, “A comprehensive review of sodium layered oxides: Powerful cathodes for Na-ion batteries,” *Energy Environ. Sci.*, vol. 8, no. 1, pp. 81–102, 2015.
- [223] R. J. Clément, P. G. Bruce, and C. P. Grey, “Review—Manganese-Based P2-Type Transition Metal Oxides as Sodium-Ion Battery Cathode Materials,” *J. Electrochem. Soc.*, vol. 162, no. 14, pp. A2589–A2604, 2015.
- [224] J. Y. Hwang, C. S. Yoon, I. Belharouak, and Y. K. Sun, “A comprehensive study of the role of transition metals in O3-type layered $\text{Na}[\text{Ni}_x\text{Co}_y\text{Mn}_z]\text{O}_2$ ($x = 1/3, 0.5, 0.6, \text{ and } 0.8$) cathodes for sodium-ion batteries,” *J. Mater. Chem. A*, vol. 4, no. 46, pp. 17952–17959, 2016.
- [225] C. Zhao *et al.*, “Revealing High Na-Content P2-Type Layered Oxides as Advanced Sodium-Ion Cathodes,” *J. Am. Chem. Soc.*, vol. 142, no. 12, pp. 5742–5750, 2020.
- [226] Y. Wang, R. Xiao, Y. S. Hu, M. Avdeev, and L. Chen, “P2- $\text{Na}_{0.6}[\text{Cr}_{0.6}\text{Ti}_{0.4}]\text{O}_2$ cation-disordered electrode for high-rate symmetric rechargeable sodium-ion batteries,” *Nat. Commun.*, vol. 6, pp. 1–9, 2015.
- [227] T. Y. Yu, J. Y. Hwang, D. Aurbach, and Y. K. Sun, “Microsphere $\text{Na}_{0.65}[\text{Ni}_{0.17}\text{Co}_{0.11}\text{Mn}_{0.72}]\text{O}_2$ Cathode Material for High-Performance Sodium-Ion Batteries,” *ACS Appl. Mater. Interfaces*, vol. 9, no. 51, pp. 44534–44541, 2017.
- [228] N. A. Katcho *et al.*, “Origins of Bistability and Na Ion Mobility Difference in P2- and O3- $\text{Na}_{2/3}\text{Fe}_{2/3}\text{Mn}_{1/3}\text{O}_2$ Cathode Polymorphs,” *Adv. Energy Mater.*, vol. 7, no. 1, 2017.
- [229] D. H. Lee, J. Xu, and Y. S. Meng, “An advanced cathode for Na-ion batteries with high rate and excellent structural stability,” *Phys. Chem. Chem. Phys.*, vol. 15, no. 9, pp. 3304–3312, 2013.
- [230] Q. Liu *et al.*, “P2-type $\text{Na}_{2/3}\text{Ni}_{1/3}\text{Mn}_{2/3}\text{O}_2$ as a cathode material with high-rate and long-life for sodium ion storage,” *J. Mater. Chem. A*, vol. 7, no. 15, pp. 9215–9221, 2019.

-
- [231] T. Liu *et al.*, “Correlation between manganese dissolution and dynamic phase stability in spinel-based lithium-ion battery,” *Nat. Commun.*, vol. 10, no. 1, pp. 1–11, 2019.
- [232] S. Kumakura, Y. Tahara, K. Kubota, K. Chihara, and S. Komaba, “Sodium and Manganese Stoichiometry of P2-Type $\text{Na}_{2/3}\text{MnO}_2$,” *Angew. Chemie - Int. Ed.*, vol. 55, no. 41, pp. 12760–12763, 2016.
- [233] C. Zhan, T. Wu, J. Lu, and K. Amine, “Dissolution, migration, and deposition of transition metal ions in Li-ion batteries exemplified by Mn-based cathodes-A critical review,” *Energy Environ. Sci.*, vol. 11, no. 2, pp. 243–257, 2018.
- [234] W. Zuo *et al.*, “Highly-stable P2- $\text{Na}_{0.67}\text{MnO}_2$ electrode enabled by lattice tailoring and surface engineering,” *Energy Storage Mater.*, vol. 26, pp. 503–512, 2020.
- [235] J. M. Paulsen, R. A. Donabarger, and J. R. Dahn, “Layered T2-, O6-, O2-, and P2-Type $\text{A}_{2/3}[\text{M}'_{1/3}\text{M}_2\text{O}_2]$ Bronzes, A = Li, Na; M' = Ni, Mg; M = Mn, Ti,” pp. 2257–2267, 2000.
- [236] T. Risthaus *et al.*, “A high-capacity P2 $\text{Na}_{2/3}\text{Ni}_{1/3}\text{Mn}_{2/3}\text{O}_2$ cathode material for sodium ion batteries with oxygen activity,” *J. Power Sources*, vol. 395, no. March, pp. 16–24, 2018.
- [237] J. Li *et al.*, “P2 - Type $\text{Na}_{0.67}\text{Mn}_{0.8}\text{Cu}_{0.1}\text{Mg}_{0.1}\text{O}_2$ as a new cathode material for sodium-ion batteries: Insights of the synergetic effects of multi-metal substitution and electrolyte optimization,” *J. Power Sources*, vol. 416, no. November 2018, pp. 184–192, 2019.
- [238] I. Hasa, S. Passerini, and J. Hassoun, “Toward high energy density cathode materials for sodium-ion batteries: investigating the beneficial effect of aluminum doping on the P2-type structure,” *J. Mater. Chem. A*, vol. 5, no. 9, pp. 4467–4477, 2017.
- [239] R. Jung, M. Metzger, F. Maglia, C. Stinner, and H. A. Gasteiger, “Chemical versus electrochemical electrolyte oxidation on NMC111, NMC622, NMC811, LNMO, and conductive carbon,” *J. Phys. Chem. Lett.*, vol. 8, no. 19, pp. 4820–4825, 2017.
- [240] Z. Liu, X. Xu, S. Ji, L. Zeng, D. Zhang, and J. Liu, “Recent Progress of P2-Type Layered Transition-Metal Oxide Cathodes for Sodium-Ion Batteries,” *Chem. - A Eur. J.*, vol. 26, no. 35, pp. 7747–7766, 2020.
- [241] J. Wang *et al.*, “Insights into P2-Type Layered Positive Electrodes for Sodium Batteries: From Long-Range Order to Short-Range Order,” *ACS Appl. Mater. Interfaces*, vol. 12, no. 4, pp. 5017–5024, 2020.
- [242] Z. Y. Li, R. Gao, L. Sun, Z. Hu, and X. Liu, “Designing an advanced P2- $\text{Na}_{0.67}\text{Mn}_{0.65}\text{Ni}_{0.2}\text{Co}_{0.15}\text{O}_2$ layered cathode material for Na-ion batteries,” *J. Mater. Chem. A*, vol. 3, no. 31, pp. 16272–16278, 2015.
- [243] T. Chen *et al.*, “A P2-type $\text{Na}_{0.44}\text{Mn}_{0.6}\text{Ni}_{0.3}\text{Cu}_{0.1}\text{O}_2$ cathode material with high energy density for sodium-ion batteries,” *J. Mater. Chem. A*, vol. 6, no. 26, pp. 12582–12588, 2018.
- [244] J. Yoshida *et al.*, “New P2 - $\text{Na}_{0.70}\text{Mn}_{0.60}\text{Ni}_{0.30}\text{Co}_{0.10}\text{O}_2$ Layered Oxide as Electrode Material for Na-Ion Batteries,” *J. Electrochem. Soc.*, vol. 161, no. 14, pp. A1987–A1991, 2014.
- [245] C. Luo, A. Langrock, X. Fan, Y. Liang, and C. Wang, “P2-type transition metal oxides for high performance Na-ion battery cathodes,” *J. Mater. Chem. A*, vol. 5, no. 34, pp. 18214–18220, 2017.
- [246] S. Xu *et al.*, “Suppressing the voltage decay of low-cost P2-type iron-based cathode materials for sodium-ion batteries,” *J. Mater. Chem. A*, vol. 6, no. 42, pp. 20795–20803, 2018.

-
- [247] E. Talaie, V. Duffort, H. L. Smith, B. Fultz, and L. F. Nazar, "Structure of the high voltage phase of layered P2-Na_{2/3-z}[Mn_{1/2}Fe_{1/2}]O₂ and the positive effect of Ni substitution on its stability," *Energy Environ. Sci.*, vol. 8, no. 8, pp. 2512–2523, 2015.
- [248] J. Y. Hwang, J. Kim, T. Y. Yu, and Y. K. Sun, "A New P2-Type Layered Oxide Cathode with Extremely High Energy Density for Sodium-Ion Batteries," *Adv. Energy Mater.*, vol. 9, no. 15, 2019.
- [249] J. Kasemchainan *et al.*, "Nature of the "Z"-phase in layered Na-ion battery cathodes," *Energy Environ. Sci.*, vol. 12, pp. 2223–2232, 2019.
- [250] Z. Lu and J. R. Dahn, "In Situ X-Ray Diffraction Study of P2-Na_{2/3}Ni_{1/3}Mn_{2/3}O₂," *J. Electrochem. Soc.*, vol. 148, no. 11, p. A1225, 2001.
- [251] L. Zhang, C. Tsolakidou, S. Mariyappan, J. M. Tarascon, and S. Trabesinger, "Unraveling gas evolution in sodium batteries by online electrochemical mass spectrometry," *Energy Storage Mater.*, vol. 42, no. July, pp. 12–21, 2021.
- [252] J. K. Papp *et al.*, "A comparison of high voltage outgassing of LiCoO₂, LiNiO₂, and Li₂MnO₃ layered Li-ion cathode materials," *Electrochim. Acta*, vol. 368, 2021.
- [253] R. Jung, M. Metzger, F. Maglia, C. Stinner, and H. A. Gasteiger, "Oxygen Release and Its Effect on the Cycling Stability of LiNi_xMn_yCo_zO₂ (NMC) Cathode Materials for Li-Ion Batteries," *J. Electrochem. Soc.*, vol. 164, no. 7, pp. A1361–A1377, 2017.
- [254] J. Wandt, A. T. S. Freiberg, A. Ogrodnik, and H. A. Gasteiger, "Singlet oxygen evolution from layered transition metal oxide cathode materials and its implications for lithium-ion batteries," *Mater. Today*, vol. 21, no. 8, pp. 825–833, 2018.
- [255] M. Metzger, B. Strehle, S. Solchenbach, and H. A. Gasteiger, "Origin of H₂ Evolution in LIBs: H₂O Reduction vs. Electrolyte Oxidation," *J. Electrochem. Soc.*, vol. 163, no. 5, pp. A798–A809, 2016.
- [256] A. Gutierrez *et al.*, "On Disrupting the Na⁺-Ion/Vacancy Ordering in P2-Type Sodium-Manganese-Nickel Oxide Cathodes for Na⁺-Ion Batteries," *J. Phys. Chem. C*, vol. 122, no. 41, pp. 23251–23260, 2018.
- [257] K. Luo *et al.*, "Charge-compensation in 3d-transition-metal-oxide intercalation cathodes through the generation of localized electron holes on oxygen," *Nat. Chem.*, vol. 8, no. 7, pp. 684–691, 2016.
- [258] R. A. House *et al.*, "What Triggers Oxygen Loss in Oxygen Redox Cathode Materials?," *Chem. Mater.*, vol. 31, no. 9, pp. 3293–3300, 2019.
- [259] H. Xu, S. Guo, and H. Zhou, "Review on anionic redox in sodium-ion batteries," *J. Mater. Chem. A*, vol. 7, no. 41, pp. 23662–23678, 2019.
- [260] J. H. Park *et al.*, "Anionic Redox Reactions in Cathodes for Sodium-Ion Batteries," *ChemElectroChem*, vol. 8, no. 4, pp. 625–643, 2021.
- [261] S. Solchenbach, G. Hong, A. T. S. Freiberg, R. Jung, and H. A. Gasteiger, "Electrolyte and SEI Decomposition Reactions of Transition Metal Ions Investigated by On-Line Electrochemical Mass Spectrometry," *J. Electrochem. Soc.*, vol. 165, no. 14, pp. A3304–A3312, 2018.

-
- [262] K. U. Schwenke, S. Solchenbach, J. Demeaux, B. L. Lucht, and H. A. Gasteiger, “ The Impact of CO₂ Evolved from VC and FEC during Formation of Graphite Anodes in Lithium-Ion Batteries ,” *J. Electrochem. Soc.*, vol. 166, no. 10, pp. A2035–A2047, 2019.
- [263] B. B. Berkes, A. Jozwiuk, H. Sommer, T. Brezesinski, and J. Janek, “Simultaneous acquisition of differential electrochemical mass spectrometry and infrared spectroscopy data for in situ characterization of gas evolution reactions in lithium-ion batteries,” *Electrochem. commun.*, vol. 60, pp. 64–69, 2015.
- [264] B. Wang *et al.*, “Which of the nickel-rich NCM and NCA is structurally superior as a cathode material for lithium-ion batteries?,” *J. Mater. Chem. A*, vol. 9, no. 23, pp. 13540–13551, 2021.
- [265] W. Li *et al.*, “Mn versus Al in Layered Oxide Cathodes in Lithium-Ion Batteries: A Comprehensive Evaluation on Long-Term Cyclability,” *Adv. Energy Mater.*, vol. 8, no. 15, 2018.

F. Curriculum Vitae

Education

- 11/2018-present PhD student
- Research field: High entropy materials for reversible energy storage
- Institute of Nanotechnology (INT), Karlsruhe Institute of Technology (KIT), Hermann-von-Helmholtz-Platz 1, 76344, Eggenstein-Leopoldshafen, Germany
- 09/2015-07/2019 Master in Material Science and Engineering
- Research field: Preparing efficient catalysts and solid electrolytes for electrochemical devices
- State Key Laboratory of Advanced Technology for Materials Synthesis and Processing
- Wuhan University of Technology, Wuhan, 430070, P.R. China
- 09/2010-07/2014 Bachelor in Materials Chemistry
- Institute of materials Science and Engineering
- Shandong University of Technology, Zibo, 255000, P.R. China

Honors and Awards

- 11/2019 The First-Class scientific research achievement award (Organized by Wuhan University of Technology)
- 08/2018 Awarded a scholarship (3.5 years) under the State Scholarship Fund organized by the China Scholarship Council (CSC) for PhD study
- 02/2018 The Third-Class scientific research achievement award (Organized by Wuhan University of Technology)
- 09/2017 The national Second-Class Scholarship
- 09/2016 The national Second-Class Scholarship
- 08/2015 The national First-Class Scholarship

Peer-reviewed publications (* = published during Ph.D. program):

1. **Junbo Wang**, Sören L. Dreyer, Kai Wang, Ziming Ding, Thomas Diemant, Guruprakash Karkera, Yanjiao Ma, Abhishek Sarkar, Bei Zhou, Mikhail V. Gorbunov, Ahmad Omar, Daria Mikhailova, Volker Presser, Maximilian Fichtner, Horst Hahn, Torsten Brezesinski, Ben Breitung, and Qingsong Wang, “P2-Type Layered High-Entropy Oxides as Sodium-Ion Cathode Materials”. (Accepted for publication in the Journal of Materials Futures)
2. Yanyan Cui, Tongtong Fu, **Junbo Wang**, Horst Hahn, Ben Breitung, Yushu Tang, Simon Schweidler, and Miriam Botros, “Photonic curing assistant for coating high entropy oxide on NCM851005”. (In submission)*
3. Yanyan Cui, Parvathy Anitha Sukkurji, Simon Schweidler, Kai Wang, Raheleh Azmi, **Junbo Wang**, Alexandra M. Nunn, Horst Hahn, Qingsong Wang, Ben Breitung, and Miriam Botros, “Tailored High Entropy Fluorides as High-Capacity Lithium-Ion Battery Cathodes: An Insight into the Conversion Reaction Mechanism”. (In submission) *
4. **Junbo Wang**, Yanyan Cui, Qingsong Wang, Kai Wang, Xiaohui Huang, David Stenzel, Abhishek Sarkar, Raheleh Azmi, Thomas Bergfeldt, Subramshu S. Bhattacharya, Robert Kruk, Horst Hahn, Simon Schweidler, Torsten Brezesinski, and Ben Breitung, “Lithium containing layered high entropy oxide structures”. Scientific Reports, 2020, 10, 18430. *
5. Ling Lin, Kai Wang, Raheleh Azmi, **Junbo Wang**, Abhishek Sarkar, Miriam Botros, Saleem Najib, Yanyan Cui, David Stenzel, Parvathy Anitha Sukkurji, Qingsong Wang, Horst Hahn, Simon Schweidler, and Ben Breitung, “Mechanochemical synthesis: route to novel rock-salt structured high-entropy oxides and oxyfluorides”, Journal of Materials Science, 2020, 55, 16879. *
6. **Junbo Wang**, David Stenzel, Raheleh Azmi, Saleem Najib, Kai Wang, Jaehoon Jeong, Abhishek Sarkar, Qingsong Wang, Parvathy Anitha Sukkurji, Thomas Bergfeldt, Miriam Botros, Julia Maibach, Horst Hahn, Torsten Brezesinski, and Ben Breitung, “Spinel to Rock-Salt Transformation in High Entropy Oxides with Li Incorporation“, Electrochem, 2020, 1, 60. *
7. **Junbo Wang**, MeilingFan, WenmaoTu, Kai Chen, Yafei Shen, Haining Zhang, “In situ growth of Co_3O_4 on nitrogen-doped hollow carbon nanospheres as air electrode for lithium-air batteries”, Journal of Alloys and Compounds, 2019, 777, 944.
8. **Junbo Wang**, Xiaofeng Li, Meiling Fan, Haining Zhang, Wenmao Tu, “Nitrogen and Sulfur Co-Doped Hollow Carbon Nanospheres Derived from Surface-Attached Polyelectrolyte Monolayers”, ChemistrySelect, 2018, 3, 3006.

Conference talks:

Junbo Wang, Abhishek Sarkar, Qingsong Wang, Ben Breitung, “Multi-Cationic and Multi-Anionic High Entropy Materials for Reversible Energy Storage”, BIT's 9th Annual World Congress of Nano Science & Technology-2019, Najing, China, 2019.

Junbo Wang, Abhishek Sarkar, Qingsong Wang, Ben Breitung, “Multi-Cationic and Multi-Anionic High Entropy Materials for Reversible Energy Storage”, Materials Science International Forum, online conference, 2021.

Junbo Wang, Qingsong Wang, Ben Breitung, “Introduction of the high-entropy concept into Na-ion batteries”, EnABLES-Thin-film Solid-state Batteries for Medical Applications, online conference, 2021.

Posters:

Junbo Wang, David Stenzel, Kai Wang, Abhishek Sarkar, Horst Hahn, Ben Breitung, “Layered High-Entropy Oxide Structures for Reversible Energy Storage”, POLiS - Joint Cluster of Excellence of KIT & Ulm University with Associated Partners JLU Gießen & ZSW, Ulm, Germany, 2020.